Functional Plasmonic Nanocircuitry

Dissertation zur Erlangung des
naturwissenschaftlichen Doktorgrades
der Julius-Maximilians-Universität Würzburg

vorgelegt von

Gary Razinskas

aus Werneck

Würzburg 2017

Eingereicht am: 13. Dezember 2017
bei der Fakultät für Physik und Astronomie

1. Gutachter: Prof. Dr. Bert Hecht
2. Gutachter: Prof. Dr. Tobias Brixner
3. Gutachter: _____
der Dissertation

Vorsitzender: Prof. Dr. Karl Brunner

1. Prüfer: Prof. Dr. Bert Hecht
2. Prüfer: Prof. Dr. Tobias Brixner
3. Prüfer: Prof. Dr. Johanna Erdmenger
im Promotionskolloquium

Tag des Promotionskolloquiums: 26. Juli 2018

Doktorurkunde ausgehändigt am: _____

Contents

Abstract v

List of publications vii

1 Introduction & overview 1

2 Classical electromagnetism 7
2.1 Maxwell's equations . . . 8
2.2 Conservation laws . . . 9
2.3 Constitutive relations . . . 9
2.4 Vector Helmholtz equation . . . 10

3 Fundamentals of plasmonics 13
3.1 Optical response of noble metals . . . 13
3.2 Surface plasmon polaritons . . . 15
3.3 Surface plasmon modes in double-interface systems . . . 19
3.3.1 Metal-insulator-metal architecture . . . 19
3.3.2 Insulator-metal-insulator architecture . . . 21

4 Numerical simulations 23
4.1 Finite-difference time-domain algorithm . . . 24
4.2 Simulation setup . . . 26
4.3 Frequency-domain eigenmode solver . . . 29
4.4 Post-processing procedures . . . 30
4.4.1 Near- to far-field projections . . . 31
4.4.2 Far-field image calculation . . . 32
4.4.3 Mode overlap analysis . . . 33
4.4.4 Mode reflectivity fitting at waveguide discontinuity . . . 36

5 Plasmonic waveguide designs 37
5.1 Bottom-up assembled nanowire geometry . . . 38
5.2 Top-down fabricated waveguide geometries . . . 41
5.2.1 Single-mode plasmonic waveguides . . . 41
5.2.2 Multi-mode plasmonic waveguides . . . 44

6 Limits of Kirchhoff's laws in plasmonics **47**
6.1 Motivation . . . 47
6.2 Idealized TWTL junction . . . 49
6.3 Dimension dependent deviations . . . 52
6.4 Finite stub tuning . . . 54
6.5 Antenna-stub system . . . 56
6.6 Conclusion . . . 58

7 Transmission of plasmons through a nanowire **59**
7.1 Motivation . . . 59
7.2 Sample fabrication and experimental setup . . . 60
7.3 Analytical model . . . 63
7.4 Simulation and experiment . . . 65
7.5 Conclusion . . . 68

8 Multimode plasmon excitation and *in situ* analysis **69**
8.1 Motivation . . . 69
8.2 Synthesis of multimode plasmonic excitations . . . 71
8.3 Analysis of multimode plasmonic excitations . . . 73
8.4 Polarization and position dependent excitation efficiency . . . 76
8.5 Group velocity of pure-mode contributions . . . 77
8.6 Conclusion . . . 77

9 Coherent control of plasmon propagation in a nanocircuit **79**
9.1 Motivation . . . 79
9.2 Directional coupler design and simulation . . . 81
9.3 Experiments . . . 89
9.3.1 Single-pulse routing and coherent spatiotemporal control . . . 90
9.3.2 Coherent switching . . . 92
9.3.3 Nonlinear relative phase change . . . 93
9.4 Conclusion . . . 96

10 Normal-incidence PEEM imaging of propagating plasmon modes **97**
10.1 Motivation . . . 97
10.2 Numerical modelling of PEEM yield . . . 99
10.3 PEEM pattern periodicity . . . 101
10.4 Spatial switching in optical and PEEM measurements . . . 105
10.5 Conclusion . . . 106

11 Prospects of plasmonic nanocircuitry **107**
11.1 Spin-optical nanocircuitry . . . 107
11.2 Quantum plasmonic nanocircuity . . . 110

12 Summary & outlook **113**

Zusammenfassung & Ausblick **117**

A Analytical model for eigenmodes of cylindrical nanowires **121**

B Analytical model of systems involving stubs and load antennas **123**
B.1 Parallel connection of stub and infinite TWTL 123
B.2 Reflection coefficient of load antenna 124
B.3 Parallel connection of stub and load antenna terminated finite TWTL . 125

Bibliography **129**

Acknowledgements **153**

Abstract

In this work, functional plasmonic nanocircuitry is examined as a key of revolutionizing state-of-the-art electronic and photonic circuitry in terms of integration density and transmission bandwidth. In this context, numerical simulations enable the design of dedicated devices, which allow fundamental control of photon flow at the nanometer scale via single or multiple plasmonic eigenmodes. The deterministic synthesis and in situ analysis of these eigenmodes is demonstrated and constitutes an indispensable requirement for the practical use of any device. By exploiting the existence of multiple eigenmodes and coherence - both not accessible in classical electronics - a nanoscale directional coupler for the ultrafast spatial and spatiotemporal coherent control of plasmon propagation is conceived. Future widespread application of plasmonic nanocircuitry in quantum technologies is boosted by the promising demonstrations of spin-optical and quantum plasmonic nanocircuitry.

Kurzfassung

In dieser Arbeit werden funktionelle plasmonische Schaltkreise als Schlüssel zur Revolutionierung modernster elektronischer und photonischer Schaltkreise in Bezug auf deren Integrationsdichte und Übertragungsbandbreite untersucht. Mit Hilfe numerischer Simulationen werden Bauelemente speziell für die Steuerung des Photonenflusses im Nanometerbereich mittels einzelner bzw. mehrerer plasmonischer Eigenmoden konzipiert. Die deterministische Synthese und Analyse solcher Eigenmoden wird aufgezeigt und stellt eine unverzichtbare Voraussetzung für die praktische Anwendung eines jeden Nanoschaltkreises dar. Durch die Existenz mehrerer Eigenmoden und Kohärenz - beide in der klassischen Elektronik nicht zugänglich - lässt sich ein nanoskaliger Richtkoppler für die ultraschnelle räumliche und räumlich-zeitliche kohärente Kontrolle der Plasmonenausbreitung entwerfen. Künftig werden plasmonische Schaltkreise aufgrund der vielversprechenden Demonstrationen von spinoptischen und quantenplasmonischen Schaltkreisen in Quantentechnologien weite Verbreitung finden.

List of publications

[A] C. Rewitz, T. Keitzl, P. Tuchscherer, J.-S. Huang, P. Geisler, G. Razinskas, B. Hecht, and T. Brixner. *Ultrafast plasmon propagation in nanowires characterized by far-field spectral interferometry.* Nano Lett. **12** (1), pp. 45-49 (2012).

[B] C. Rewitz, T. Keitzl, P. Tuchscherer, S. Goetz, P. Geisler, G. Razinskas, B. Hecht, and T. Brixner. *Spectral-interference microscopy for characterization of functional plasmonic elements.* Opt. Express **20** (13), pp. 14632-14647 (2012).

[C] T. Brixner, M. Aeschlimann, A. Fischer, P. Geisler, S. Goetz, B. Hecht, J.-S. Huang, T. Keitzl, C. Kramer, P. Melchior, W. Pfeiffer, G. Razinskas, C. Rewitz, C. Schneider, C. Strüber, P. Tuchscherer, and D. V. Voronine. *Coherent spectroscopies on ultrashort time and length scales.* EPJ Web of Conferences **41**, p. 09017 (2013).

[D] P. Geisler*, G. Razinskas*, E. Krauss, X.-F. Wu, C. Rewitz, P. Tuchscherer, S. Goetz, C.-B. Huang, T. Brixner, and B. Hecht. *Multimode plasmon excitation and in situ analysis in top-down fabricated nanocircuits.* Phys. Rev. Lett. **111** (18), p. 183901 (2013).

[E] C. Rewitz, G. Razinskas, P. Geisler, E. Krauss, S. Goetz, M. Pawłowska, B. Hecht, and T. Brixner. *Coherent control of plasmon propagation in a nanocircuit.* Phys. Rev. Appl. **1** (1), p. 014007 (2014).

[F] P. Then, G. Razinskas, T. Feichtner, P. Haas, A. Wild, N. Bellini, R. Osellame, G. Cerullo, and B. Hecht. *Remote detection of single emitters via optical waveguides.* Phys. Rev. A **89** (5), p. 053801 (2014).

[G] M. Pawłowska, S. Goetz, C. Dreher, M. Wurdack, E. Krauss, G. Razinskas, P. Geisler, B. Hecht, and T. Brixner. *Shaping and spatiotemporal characterization of sub-10-fs pulses focused by a high-NA objective.* Opt. Express **22** (25), pp. 31496-31510 (2014).

[H] P. Klaer*, G. Razinskas*, M. Lehr, K. Krewer, F. Schertz, X.-F. Wu, B. Hecht, G. Schönhense, and H. J. Elmers. *Robustness of plasmonic angular momentum confinement in cross resonant optical antennas.* Appl. Phys. Lett. **106** (26), p. 261101 (2015).

[I] T.-M. Liu, T. Wang, A. H. Reid, M. Savoini, X. Wu, B. Koene, P. Granitzka, C. E. Graves, D. J. Higley, Z. Chen, G. Razinskas, M. Hantschmann, A. Scherz, J. Stöhr, A. Tsukamoto, B. Hecht, A. V. Kimel, A. Kirilyuk, T. Rasing, and H. A. Dürr. *Nanoscale confinement of all-optical magnetic switching in TbFeCo - Competition with nanoscale heterogeneity.* Nano Lett. **15** (10), pp. 6862-6868 (2015).

[J] S. Goetz, G. Razinskas, E. Krauss, C. Dreher, M. Wurdack, P. Geisler, M. Pawłowska, B. Hecht, and T. Brixner. *Investigation of the nonlinear refractive index of single-crystalline thin gold films and plasmonic nanostructures.* Appl. Phys. B **122** (4), pp. 1-10 (2016).

[K] P. Klaer, G. Razinskas, M. Lehr, X. Wu, B. Hecht, F. Schertz, H.-J. Butt, G. Schönhense, and H. J. Elmers. *Polarization dependence of plasmonic near-field enhanced photoemission from cross antennas.* Appl. Phys. B **122** (5), pp. 1-7 (2016).

[L] K. Chen, G. Razinskas, T. Feichtner, S. Großmann, S. Christiansen, and B. Hecht. *Electromechanically tunable suspended optical nanoantenna.* Nano Lett. **16** (4), pp. 2680-2685 (2016).

[M] G. Razinskas, D. Kilbane, P. Melchior, P. Geisler, E. Krauss, S. Mathias, B. Hecht, and M. Aeschlimann. *Normal-incidence PEEM imaging of propagating modes in a plasmonic nanocircuit.* Nano Lett. **16** (11), pp. 6832-6837 (2016).

[N] X. Wu, P. Jiang, G. Razinskas, Y. Huo, H. Zhang, M. Kamp, A. Rastelli, O. G. Schmidt, B. Hecht, K. Lindfors, and M. Lippitz. *On-chip single-plasmon nanocircuit driven by a self-assembled quantum dot.* Nano Lett. **17** (7), pp. 4291-4296 (2017).

[O] P. Geisler*, E. Krauss*, G. Razinskas*, and B. Hecht. *Transmission of plasmons through a nanowire.* ACS Photonics **4** (7), pp. 1615-1620 (2017).

[P] G. Razinskas, P. Biagioni, and B. Hecht. *Limits of Kirchhoff's laws in plasmonics.* Sci. Rep. **8** (1921), pp. 1-9 (2018)

* authors contributed equally

Considerable parts of selected peer-reviewed publications listed on the previous pages have been used in this dissertation as detailed in the following table. Sources of published figures within the dissertation are indicated at the end of the respective figure captions.

Publication	Usage	Dissertation
[P]	text reproduced and modified	Chap. 6
[O]	text reproduced and modified	Chap. 7
[D]	text reproduced, rearranged, and extended	Chap. 8
[E]	text reproduced, modified, and extended	Chap. 9
[J]	parts of text reproduced and modified	Chap. 9
[M]	text reproduced and modified	Chap. 10
[N]	parts of text modified	Chap. 11
[P]	text reproduced and modified	App. B

Chapter 1

Introduction & overview

Today's electronic integrated circuits, including micro-processors, micro-controller, and static random-access memory are based on complementary metal-oxide-semiconductor (CMOS) technology. Enormous technological advances over the past five decades made Moore's law [1], which predicts a doubling of transistor numbers every two years [2], a self-fulfilling prophecy. In 2017, this exponential increase in transistor density lead to remarkable transistor feature sizes approaching 10 nm (in accordance with the 10 nm technology node defined by the International Technology Roadmap for Semiconductors) allowing over one billion transistors on a single micro-chip.

The scaling toward smaller, faster, and more efficient devices, however, indisputably brings about fundamental challenges and limitations [3] in processing data with electrons, as evident from the slowed progression in processor speeds and bit rates. Their origin is associated with both thermal [4, 5] and signal delay issues arising due to the electrical interconnects that are necessary to transmit information from one place to another. The latter one is dominated by resistive-capacitive (RC) delay τ, which is determined by the product of the interconnect's distributed resistance R and capacitance C. While a shrinking of the wire's cross-sectional area A leaves the capacitance almost unchanged [6], its resistance is increased according to $R = \rho\frac{l}{A}$, where ρ and l are the interconnect's electrical resistivity and length, respectively. A substitution of aluminum wires by copper wires reduces this resistance and thus the delay.

The increasingly important role of the RC delay is reflected by the upper limit of the achievable bit rate $B = \frac{1}{\tau} \leq B_0 \frac{A}{l^2}$ with $B_0 \approx 10^{16}$ bits/s for typical on-chip nano-electronic interconnects [7]. The scale invariance of B under growing and shrinking of all interconnect dimensions hinders a steady increase in accessible bit rate capacities, in contrast to the ever decreasing transistor delay for shrinking dimensions. Instead, to further boost central processing unit (CPU) performance multicore technologies are exploited to keep up with the demand.

On the other hand, on scales much larger than the footprint size of modern electronics fiber-optics has become the method of choice in digital communication, e.g. for long haul information exchange. Here, spatially and temporally coherent light of mostly semiconductor lasers routinely forms a pulsed electromagnetic carrier wave that is transmitted along dielectric optical fibers. Modulation of this carrier wave enables the transport of data with unprecedented bandwidth compared to the aforementioned cop-

per interconnection. Long-distance information transmission is guaranteed by signal amplification.

The transfer of this technology on chips, as first proposed in a seminal paper by Goodman [8], can circumvent the previously mentioned limitations of electrical interconnects and allow for incomparable bit rate capabilities [9, 10]. However, this comes at the price of a large size mismatch between electronic and photonic components hampering the interfacing of both technologies on an actual chip. In contrast to their electronic counterparts, the fundamental law of diffraction limits the physical dimensions of dielectric photonic waveguides and their supported eigenmodes to about half the wavelength of light in the material. This prevents the same miniaturization of optical devices as observed in state-of-the-art electronic circuits. However, such miniaturization is necessary for a denser waveguide packaging without crosstalk and thus is a prerequisite for broadband data processing technology to compete with cutting-edge nanoelectronic circuits.

In quest of new chip-scale device technologies that can bridge the gap between nanoscale electronics and microscale photonics, plasmonics has evolved as a promising candidate [11]. Upon interaction of noble metals with visible light quantized coherent oscillations of their delocalized free electron gas accompanied by a subwavelength confinement of electromagnetic fields at interfaces with dielectrics, termed surface plasmon polaritons, build up. Thanks to these intriguing properties the diffraction limit – a seemingly unsurpassable obstacle – can be overcome. In metallic nanoparticles the oscillation of the electron gas is spatially bound and, just as for classical harmonic oscillators, can be of resonant fashion. Such localized surface plasmon resonances are characterized by (i) a strong spatial electromagnetic near-field confinement in the nanoparticle's vicinity accompanied by (ii) an enhancement of the field strength by orders of magnitude. Based on the great promise of these two properties, vivid research is carried out in a diverse range of potential applications from light concentration into deep-subwavelength volumes [12, 13], to sensing [14–17], single-molecule spectroscopy [18–20], generation of light [21–23], and photovoltaics [24, 25].

Besides these localized plasmon phenomena, potential applications for on-chip integrated optical signal guidance and processing stimulated a variety of plasmon waveguide designs that have been prototyped in the past years such as chains of metal particles [26–29], periodic corrugations [30], channels [31–33] and wedges in flat metal films [34], metallic wires of nanoscale cross section [35–39], and different two-conductor waveguides separated by a nanoscale gap [40–47]. Common to all these geometries are considerably shortened effective wavelengths of surface plasmon polaritons compared to free-space light [35, 48–50] and corresponding eigenmode profiles with a strong transverse field confinement – thus terming them subwavelength waveguides. The two-conductor waveguide structures in particular are promising candidates since their supported gap plasmon modes show minimal crosstalk with adjacent waveguides enabling a high degree of spatial integration. Moreover, the high field confinement in plasmonic waveguides makes them an ideal candidate for sensing [15, 51, 52] and subdiffraction information processing [53–58], and their ability to strongly couple to

quantum emitters [59–61] qualifies them as a building block for nano quantum optical networks [62, 63].

Today, the substitution of electrical impulses in electronic circuitry by plasmons supported in specifically designed nanocircuits is within reach. This entirely new class of circuitry, i.e. plasmonic nanocircuity, is the subject of this thesis. Recent progress in nanotechnology enables the fabrication of plasmonic circuits composed of optical nanoantennas [64–66] and waveguides [67, 68], that support guided plasmon modes. Thanks to their deep subwavelength sizes as well as their electrically conducting materials, plasmonic nanocircuits are fully compatible to their electronic counterparts, while at the same time preserving the speed of photonics [3]. Synergetic integration of all three technologies, i.e. electronics, conventional photonics, and plasmonics, promises to fully exploit nanoscale functionalities and to keep chip-scale technology further on track with Moore's law.

First experiments to manipulate propagating plasmons have been performed using networks of chemically grown silver nanowires [56, 69–73] or slot-less gold nanostructures [74]. For future nano-optical circuits, controlling the spatial and temporal evolution of surface plasmons are key features. So far, the strong subwavelength electromagnetic energy confinement [11, 35, 48] of propagating plasmonic modes supported by noble-metal nanowires led to the realization of nanometer-scale proof-of-concept circuits with well-defined built-in (passive) functionality [58, 75, 76] such as splitting or filtering [33]. Moreover, (active) coherent control of femtosecond optical energy localization in nanoscale random structures and V-shapes [77] as well as coherent control of plasmon routing has been proposed [78, 79].

The present work aims to design plasmonic nanocircuits that readily allow the fundamental control of photon flow at the nanometer scale by use of numerical simulations. Each integrated plasmonic element consists of an input capable of converting optical far-field excitations into guided plasmonic modes. These modes propagate along the nanocircuit and are processed according to the nanocircuit's functionality. Lastly, the result of this operation is converted back into far-field light at one or multiple outputs. In addition, a detailed insight into the underlying physical phenomena and limitations of such plasmonic nanocircuits is gathered in this work. Therefore, Chap. 2 starts with a brief summary of classical electromagnetism in matter in a depth necessary for understanding the encountered phenomena and the applied simulation technique. The appealing properties of noble metals in the optical regime and the resulting physics of plasmons are detailed in Chap. 3. Afterwards, in Chap. 4 the numerical simulation method is introduced together with the most important evaluation concepts. The different plasmonic waveguide geometries used as basis for the subsequently studied nanocircuits are introduced in Chap. 5. There, the inevitable compromise between the mode's propagation length, its degree of confinement, and its field enhancement is also addressed.

There is a conflict between time-consuming numerical simulations and the practically unlimited number of possible plasmonic nanocircuits to study. Chapter 6 addresses this issue by transferring ideas from classical electronics to plasmonics. The

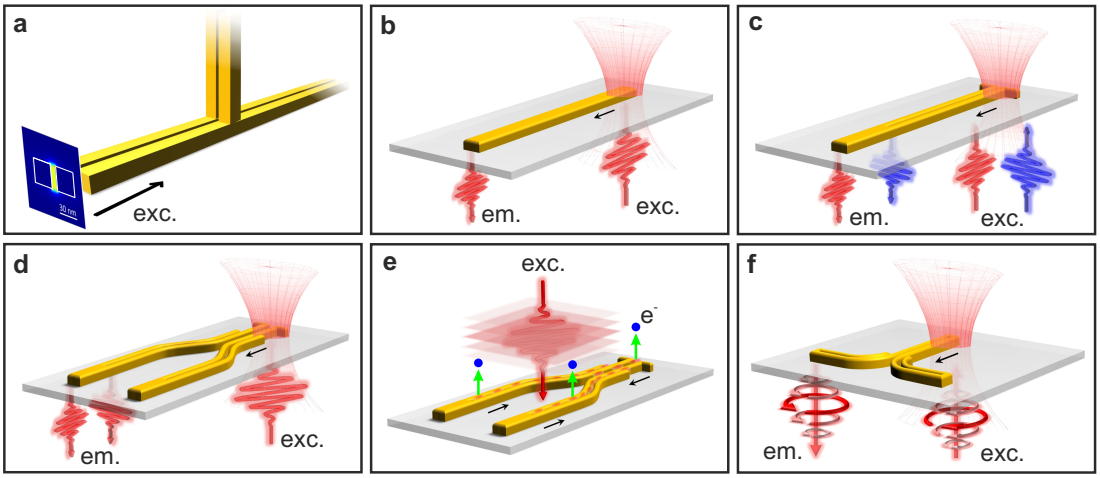

Figure 1.1: Overview of nanocircuit designs investigated in this thesis. (a) Junction of plasmonic TWTLs. (b) Single gold nanowire. (c) Mode detector nanocircuit. (d) Nanoscale directional coupler under optical investigation. (e) Nanoscale directional coupler for PEEM measurements. (f) Spin-optical nanocircuit. The respective excitation and emission spot positions and polarizations are indicated. Panels d and e adapted from [80]. © 2016 American Chemical Society.

power of electronic circuit design is based on the fact that complex circuitry can be created by arranging simple circuit elements into networks. The circuit properties can then be calculated using Kirchhoff's laws. It would be a great asset if similar design principles could be used in nanophotonics to create complex nanophotonic circuitry based on simple building blocks. However, at such short wavelengths the applicability of Kirchhoff's laws cannot be taken for granted any more. By studying a junction of plasmonic two-wire transmission lines (TWTLs) [Fig. 1.1a], which represents a fundamental building block of nanophotonic circuitry, a new phenomenological parameter relating the geometrical parameters of the junction to the wavelength of propagation is identified which allows to judge the degree of validity of Kirchhoff's laws. As an example and illustration of the power of this approach a system composed of a TWTL and a nanoantenna as a load is investigated. By addition of a parallel stub designed according to Kirchhoff's laws maximum signal transfer to the nanoantenna is achieved.

The design of any functional plasmonic device requires the exact quantitative understanding of all involved plasmonic and non-plasmonic propagation channels. In Chap. 7 a simple showcase system, i.e. a single, straight nanowire, is studied [Fig. 1.1b]. Subtle but important and so far unnoticed propagation channels are revealed by simulations and confirmed in experiments. It is shown that the transmission through finite-length nanowires can be described by Fabry-Pérot oscillations that beat with free-space propagating light launched at the incoupling end. Furthermore, a fully analytical model is established that shows quantitative agreement with simulated and experimental length-dependent transmission signals.

Chapter 8 focuses on a nanocircuit design [Fig. 1.1c] capable of a deterministic synthesis and in-situ optical analysis of arbitrary multimodal excitations. The propagation and far-field coupling of multiple (in the present case two) guided plasmonic modes is independent of each other, thus in analogy to multimode optical fibers the simultaneous transmission of multiple signals is possible. These findings and achievements demonstrate a new level of control in plasmonic nanocircuitry.

By exploiting the existence of multiple eigenmodes and coherence - both not accessible in classical electronics - Chap. 9 builds upon the preceding chapters by designing and optimizing an essential element of functional plasmonic nanocircuitry, i.e. a nanoscale directional coupler [Fig. 1.1d], allowing for efficient coherent control of highly confined propagating near-fields using the simplest possible control field, i.e., linearly polarized light, thereby avoiding the use of closed-loop learning algorithms. In contrast to classical electronic circuits, where a symmetric bifurcation inevitably causes an equal splitting of any input current pulse towards the two output ports, a fundamentally different behavior is induced representing a very intuitive classical analogue to quantum control in molecules. Furthermore, some insight into the feasibility of nonlinear all-plasmonic switching based on gold is given.

The same device is further investigated in Chap. 10 using normal-incidence two-photon photoemission electron microscopy (PEEM) [Fig. 1.1e]. It is found that the recorded photoemission yield can be heuristically modeled with high precision by considering the 4^{th} power of the numerically simulated electric near-field around the nanocircuit. This potentially paves the road for a future widespread application of normal-incidence PEEM in validating plasmonic nanocircuits.

Finally, Chap. 11 sheds light onto future prospects of plasmonic nanocircuitry. A spin-optical nano device [Fig. 1.1f] as well as a single-plasmon nanocircuit are introduced as examples. The former uses the spin of photons as a carrier of information and might enable a variety of novel devices, just as spintronics did in electronics by using the intrinsic spin of electrons. The latter uses a self-assembled quantum dot that efficiently excites narrow-band single plasmons and demonstrates the feasibility of fully on-chip plasmonic nanocircuits for quantum optical applications.

Chapter 2

Classical electromagnetism

> *"Since Maxwell's time, physical reality has been thought of as represented by continuous fields, governed by partial differential equations, and not capable of any mechanical interpretation. This change in the conception of reality is the most profound and the most fruitful that physics has experienced since the time of Newton."*
>
> Albert Einstein [81] in honor of the centenary of Maxwell's birth (1931).

Classical electromagnetism, the investigation of electric and magnetic fields and their mutual interaction, has been the driving force of core technologies of the 20^{th} and the early 21^{st} century. Its theory, however, dates back to decades of experimental discoveries and advances of many scientists and engineers in the 18^{th} and 19^{th} century, such as the description of electrostatic attraction and repulsion forces between electrically charged particles by Charles Augustin de Coulomb[1] and the observed interaction of electric currents and magnetic fields by Michael Faraday[2], to name but a few.

By mathematical distillation of all the knowledge of his time and huge conceptional leaps James Clerk Maxwell[3] successfully pioneered a fundamental unification of electricity, magnetism, and light. Formulated over 150 years ago, Maxwell's partial differential equations provide a complete description of classical electromagnetic phenomena and up to the present day enable great advances in modern electrical, information, and communication technologies. Furthermore, in physics Maxwell's seminal work paved the way for such revolutionary ideas as Planck's[4] quantum theory [82] and Einstein's theory of special relativity [83]. Even Albert Einstein acknowledged that "one scientific epoch ended and another began with James Clerk Maxwell".

This chapter aims to give the reader a short overview over Maxwell's fundamental equations of classical electromagnetism and some important implications of his theory in a depth necessary for the understanding of the physical behavior of nano-optical systems. For further in-depth reading about classical electromagnetism the reader is referred to comprehensive standard literature, e.g. [84], with special emphasis on nanoscale effects available in [85].

[1] French physicist (* 14. June 1736; † 23. August 1806)
[2] English scientist (* 22. September 1791; † 25. August 1867)
[3] Scottish physicist (* 13. June 1831; † 5. November 1879)
[4] German physicist (* 23. April 1858; † 04. October 1947)

2.1 Maxwell's equations

Maxwell's seminal work "A dynamical theory of the electromagnetic field" from 1865 [86] allows the description of all classical (i.e., non-quantum) electromagnetic phenomena in a closed theoretical form, relating the characteristic quantities of electromagnetic fields, i.e. electric field $\mathbf{E}$ and magnetic field $\mathbf{H}$, with the electric displacement $\mathbf{D}$ and magnetic induction $\mathbf{B}$. Neglecting the singular character of electric charges and their associated currents by using the macroscopic quantities charge density ρ and current density $\mathbf{j}$ Maxwell's famous equations written in the convenient vector calculus formulation introduced by Oliver Heaviside[5] read[6]:

$$\nabla \times \mathbf{E}(\mathbf{r},t) = -\frac{\partial \mathbf{B}(\mathbf{r},t)}{\partial t}, \tag{2.1a}$$

$$\nabla \times \mathbf{H}(\mathbf{r},t) = \frac{\partial \mathbf{D}(\mathbf{r},t)}{\partial t} + \mathbf{j}(\mathbf{r},t), \tag{2.1b}$$

$$\nabla \cdot \mathbf{D}(\mathbf{r},t) = \rho(\mathbf{r},t), \tag{2.1c}$$

$$\nabla \cdot \mathbf{B}(\mathbf{r},t) = 0. \tag{2.1d}$$

These four equations describe the generation of electromagnetic fields from distributions of charges and currents and their evolution in time, thus building the axiomatic basis for electromagnetism, just as Newton's axioms for mechanics.

Any solution of Maxwell's equations with arbitrary time dependency can be represented as a linear combination of single-frequency solutions via the inverse Fourier transform, reading e.g. for the electric field

$$\mathbf{E}(\mathbf{r},t) = \int_{-\infty}^{\infty} \mathbf{E}(\mathbf{r},\omega) e^{-i\omega t} \mathrm{d}\omega. \tag{2.2}$$

Thereby, Eqs. (2.1) transform into the time harmonic (phasor) Maxwell's equations

$$\nabla \times \mathbf{E}(\mathbf{r},\omega) = i\omega \mathbf{B}(\mathbf{r},\omega), \tag{2.3a}$$

$$\nabla \times \mathbf{H}(\mathbf{r},\omega) = -i\omega \mathbf{D}(\mathbf{r},\omega) + \mathbf{j}(\mathbf{r},\omega), \tag{2.3b}$$

$$\nabla \cdot \mathbf{D}(\mathbf{r},\omega) = \rho(\mathbf{r},\omega), \tag{2.3c}$$

$$\nabla \cdot \mathbf{B}(\mathbf{r},\omega) = 0. \tag{2.3d}$$

Here, all quantities are functions of position $\mathbf{r}$ and angular frequency ω. The spectral representation of any field quantity is obtained from the corresponding time dependent quantity via Fourier transformation. This yields, e.g., for the electric field

$$\mathbf{E}(\mathbf{r},\omega) = \frac{1}{2\pi} \int_{-\infty}^{\infty} \mathbf{E}(\mathbf{r},t) e^{i\omega t} \mathrm{d}t. \tag{2.4}$$

[5] English scientist (* 18. May 1850; † 03. February 1925)
[6] SI units are used throughout this work.

2.2 Conservation laws

The continuity equation stating the conservation of charges is implicitly contained in the above equations by combining Eq. (2.1c) with the divergence of Eq. (2.1b), thus reading

$$\nabla \cdot \mathbf{j}(\mathbf{r}, t) + \frac{\partial \rho(\mathbf{r}, t)}{\partial t} = 0. \tag{2.5}$$

In case of a time-harmonic variation of the fields and linear, non-dispersive media, Poynting's theorem expressing the conservation of electromagnetic energy reads [84]

$$-\left\langle \frac{\partial W}{\partial t} \right\rangle = \frac{1}{2} Re\left[\mathbf{j}^* \cdot \mathbf{E}\right] + \nabla \cdot \langle \mathbf{S} \rangle . \tag{2.6}$$

The time-averaged change of electromagnetic energy density W is denoted by $\left\langle \frac{\partial W}{\partial t} \right\rangle$, with $W = \frac{1}{2}\left[\mathbf{E} \cdot \mathbf{D}^* - \mathbf{B} \cdot \mathbf{H}^*\right]$. The first term on the right-hand side of Eq. (2.6) accounts for the mean energy dissipation, the second term equals the mean net energy flow, represented by the time average of the Poynting vector $\mathbf{S}$,

$$\mathbf{S} = \mathbf{E} \times \mathbf{H}^*. \tag{2.7}$$

By integrating the Poynting vector over a surface A with normal vector $\mathbf{n}$ the average power flow P through this surface is obtained according to

$$\langle P \rangle = \frac{1}{2} \iint_A Re\left[\mathbf{S}\right] \cdot \mathbf{n} \, \mathrm{d}A. \tag{2.8}$$

2.3 Constitutive relations

Self-consistent solutions for electromagnetic fields require a supplement to Maxwell's equations by relating $\mathbf{D}$ with $\mathbf{E}$, $\mathbf{B}$ with $\mathbf{H}$, as well as $\mathbf{j}$ with $\mathbf{E}$, thus accounting for the behavior of matter under the influence of external fields. This connection is done by introducing the macroscopic polarization $\mathbf{P}$ and magnetization $\mathbf{M}$ as follows:

$$\mathbf{D}(\mathbf{r}, \omega) = \varepsilon_0 \mathbf{E}(\mathbf{r}, \omega) + \mathbf{P}(\mathbf{r}, \omega), \tag{2.9a}$$

$$\mathbf{B}(\mathbf{r}, \omega) = \mu_0 \mathbf{H}(\mathbf{r}, \omega) + \mu_0 \mathbf{M}(\mathbf{r}, \omega), \tag{2.9b}$$

where ε_0 and μ_0 respectively denote the electric permittivity[7] and the magnetic permeability[8] of vacuum, which are linked to the vacuum speed of light c via $c = \frac{1}{\sqrt{\varepsilon_0 \mu_0}}$.

[7] $\varepsilon_0 \approx 8.854 \cdot 10^{-12} \frac{As}{Vm}$

[8] $\mu_0 = 4\pi \cdot 10^{-7} \frac{Vs}{Am}$

For linear and isotropic media, as are usually encountered in this work,[9] the polarization $\mathbf{P}$ and magnetization $\mathbf{M}$ at a given angular frequency depend linearly on $\mathbf{E}$ and $\mathbf{H}$ via

$$\mathbf{P}(\mathbf{r},\omega) = \varepsilon_0 \chi_e(\mathbf{r},\omega)\mathbf{E}(\mathbf{r},\omega), \tag{2.10a}$$
$$\mathbf{M}(\mathbf{r},\omega) = \chi_m(\mathbf{r},\omega)\mathbf{H}(\mathbf{r},\omega), \tag{2.10b}$$

where the proportionality constants are called electric and magnetic susceptibility χ_e and χ_m. In general, both material quantities are frequency dependent, i.e. dispersive, due to a non-instantaneous polarization response to time-varying fields.

Equations (2.9) can be rewritten as the constitutive relations

$$\mathbf{D}(\mathbf{r},\omega) = \varepsilon_0 \varepsilon(\mathbf{r},\omega)\mathbf{E}(\mathbf{r},\omega), \tag{2.11a}$$
$$\mathbf{B}(\mathbf{r},\omega) = \mu_0 \mu(\mathbf{r},\omega)\mathbf{H}(\mathbf{r},\omega), \tag{2.11b}$$

by introducing the macroscopic response functions of matter $\varepsilon = 1 + \chi_e$ and $\mu = 1 + \chi_m$, known as permittivity and permeability, respectively. In general, both are second rank tensors and depend on material, position, direction and field strength. In this work, however, the almost exclusive concern are electromagnetic phenomena of homogeneous, local, isotropic, linear[9], and nonmagnetic media in the visible and near-infrared spectral region, thus ε is a field strength independent scalar and intrinsic magnetic effects can safely be neglected ($\mathbf{M} = 0$, $\mu = 1$). The dispersive character of ε for gold is extensively analyzed in Sec. 3.1.

Finally, for materials with conductivity σ a linear relationship between current density $\mathbf{j}$ and electric field $\mathbf{E}$ can be established according to

$$\mathbf{j}(\mathbf{r},\omega) = \sigma(\mathbf{r},\omega)\mathbf{E}(\mathbf{r},\omega), \tag{2.12}$$

which is known as Ohm's law in differential form.

2.4 Vector Helmholtz equation

In general, the electric field $\mathbf{E}$ and the magnetic field $\mathbf{H}$ of a monochromatic wave can be expressed as

$$\mathbf{E}(\mathbf{r},t) = \mathbf{E}(\mathbf{r})e^{-i\omega t}, \tag{2.13a}$$
$$\mathbf{H}(\mathbf{r},t) = \mathbf{H}(\mathbf{r})e^{-i\omega t}. \tag{2.13b}$$

[9] The regime of nonlinear effects in gold is approached in Chap. 9.

By evaluating the time derivatives in Eq. (2.1) and inserting the constitutive relations (2.11) Maxwell's equations can then be written as

$$\nabla \times \mathbf{E}(\mathbf{r}) = i\omega\mu_0 \mathbf{H}(\mathbf{r}), \tag{2.14a}$$
$$\nabla \times \mathbf{H}(\mathbf{r}) = -i\omega\varepsilon_0\varepsilon(\mathbf{r})\mathbf{E}(\mathbf{r}), \tag{2.14b}$$
$$\nabla \cdot [\varepsilon_0\varepsilon(\mathbf{r})\mathbf{E}(\mathbf{r})] = 0, \tag{2.14c}$$
$$\nabla \cdot [\mu_0 \mathbf{H}(\mathbf{r})] = 0, \tag{2.14d}$$

where the absence of source currents and charges has been assumed, which is the relevant condition encountered in this work.

The homogeneous vector wave equation is obtained from Eqs. (2.14) by eliminating either the electric or the magnetic fields. For the electric field, when applying the curl to Eq. (2.14a) and substituting Eq. (2.14b) one obtains[10]

$$\nabla^2\mathbf{E} + \frac{\omega^2}{c^2}\varepsilon(\mathbf{r})\mathbf{E} = \nabla(\nabla \cdot \mathbf{E}). \tag{2.15}$$

Calculating the divergence of Eq. (2.14c) the $\nabla \cdot \mathbf{E}$ term can be elaborated[11]

$$\nabla \cdot \mathbf{E} = -\mathbf{E} \cdot \nabla \ln \varepsilon(\mathbf{r}). \tag{2.16}$$

By substituting this result into Eq. (2.15), the following homogeneous vector wave equation for $\mathbf{E}$ is obtained:

$$\nabla^2\mathbf{E} + \frac{\omega^2}{c^2}\varepsilon(\mathbf{r})\mathbf{E} = -\nabla\left[\mathbf{E} \cdot \nabla \ln \varepsilon(\mathbf{r})\right]. \tag{2.17}$$

In a similar manner the homogeneous vector wave equation for $\mathbf{H}$ is derived as

$$\nabla^2\mathbf{H} + \frac{\omega^2}{c^2}\varepsilon(\mathbf{r})\mathbf{H} = [\nabla \times \mathbf{H}] \times \nabla \ln \varepsilon(\mathbf{r}). \tag{2.18}$$

In most practical situations the entire space can be subdivided into domains D_i characterized by homogeneous material permittivities ε_i. Instead of solving Eqs. (2.17) and (2.18) directly for the complete space one can solve for each domain D_i separately the simpler wave equations

$$\left(\nabla^2 + \mathbf{k}_i^2\right)\mathbf{E}_i = 0, \tag{2.19a}$$
$$\left(\nabla^2 + \mathbf{k}_i^2\right)\mathbf{H}_i = 0, \tag{2.19b}$$

where $k_i = (\omega/c)\sqrt{\varepsilon_i}$ is the wave number in domain D_i. Within each domain the resulting field vectors are continuous functions of position and time, with continuous

[10] The vector identity $\nabla \times (\nabla \times \mathbf{A}) = \nabla(\nabla \cdot \mathbf{A}) - \nabla^2\mathbf{A}$ is applied. $\mathbf{A}$ denotes a vector, ∇ the gradient operator, and ∇^2 the vector Laplacian operator.

[11] The vector identity $\nabla \cdot (\nabla \times \mathbf{A}) = 0$ is applied.

derivatives [87]. However, field discontinuities may occur at interfaces between different media due to the accompanying abrupt change in physical properties. Thus, a correct connection of all domain solutions [Eqs. (2.19)] at the domain boundaries is required to recover the solution for the complete system.

Since Maxwell's equations are valid everywhere including the domain boundaries, they completely govern the behavior of the electromagnetic field components at the boundary. The tangential field components at the boundary ∂D_{ij} between two domains i and j satisfy the following boundary conditions [85]

$$\mathbf{n} \times (\mathbf{E}_i - \mathbf{E}_j) = \mathbf{0}, \tag{2.20a}$$

$$\mathbf{n} \times (\mathbf{H}_i - \mathbf{H}_j) = \mathbf{j_s}, \tag{2.20b}$$

with the unit vector normal to the boundary ∂D_{ij} and the surface current density denoted as $\mathbf{n}$ and j_s, respectively. On the other hand, the normal field components obey

$$\mathbf{n} \cdot (\mathbf{D}_i - \mathbf{D}_j) = \sigma_s, \tag{2.21a}$$

$$\mathbf{n} \cdot (\mathbf{B}_i - \mathbf{B}_j) = 0. \tag{2.21b}$$

where σ_s is the surface charge density. In the absence of free charges and currents in the domains j_s and σ_s vanish.

In a limitless region of homogeneous, isotropic space (e.g. free space with $\varepsilon = 1$ independent of position $\mathbf{r}$) and Cartesian coordinates the simplest solutions of Eqs. (2.19) are propagating plane waves of the form

$$\mathbf{E}(\mathbf{r}, t) = \mathbf{E}_0 \, e^{i(\mathbf{k}\cdot\mathbf{r} - \omega t)}, \tag{2.22a}$$

$$\mathbf{H}(\mathbf{r}, t) = \mathbf{H}_0 \, e^{i(\mathbf{k}\cdot\mathbf{r} - \omega t)}, \tag{2.22b}$$

resulting in the linear free space dispersion relation $\omega = c|\mathbf{k}|$. The wave vector $\mathbf{k}$ is oriented along the direction of propagation. $\mathbf{E}$ and $\mathbf{H}$ of such a transversal wave are perpendicular to each other. Furthermore, Eqs. (2.14c) and (2.14d) additionally require the fields to be perpendicular to $\mathbf{k}$.

Chapter 3

Fundamentals of plasmonics

The optical properties of plasmons arising from the interaction of electromagnetic fields with noble metal nanostructures are essentially dictated by both the metal's frequency-dependent dielectric response function and the structure's geometry. In this chapter both aspects are addressed, starting in Sec. 3.1 with studying the dielectric function of metals in the optical regime, which notably shows a negative real part responsible for plasmon formation. The subsequent sections focus on the unique properties of surface plasmon polaritons for simple two-dimensional (2D) waveguide geometries, i.e single- [Sec. 3.2] and double-interface systems [Sec. 3.3]. We limit our study to gold as the metal, since all nanostructures throughout this thesis were fabricated from this material. Reasons for the choice of gold range from its chemical stability, to the excellent optical properties in the red and near-infrared parts of the optical spectrum used for excitation of our structures, and the availability of high-quality monocrystalline gold platelets [88, 89].

3.1 Optical response of noble metals

Though our interest lies in nano-sized metallic structures, the minute spacing of electron energy levels compared to the thermal energy $k_B T$ caused by the high density of free electrons nevertheless allows a classical instead of a quantum mechanical description of metal optics. A quantum plasmonic description [90, 91] only becomes necessary for single-digit nanometer sized particles [92] or sub-nanometer separation distances between nanoparticles [93, 94] to, e.g., account for electron tunneling effects [95]. Within the realm of Maxwell's equations (2.3) the optical response of metals is governed by the complex frequency dependent permittivity $\varepsilon(\omega) = \varepsilon'(\omega) + i\varepsilon''(\omega)$, in the following referred to as the dielectric function. It relates the external light field to the macroscopic polarization, as defined in Eqs. (2.9a) and (2.11a). In first approximation Drude-Sommerfeld theory is applied to describe the exclusive effect of the free electron gas, that can oscillate with respect to the fixed ion core background. For time-harmonic excitation fields of amplitude $\mathbf{E}_0$ and angular frequency ω the equation of motion of free electrons that lack a restoring force reads [85]

$$m_e \frac{\partial^2 \mathbf{r}}{\partial t^2} + m_e \Gamma \frac{\partial \mathbf{r}}{\partial t} = e\mathbf{E}_0 e^{-i\omega t}, \tag{3.1}$$

where e and m_e denote charge and effective mass of the free electrons, respectively. The damping constant $\Gamma = \frac{v_F}{l}$ measures the frequency of scattering events for electrons with Fermi velocity v_F and mean free path l. Solving Eq. (3.1) yields for the dielectric function

$$\varepsilon_{Drude}(\omega) = 1 - \frac{\omega_p^2}{\omega^2 + i\Gamma\omega}, \tag{3.2}$$

where the volume plasma frequency $\omega_p = \sqrt{\frac{ne^2}{\varepsilon_0 m_e}}$ with electron density n is introduced. Figure 3.1a shows a fit of Eq. (3.2) to experimental data obtained by Johnson and Christy [96]. While the Drude-Sommerfeld model represents the dielectric function of gold in the long wavelength regime reasonably well, it is inadequate in doing so for wavelengths below $\lambda = 650\,\mathrm{nm}$.

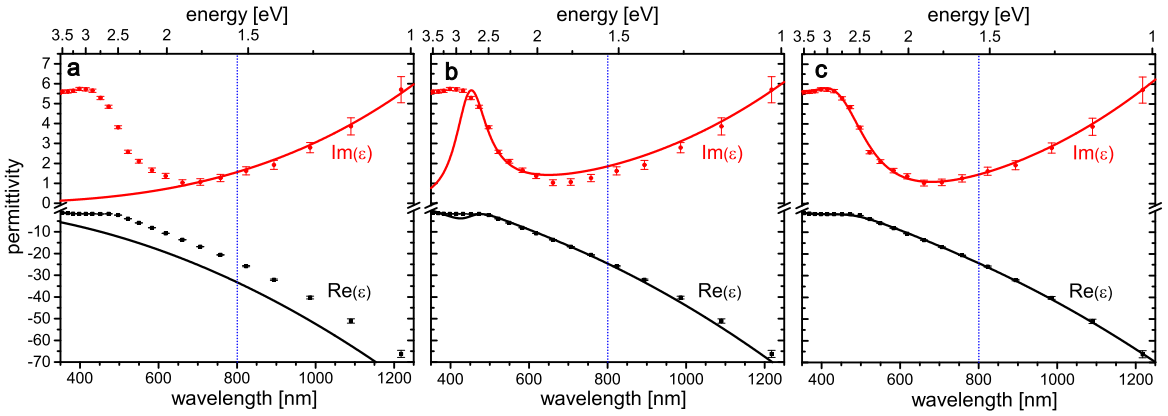

Figure 3.1: Dielectric function of gold in the extended visible spectrum. Comparison of experimental data [96] (symbols) with a fit of (a) the pure Drude-Sommerfeld theory, (b) the Drude-Sommerfeld theory supplemented by an interband transition, and (c) the Etchegoin model [97]. The model constants are obtained from [85] and take the values in (a) $\hbar\omega_p = 8.95\,\mathrm{eV}$ and $\hbar\Gamma = 65.8\,\mathrm{meV}$ and in (b) $\hbar\widetilde{\omega}_p = 2.96\,\mathrm{eV}$, $\hbar\gamma = 0.59\,\mathrm{eV}$, $\omega_0 = 2\pi c/\lambda$ ($\lambda = 450\,\mathrm{nm}$) and $\varepsilon_\infty = 5$. Note the different scales for the abscissae.

In this wavelength region the energy of photons is higher than the threshold for transitions of bound electrons from filled valence bands below the Fermi surface (d bands in gold) to unoccupied states in the conduction band (sp band in gold). These interband transitions can be accounted for by adding a restoring force term to Eq. (3.1), that then reads for bound electrons [85]

$$m\frac{\partial^2 \mathbf{r}}{\partial t^2} + m\gamma\frac{\partial \mathbf{r}}{\partial t} + \alpha\mathbf{r} = e\mathbf{E}_0 e^{-i\omega t}, \tag{3.3}$$

where m and γ are separate effective mass and damping constants for bound electrons, respectively. α accounts for the parabolic restoring potential seen by the bound electrons. The contribution of a single interband transition to the dielectric function is

given by a Lorentz-oscillator term of the form

$$\varepsilon_{Interband}(\omega) = 1 + \frac{\widetilde{\omega}_p^2}{(\omega_0^2 - \omega^2) - i\gamma\omega}, \tag{3.4}$$

with eigenfrequency $\omega_0 = \sqrt{\alpha/m}$ and $\widetilde{\omega}_p = \sqrt{\frac{\widetilde{n}e^2}{\varepsilon_0 m}}$ depending on the density of bound electrons $\widetilde{n}$. The integrated effect of further interband transitions at higher energies can be included in a constant offset ε_∞. In fact, combining the free electron [Eq. (3.2)] and interband absorption [Eq. (3.4)] contribution the dielectric function can be reproduced much more accurately down to wavelengths of about $\lambda = 500\,\mathrm{nm}$ [98], as obvious from Fig. 3.1b. By adding a sufficient number of Lorentz-oscillator terms the dielectric function can be approximated to any desired accuracy. However, a physically more meaningful analytical model of the dielectric function of gold was presented by Etchegoin et al. [97] based on the method of critical points. Their model[1] nicely fits the data of [96] [Fig. 3.1c], and thus is used in all simulations presented in this work.

3.2 Surface plasmon polaritons

Coherent oscillations of the metal's delocalized electron plasma about the positive ion cores, as described in the Drude-Sommerfeld theory [cf. Sec. 3.1], are termed plasma oscillations, with their quanta called plasmons. Interesting phenomena arise at surfaces between metals and dielectrics where the electron motion in so-called surface plasmons is associated with electromagnetic fields that propagate along the interface while being evanescently confined in the perpendicular direction thus preventing energy transport away from the interface [100]. Such surface plasmon polaritons (SPPs) are solutions of the homogeneous Helmholtz equation (2.17) for a planar interface between two half-spaces described by the respective dielectric functions of the metal $\varepsilon_1(\omega) = \varepsilon_1'(\omega) + i\varepsilon_1''(\omega)$ and the dielectric $\varepsilon_2(\omega)$, as sketched in Fig. 3.2a. Without loss of generality, the interface is oriented perpendicular to the z-direction and wave propagation along the positive x-direction is assumed.

The only allowed self-consistent solutions are transverse magnetic (TM) polarized surface waves with non-vanishing E_x, E_z and H_y field components. The electric fields in the two half-spaces j can then be written as [85]

$$\mathbf{E}_j = \begin{pmatrix} E_{j,x} \\ 0 \\ E_{j,z} \end{pmatrix} e^{i(k_{\mathrm{SPP}}x - \omega t)} e^{ik_{z,j}|z|}, \quad j = 1, 2 \tag{3.5}$$

where the parallel wave vector k_{SPP} (i.e. the component along the propagation direction) is equivalent to the SPP's propagation constant. $k_{z,j}$ corresponds to the normal component of the wave vector in half-space j and the absolute value of z has been used to ensure an exponential decay into both half-spaces.

[1] Note the erratum [99] to the original publication.

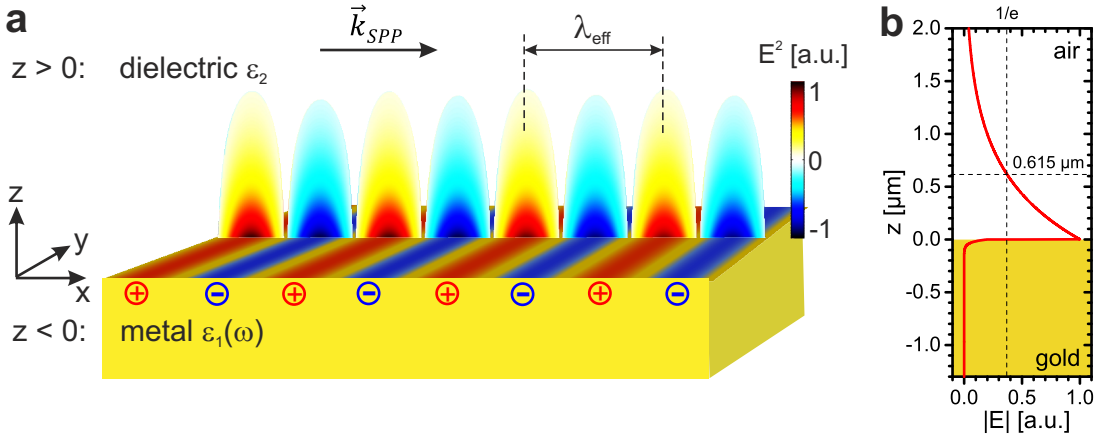

Figure 3.2: Surface plasmon polariton at plane interface. (a) Illustration of coupled field and charge density distribution of a bound SPP mode traveling in positive x-direction along an interface between a metal and a dielectric represented by dielectric functions ε_1 and ε_2, respectively. The interface is defined as $z = 0$ in a Cartesian coordinate system. (b) Exponential electric field decay into the adjacent half-spaces for a gold-air interface at vacuum wavelength 800 nm, giving rise to energy confinement in z-direction.

By requiring the continuity of the tangential (normal) component of $\mathbf{E}$ ($\mathbf{D}$) at the boundary in accordance with Eq. (2.20a) (Eq. (2.21a) with $\sigma_s = 0$) in combination with the continuity of the parallel wave vector k_{SPP} the following dispersion relations, i.e. relations between wave vectors and angular frequency ω, result:

$$k_{\mathrm{SPP}} = \sqrt{\frac{\varepsilon_1\varepsilon_2}{\varepsilon_1+\varepsilon_2}}\frac{\omega}{c} \rightarrow \omega = \sqrt{\frac{\varepsilon_1+\varepsilon_2}{\varepsilon_1\varepsilon_2}}\, c\, k_{\mathrm{SPP}}, \tag{3.6a}$$

$$k_{z,j} = \sqrt{\frac{\varepsilon_j^2}{\varepsilon_1+\varepsilon_2}}\frac{\omega}{c}, \quad j = 1,2. \tag{3.6b}$$

The metal's non-negligible imaginary part of the dielectric function results in a complex SPP wave vector $k_{\mathrm{SPP}} = \beta + i\alpha$ causing damping upon propagation due to Ohmic losses. In contrast, free space photons in the dielectric are described by a linear dispersion relation given by

$$\omega = \frac{c}{\sqrt{\varepsilon_2}}k, \tag{3.7}$$

commonly referred to as light line. Necessary requirements for a bound interface mode to exist are imaginary normal wave vector components $k_{z,j}$. Equation (3.6b) infers for the involved dielectric functions the condition $\mathrm{Re}\left[\varepsilon_1(\omega)+\varepsilon_2(\omega)\right] < 0$. Furthermore, propagation along the interface requires a positive real part of the SPP propagation constant k_{SPP} and thus imposes $\mathrm{Re}\left[\varepsilon_1(\omega)\cdot\varepsilon_2(\omega)\right] < 0$. A metal-dielectric interface satisfies both conditions in the optical regime, i.e. $\mathrm{Re}\left[\varepsilon_1(\omega)\right] < -\mathrm{Re}\left[\varepsilon_2(\omega)\right]$, as can be seen by inspection of Fig. 3.1.

The finite value of the attenuation constant α manifests itself in a finite SPP propagation length l_{decay} (1/e intensity decay length), which is defined as

$$l_{\mathrm{decay}} = \frac{1}{2\alpha}. \tag{3.8}$$

An SPP propagation length of $l_{\mathrm{decay}} = 86\,\mu\mathrm{m}$ is obtained for a gold-air interface at $\lambda = 800\,\mathrm{nm}$. The SPP effective wavelength λ_{eff} is obtained via

$$\lambda_{\mathrm{eff}} = \frac{2\pi}{\beta}, \tag{3.9}$$

taking a value of 788 nm for a gold-air interface at $\lambda = 800\,\mathrm{nm}$. With distance from the interface the SPP's evanescent fields decay exponentially into both neighboring media, as illustrated in Fig. 3.2b. This is due to the mostly imaginary $k_{z,j}$ [Eq. (3.6b)]. The near-field penetration depths l_z (1/e amplitude decay) into gold and air take values of $l_{z,1} = 1/\mathrm{Im}\,[k_{z,1}] = 25\,\mathrm{nm}$ and $l_{z,2} = 1/\mathrm{Im}\,[k_{z,2}] = 615\,\mathrm{nm}$, respectively, showing a much shorter penetration depth into the metal.

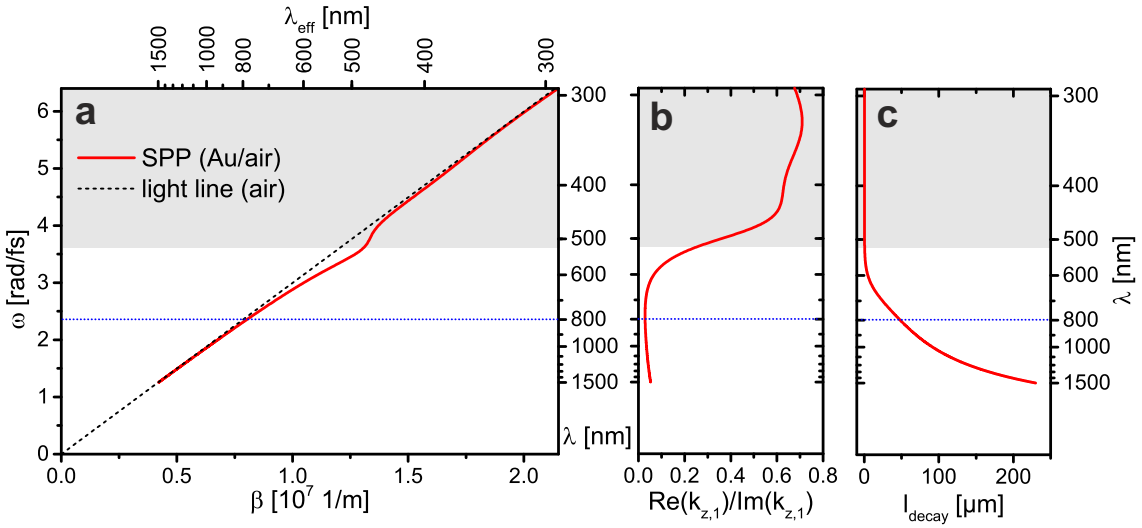

Figure 3.3: Properties of SPPs. (a) SPP dispersion relation for a gold-air interface (red solid line) together with the light line in air (black dashed line). Gold is modeled after [97]. (b) Fraction of real to imaginary part of transverse wave vector $k_{z,1}$ in gold. (c) Corresponding SPP propagation length. The gray shaded area denotes the high energy Brewster mode regime.

Compliance with both energy and momentum conservation is required for SPP excitation. To this end, the SPP dispersion relation $\omega(\beta)$ [Eq. (3.6a)] for a single plane gold-air interface is depicted exemplarily in Fig. 3.3a (red solid line) together with the dispersion of free space photons in air [Eq. (3.7) - black dashed line]. Here, the dispersive character of the dielectric function of gold $\varepsilon_1(\omega)$ in the visible to near-infrared region of the electromagnetic spectrum is modeled as explained in Sec. 3.1,

while the permittivity of air is set to $\varepsilon_2 = 1$ irrespective of frequency. The dispersion relation can be divided in two branches, a high-energy and a low-energy branch. The first one, the so-called Brewster mode, describes waves propagating into the gold instead of true surface waves [85], as obvious from the strongly increased real part of $k_{z,1}$ shown in Fig. 3.3b and negligible SPP propagation length l_{decay} shown in Fig. 3.3c. Thus, we are not interested further in this branch.

Only the low-energy branch corresponds to true SPPs, which always possess a larger wave vector than free space photons of the same frequency. This manifests itself in the SPP dispersion relation lying below the light line. The wave vector difference is small for low frequencies, where gold better resembles an ideal conductor that prohibits fields to penetrate it, resulting in quasi plane wave modes in the air half-space with infinite extension. This can be made a general rule also for the more complex waveguide geometries studied later, that whenever the SPP dispersion approaches the light line of adjacent dielectrics the SPP mode becomes more photonic-like with only little confinement accompanied by a large propagation length. In contrast, for higher frequencies within the low-energy branch gold behaves more and more like an electron plasma and efficient coupling to this results in a large wave vector difference. Due to this wave vector difference SPPs on a smooth metal interface cannot directly be excited by light from the far-field. Thus, special excitation schemes are required to overcome the momentum mismatch and generate SPPs. To this end, the use of prism couplers in the Otto [101] and Kretschmann [102] configurations or high numerical aperture objectives providing large angular components [103] are commonly exploited. In turn, reciprocity implies that such SPPs are also non-radiative in nature. In the following, we will show the evolution of λ_{eff} and l_{decay} instead of dispersion curves since we are mostly interested in how these two properties change depending on structure dimensions.

With applications such as optical information transport via SPPs in mind, the group velocity v_g constitutes the relevant measure for the propagation speed of a broadband pulse. For a certain angular frequency ω_0 it can be directly deduced from the dispersion relation by calculating its slope [104]

$$v_g = \frac{\partial \omega}{\partial \beta}|_{\omega_0}. \tag{3.10}$$

For the gold-air interface at $\lambda = 800\,\mathrm{nm}$ considered above the group velocity takes a value of $v_g = 0.93\ c$ and thus is expectedly slower than the speed of light in air. The group velocity is not to be confused with the phase velocity, i.e. the speed of phase fronts of single-frequency components. This is defined as $v_p = \frac{\omega}{\beta}$ and usually, depending on the spectral characteristics of the dielectric function, is slightly different than v_g. For the specific example from above, the phase velocity at $\lambda = 800\,\mathrm{nm}$ is calculated to be $v_p = 0.98\ c$.

3.3 Surface plasmon modes in double-interface systems

Having introduced the basic concept of SPPs at single metal-dielectric interfaces in the previous section, we now want to proceed by focusing on two specific three layer geometries as depicted in Fig. 3.4: the metal-insulator-metal [MIM, Fig. 3.4a] and the insulator-metal-insulator [IMI, Fig. 3.4b] configuration [105]. Each single interface of such systems is capable of independently sustaining a bound SPP [cf. Sec. 3.2], as long as the interface separation t is much larger than the SPP's evanescent decay length l_z in the respective inner medium. Otherwise, mutual coupling of SPPs associated with individual metal-insulator interfaces results in mode hybridization of symmetric or antisymmetric nature [106–108], just as for atomic orbitals in molecules. In the following, the propagation properties of these different solutions are examined for symmetric systems with identical substrate and superstrate material. For non-symmetric systems, on the other hand, different modes exist [109], which are not governed in this thesis. Furthermore, only the supported fundamental bound modes with potential applications in waveguiding are treated here omitting the family of leaky and oscillatory modes [107].

3.3.1 Metal-insulator-metal architecture

Bound modes, i.e. solutions of the wave equation in the absence of driving terms, can in general be found by solving the characteristic equation imposed by the boundary conditions of the system under investigation. For the symmetric MIM geometry only an implicit expression for the dispersion relation linking k_{SPP} with ω can be obtained [110]. Therefore, we have numerically solved for the modes of a MIM waveguide formed by an air gap in gold by means of the finite-difference frequency-domain method [cf. Sec. 4.3].

Within a certain parameter range the symmetric MIM geometry can support two fundamental bound modes with amplitudes of their field components as illustrated in Fig. 3.4c. The mode symmetry with respect to the mid-plane of the dielectric layer is defined by the longitudinal field component E_x, yielding a symmetric (left, light green dashed curve) and an antisymmetric mode (right, light blue dashed curve). The respective symmetry is also evident from inspection of the surface charge densities upon both metal surfaces, as schematically sketched in Fig. 3.4c. Notably, in contrast the transverse field component E_z shows the opposite symmetry. Therefore, the symmetric mode (also called quasi-TM mode) possesses a node for the E_z component between the two interfaces (left, green solid line), while for the antisymmetric mode (also called quasi-TE mode) E_z inside the dielectric has the same sign across the gap (right, blue solid line).

Figures 3.5a-c show general trends in the characteristic properties of both modes. Most notably, while the antisymmetric mode experiences no cutoff for vanishing dielec-

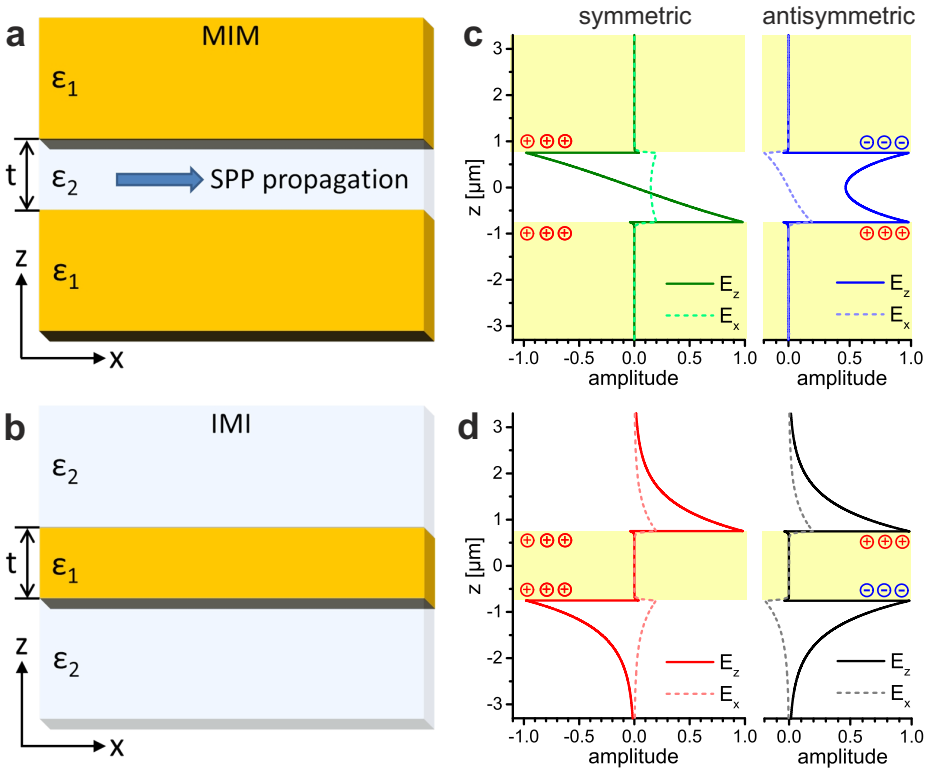

Figure 3.4: Modes of symmetric multilayer systems. (a) Schematic illustration of a MIM heterostructure. The metal extends indefinitely on both sides of the dielectric. (b) Schematic illustration of an IMI heterostructure. (c) Field components of the symmetric (left, green curves) and antisymmetric (right, blue curves) bound modes for the MIM geometry composed of gold and air. (d) Field components of the symmetric (left, red curves) and antisymmetric (right, black curves) bound modes for the IMI geometry composed of gold and air. All modes are calculated for a center layer thickness $t = 1.5\,\mu$m at a vacuum wavelength of 800 nm, ensuring that none of these fundamental modes is already in cutoff.

tric, the symmetric mode does so [109], e.g. at $\lambda = 800\,$nm the symmetric mode is in cutoff for dielectric layer thicknesses $t < 1.25\,\mu$m. Toward smaller values of t, i.e. for decreasing gaps between the two metal layers, the antisymmetric mode's effective wavelength drastically reduces toward the limit $\lambda_{\text{eff}} \to 0$ [Fig. 3.5a] [111], equivalent to a strong increase in propagation constant β reaching values exceeding those of a single metal-dielectric interface. A large β implies a strong near-field confinement in the transverse direction, which in turn results in small propagation lengths, as seen in Fig. 3.5b. Absorption in gold is limiting the propagation length, thus high mode confinement results in a larger fraction of the fields to be within the gold [Fig. 3.5c] and consequently high losses. Finally, for large propagation constants also the group velocity decreases [Fig. 3.5c].

From the two bound MIM modes, the antisymmetric one is especially appealing for waveguide applications [45, 112], since it can in principle be squeezed unlimitedly in

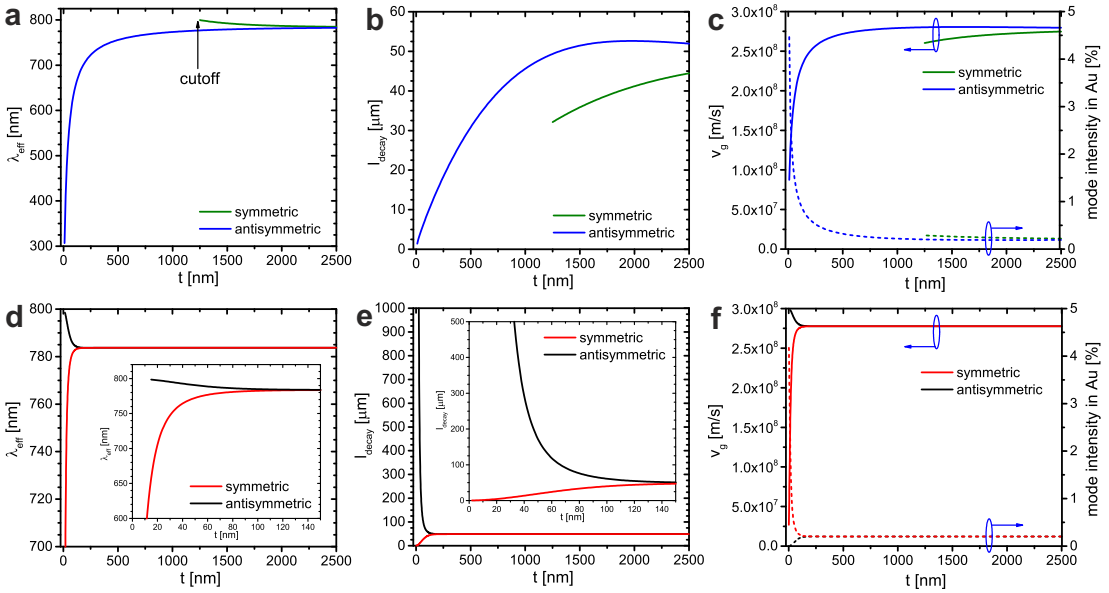

Figure 3.5: Mode properties of multilayer systems. (a) Effective wavelength, (b) propagation length, and (c) group velocity and fraction of mode intensity in Au for MIM heterostructures with varying dielectric layer thickness t. (d)-(f) Same as (a)-(c), but for IMI heterostructures. For all simulations, Au modeled according to [97] and air have been chosen as metal and dielectric, respectively. The results are obtained for a vacuum wavelength of 800 nm.

its transverse cross section even for excitation wavelengths in the red or near-infrared, as long as the width of the dielectric is made sufficiently small. This is contrary to the single interface SPP mode that requires frequencies close to the surface plasmon frequency ω_{sp} to show strong field confinement [see Sec. 3.2]. However, this inevitably comes at the price of small propagation lengths imposing a general trade-off in plasmonics between strong field confinement and propagation losses [111]. Nevertheless, it can be shown that the available dielectric space is most efficiently exploited by the antisymmetric MIM mode [113, 114], resulting in fairly small absorption [111]. In future, plasmon amplification techniques might help solving this issue [115–118].

3.3.2 Insulator-metal-insulator architecture

Just as their MIM counterparts, IMI multilayer structures also support two fundamental bound modes distinguished by the hybridization symmetry of the single surface modes. The field amplitudes for symmetric (left, red curves) and antisymmetric (right, black curves) mode are depicted in Fig. 3.4d with general trends in the characteristic properties of both modes shown in Figs. 3.5d-f. Regarding the symmetric mode, the effective wavelength [Fig. 3.5d] decreases to 0 for infinitely thin gold films, equivalent to an indefinite increase of both real and imaginary parts of k_{SPP}. As a consequence, the propagation length of the symmetric IMI mode gets very small [Fig. 3.5e] due to strong Ohmic damping arising from the large fraction of mode intensity inside the

gold [Fig. 3.5f]. Contrary to this so-called short-range SPP, the dispersion relation of the antisymmetric IMI mode in the limit of very thin gold films approaches the light line. It resembles a photonic-like plane wave supported by the homogeneous dielectric environment and is characterized by low losses at the expense of poor confinement [119]. This remarkable feature of long propagation lengths [Fig. 3.5e] caused by the fields being pushed out of the gold [Fig. 3.5f] dubs the mode long-range SPP [120] and might be employed for practical components in integrated plasmonic circuitry [121].

Chapter 4

Numerical simulations

The analytical solution of Maxwell's equations is a complex task limiting closed form solutions to a few simple geometries, such as spherical particles in the framework of Mie theory [122, 123] or plane interfaces as described in Chap. 3. For more advanced problems, numerical approximations of Maxwell's equations are usually required to make reliable predictions of the present classical electromagnetic effects. Nowadays, scientists around the world use such computational electromagnetics to investigate, among others, electromagnetic scattering, radiation, and waveguiding phenomena. A myriad of algorithms is used for this task, with the most recognized ones being the finite element method (FEM), the method of moments (MoM), and the finite-difference time-domain (FDTD) method. An extensive overview of these full-wave techniques is given in [124]. However, within this thesis the FDTD algorithm is exclusively used, which is justified given that this method is the preferred choice when studying guided wave problems.

In plasmonics, numerical simulations are particularly important as a tool to study complex nanostructures. Firstly, due to their time-consuming and expensive fabrication new concepts are often tested and optimized in simulations before the actual experiments with promising structures are performed. Secondly, to draw solid conclusions from experimental data a comparison with simulation results can often help, since there - in contrast to the actual experiments - additional relevant properties are accessible such as the spatial near-field distribution around the nanostructure.

This chapter gives a synoptic view of the FDTD algorithm [Sec. 4.1] together with emphasis on practical simulation aspects [Sec. 4.2]. For a primal read the extensive text book of Taflove and Hagness [125] is highly recommended. All FDTD simulations presented in this work were performed with commercial software (FDTD Solutions, Lumerical Solutions Inc., Canada) in versions 5 to 8.12.590. The software's documentation can be found online [126]. Subsequently, the frequency-domain eigenmode solver used to numerically obtain eigenmode characteristics of investigated waveguide structures is introduced in Sec. 4.3. Finally, Sec. 4.4 briefly summarizes the most frequently employed post-processing procedures important for the derivation and understanding of later results.

4.1 Finite-difference time-domain algorithm

The FDTD algorithm relies on central-difference approximations to the space and time partial derivatives in Maxwell's curl Eqs. (2.1a) and (2.1b)[1]. Rewriting them component-wise in Cartesian coordinates under the assumption of time independent parameters ε, μ, and σ, one yields a system of six coupled partial differential equations, that can be compactly written as

$$\frac{\partial E_p}{\partial t} = \frac{1}{\varepsilon}\left(\frac{\partial H_r}{\partial q} - \frac{\partial H_q}{\partial r} - \sigma E_p\right), \tag{4.1a}$$

$$\frac{\partial H_p}{\partial t} = \frac{1}{\mu}\left(\frac{\partial E_q}{\partial r} - \frac{\partial E_r}{\partial q}\right), \tag{4.1b}$$

with $\{p, q, r\}$ being cyclic permutations of $\{x, y, z\}$. This immediately suggests a leapfrog-type marching-in-time scheme with finite time steps Δt, wherein electric and magnetic field updates are staggered by $\Delta t/2$ with respect to each other. Consequently, updated values for the electric (magnetic) field in time are computed from the electric (magnetic) field in the previous time step and the local curl of the magnetic (electric) field, as implied by Eq. (4.1a) (Eq. (4.1b)). This iterative update, as sketched in Fig. 4.1a, is repeated until the termination criterion of negligible energy remaining in the simulation domain is met.

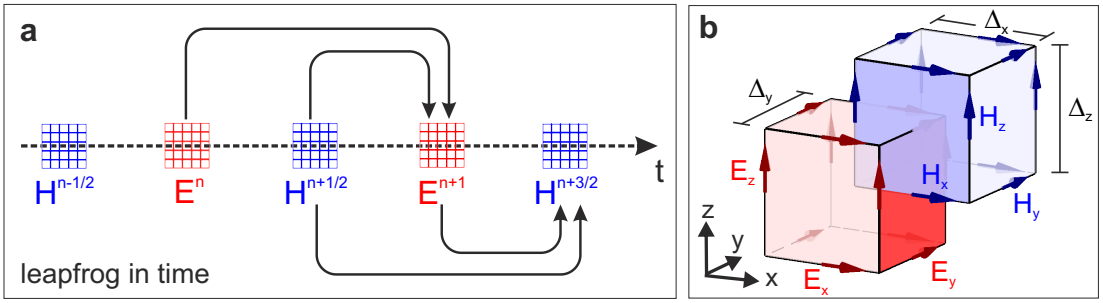

Figure 4.1: Discretizations involved in the FDTD algorithm for solving Maxwell's equations. (a) Leapfrog time marching of electric and magnetic fields. (b) Cubic unit cell of the interleaved lattice used for discretization in space. The electric and magnetic field components are situated on the respective cube edge centers of the primal (red) and interleaved (blue) unit cell. The natural implementations of the integral forms of Ampere's [Eq. (2.1b)] and Faraday's [Eq. (2.1a)] law are highlighted for the E_y and H_x components by the bluish and reddish planes, respectively.

The discretization in time allows for the numerical approximation of the first partial time derivatives in Eqs. (4.1a) and (4.1b) by second-order accurate center-differences

[1] Although not explicitly enforced by the FDTD algorithm, the obtained field quantities nevertheless satisfy the Gauss' laws relations (2.1c) and (2.1d), as pointed out in [125].

of the form

$$\frac{\partial u^n}{\partial t} = \frac{u^{n+1/2} - u^{n-1/2}}{\Delta t} + \mathcal{O}(\Delta t^2), \tag{4.2}$$

where u^n represents any component of $\mathbf{E}$ and $\mathbf{H}$ at integer time step n. While at this point both fields are still continuous in space, FDTD further requires a discretization in space that naturally allows for the computation of the curl of all field components. This is commonly achieved by the nested nature of two interleaved cuboid-shaped lattices with lattice constants Δ_x, Δ_y, and Δ_z, that are shifted in all three dimensions relative to each other by half of the respective lattice constant and represent the components of the electric and magnetic field, respectively. The unit cell of this segmentation, which was originally introduced by Kane Yee in 1966 [127] and since then proved to be very robust, is shown in Fig. 4.1b.

Space discretization by means of Yee cells allows for the numerical approximation of the first partial space derivatives in Eqs. (4.1a) and (4.1b) by second-order accurate center-differences [125], e.g. reading for the derivative of u in x-direction

$$\frac{\partial u^n(i,j,k)}{\partial x} = \frac{u^n(i+\frac{1}{2},j,k) - u^n(i-\frac{1}{2},j,k)}{\Delta_x} + \mathcal{O}(\Delta_x^2), \tag{4.3}$$

where (i,j,k) represents the Yee cell indices in x-, y-, and z-direction. This space lattice further maps the permittivity and permeability of physical structures within the simulation domain onto the electric and magnetic fields, respectively.

Spatial and temporal discretizations of the FDTD algorithm inherently bring about limitations in the accuracy, as evident from the numerical dispersion [128]

$$\left[\frac{1}{\tilde{c}\,\Delta t}\sin\left(\frac{\omega\,\Delta t}{2}\right)\right]^2 = \sum_{l=\{x,y,z\}}\left[\frac{1}{\Delta_l}\sin\left(\frac{\tilde{k}_l\,\Delta_l}{2}\right)\right]^2, \tag{4.4}$$

showing a discrepancy in the phase velocities $\tilde{c}$ and c of numerically and physically propagating waves, respectively. Only in the limit $\{\Delta t, \Delta_x, \Delta_y, \Delta_z\} \to 0$ agreement with the analytical dispersion $\left(\frac{\omega}{c}\right)^2 = \sum_{l=\{x,y,z\}} k_l^2$ is reached. As can be inferred from the numerical dispersion relation Eq. (4.4), the stability of the FDTD algorithm requires the Courant criterion to be satisfied, which sets the following upper bound on the time step [128]:

$$\Delta t \leq \frac{1}{v_{\max}}\left(\frac{1}{\Delta_x^2} + \frac{1}{\Delta_y^2} + \frac{1}{\Delta_z^2}\right)^{-1/2}, \tag{4.5}$$

where $v_{\max}$ is the maximum phase velocity possible in the simulation domain.

4.2 Simulation setup

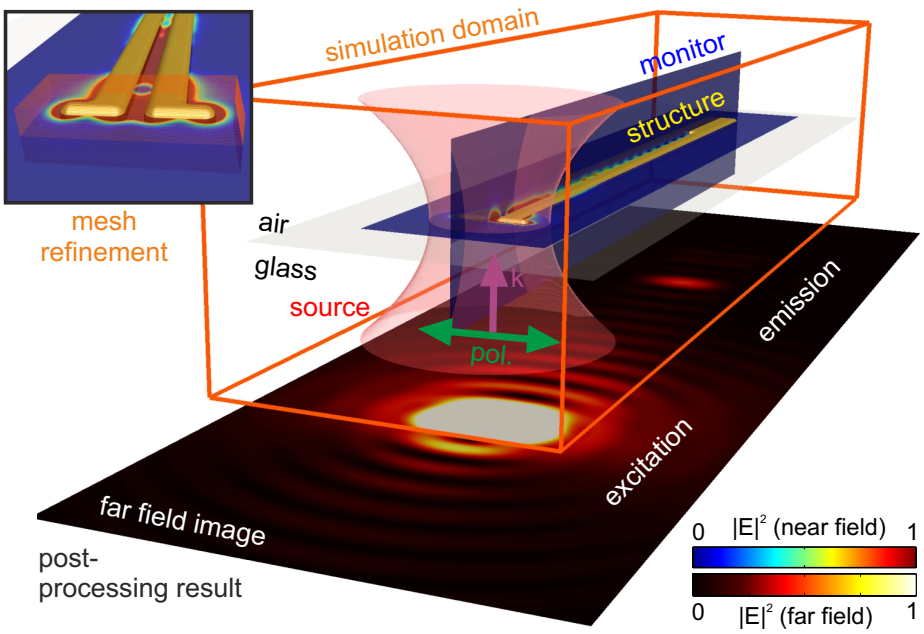

Figure 4.2: FDTD simulation setup. The simulation domain includes the physical structures of interest, in this particular case a mode detector device as introduced in Chap. 8, and is confined by PML layers (orange box). An excitation source, here a Gaussian beam focused onto the incoupling antenna, injects electromagnetic fields into the simulation domain, which are recorded by monitors. Information outside of the simulation domain, such as far field images, can be retrieved by post-processing techniques, as detailed in Sec. 4.4. (inset) The region around the nanoantenna is placed into a mesh override region allowing for a finer discretization.

The basic elements of a typical FDTD simulation are illustrated in Fig. 4.2 with essential simulation parameters briefly discussed in the following. In order to numerically tackle a give problem, the computational domain, i.e. a finite region of space containing the physical structures of interest, must be defined. Only within this simulation region the FDTD method solves for the electromagnetic fields. A typical guideline is to ensure a spacing between structure and simulation boundary on the order of the longest considered excitation wavelength to avoid spurious absorption of the structure's evanescent fields at the boundary. For an exception of this guideline see Sec. 4.4.1. Since the boundary is artificial in the sense that it is not present in the real unbounded system but just used to make the problem numerically tractable, a reflection of energy at the boundary needs to be avoided for faultless results. Therefore, a highly effective artificial absorbing material, called perfectly matched layer (PML), has been introduced [129, 130] and surrounds the simulation region, thus mimicking an infinite computational domain. This beneficial property specifically applies to the

present case of plasmonic modes. Moreover, if the studied structure and its excitation are inherently mirror symmetric it is advisable to reduce the computational effort by using symmetric or antisymmetric boundary conditions.

The meshing of the simulation region, i.e. the spatial discretization according to Yee's algorithm, has to take the following two aspects into consideration. Firstly, the structure itself needs to be accurately resolved within the created grid. This is particularly important for curved objects, since otherwise the object's representation in the simulation includes sharp corners and edges due to stair-casing instead of a smooth surface. For metal structures in particular this leads to a concentration of charges in artificial edges and corners and unwanted strong local fields due to the lightning rod effect. Secondly, plasmonic excitations on metallic nanostructures are accompanied by strong field gradients in the structure's vicinity, as introduced in Sec. 3.2, which need to be reproduced by the chosen grid to be able to achieve a correct behavior in simulations. In contrast to the originally introduced uniform grid of cuboid Yee cells [cf. Sec. 4.1], the commercial software allows for a more sophisticated non-uniform grid. This is highly beneficial as it allows for sub-gridding pre-defined volumes enclosing plasmonic structures using smaller cell sizes and hence additional resolution where needed [see Fig. 4.2, inset], while other areas not containing metallic materials can have significantly larger cell dimensions and still accurately describe, e.g., propagating free space radiation. In lack of analytical solutions to the complex systems studied in this thesis the optimal Yee cell size in terms of accuracy on the one hand and simulation time and memory requirements on the other hand is obtained by convergence tests using decreasing mesh sizes. Typical optimal cell sizes for terminations of metallic waveguides or isolated nanoantennas are $1 \times 1 \times 1\,\mathrm{nm}^3$, while for pure plasmon propagation along propagation direction invariant waveguides the mesh size in this direction can be increased to 4 nm - 8 nm. For regions far away from metallic material grid sizes in the order of 15 nm to 20 nm are acceptable.

A variety of ways exists to model different types of materials within the simulations. In the present case, glass is assumed to be non-dispersive in the considered wavelength range and consequently is implemented as a dielectric material with a constant, real refractive index of 1.51. In contrast, the dielectric function of gold is strongly wavelength dependent in the visible spectral range, as shown in Sec. 3.1. To account for this dispersive nature, sampled gold material data from a critical point fit [97, 99] to experimental data of Johnson and Christy [96] are used.[2] An automatic fitting routine within the software generates a multi-coefficient material model of these data over the relevant wavelength range.

As the constitutive relation (2.11a) is a frequency-domain expression but the FDTD method is a time-domain technique, an inverse Fourier transformation of Eq. (2.11a) is

[2] This data set is a well established standard for gold. However, a recent collection of spectroscopic ellipsometry measurements suggests differences in the dielectric function depending on the morphology of gold [131]. Consequently, some uncertainty is introduced by the choice of the concrete material data, which is however found to be only of minor impact and none of the observations in this work is affected by our choice.

required to obtain the time-domain electric displacement. Multiplication of harmonic functions in the frequency domain is equivalent to a convolution in the time domain, hence one yields the convolutional (and causal) constitutive relation

$$\mathbf{D}(\mathbf{r},t) = \varepsilon_0 \int_{\tau=0}^{t} \varepsilon(\mathbf{r},t-\tau)\mathbf{E}(\mathbf{r},\tau)\mathrm{d}\tau, \tag{4.6}$$

with $\varepsilon(\mathbf{r},t)$ as the inverse Fourier transform of $\varepsilon(\mathbf{r},\omega)$

$$\varepsilon(\mathbf{r},t) = \int_{-\infty}^{\infty} \varepsilon(\mathbf{r},\omega)e^{-i\omega t}\mathrm{d}\omega. \tag{4.7}$$

The time-domain function $\varepsilon(\mathbf{r},t)$, which has to obey Kramers-Kronig constraints, describes the impulse response of the medium.

Another fundamental element for modeling a system is an appropriate excitation source, with which electromagnetic energy is introduced into the simulation region. A variety of accurate electromagnetic wave sources is available with the two most commonly used ones in this work being the Gaussian beam source and the mode source. The Gaussian beam source injects a fully vectorial beam with Gaussian beam profile and an adjustable numerical aperture, thus resembling a laser beam excitation focused by an objective. In contrast, the mode source directly injects a guided mode into a plasmonic waveguide. Therefore, first the 2D modal profile in a cross-sectional cut perpendicular to the waveguide direction is obtained using an eigenmode solver [see Sec. 4.3]. This modal profile is then applied to an electromagnetic source and, since modal profile of the source and the waveguide are perfectly matching, all energy is coupled into the waveguide mode without excitation of free space waves. In simulations, the time signal of the source $s(t)$ is specified to be a few cycle pulse with typical pulse duration of 5 fs and center wavelength as required from the experiment.

With the aforementioned building blocks simulations can be carried out, which according to the FDTD algorithm introduced in Sec. 4.1 calculate the electromagnetic fields at each grid point and every simulation time step. Since this vast amount of data is impossible to store, fields are only recorded in pre-specified monitors, i.e. one-, two- or three-dimensional sub-regions of the simulation region. Such monitors can either directly record the time evolution of field quantities, or by a Fourier transformation of these transient field data the corresponding frequency-domain results according to

$$\mathbf{E}(\mathbf{r},\omega) = \frac{1}{2\pi}\int_{0}^{\infty} \mathbf{E}(\mathbf{r},t)e^{i\omega t}\mathrm{d}t. \tag{4.8}$$

Unlike their time-domain counterparts frequency-domain electric fields are inherently complex quantities comprising magnitude and phase information. Frequency-domain monitors calculate the integral in Eq. (4.8) only up to the time when the simulation is

ended assuming zero fields beyond this point. To still ensure a physically meaningful transformation, the simulation must only be terminated if the energy in the simulation volume has dropped far enough so that most of the excitation power has already left the simulation region. A final field strength decrease of 5 orders of magnitude compared to its peak value is an appropriate condition to terminate the simulation. The simulated frequency-dependent electric field results from Eq. (4.8) not only depend on the system under investigation, but also on the exact shape of the source pulse $s(t)$. A useful normalization of $\mathbf{E}(\mathbf{r},\omega)$ is obtain by dividing Eq. (4.8) with the Fourier transform of the source pulse, i.e.

$$\mathbf{s}(\omega) = \frac{1}{2\pi}\int_0^\infty \mathbf{s}(t)e^{i\omega t}\mathrm{d}t. \tag{4.9}$$

By this normalization the impulse response of the system is returned, which is completely independent of the exact properties of the excitation pulse.

4.3 Frequency-domain eigenmode solver

From the plethora of optical/plasmonic waveguide geometries only a few simple ones [as shown in Secs. 3.2, 3.3 and 5.1] possess analytical solutions. The modal characteristics of more complex waveguide structures can only be determined by rigorous numerical methods [132, 133]. From the many available modeling techniques in this work we adopt the full-vectorial finite-difference frequency-domain (FDFD) method to obtain eigenmodes of plasmonic waveguides and their mode characteristics (MODE Solutions, Lumerical Solutions Inc., Canada). As within the FDTD algorithm [see Sec. 4.1] the underlying discretization scheme is based on finite-difference approximations of the derivative operators in Maxwell's equations using Yee's 2D grid.

The following considerations assume the involved materials to be non-magnetic, i.e. imply that μ is unity over the entire waveguide cross section. Furthermore, the waveguide is oriented along the x-direction, thus the permittivity ε is assumed to be translationally invariant along this propagation direction, i.e. $\varepsilon = \varepsilon(y,z)$. Then, the solutions of Maxwell's equations take the form of plane waves with time-harmonic dependence

$$\mathbf{E}(x,y,z) = [\mathbf{E}_t(y,z) + E_x(y,z)\hat{\mathbf{x}}]\, e^{i(k_{\mathrm{SPP}}x-\omega t)}, \tag{4.10a}$$

$$\mathbf{H}(x,y,z) = [\mathbf{H}_t(y,z) + H_x(y,z)\hat{\mathbf{x}}]\, e^{i(k_{\mathrm{SPP}}x-\omega t)}, \tag{4.10b}$$

where $\mathbf{E}(y,z)$ and $\mathbf{H}(y,z)$ have been decomposed into components transverse and parallel to the plasmon propagation direction, denoted by subscripts t and x, respectively. $\hat{\mathbf{x}}$ is the unit vector parallel to the waveguide axis. Building on Sec. 2.4, the homogeneous vector Helmholtz Eqs. (2.17) and (2.18) simplify to wave equations for the

transverse fields

$$\left(\nabla_t^2 + \varepsilon k^2 - k_{\mathrm{SPP}}^2\right) \mathbf{E}_t = -\left(\nabla_t + ik_{\mathrm{SPP}}\hat{\mathbf{x}}\right)\left(\mathbf{E}_t \cdot \nabla_t \ln \varepsilon\right), \tag{4.11a}$$

$$\left(\nabla_t^2 + \varepsilon k^2 - k_{\mathrm{SPP}}^2\right) \mathbf{H}_t = \left[\left(\nabla_t + ik_{\mathrm{SPP}}\hat{\mathbf{x}}\right) \times \mathbf{H}_t\right] \times \nabla_t \ln \varepsilon, \tag{4.11b}$$

with the gradient operator in transverse direction defined as $\nabla_t = \hat{\mathbf{y}}\frac{\partial}{\partial y} + \hat{\mathbf{z}}\frac{\partial}{\partial z}$.

Application of the finite-difference algorithm, i.e. approximation of derivatives by ratios of finite differences, on a cross-sectional mesh of the waveguide yields a matrix eigenvalue equation in terms of the transverse electric fields [134]

$$\mathbf{A}\begin{bmatrix} E_y \\ E_z \end{bmatrix} = \begin{bmatrix} A_{yy} & A_{yz} \\ A_{zy} & A_{zz} \end{bmatrix}\begin{bmatrix} E_y \\ E_z \end{bmatrix} = k_{\mathrm{SPP}}^2 \begin{bmatrix} E_y \\ E_z \end{bmatrix} \tag{4.12}$$

with the eigenvalues k_{SPP}^2. The implementation of the coefficient matrix $\mathbf{A}$ uses an index averaging technique for the finite differences in Eq. (4.11a) and thus reduces stair-casing problems for curved surfaces, as detailed in [134]. Solving Eq. (4.12) using sparse matrix techniques the transverse mode fields $\mathbf{E}_t(y, z)$ are obtained, which readily allow the calculation of $E_x(y, z)$. Thus, both field profiles and corresponding propagation properties for eigenmodes of arbitrarily shaped waveguides can numerically be calculated. In a manner similar to Eq. (4.12) one can alternatively obtain an eigenvalue equation for the magnetic fields $\mathbf{H}$ from Eq. (4.11b).

In terms of customizable settings and the obtainable results FDFD simulations are less complex compared to the previously introduced FDTD simulations [see Sec. 4.2], however, the accuracy of results nevertheless needs to be demonstrated. Common sources of errors are related to the simulation area size and the discretization of this area, especially in regions containing metals. Evanescent mode fields overlapping with the absorbing PML simulation boundaries constitute the first type of error. If the simulation area is not sufficiently large, electromagnetic energy gets lost in the boundaries. This results in deviations most dominantly of the imaginary part of k_{SPP}. Those deviations are especially pronounced for weakly confined modes that require a particularly large simulation area for convergence of results. The second source of error is associated with the ability to resolve the structure's geometrical features as well as the near-field's strong spatial variations. This effect is studied exemplarily for a cylindrical metallic nanowire waveguide in a homogeneous dielectric surrounding [35, 48] in Sec. 5.1, as this case can in addition be addressed fully analytically [135], thus providing an important reference.

4.4 Post-processing procedures

This section shortly summarizes the most frequently used post-processing procedures used throughout this work, i.e. near- to far-field projections, far-field image calculation, mode overlap analysis, and fitting of the mode's reflectivity at waveguide discontinuities.

4.4.1 Near- to far-field projections

In view of the previously mentioned finite computational domain the FDTD solver only determines near-field data in close proximity to the structure. If one is interested in modeling the corresponding electromagnetic fields in the intermediate or distant far-field regions, near- to far-field projections provide a numerically efficient way to accomplish this task as a post-processing step. These projections can be understood as a decomposition of the near-field data using a set of plane waves propagating at different angles as its basis. A detailed review of the underlying method can be found in [125]. In this work, we typically encounter structures that reside on glass-air interfaces and knowledge of their far-field emission patterns, i.e. the angular distribution of the emission, into both air and glass half-spaces is mandatory, with particular importance of the latter one as this is also experimentally accessible. Therefore, the results of the near-field decomposition are propagated to a hemisphere in one meter distance in air and glass, respectively, as schematically illustrated for the glass half-space in Fig. 4.3a.

The requirement for a far-field projection into the glass (air) half-space is the knowledge of the electromagnetic fields (i.e. $\mathbf{E}$ and $\mathbf{H}$) in a plane parallel to the interface situated completely in the glass (air) half-space. In the following, far-field emission patterns of a key component of plasmonic nanocircuitry, that is a linear dipole antenna, are investigated. The antenna dimensions, as denoted in the caption of Fig. 4.3, are chosen in order to support a fundamental dipolar resonance at 800 nm wavelength. The far-field projection onto the hemisphere in glass is shown in Fig. 4.3b together with cuts parallel and perpendicular to the nanoantenna axis in Fig. 4.3c. The perfect dipolar antenna far-field emission pattern is revealed by comparison with the emission pattern of an individual electric dipole placed 15 nm above the glass-air interface, i.e., at the antenna's mid-height, as displayed in Fig. 4.3c by the black dashed curves. A simpler illustration of the far-field emission pattern is obtained by a top-view of the hemisphere in Fig. 4.3b, yielding Fig. 4.3d. This planar representation is used throughout this thesis.

To ensure accurate results the lateral extension of the near-field monitor used for the projection must be large enough to record most of the light propagating into the far-field and to suffice the underlying assumption of zero fields beyond the edge of the monitor. Figure 4.4 shows cuts through the far-field emission pattern of a dipole situated 15 nm above a glass substrate in air for different extensions of this monitor. Comparing with the analytical solution of this simple problem [85] considerable errors in the far-field data become apparent, especially in the region of the classically forbidden light, when using too narrow monitors. A trade-off between simulation accuracy and the size of the simulation domain, that determines the required simulation time, needs to be found depending on the complexity of the system under investigation. For accurate far-field emission patterns a minimum monitor size of $20 \times 20\,\mu\mathrm{m}^2$ is recommended, requiring at least the same lateral simulation domain span.

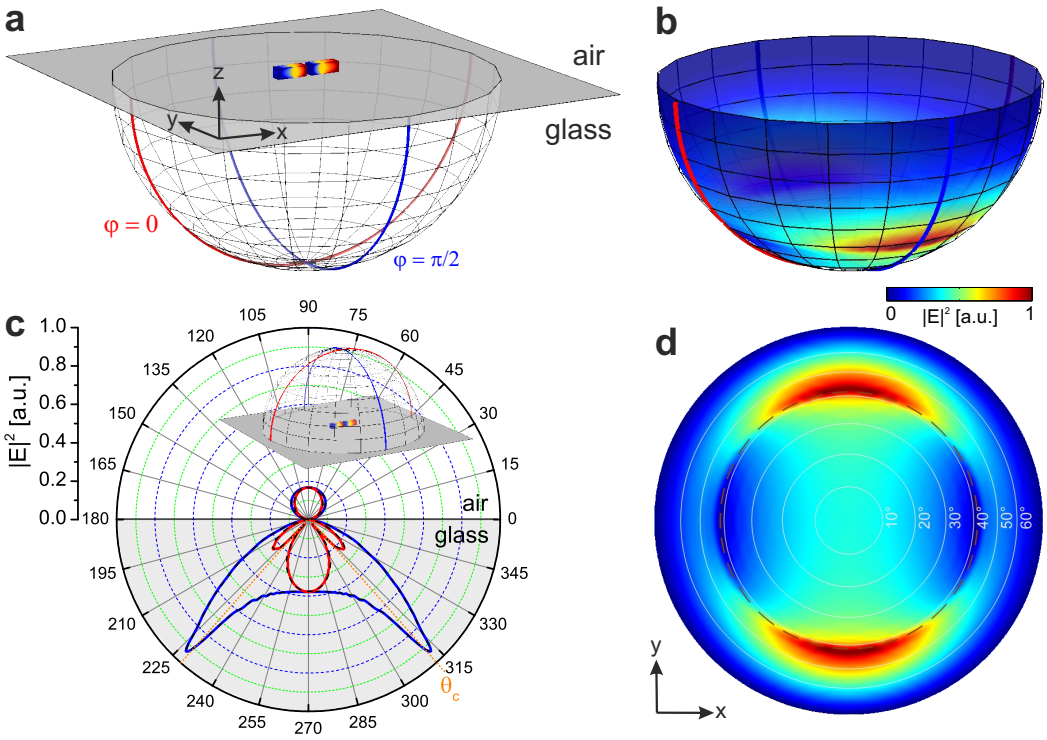

Figure 4.3: Calculation of far-field emission pattern. (a) Visualization of the hemisphere used to record the emission pattern in the glass half-space. A gap nanoantenna (arm length = 85 nm, width = 30 nm, height = 30 nm, gap = 10 nm) resonating in its fundamental dipolar mode at 800 nm wavelength, as evidenced by its charge distribution, serves as an example. Dimensions are not to scale. (b) The nanoantenna's far-field emission pattern projected onto the hemisphere in glass. (c) Cuts through the far-field emission pattern parallel (red) and perpendicular (blue) to the nanoantenna axis. Equivalent cuts are obtained for an individual dipole 15 nm above a glass-air interface (black dashed curves). The hemisphere used to record the emission pattern in the air half-space is shown as an inset. (d) Top-view of the hemisphere of (b).

4.4.2 Far-field image calculation

Experimentally the structures are characterized by a home-built inverted microscope setup [see Sec. 7.2]. Therefore, a post-processing of the simulation data is needed in order to facilitate a comparison with experimental images recorded by the microscope. Most importantly the effect of the microscope objective with its numerical aperture (NA) limiting the resolution of finest details needs to be considered. To this end, first a near-field decomposition into a series of plane waves propagating at different angles is performed as described in Sec. 4.4.1. Subsequently, the obtained emission pattern is filtered by discarding any plane wave contributions with angles outside the defined collection NA of the objective. Finally, the remaining plane wave contributions are re-focused onto an image plane coinciding with the objective's focal plane to reconstruct

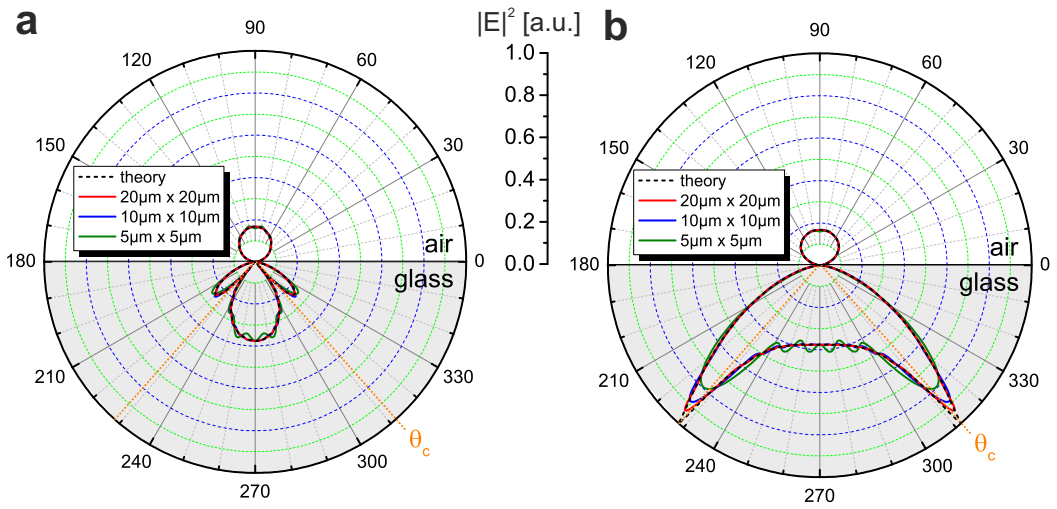

Figure 4.4: Accuracy of far-field emission pattern calculation. Cuts through the simulated emission pattern (a) parallel and (b) perpendicular to the dipole moment of an electric dipole. The lateral extension of the square monitors used for the far-field projection is 5 μm (green), 10 μm (blue), and 20 μm (red). The theoretical curves, as obtained after [85], are shown in black. Both theoretical and simulated emission patterns are obtained for an electric dipole source located 15 nm above a glass-air interface with polarization parallel to it and oscillation wavelength of 800 nm. The critical angle for total internal reflection θ_c is shown in orange as a guide for the eye.

a simulated microscope image. Technically this is done by a chirped z-transform of the filtered set of data [126]. A schematic of the simplified imaging system is given in Fig. 4.5 showing the image construction for plasmon transmission through a gold nanowire, as discussed in detail in Chap. 7. In the corresponding experimental setup, which is equipped with an NA = 1.3 microscope objective, light can pass through the objective up to a maximum half-angle of the light cone of $\theta_{\mathrm{NA}} = 59.4°$. The filtering by propagation angle as well as a schematic sketch of the marginal rays is included in Fig. 4.5.

4.4.3 Mode overlap analysis

The mode-specific incoupling efficiency η_{in} constitutes an important quantity in studies of the optical excitation of nanocircuits. It quantifies the efficiency of power transfer from an external excitation, e.g. a Gaussian beam, to the respective waveguide eigenmode [64]. In simulations and as detailed below, its value is obtained by means of a mode expansion analysis [126] and is denoted as η_{in}^{s}.

For a given waveguide supporting a complete set of source-free solutions to Maxwell's equations [see Sec. 4.3], i.e. m orthogonal eigenmodes Φ_m determined by their fields $\mathbf{E}_m$ and $\mathbf{H}_m$, any arbitrary input field can be expressed in terms of a weighted summation

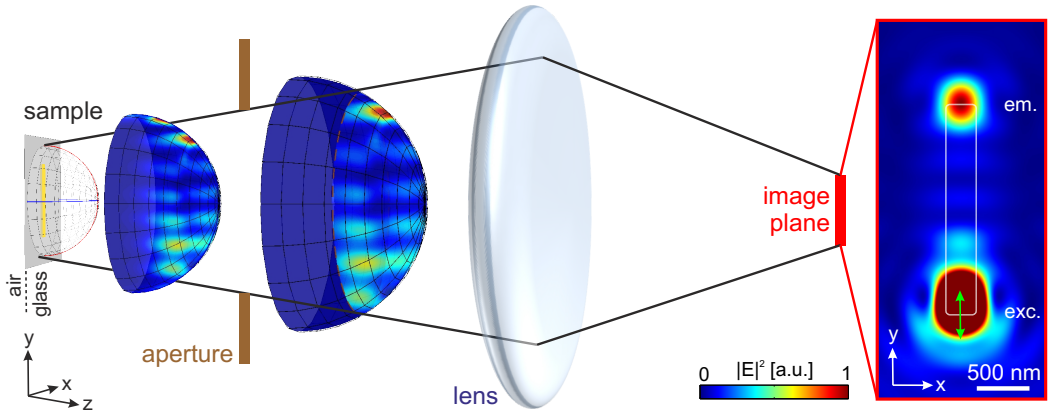

Figure 4.5: Schematic representation of the simplified imaging system used to acquire simulated microscope images. The sample (left), a 2 μm long single gold nanowire with lateral dimensions as described in Chap. 7, is excited by a tightly focused Gaussian beam (NA = 1.3, $\lambda = 800\,\mathrm{nm}$). The same objective, here represented by a simple lens, collects the emitted light and focuses it to the image plane (right). An aperture limits the angles of light that can pass the objective in accordance with the objective's NA.

of all these eigenmodes according to

$$\mathbf{E}_{in} = \sum_m a_m \mathbf{E}_m^+ + \sum_m b_m \mathbf{E}_m^-, \tag{4.13a}$$

$$\mathbf{H}_{in} = \sum_m a_m \mathbf{H}_m^+ + \sum_m b_m \mathbf{H}_m^-. \tag{4.13b}$$

Here, a_m and b_m represent the respective complex expansion coefficients (modal amplitudes) of the forward and backward propagating mode m (denoted by the superscripts $+$ and $-$, respectively) and describe the amplitude contributing to the total field. The first summation combines all forward propagating modes traveling in positive x-direction, the second summation all backward propagating modes.

Considering the definition of propagating modes [Eq. (4.10)], a positive propagation constant β results in a waveguide mode traveling in positive x-direction, while the corresponding backward propagating mode is simply obtained by the transformation $\beta \to -\beta$. Symmetry considerations result in the following relations [136]:

$$\mathbf{E}_m^- = \mathbf{E}_{t,m}^+ - E_{x,m}^+ \hat{\mathbf{x}}, \tag{4.14a}$$

$$\mathbf{H}_m^- = -\mathbf{H}_{t,m}^+ + H_{x,m}^+ \hat{\mathbf{x}}, \tag{4.14b}$$

with $\mathbf{E}_{t,m}^+$ and $\mathbf{H}_{t,m}^+$ describing the transverse field components of the forward propagating mode. Only transverse field components are relevant for the orthogonality relation, which is defined for forward propagating modes as

$$\frac{1}{2} \int \left(\mathbf{E}_m^+ \times \mathbf{H}_n^{+*} \right) \mathrm{d}\mathbf{S} = \delta_{mn} N_m \tag{4.15}$$

with the normalization factor N_m.[3] Equivalently, if either or both modes are backward propagating, the orthogonality relation [Eq. (4.15)] can be re-expressed by

$$\frac{1}{2}\int \left(\mathbf{E}_m^- \times \mathbf{H}_n^{+*}\right) \mathrm{d}\mathbf{S} = \delta_{mn} N_m, \tag{4.16a}$$

$$\frac{1}{2}\int \left(\mathbf{E}_m^+ \times \mathbf{H}_n^{-*}\right) \mathrm{d}\mathbf{S} = -\delta_{mn} N_m, \tag{4.16b}$$

$$\frac{1}{2}\int \left(\mathbf{E}_m^- \times \mathbf{H}_n^{-*}\right) \mathrm{d}\mathbf{S} = -\delta_{mn} N_m. \tag{4.16c}$$

Starting from Eq. (4.13) the complex modal amplitudes for any mode m can be determined by calculating the overlap integrals

$$\frac{1}{2}\int \left(\mathbf{E}_{in} \times \mathbf{H}_m^{+*}\right) \mathrm{d}\mathbf{S} = (a_m + b_m) N_m, \tag{4.17a}$$

$$\frac{1}{2}\int \left(\mathbf{E}_m^{+*} \times \mathbf{H}_{in}\right) \mathrm{d}\mathbf{S} = (a_m - b_m) N_m^*, \tag{4.17b}$$

where the orthogonality relations Eqs. (4.15) and (4.16) have been applied. After some algebra one obtains the wanted modal amplitudes

$$a_m = \frac{1}{4}\left[\frac{\int \left(\mathbf{E}_{in} \times \mathbf{H}_m^{+*}\right) \mathrm{d}\mathbf{S}}{N_m} + \frac{\int \left(\mathbf{E}_m^{+*} \times \mathbf{H}_{in}\right) \mathrm{d}\mathbf{S}}{N_m^*}\right], \tag{4.18a}$$

$$b_m = \frac{1}{4}\left[\frac{\int \left(\mathbf{E}_{in} \times \mathbf{H}_m^{+*}\right) \mathrm{d}\mathbf{S}}{N_m} - \frac{\int \left(\mathbf{E}_m^{+*} \times \mathbf{H}_{in}\right) \mathrm{d}\mathbf{S}}{N_m^*}\right]. \tag{4.18b}$$

A simulated field distribution $\{\mathbf{E}_{in}, \mathbf{H}_{in}\}$ recorded in a cross-sectional cut of the waveguide at a distance x from its incoupling end can thus be analyzed to yield the power in each mode at this position. In this context, simulations allow to simplify the system by suppressing any backward propagating modes by extending the waveguide into the absorbing PML boundaries (i.e. $b_m = 0$). Thus, the power in the forward propagating mode at position x along the waveguide is obtained via $p_m(x) = |a_m|^2 N_m$. By accounting for the mode's exponential intensity decay [see Sec. 4.3] this value can be extrapolated toward the waveguide input position. Consequently, the mode's incoupling efficiency $\eta^s_{\mathrm{in,m}}$ reads as

$$\eta^s_{\mathrm{in,m}} = \frac{p_m(x)}{p_0} \times \left[e^{-x/l_{\mathrm{decay}}}\right]^{-1}, \tag{4.19}$$

where p_0 is the source power and l_{decay} the intensity decay length of the mode. In general, the excitation power is not completely transferred into well-defined waveguide modes, but instead is partially propagating as unbound free space radiation, therefore p_m is always smaller than p_0.

[3] Only in the case of guided modes in non-absorbing waveguides, N_m is a real number describing the power carried by mode m. More generally, N_m is a complex quantity with its real part describing the power carried by mode m.

4.4.4 Mode reflectivity fitting at waveguide discontinuity

Along an unlimited plasmonic waveguide of uniform transverse refractive index profile the electric field amplitude and phase evolution of any guided eigenmode of wave vector k_{SPP} is fully governed by a propagation factor of the form $e^{ik_{\mathrm{SPP}}x}$. This manifests itself in an inevitable exponential decay of the mode intensity along the propagation direction. In contrast, a waveguide discontinuity, i.e. any abrupt change in the transverse refractive index profile, additionally results in partial mode reflection. As an example, the termination of a single nanowire waveguide, as investigated in detail in Chap. 7, is studied here.

By recording the near-field intensity forming around the nanowire upon excitation of its single guided eigenmode, as illustrated in Fig. 4.6a, the complex reflection coefficient $\Gamma = |\Gamma|e^{i\theta_\Gamma}$ can be obtained by analyzing the standing wave pattern. To this end, the standing wave's total field intensity I measured along a linecut in close proximity to the waveguide [Fig. 4.6b] is fitted by an analytical model [64]

$$I(x) = \left| A_0 \left[e^{ik_{\mathrm{SPP}}x} + e^{ik_{\mathrm{SPP}}(L-x)} \Gamma e^{ik_{\mathrm{SPP}}L} \right] \right|^2 , \tag{4.20}$$

where a semi-infinite nanowire is assumed, as in the actual simulation, and consequently only one reflection at the wire termination (position L) needs to be considered. A_0 is the mode's initial field amplitude. Since reflection is a consequence of impedance mismatch, Γ is very sensitive to the condition of the nanowire end, including its surrounding environment.

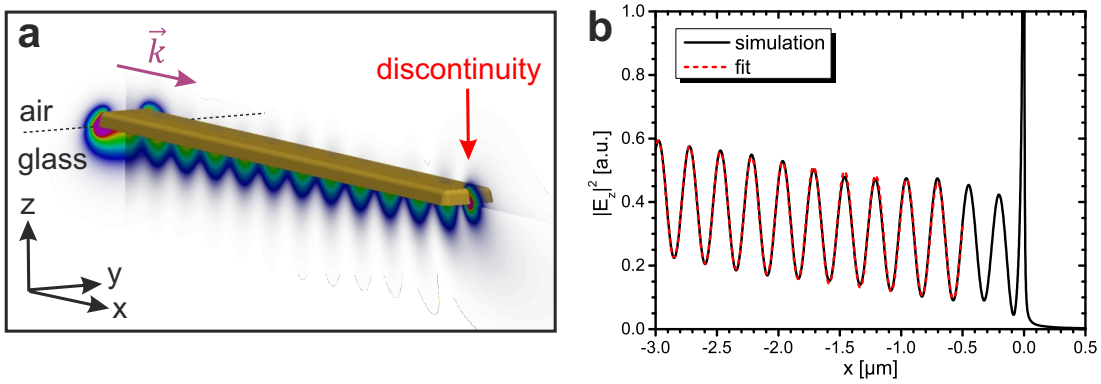

Figure 4.6: Mode reflectivity at discontinuity. (a) Standing wave pattern forming upon reflection of the single nanowire mode ($\lambda = 800\,\mathrm{nm}$) at a wire termination. (b) Nonlinear fitting of the intensity linecut recorded 5 nm below the nanowire in glass by means of Eq. (4.20) with k_{SPP} as obtained according to Sec. 4.3, yielding a reflection amplitude of $\Gamma = 0.42$ and a reflection phase of $\theta_\Gamma = 1.39$. The nanowire termination is at $L = 0\,\mathrm{nm}$.

Chapter 5

Plasmonic waveguide designs

In open space waves emitted from a localized source propagate in all directions as spherical waves. Thereby, the waves' intensity falls off with source distance R proportional to $\frac{1}{R^2}$. A waveguide is a structure designed to facilitate guiding of waves, in the particular case of this work electromagnetic waves in the optical spectrum, and thus signal transmission from one input port to one or more output ports with a significantly reduced signal decrease compared to the unbound expansion into three-dimensional space with the aforementioned inverse square law. Depending on their application waveguides in the optical regime can be constructed from either dielectrics or noble metals, thus forming photonic or plasmonic waveguides, respectively.

In photonic-based integrated optics, miniaturization and packaging density are fundamentally limited by the wavelength-scale modal profiles of guided photonic modes [137]. In contrast, plasmonic modes supported by noble-metal nanostructures offer strong subwavelength confinement [11, 75, 110] and therefore promise the realization of nanometer-scale integrated optical circuits with well-defined functionality [33, 53, 64, 138–140], and thus are the subject of this work.

A common feature of the plasmonic waveguide configurations showcased in Secs. 3.2 and 3.3 is a confinement of the near-field in one direction only, which is perpendicular to 2D interfaces. Consequently, plasmon propagation can take place in all directions within these 2D planes, hence naming the structures 2D plasmonic waveguides. Ultimately, we are interested in guiding plasmonic excitations in one direction only. The fabrication of such one-dimensional (1D) plasmonic waveguides can be categorized into two routes, namely the *bottom-up* and the *top-down* approach.

In the former approach plasmonic waveguides are self-assembled via chemical synthesis, yielding nanowires of cylindrical shape, that are introduced in Sec. 5.1. However, the envisaged plasmonic nanocircuits require the facility to deliberately build advanced waveguide networks. Thus, a sophisticated top-down nanofabrication technique, in the present case focused-ion-beam (FIB) milling, is needed. This allows for arbitrary patterning of a bulk substrate, here monocrystalline gold platelets, into desired networks of single- or multi-mode waveguides, as presented in Sec. 5.2. The findings of this chapter are of relevance for the design of all subsequently studied functional plasmonic nano-devices for signal processing.

5.1 Bottom-up assembled nanowire geometry

Chemically grown noble metal nanowires can readily be described as circular metal cylinders[1], thus representing a simple and analytically treatable 1D waveguide. In the following, a nanowire of radius R embedded in a homogeneous dielectric of infinite extent is considered [see sketch in Fig. 5.1a] [35, 48]. The nanowire is oriented along the z axis. The derivation of the resulting transcendental equation [Eq. (A.4)] for the complex propagation constant k_{SPP} of the fundamental TM_0 mode, from which λ_{eff} and l_{decay} can be deduced, is given in Appendix A. Both quantities critically depend on the nanowire radius R [35, 48], as illustrated in Fig. 5.1b for gold nanowires in air at a wavelength of $\lambda = 800\,\mathrm{nm}$, confirming that the mode experiences no cutoff for decreasing R.

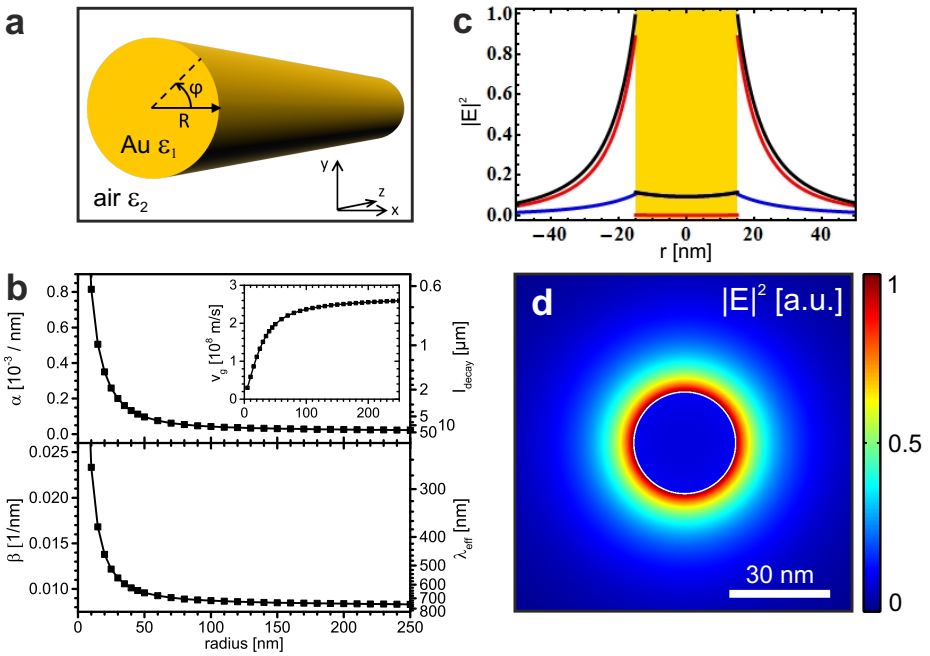

Figure 5.1: Cylindrical gold nanowire waveguide. (a) Illustration of the nanowire within the used coordinate system. (b) Mode properties of the 0^{th}-order guided modes for varying nanowire radius. (c) Analytical electric field components of the 0^{th}-order guided mode along a radial cut of a nanowire (R = 15 nm). The black line denotes the total electric field intensity, the red and blue lines its radial and z-component, respectively. (d) Analytical full-2D transverse intensity profile of the 0^{th}-order guided mode for the same nanowire. All results are obtained for a vacuum wavelength of 800 nm.

In view of applications in the field of optical communication, the propagation of ultrashort pulses representing bits of information is of fundamental importance and needs to be characterized in detail. Of particular interest in this context is the speed

[1] Geometrical aberration, e.g. pentagonal or hexagonal cross sections, have also been observed [141].

of propagation, i.e., the plasmon group velocity as defined in Eq. (3.10). The inset of Fig. 5.1b shows a strong dependency on the wire geometry, encompassing peculiar effects such as the vanishing group velocity in adiabatic focusing [142, 143]. Similar behavior is not known for electronic integrated circuits and can lead to characteristic signal delays in information processing systems.

Experimentally, this behavior was confirmed within a close collaboration with the work group of Tobias Brixner[2] using far-field spectral interferometry [144]. His group developed a microscope setup [145] capable of fully characterizing both amplitude and phase of propagating plasmons. This is achieved by interference of the signal transmitted through a plasmonic waveguide in the form of ultrashort pulses with a reference pulse. Consequently, for known distance of propagation the group velocity can be derived. Detailed results of this study can be found in [146].[3]

The analytically obtained electric field components of the fundamental TM_0 mode along a radial cut for an exemplary gold nanowire with radius $R = 15\,\mathrm{nm}$ are shown in Fig. 5.1c, together with the full-2D intensity profile in Fig. 5.1d. Both demonstrate the nonlinear intensity decay away from the gold-air boundary. This high intensity confinement in two dimensions is accompanied by propagation lengths l_{decay} [Eq. (3.8)] that are comparatively smaller than for the plane gold-air interface. While such cylindrical waveguides are typically single-mode for small radii, they can support higher orders of bound modes for larger radii, e.g., due to the appearance of an additional mode with azimuthal dependence $m = 1$.

Although self-assembled nanowires are extensively studied, e.g. in [50, 147], their applicability as building blocks of future plasmonic nanocircuits is practically limited for several reasons. Firstly, chemical growth usually results in an ensemble of nanowires with disperse diameters and lengths, requiring a time-consuming pre-selection of suitable nanowires. Secondly, structural uncertainties, such as the uncontrolled shape of the end facets, have a strong influence on the far-field excitation and emission properties of the nanowire modes [148–150]. Lastly, cumbersome micro-manipulation is required for pushing multiple nanowires in place. Nevertheless, simple functionalities, such as plasmon routing and logic gates, have successfully been implemented [56, 69, 71].

This section concludes with a short discussion of the accuracy of FDFD simulations, as introduced in Sec. 4.3. For the present structure the dominant simulation error is associated with the ability to resolve the structure's geometrical features as well as the near-field's strong spatial variations. The properties of the 0^{th}-order quasi-TM mode for a nanowire with 15 nm radius and varying discretization accuracy are shown in Fig. 5.2a. An edge length of 0.5 nm for the square-grid used for discretization gives values that are nicely converged to the theoretically expected values, although a rough agreement is still captured for more coarse discretizations.

[2] Institut für Physikalische und Theoretische Chemie, Universität Würzburg, Am Hubland, 97074 Würzburg, Germany

[3] In contrast to the waveguides presented in this thesis, the nanowires in [146] were made from silver.

This discretization of the circular wire cross section inevitably leads to sharp corners and unphysically high mode fields, as can be seen very drastically in Fig. 5.2b showing the mode profile calculated with 5 nm discretization steps. Reducing this by a factor of ten results in a mode profile [see Fig. 5.2c] that nicely compares with the analytical one depicted in Fig. 5.1d.

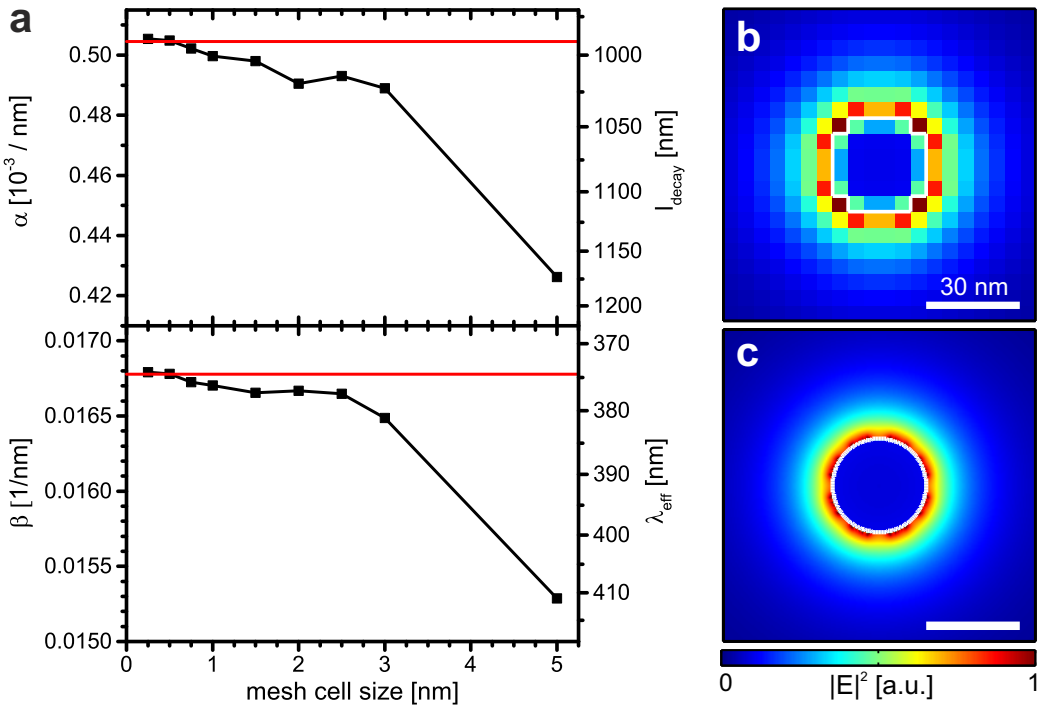

Figure 5.2: Discretization in FDFD simulations. (a) Mode properties of the 0^{th}-order quasi-TM nanowire mode (R = 15 nm) for varying edge lengths of the square-grid used for discretization. The analytical values obtained after Eq. (A.4) are indicated by the red lines. (b) The mode's intensity profile calculated using a square-grid discretization of 5 nm edge length. (c) Same as in (b), but for discretization with edge length of 0.5 nm. All results are obtained for a wavelength of 800 nm.

In general, such characterizations of numerical errors need to be done whenever a new geometry is introduced. As in the previously shown example, if an analytical model is available a comparison with this is the method of choice. However, for the waveguide structures considered later in this work there is no such exact analytical model available to compare with. Thus, convergence tests are performed by comparing results for increasing simulation accuracy in order to establish a good tradeoff between sufficiently accurate simulation results and manageable simulation requirements, yielding an ideal mesh cell edge length of 0.5 nm.

5.2 Top-down fabricated waveguide geometries

Due to the aforementioned limitations of bottom-up fabrication, the route followed in this work concerns studying nanoscale waveguides and resultant functional plasmonic nanocircuits that eventually can be top-down fabricated from monocrystalline gold platelets as a substrate. Moreover, the intended optical experiments require structures that are supported by a transparent substrate, in our case glass, thus lifting the symmetry of the waveguide surrounding.

5.2.1 Single-mode plasmonic waveguides

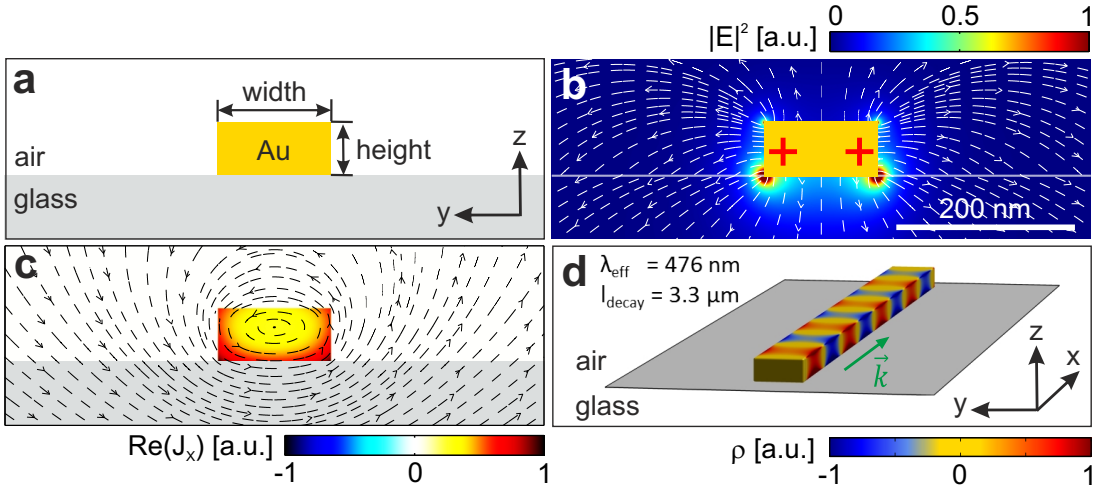

Figure 5.3: Eigenmode of solitary rectangular nanowire. (a) Sketch of a nanowire, defined by its width and height, residing on a glass substrate. (b) Mode profile of a gold nanowire with cross section of $125 \times 60\,\mathrm{nm}^2$ at vacuum wavelength of 800 nm. Electric field lines are indicated by the thin white lines. (c) Current density distribution in direction of the nanowire axis for the identical geometry. Magnetic field lines are indicated by the thin black lines. (d) Instantaneous charge distribution along a $2\,\mu$m long piece of nanowire. The values for λ_{eff} and l_{decay} are stated.

With this in mind, the simplest top-down fabricated plasmonic waveguide is a solitary nanowire (as is the cylindrical nanowire) with a rectangular cross-sectional geometry [Fig. 5.3a], representing a 1D insulator-metal-insulator waveguide. The modal intensity profile of an exemplary nanowire made from gold is presented in Fig. 5.3b. For sufficiently small nanowire dimensions, as is the case in the present work, this 0^{th}-order quasi-TM mode is the only guided mode at the wavelength of consideration. Thus, in the following it is simply referred to as the fundamental single nanowire mode. It is noted, that the presence of the high refractive index glass substrate pulls the near-fields toward the substrate side, thus highest mode intensity builds up in the glass directly below the structure. This feature is also present in the corresponding

current density distribution along the nanowire [Fig. 5.3c], where strongest currents in gold can be found close to the substrate. As the electromagnetic penetration depth and the nanowire dimensions are of same order, volume instead of surface currents are present [151], in clear contrast to classical RF theory. These volume currents are accompanied by induced magnetic fields, with their field lines closely resembling those of a classical current-carrying conductor. In a transverse cut through the nanowire net charges are accumulated, while the charge balancing happens along the propagation direction, as indicated by the instantaneous charge distribution in Fig. 5.3d.

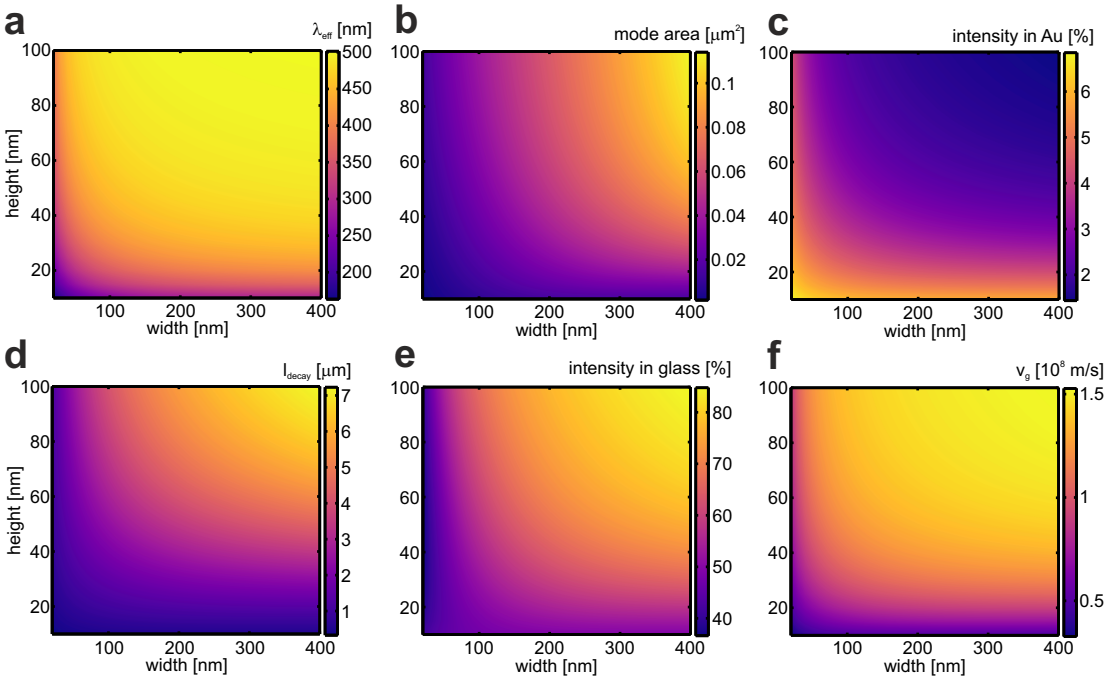

Figure 5.4: Mode properties of solitary rectangular Au nanowires. (a) Effective wavelength, (b) mode area, (c) fraction of intensity in gold, (d) propagation length, (e) fraction of intensity in glass, and (f) group velocity for varying nanowire width and height at fixed vacuum wavelength of 800 nm.

Changing the dimensions of the rectangular nanowire, i.e. its width and height, has a strong impact on the properties of guided SPPs, similar to the previously shown cylindrical wire in Fig. 5.1b. For the guided fundamental modes of single gold nanowires at a wavelength of 800 nm the trends are shown in Fig. 5.4. Apparently, a change in either nanowire width or height has similar consequences on the mode's properties. A decrease in either of the two nanowire dimensions results in a decrease of the effective wavelength [Fig. 5.4a] caused by the increasing mode confinement. This is evident from the decreasing mode area [Fig. 5.4b], as calculated according to [126], which simply means that the mode is more localized around the gold allowing more fields to penetrate into the gold [Fig. 5.4c]. A larger intensity inside the metal of course is accompanied by increased inherent Ohmic losses and a decreasing propagation length,

as shown in Fig. 5.4d. On the other hand, for large wire dimensions the intensity is less localized and tends to be mostly dragged into the glass substrate [Fig. 5.4e], explaining why the group velocity approaches the speed of light in glass [Fig. 5.4f]. Due to the finite penetration depth in gold all above mentioned quantities show a saturating behavior in the limit of very large wire dimensions.

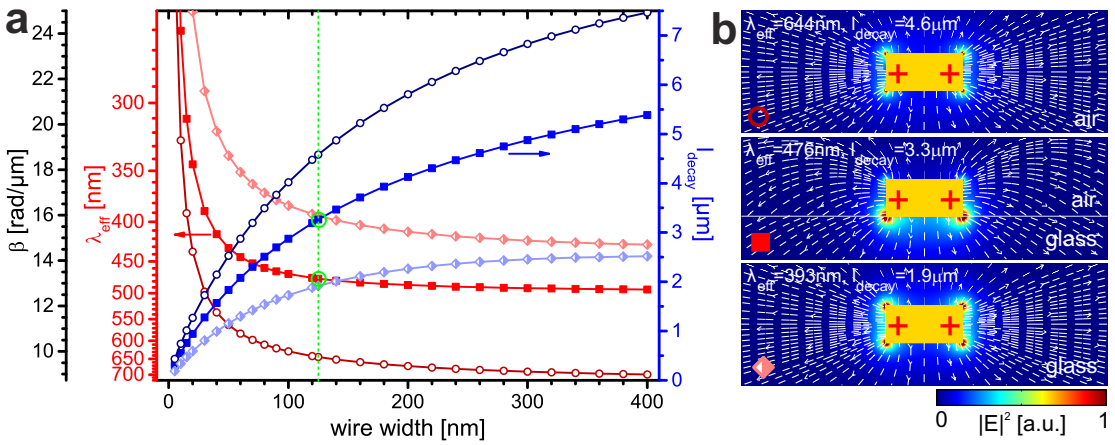

Figure 5.5: Mode properties of single Au nanowires in different surroundings. (a) Propagation constant and effective wavelength (left abscissae, reddish curves) along with corresponding propagation length (right abscissa, bluish curves) of the fundamental guided SPP of a single nanowire situated in air (hollow circles), on a glass-air interface (solid rectangles), and in glass (diamonds). The nanowire height is fixed at 60 nm, the vacuum wavelength is 800 nm. (b) Representative mode profiles for the three surroundings (top: air, middle: glass-air, bottom: glass) for a nanowire of width 125 nm. Electric field lines are indicated by the thin white lines. All mode profiles are normalized to the same power in the mode.

Both effective wavelength and propagation length are sensitive to the surrounding environment. Figure 5.5 shows both data for nanowires on top of a glass half-space as well as embedded in homogeneous media representing air and glass, respectively. For the homogeneous environment the higher refractive index of glass results in consistently smaller effective wavelengths and propagation lengths for all wire widths [Fig. 5.5a]. The inhomogeneous glass-air interface consequently falls in between the homogeneous cases. The mode profiles for the three situations are illustrated in Fig. 5.5b. Apart from the obvious symmetry of the modes in homogeneous environments the stronger confinement in case of homogeneous glass compared to air is in agreement with the respective mode properties.

5.2.2 Multi-mode plasmonic waveguides

In assemblies of two parallel nanowires separated by a nanoscale dielectric gap, known as two-wire transmission lines (TWTLs), the individual single nanowire modes couple via near-field interaction. As part of the mode hybridization, which similarly occurs in strongly coupled nanoparticle dimers [152–154], two fundamental TWTL eigenmodes arise with distinct mode symmetry, which is determined by the difference in phase between the currents on both nanowires. For the antisymmetric TWTL mode, with its mode profile shown in Fig. 5.6a, the π phase difference in the currents [Fig. 5.6b] results in opposite charges across the nanogap and hence strongly localized fields [64], which promise great potential for enhanced nanoscale light-matter interaction [53, 155, 156]. This quasi-TE mode is analogous to the fundamental bound MIM mode studied in Sec. 3.3.1. Charge balancing again happens along the propagation direction, as shown in Fig. 5.6c.

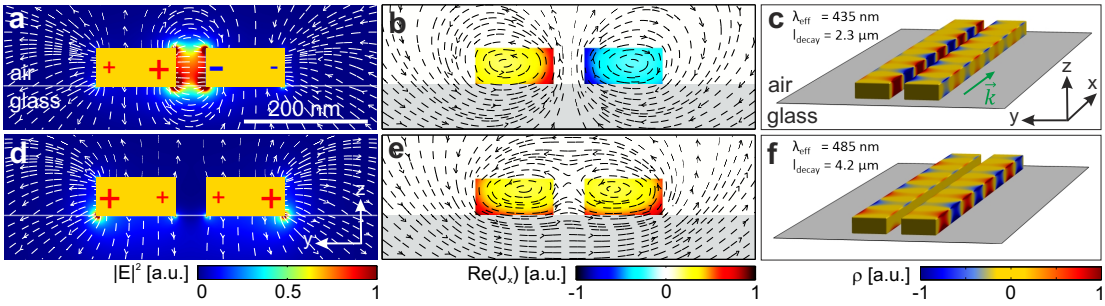

Figure 5.6: TWTL eigenmodes. (a) Antisymmetric mode profile for a TWTL with nanowire cross sections of $125 \times 60\,\mathrm{nm}^2$ and a nanogap size of 50 nm at vacuum wavelength of 800 nm. The instantaneous charge distribution is symbolized by + and -. Electric field lines are indicated by the thin white lines. (b) Corresponding current density distribution in direction of the TWTL axis for the identical geometry. Magnetic field lines are indicated by the thin black lines. (c) Instantaneous charge distribution of antisymmetric mode propagating along a 2 μm long piece of TWTL. The values for λ_{eff} and l_{decay} are stated. (d)-(f) Same as (a)-(c), but for the symmetric TWTL mode. Both mode profiles in (a) and (d) are normalized to the same power as those in Fig. 5.5.

The intensity distribution of the symmetric TWTL mode is shown in Fig. 5.6d. Here, in-phase currents [Fig. 5.6e] lead to a symmetric charge distribution [Fig. 5.6f] and minimal fields within the nanogap, while most intensity is guided at the outer surface towards the substrate. Thus, contrary to the antisymmetric mode it can only weakly interact with matter in the nanogap. This symmetric mode is quasi-TM polarized, similar to the fundamental bound IMI mode studied in Sec. 3.3.2.

The appearance of the two aforementioned TWTL modes on the basis of coupling between guided single wire modes can be illustrated by a splitting of the wave vector's real part β at fixed operation wavelength. Figure 5.7 shows β and the propagation length against the nanogap size. By decreasing the size of the nanogap and thus enhancing the near-field coupling the wave vector difference between antisymmetric and symmetric mode increases considerably. This strong coupling is unique to plasmonic waveguides, since it is absent for photonic-type modes in both photonic crystal waveguides and dielectric waveguides. Also, the antisymmetric mode is much more influenced by a change in gap size making it more sensitive to fabrication-induced uncertainties. For gap sizes exceeding 250 nm the coupling between the two individual nanowires is negligible, thus the propagation constant as well as the propagation length reach the values of a solitary single nanowire mode.

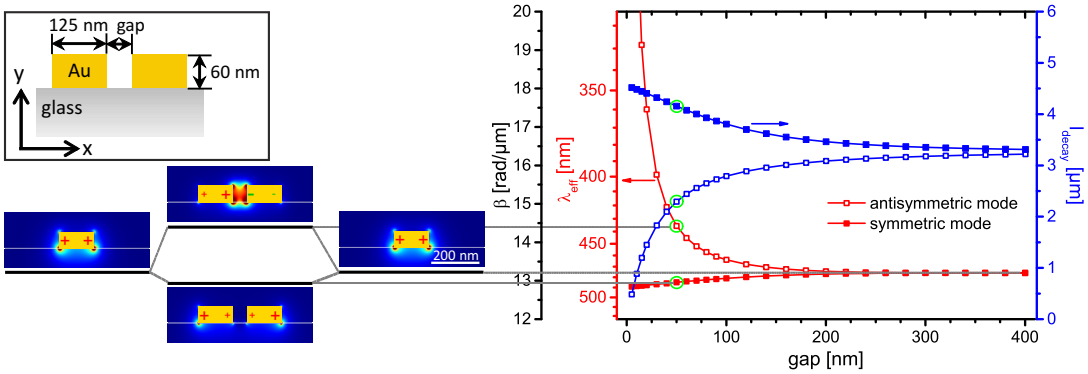

Figure 5.7: Mode hybridization due to coupling of individual nanowire modes for varying separation. The nanowire's cross section is $125 \times 60\,\mathrm{nm}^2$, the vacuum wavelength is 800 nm. Propagation constant, effective wavelength, and propagation length of symmetric and antisymmetric mode show a gap-size dependent splitting. For a nanogap of 50 nm the intensity profiles of symmetric and antisymmetric mode are plotted on their respective propagation constant levels on the left. The uncoupled solitary nanowire mode is additionally added. All mode profiles are normalized to the same power in the mode.

It is noted, that the well-studied eigenmodes of a slit waveguide and a single nanowire constitute the limiting cases of antisymmetric and symmetric TWTL eigenmodes, respectively, as obvious from comparison of Fig. 5.8 with Fig. 5.6. The benefit of TWTLs thus is their ability to support two eigenmodes of different symmetry on the same structure. This allows for the preparation of arbitrary mode superpositions. From Chap. 8 onwards this possibility is utilized for advanced functionality in plasmonic nanocircuity.

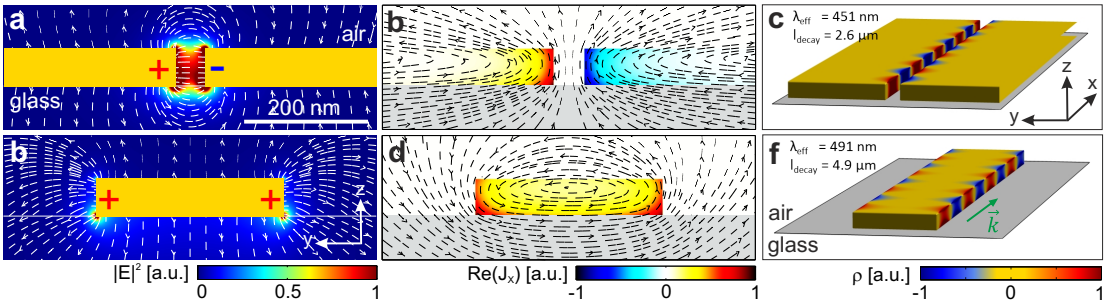

Figure 5.8: Eigenmodes of slit waveguide and single nanowire, constituting the limiting cases of antisymmetric and symmetric TWTL eigenmodes, as shown in Fig. 5.6. (a) Mode profile of the gap mode of a 50 nm wide nanoslit in gold at vacuum wavelength of 800 nm. The instantaneous charge distribution is symbolized by + and -. Electric field lines are indicated by the thin white lines. (b) Corresponding current density distribution in direction of the slit axis for the identical geometry. Magnetic field lines are indicated by the thin black lines. (c) Instantaneous charge distribution of the gap mode along a 2 μm long piece of the nanoslit. The values for λ_{eff} and l_{decay} are stated. (d)-(f) Same as (a)-(c), but for the single nanowire mode with 300 nm total nanowire width. Both mode profiles in (a) and (d) are normalized to the same power as those in Fig. 5.5.

Chapter 6

Limits of Kirchhoff's laws in plasmonics

The power of electronic circuit design is based on the fact that complex circuitry can be created by arranging simple circuit elements into networks. The circuit properties can then be calculated using Kirchhoff's laws. It would be a great asset if similar design principles could be used in nanophotonics to create complex nanophotonic circuitry based on simple building blocks. However, at such short wavelengths the applicability of Kirchhoff's laws cannot be taken for granted any more.

In this chapter, we investigate the validity of Kirchhoff's laws in plasmonic nanocircuitry by studying a junction of plasmonic TWTLs, which represents a fundamental building block of nanophotonic circuitry. We identify a new phenomenological parameter relating the geometrical parameters of the junction to the wavelength of propagation. This allows to judge the degree of validity of Kirchhoff's laws. As an example and illustration of the power of the suggested approach we investigate a system composed of a TWTL and a nanoantenna as a load. By addition of a parallel stub designed according to Kirchhoff's laws we achieve maximum signal transfer to the nanoantenna. Most of this chapter has been published in [157].

6.1 Motivation

The strong subwavelength light confinement of guided plasmonic modes supported by noble-metal nanowires [11, 35, 48] is a prerequisite for the realization of optical nanocircuits bridging the size mismatch between nanoelectronics and micrometer-scaled optical devices. At the core of such optical nanocircuits lies a very small footprint network of optical transmission lines enabling the controlled distribution and manipulation of plasmonic excitations. Devices featuring well-defined built-in functionalities [75, 76] such as directional switching [56, 69, 158] or filtering [33] have been realized. Junctions of such transmission lines represent one of the fundamental building blocks of any such network.

The power of electronic circuit design is based on the fact that complex circuitry can be replaced by simple circuit elements described by a discrete impedance. Circuit elements can then be arranged into networks, whose functionality can be analyzed

based on Kirchhoff's laws. Naturally, some efforts have also been devoted to the use of Kirchhoff's laws for the description of circuit elements and circuitry at optical frequencies. The figurative representation and modularization of nano-optical systems enabled by the application of equivalent circuit models provides significant insight into their optical response and can be used to improve the overall performance of plasmonic nanostructures such as isolated nanospheres [159], dipole [160–165] and more elaborate [166] nanoantennas, or plasmonic waveguide components [64, 167]. As a well-established principle of classical transmission line theory, the impedance description of lumped and distributed circuit elements [162, 168, 169] has also been successfully applied to improve the impedance matching between a plasmonic waveguide and a nanoantenna [64, 170] and between waveguide segments of different geometry and/or orientation [171–174]. However, at the short wavelengths involved and given the finite dimensions of nano-optical circuitry the applicability of Kirchhoff's laws cannot be taken for granted. Yet there is no systematic study as to what extent circuit theory can be applied to subwavelength plasmonic systems.

In spite of the similarities, the optical (plasmonic) regime shows significant differences from the radio frequency (RF) regime. Firstly, at optical frequencies noble metals do not behave as perfect conductors but, due to the small negative real part of their permittivity, as plasmonic materials [see Chap. 3]. This holds several implications, for example the non-negligible skin depth compared to the wire cross section [see Sec. 5.2.1], which in turn creates volume currents with no counterparts in RF [175]. Secondly, the lumped element model of electronic circuits and Kirchhoff's laws can be understood as an approximation of Maxwell's equations in the low-frequency domain (quasistatic limit), equivalent to assuming the involved wires, when compared to the circuit's operation wavelength, as quasi 1D in cross section and their junctions as point-like objects. While in the RF regime with typical ratios of wire dimension to wavelength on the order of 10^{-3} (estimated for a common twin lead cable at 100 MHz frequency) this limit is satisfied, in the optical regime the approximation has to be questioned. Even with state-of-the-art fabrication techniques the realizable dimensions (i.e. the nanowire cross section and the inter-wire distance) are in the range of a few tens of nanometers, thus such realistic nanowires and their junctions are rather laterally extended objects in a size range comparable to the effective wavelength of the supported eigenmodes. This is reflected by ratios of wire dimension to wavelength exceeding 0.1, as further detailed below. Finally, at variance with the purely transverse guided modes sustained by perfect conductors (which is the case in the RF regime), plasmonic modes possess a significant longitudinal component that is not taken into account in the standard impedance description.

In this chapter, the validity of Kirchhoff's circuit laws in the optical regime is investigated by considering a fundamental, yet simple system, i.e. a junction of TWTLs supporting an antisymmetric guided plasmonic mode. The first part of this chapter deals with an idealized junction of infinite TWTLs of uniform cross-sectional geometry with one input and two outputs. We show by FDTD simulations that clear deviations occur from the expected behavior derived from Kirchhoff's circuit laws applied to the

same waveguide junction [Sec. 6.2]. By varying the TWTL's cross-sectional dimensions, the deviation from Kirchhoff theory can clearly be correlated with an increasing finite extension of the structure, as observed in Sec. 6.3. Despite the significant deviations, which cannot be completely neglected even for nanowire dimensions at the limit of current microfabrication techniques, we show that Kirchhoff's laws can still be used as a qualitative guideline to compose nano-optical circuitry that is then subject to further (numerical) optimization. The second part of this chapter highlights additional deviations due to mutual coupling of discrete circuit components located in close proximity. It is based on the example of a system composed of a TWTL and a nanoantenna as the load. By addition of a parallel stub [Sec. 6.4] designed according to Kirchhoff's laws we realize maximum transfer of signal between circuit elements in Sec. 6.5, a necessary prerequisite for the design of efficient devices, and use this example to further test the validity of the lumped-element impedance approach.

6.2 Idealized TWTL junction

A classical TWTL consists of a pair of parallel conducting wires separated by a uniform distance. Wire geometry and separation determine its characteristic impedance Z_0. It is a fact of classical transmission line theory that the parallel connection of two such idealized infinitely long TWTLs [as shown in Fig. 6.1a] results in an equal splitting of any input current. This is an implication of the node analysis by means of Kirchhoff's circuit laws. To be more specific, if two impedances are connected in parallel, the voltage drop across both of them is identical, thus according to Ohm's law the current entering the junction is split inversely proportional to their impedances. Therefore, for two identical parallel impedances the current splits equally. The optical analogue, the simplified plasmonic TWTL junction geometry studied in the following, is sketched in Fig. 6.1b. An input TWTL [marked as s in Fig. 6.1b] of characteristic impedance Z_0 branches into two perpendicularly oriented TWTLs [marked as t and u in Fig. 6.1b] of identical cross section extending to infinity. For reasons of simplicity the investigated TWTL structure is placed in vacuum to ensure that both the vertical and the horizontal TWTLs support the same propagating mode with identical Z_0 and to exclude any parasitic effects of a substrate. In the simulations presented here, two nanowires of squared cross section consisting of gold and separated by a small gap build up the TWTL. In a first step, we calculate the mode profile of the antisymmetric TWTL eigenmode at a wavelength $\lambda = 830\,\mathrm{nm}$ [Fig. 6.1b, inset] for a given wire cross section by means of a full-vectorial eigenmode solver [see Sec. 4.3]. Afterwards, full-3D FDTD simulations [see Sec. 4.1] are carried out at the same wavelength exciting the structure from the input TWTL side (s) by direct injection of the previously calculated mode. Infinitely long TWTLs are mimicked in the simulations by extending them into the perfectly matched layer boundaries surrounding the simulation volume, thus avoiding any back-reflection to the junction region. The whole TWTL junction region is covered by a uniform mesh of $1 \times 1 \times 1\,\mathrm{nm}^3$ cell size.

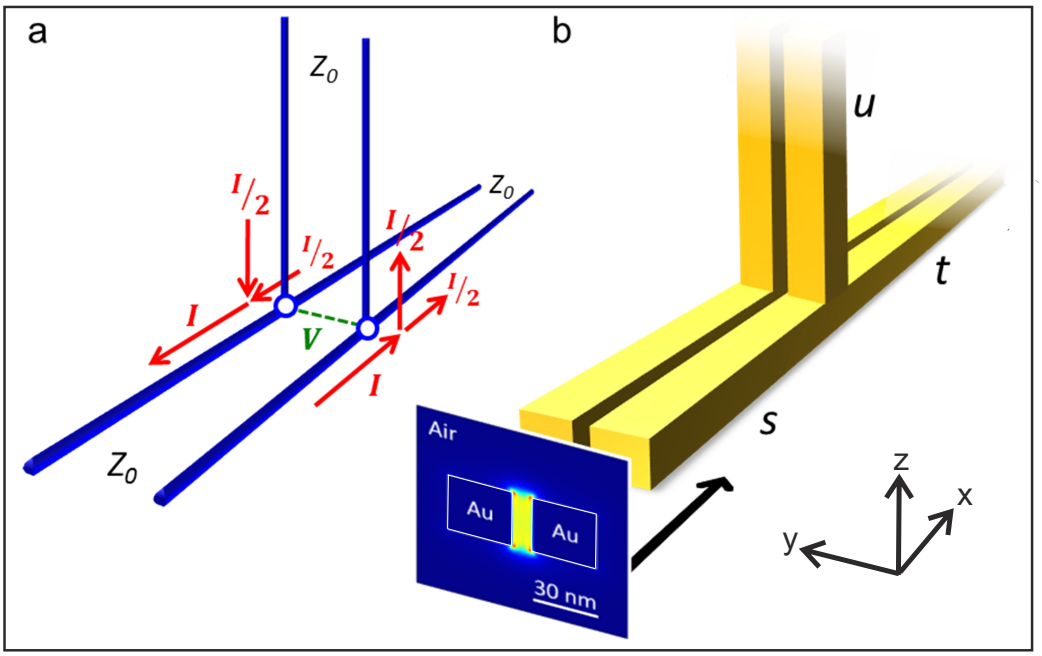

Figure 6.1: Classical vs. plasmonic transmission lines. (a) Two classical TWTLs of identical characteristic impedance Z_0 connected in parallel resulting in an equal splitting of electrical currents at the point junction. (b) Equivalent junction of two plasmonic TWTLs, an idealized building block of optical nanocircuits. Inset: The guided antisymmetric mode (electric field intensity $|E|^2$ at free-space wavelength $\lambda = 830\,\mathrm{nm}$) is directly launched from the left and propagates along the nano-sized TWTL, where the mode intensity is split at the parallel junction. Figure taken from [157].

Figures 6.2a-d show simulation results for a small-sized TWTL composed of nanowires with a $30 \times 30\,\mathrm{nm}^2$ cross section separated by a 10 nm gap. When exciting the TWTL's antisymmetric eigenmode [see Fig. 6.2a, inset] in a single infinite TWTL, the intensity is exponentially damped along the propagation direction [Fig. 6.2a]. As the parallel junction is formed by introducing the upward TWTL (u) [Fig. 6.2b] the intensity transmitted through the junction region into the horizontal output TWTL (t) is significantly reduced, in favor of both mode intensity propagating in the upward direction and mode intensity being reflected due to the impedance mismatch at the junction. The latter results in the formation of a standing wave intensity pattern on the input side, as obvious from Fig. 6.2c, where we plot the intensity difference between the simulation results of Fig. 6.2b and those of Fig. 6.2a.

We introduce two figures of merit to analyze the junction and quantify the difference between the plasmonic TWTL junctions and their RF counterparts, namely the power splitting ratio and the (complex) reflection coefficient $\Gamma = |\Gamma|e^{i\theta_\Gamma}$, where $|\Gamma|$ and θ_Γ denote the reflection amplitude and phase, respectively. Firstly, the power splitting ratio is obtained by applying a mode overlap analysis [in accordance with Sec. 4.4.3] using 2D near-field data in cuts through the horizontal (vertical) output

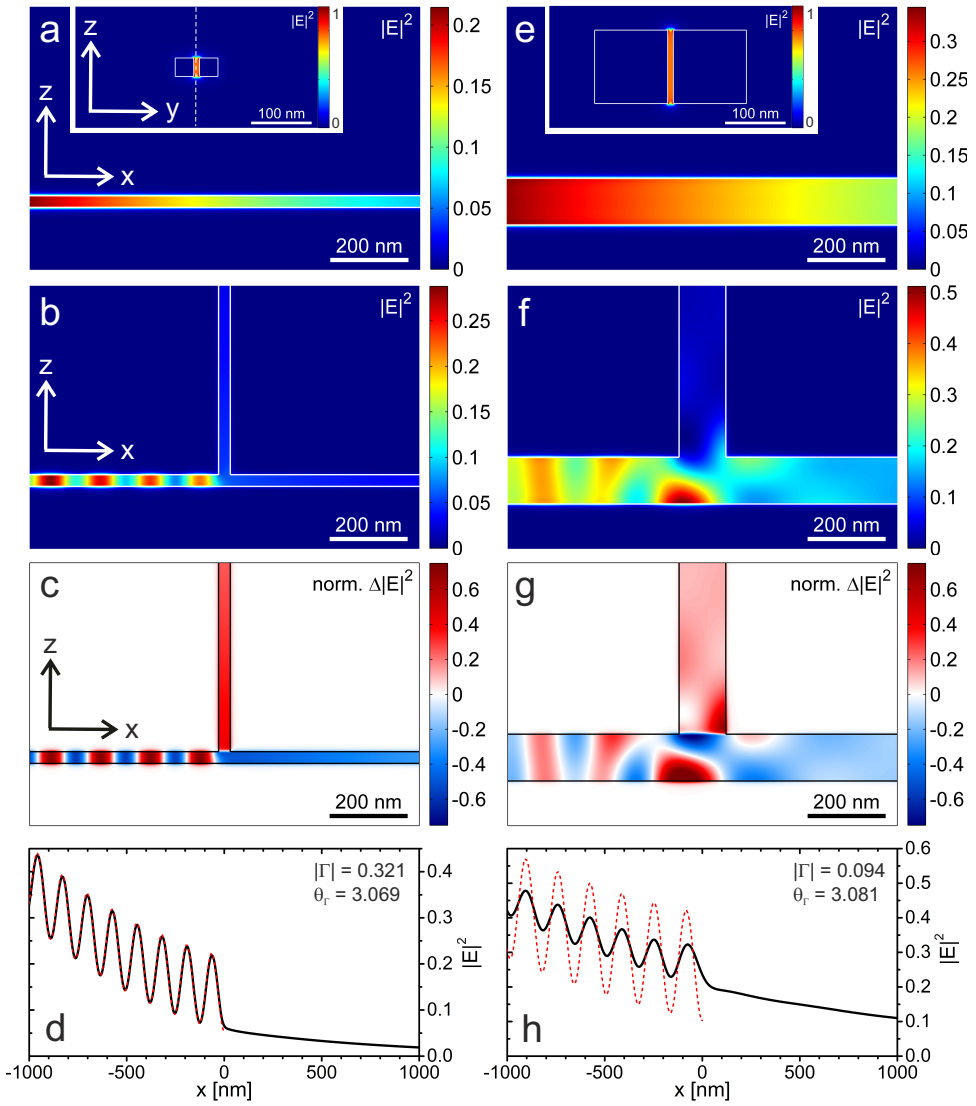

Figure 6.2: Parallel junction of plasmonic TWTLs. (a) Optical near-field intensity distribution in a cut through the gap centered between small-sized nanowires (width = height = 30 nm, gap = 10 nm) of an unconnected TWTL. Inset: modal profile of the guided antisymmetric mode with most of its intensity localized in the nanowire gap. The dashed white line indicates the plane used to record the near-field intensity cut. (b) Same as in (a) but for a parallel junction of TWTLs. (c) Intensity difference plot obtained from the maps with (b) and without (a) the upward pointing semi-infinite TWTL. (d) Standing wave pattern forming along the TWTL due to partial reflection of the antisymmetric mode at the TWTL junction used to extract the reflection coefficient according to the method described in Sec. 4.4.4. The theoretically expected behavior (red dashed line) corresponding to $|\Gamma| = 1/3$ and $\theta_\Gamma = \pi$ is added as a guide for the eye. The intensity distribution (black solid line) is recorded mid-height in the gap center of the horizontal TWTL. (e)-(h) The same as (a)-(d), but for a parallel junction of wider TWTLs (width = height = 120 nm, gap = 10 nm). Figure taken from [157].

TWTL at equal distances from the junction center to determine the remaining power in the antisymmetric mode in the horizontal (vertical) output. With this, the power splitting ratio is determined as the ratio of powers in the antisymmetric mode along the horizontal and the vertical output TWTL, respectively. As a measure for the deviations from the RF behavior we exploit the fact that in classical transmission line theory Kirchhoff's circuit laws together with Ohm's law predict an equal splitting of power at a parallel junction of two identical semi-infinite TWTLs.

Secondly, further insight into the behavior of the junction region is obtained by determining Γ at the junction position as a direct measure of the degree of impedance matching. The input impedance Z_{tot} of a parallel junction of horizontal and vertical semi-infinite output TWTLs with the same Z_0 is $Z_{\mathrm{tot}} = Z_0/2$, which is not impedance matched to the characteristic impedance of the input TWTL. Consequently, the guided plasmon mode is partially reflected as it reaches the junction, which according to the definition of Γ,

$$\Gamma = \frac{Z_{tot} - Z_0}{Z_{tot} + Z_0}, \tag{6.1}$$

results in a theoretically expected reflection amplitude $|\Gamma| = 1/3$ and a phase accumulation $\theta_\Gamma = \pi$. In numerical simulations, Γ is obtained by fitting Eq. (4.20) to the total intensity I_{total} of the forming standing wave pattern along a linecut centered in the gap of the input TWTL.

For the geometry studied in Figs. 6.2a-d one observes that the intensity in the antisymmetric mode entering the horizontal output is only 10% larger than the intensity directed into the vertical output. Similarly, as shown in Fig. 6.2d, the reflection amplitude $\Gamma = 0.321$ and phase $\theta_\Gamma = 3.069$ obtained by fitting of Eq. (4.20) to the standing wave pattern also reveal very small differences from transmission line theory predictions of 3.7% and 2.3%, respectively. In the regime investigated in Figs. 6.2a-d, therefore, Kirchhoff's laws respresent a valuable asset, providing accurate predictions for the response of the plasmonic circuit.

6.3 Dimension dependent deviations

The influence of the structure size on the observed deviations from RF theory is demonstrated in Figs. 6.2e-h, showing equivalent simulation results for a wider TWTL with nanowire cross section of $120 \times 120\,\mathrm{nm}^2$ and a gap of 10 nm. Here, the intensity distribution in the gap region becomes notably asymmetric, as seen in Figs. 6.2f,g, leading to the presence of anomalous field gradients at the junction, which deviate markedly from the expected transversal wavefronts of the guided modes. The resulting deviation from the RF-like behavior is manifested in a very poor power splitting ratio of 5.51 and calculated reflection amplitude $\Gamma = 0.094$ and phase $\theta_\Gamma = 3.081$ [Fig. 6.2h]. To investigate in more detail the influence of the lateral dimensions of the plasmonic waveguide on the degree of agreement with RF theory, we systematically varied the nanowire width [Figs. 6.3a-c] and the gap distance [Figs. 6.3d-f], separately.

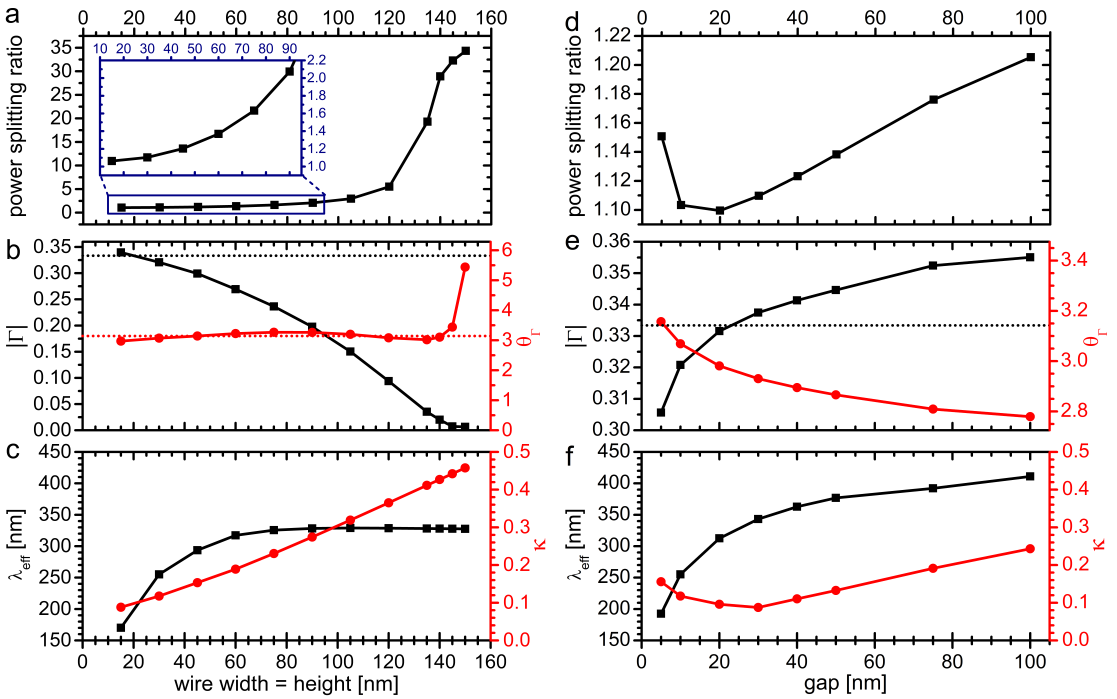

Figure 6.3: Variation of plasmonic TWTL dimensions. (a) Power splitting ratio, (b) reflection amplitude (black curve) and phase (red curve), and (c) λ_{eff} (black curve) and κ (red curve) as a function of nanowire width. The gap is kept constant at 10 nm. (d) Power splitting ratio, (e) reflection amplitude (black curve) and phase (red curve), and (f) λ_{eff} (black curve) and κ (red curve) as a function of the gap size. The nanowire width and the height are kept constant at 30 nm. Figure taken from [157].

On the one side, as the width and the height of the nanowires with square cross section are simultaneously increased (with a fixed gap of 10 nm) the power splitting ratio [Fig. 6.3a] gradually increases and deviates more from the expected ratio of 1. Thus, especially for wider wires, the guided mode tends to propagate mostly horizontally, whereas only little intensity is re-directed to the upward oriented TWTL. Similarly, the reflection amplitude displayed in Fig. 6.3b (black curve) drastically decreases for increasing wire dimensions, again deviating more and more from the expected value of $|\Gamma| = 1/3$. It is noted that the reflection phase [Fig. 6.3b, red curve] in contrast does not show such a monotone behavior, but still shows a strong deviation from the expected value of $\theta_\Gamma = \pi$ beyond a wire width of 140 nm. The observed increase in deviations from RF theory derived from the two figures of merit can be tentatively correlated to a phenomenological characteristic TWTL dimension κ, which is defined as the ratio of the largest TWTL physical dimension, which can be either the nanowire width or the gap distance, and the effective wavelength λ_{eff} of the antisymmetric mode supported by the specific TWTL cross section. Originally, the lumped circuit model and consequently Kirchhoff's circuit laws were derived under the assumption of very small characteristic circuit cross sections compared to the circuit's operation wave-

length, i.e. $\kappa \ll 1$. Figure 6.3c shows the evolution of λ_{eff} (black curve) as a function of the nanowire width, demonstrating an initial increase of λ_{eff} followed by a saturation behavior for wires exceeding about 100 nm in width. With this the evolution of the phenomenological parameter κ is derived, showing a steady increase as the nanowire width grows and reaches values of almost 0.5 for the widest wires studied [Fig. 6.3c, red curve]. Here, the validity of the assumption of $\kappa \ll 1$ clearly breaks down, an occurrence that correlates with the strongly deviating behavior of TWTL junctions composed of extended nanowires.

On the other side, as the gap is increased (with a fixed cross section of $30 \times 30\,\text{nm}^2$) the power splitting ratio [Fig. 6.3d] first decreases reaching a minimum (and thus best agreement with theory) for a gap of 20 nm, then it starts increasing again for larger gaps. However, even for the largest investigated gap of 100 nm the deviation remains rather small (less than 20 % increase). Similarly, the reflection amplitude [Fig. 6.3e, black curve] shows best agreement with the expected value of $|\Gamma| = 1/3$ for a gap width of 20 nm. This behavior can be again phenomenologically correlated with the relative characteristic TWTL dimension κ. As shown in Fig. 6.3f, λ_{eff} increases with gap size, however the TWTL's largest physical dimension is not changing up to a gap of 30 nm, since only then the gap distance and the nanowire width become equal in size. Therefore, κ is not monotonically increasing, but instead shows a minimum for 30 nm gap sizes. Also, in the presented gap scan κ has overall smaller values compared to the nanowire width scan [Fig. 6.3c], supporting the generally better agreement with the lumped circuit model.

6.4 Finite stub tuning

Based on this analysis, and thanks to the improved understanding gained on the reasons and the relevance of the deviations from Kirchhoff's laws, we can infer that it is possible with reasonable accuracy to extend the range of validity of Kirchhoff's analysis to plasmonic waveguide networks in the optical regime provided that $\kappa \lesssim 0.1$.[1] In this case the lumped circuit approximation commonly used in the RF regime can be applied on safe grounds. This is highly beneficial because it allows one to simplify complex relevant problems such as the optimization of power transfer in a system composed of a TWTL and a nanoantenna as the load by addition of a suitable parallel-connected tuning element. As an intermediate step toward this goal, we first apply the circuit description to a system composed of an infinite TWTL and a parallel-connected finite TWTL section of length L (usually referred to as a 'stub' [176, 177]), as sketched in Fig. 6.4a. For this geometry one expects reflection at the stub termination and thus resonances building up within the stub. In this study, in order to further corroborate the role played by the phenomenological parameter κ, the geometrical cross section

[1] It should be noted, though, that the numerical case study at hand of course cannot be taken as a general proof for the validity of the κ-criterion. Nevertheless, we believe that similar threshold values will be found in different systems as well.

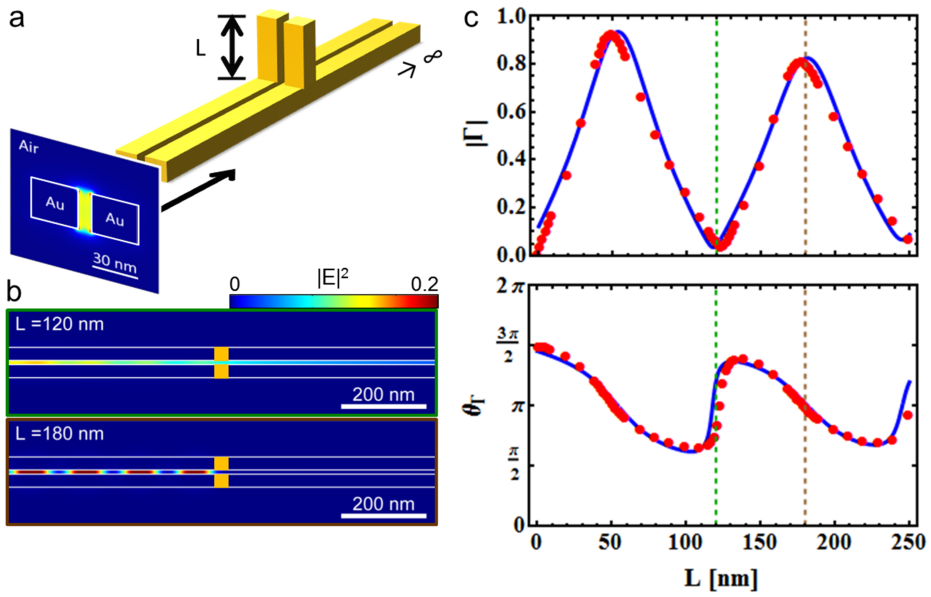

Figure 6.4: Finite stub reflectivity tuning. (a) Sketch of the investigated system featuring an infinite TWTL connected in parallel with a finite stub of length L. The displayed antisymmetric mode is directly launched from the left and propagates along the nano-sized TWTL. (b) The mode's standing wave pattern along a cut at midheight through the TWTL for high impedance stub ($L = 120\,\text{nm}$, top) and low impedance stub ($L = 180\,\text{nm}$, bottom). (c) Reflection amplitude (top) and phase (bottom) for systems of varying stub length L. The red dots are obtained by fitting of FDTD simulation data with the model described in Eq. (4.20), while the blue solid lines are obtained by the analytical model [see Appendix B.1]. Figure taken from [157].

of the TWTL is chosen as in Figs. 6.2a-d, i.e. the individual nanowires have a cross section of $30 \times 30\,\text{nm}^2$ and a gap of 10 nm. Thus, κ takes a value of 0.036 and the geometry is expected to show good agreement with the theory based on Kirchoff's laws. Figure 6.4b shows the simulated near-field intensity distribution within the infinite TWTL when connected in parallel with a high impedance stub ($L = 120\,\text{nm}$, top) and a low impedance stub ($L = 180\,\text{nm}$, bottom). The high reflectivity observed for the case of the low impedance stub is a direct consequence of the destructive interference along the output TWTL. Figure 6.4c shows the reflection amplitude and phase for varying stub length L as measured at the stub connection position obtained by full-3D FDTD simulations (red dots). As expected, the reflection amplitude can be tuned over a wide range of values by adjusting L. Note that nearly full and nearly zero reflectivity can be obtained. Moreover, the observed modulation period matches $\lambda_{\text{eff}}/2$ of the antisymmetric waveguide mode due to the formation of resonances in the stub. When compared to the analytical circuit model [see Appendix B.1], the features are qualitatively reproduced fairly well, apart from residual deviations for specific stub lengths, especially around reflection maxima and minima corresponding to low and high impedance stubs, respectively.

6.5 Antenna-stub system

Based on the demonstrated ability of tuning the reflectivity by a stub, we now incorporate a parallel stub into a prototypical nanocircuit relevant for applications. In this nanocircuit [shown in Fig. 6.5a] the concept of impedance matching is applied by connecting a defined stub of length L in parallel at a distance d from a load nanoantenna of length l_{ant} in order to fulfill the condition of minimizing the system's reflectivity or achieve maximum signal transfer to the nanoantenna. Note that with complex impedances minimum voltage reflectivity and maximum power transfer are two different conditions [64, 178]. The equivalent circuit representation is detailed in the inset of Fig. 6.5a. The complexity of such a system, together with the potentially large scattering background that might be present in the surroundings of the circuit due to the large radiation resistance of the antenna, opens up further relevant issues. In particular, this system is the perfect candidate to check for spurious deviations from the simple theory because of near-field coupling and/or radiative cross-talk between the lumped elements (here, the antenna and the stub) not included in the RF model. An exhaustive study of the practically unlimited number of possible nanocircuits with different combinations of L, d, and l_{ant} is beyond the scope of this work.

Instead, we concentrate on two specific loading conditions, namely an open-end termination (i.e. $l_{\mathrm{ant}} = 70\,\mathrm{nm}$) and a resonant nanoantenna (i.e. $l_{\mathrm{ant}} = 230\,\mathrm{nm}$). As in the classical transmission line theory, the open end termination of the plasmonic TWTL under investigation results in a nearly perfect reflectivity ($|\Gamma| = 97.4\,\%$), while the termination with a resonant nanoantenna leads to a minimum in reflectivity ($|\Gamma| = 37.6\,\%$) [see Appendix B.2, Fig. B.1]. Figures 6.5b,c show plots of the simulated reflection amplitude and phase for varying stub length L and fixed stub distance $d = 200\,\mathrm{nm}$ (red dots) for open end and resonant nanoantenna termination, respectively. Simulation data for a third, non-resonant antenna of length $l_{\mathrm{ant}} = 290\,\mathrm{nm}$ with an intermediate reflection amplitude together with additional distances d in the range from 50 nm to 2 μm for each antenna length are presented in Figs. B.2, B.3, and B.4 [Appendix B.3]. When compared to the analytical circuit model (blue solid line) some clear deviations are identified. While this disagreement can again be in part attributed to the small deviations already observed before for the junction of infinite TWTLs, the newly introduced coupling between nearby elements in this system, through scattered fields / near-field coupling or through guided fields bouncing back and forth between the stub and the load, may lead to additional deviations. From all the presented data one can draw some tentative conclusions concerning the degree of agreement between the simulations and the model. Generally, smaller distances d between the stub and the load result in larger deviations [see e.g. Fig. B.2]. On the one side, the fact that the main deviations are observed if d gets smaller than about 500 nm is consistent with a mode propagation length of about 900 nm for the guided mode, since coupling effects through guided modes in the antenna-stub cavity become less important as the round trip distance gets longer than the propagation length. On the other side, if scattered fields would be the main source of coupling instead of guided modes, we should see

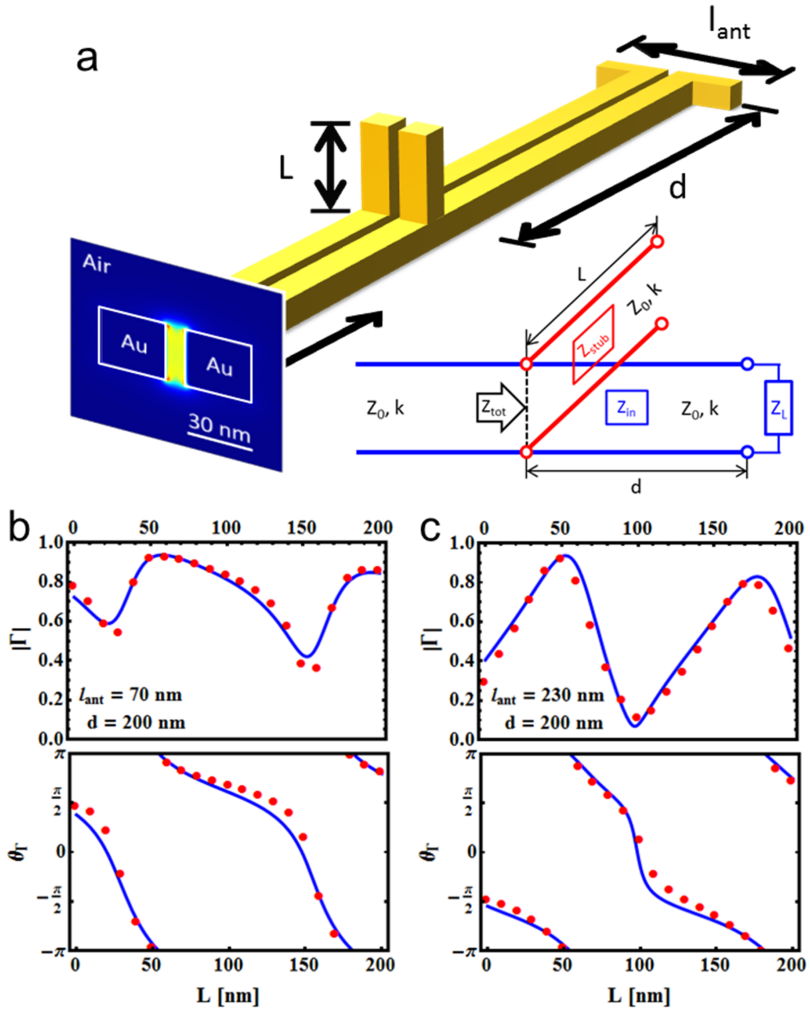

Figure 6.5: Tuning the reflectivity in a nanoantenna-terminated TWTL by a parallel stub. (a) Sketch of the investigated system featuring a finite TWTL terminated by an optical antenna of length l_{ant} connected in parallel with a finite stub of length L at a distance d from the antenna. The displayed antisymmetric mode is directly launched from the left and propagates along the nano-sized TWTL. Inset: Equivalent circuit representation of the system. (b) Reflection amplitude (top) and phase (bottom) for varying stub length L in a system with open end termination ($l_{\mathrm{ant}} = 70\,\mathrm{nm}$) and $d = 200\,\mathrm{nm}$. (b) Reflection amplitude (top) and phase (bottom) for varying stub length L in a system with resonant antenna termination ($l_{\mathrm{ant}} = 230\,\mathrm{nm}$) and $d = 200\,\mathrm{nm}$. The red dots are obtained by fitting of FDTD simulation data with the model described in Eq. (4.20), while the blue solid lines are obtained by the analytical model [Appendix B.3]. Figure taken from [157].

larger disagreement for antenna terminations with large radiation efficiencies, which is not the case. Instead, the system terminated by the resonant load antenna [Figs. 6.5c and B.3] seems to show the best agreement, even for a 100 nm distance. Therefore, it is tentatively suggested that the guided fields bouncing back and forth between the stub and the load are responsible for the observed deviations since they cause an increased coupling, resulting in larger disagreement for elements that have a high reflectivity for the guided mode such as the open end termination [Figs. 6.5b and B.2]. Consistently with its intermediate reflectivity value, the non-resonant antenna [$l_{\mathrm{ant}} = 290$ nm, Fig. B.4] shows a degree of agreement which is in between the open end and the resonant antenna. Lastly, the deviation reaches a maximum when the reflectivity amplitude of the overall system is minimum, meaning that the energy is effectively "stored" in the cavity formed between the stub and the load. To consider these effects in the lumped circuit model, one should add a dependent current source describing the coupling between the individual elements [159], with significant additional complexity.

Despite all the mentioned deviations, the lumped circuit model still can serve as a rough guideline to compose complex nano-optical circuitry by taking advantage of the possibility inherent to an analytical model, i.e. the rapid scanning of multi-dimensional parameter spaces for optimization purposes. A limited set of time-consuming numerical simulations can subsequently be performed to fine-tune these pre-optimized parameters to further take into account additional coupling effects.

6.6 Conclusion

In conclusion, by investigating a junction of plasmonic TWTLs we obtain insight into the reasons for and the strength of the deviations from Kirchhoff's laws at the junction of plasmonic waveguides. We find that the validity of Kirchhoff's laws can tentatively be checked via the value of a phenomenological parameter κ relating the geometrical parameters of the transmission line with the plasmon's effective wavelength. In the regime of small κ the junction behaves according to Kirchhoff's theory. Beyond such regime, for large values of κ, increasing deviations occur and the equivalent impedance description can only provide rough, but nevertheless useful, guidelines for the design of more complex plasmonic circuitry. Moreover, we investigate the influence of the coupling between individual plasmonic elements with a system composed of a TWTL and a nanoantenna as a load by addition of a suitable stub connected in parallel and give some tentative explanations for the different degrees of agreement observed for various structure parameters. Experimentally, the accurate and reproducible fabrication of the presented nano-optical circuits, however, is very challenging, not only because of the narrow gap sizes, which can be produced with some effort from high-quality substrates, e.g. monocrystalline gold platelets, by state-of-the-art nanofabrication techniques such as milling with helium ions, but even more since the devices are not planar but instead real three-dimensional. Therefore, with experimental implementations in mind we now turn to devices that can be fabricated by a more straight forward approach.

Chapter 7

Transmission of plasmons through a nanowire

Plasmonics is often considered to be not very precise since the reproducibility of fabricated nanostructures is limited. Indeed, even the simple problem of plasmon transmission through a nanowire has caused some discussion in the literature. On the other hand, exact quantitative understanding of this problem is of importance for designing and creating functional devices in the field of plasmonic nanocircuitry, but also in related fields, such as surface metamaterials, also dealing with plasmonic nanowires.

In this chapter, a systematic numerical study of finite-length nanowires reveals so far unnoticed propagation channels that noticeably modulate the wire transmission signals for single-mode plasmon excitation. By incorporating these additional channels into a Fabry-Pérot model, a fully analytical, quantitatively correct description of these observations is obtained. The results of this chapter have been published in [179]. Most parts of text and graphics are taken one-to-one from this publication.

7.1 Motivation

High-precision experiments of simple physical systems often reveal subtle but important effects or can be used to test theoretical descriptions of experimental results. Validated theoretical descriptions can then be used with confidence to model more complex systems. Yet, systematic high-precision experiments of light transmission through nanowires to date hardly exist. The characterization of such waveguides often relies on leakage radiation [180] or mode imaging with fluorophores [71, 181], which both lead to increased damping during ongoing propagation and may be affected by photobleaching. Coherent white-light transmission spectra of single wires can also be used to analyze their transmission [147]. However, this method requires knowledge of the waveguide's wavelength-dependent optical functions [97] in a broad wavelength range as well as the analysis of wavelength-dependent incoupling and outcoupling efficiencies [182]. As a result, the transmission efficiency of light through such nanowires in many experiments significantly deviates from theoretical expectations based on bulk dielectric constants [183]. Up to now, the origin of such deviations remains unknown since the structural uncertainties of bottom-up and top-down fabricated nanowires are not small enough to allow for conclusive analyzes.

This chapter presents a systematic study of monochromatic light transmission through gold nanowires of equal cross section but variable length. By varying the length and keeping the operation wavelength fixed, complexity is avoided since each unknown, like the in- and outcoupling efficiency, can be described by a single (complex) number. Section 7.2 briefly introduces both the sample fabrication and the experimental setup, and thus provides the basis for the accurate analytical modeling in Sec. 7.3. We demonstrate by simulations and experiments [Sec. 7.4] that a quantitatively correct description of the length-dependent nanowire transmission can be obtained by also taking into account free-space propagating modes launched by scattering of the excitation spot at the wire input in addition to Fabry-Pérot-type internal plasmon resonances. These free-space propagating modes interact with the outcoupling end of the wire and beat with the regularly emitted photons originating from the wire plasmon's radiative decay. This leads to significant amplitude modulations of the Fabry-Pérot transmission resonances. The quantitative agreement between our fully analytical model, numerical simulations, and measurements validates our model and yields values of propagation parameters that are compatible with bulk dielectric constants and for which remaining sources of uncertainties are clearly identified.

7.2 Sample fabrication and experimental setup

The experimental observation and distinction of the different propagation channels sets demanding requirements on the sample's geometrical precision, as is detailed in Sec. 7.4. Therefore, a state-of-the-art combined bottom-up and top-down nanofabrication strategy is applied. In a first bottom-up fabrication step laterally extended, yet thin monocrystalline gold films, henceforth referred to as gold platelets, are created by means of wet chemical synthesis from a gold salt solution [88, 89]. Their unique properties (e.g. ultra-smooth surfaces) render them ideal substrates for nanotechnology [184–189]. In a subsequent top-down fabrication step high energetic gallium ions focused to positions controlled by means of electron optics are capable of sputtering gold atoms from the surface layers of the monocrystalline gold platelet by transferring part of their momentum and kinetic energy and thus overcoming the binding energy of gold, as sketched in Fig. 7.1a.

Focused-ion beam milling allows for the deliberate design of almost arbitrarily sophisticated devices beyond the simple nanowires studied here [see e.g. the subsequent chapters]. Undesired effects of this nanopatterning include ion implantation into the substrate upon impact (instead of backscattering into the vacuum chamber), amorphization of the remaining gold structure, as well as a partial redeposition of ablated gold atoms in proximity to the patterning position. Throughout this work, both sample fabrication (FIB) and characterization (scanning electron microscopy, SEM) were performed by a dual-beam system within the same vacuum chamber (Helios Nanolab Dualbeam, FEI Company) operated by co-workers. To provide optimal conditions for focused-ion beam milling (i.e. no ion beam distortion) the sample was fabricated on a

conductive substrate (silicon) and then transferred to a clean and flat glass substrate (no adhesion layers) by means of a PMMA film, as depicted in Fig. 7.1b. Transfer to the glass substrate avoids the presence of a glass ridge below the nanowires and excludes fabrication-induced surface roughness as well as Ga^+-ion impurities within the milling area [190].

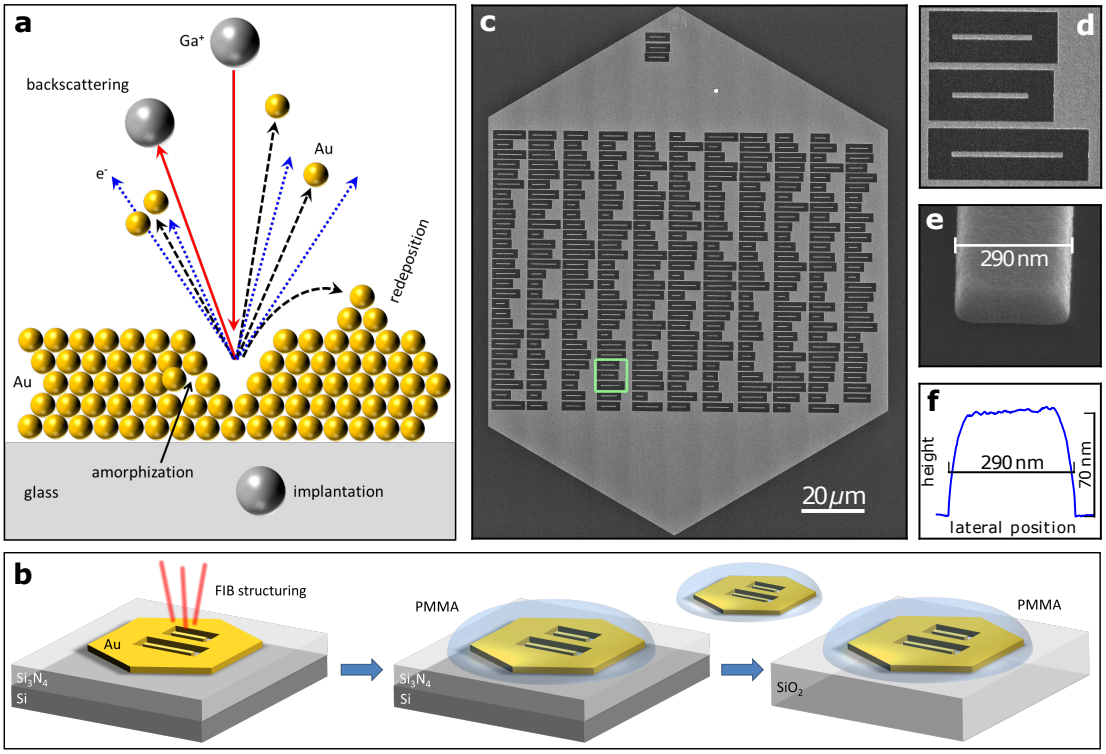

Figure 7.1: (a) Illustration of beam-sample interactions in FIB as discussed in the text. (b) Illustration of the transfer protocol. (c-e) SEM images of the sample showing (c) the full platelet including the focused-ion beam milled area of the platelet with the array of single nanowires of random wire lengths as well as (d,e) two closeups at different zoom levels. (f) Atomic force microscopy (AFM) line profile along one wire's cross section. Panels c-f taken from [179]. © 2017 American Chemical Society.

Aiming for a high-precision experiment that can reveal the effects of all relevant propagation channels on the overall apparent wire transmission, we prepared a sample consisting of 306 gold nanowires ranging from 1940 nm to 8040 nm in nominal length with a length increment of 20 nm [Fig. 7.1c] from a single monocrystalline gold platelet. Therefore, structural detail and plasmon propagation are not limited by the grain boundaries of multi-crystalline gold films [88, 147] ensuring uniform milling conditions. For such high-precision fabrication, differences between the structuring parameters and the exact final results depend on the fine adjustments of the whole setup. To ensure these differences are identical for all structures, we use a single patterning step to

create the whole array. The wire lengths were distributed randomly over the array to avoid artifacts due to changes of fabrication or measurement conditions. All resulting wires are of uniform quality, showing no observable differences in SEM images apart from the wire length. Simulations show that the remaining gold frames [Fig. 7.1d] around the wires do not affect the in- or outcoupled intensity.

To experimentally characterize the transmission properties of nanowires of different lengths, we use a home-built inverted microscope setup, as schematically sketched in Fig. 7.2. Nanofabricated gold nanowires supported by a cover glass are mounted above an oil immersion microscope objective (Leica, 1.30 NA, ∞, PL Fluotar 100×), which is used to focus a laser beam ($\lambda = 800\,\mathrm{nm}$, 12 nm FWHM spectral line width, 80 MHz repetition rate, 50 nW average power measured in front of the objective, NKT Photonics, SuperK Power with SpectraK AOTF, masterseed pulse duration 5 ps, after AOTF about 300 ps) via a $\lambda/2$-plate (Foctec, AWP210H NIR) to a diffraction-limited (390 nm diameter) spot at the air–glass interface that is linearly polarized along the wire axis.

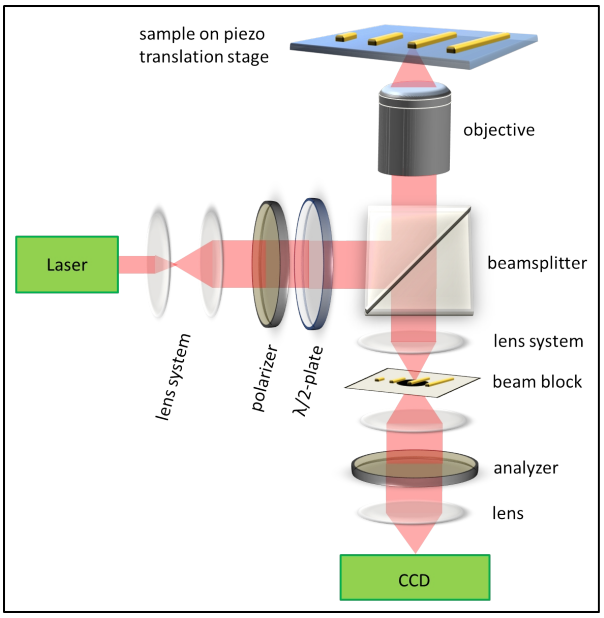

Figure 7.2: Sketch of the experimental setup used for far-field optical characterization. Details are given in the text.

The same objective is used to image the emitted and reflected light onto a CCD camera (Andor, DV887AC-FI EMCCD) via a 50/50 nonpolarizing beamsplitter (Thorlabs, CM1-BS013). In order to avoid saturation of the CCD, the strong reflection of the excitation spot is suppressed by a small beam block (OD 2) introduced in an intermediate image plane. The exact position of the excitation spot with respect to the wire end can be adjusted with nanometer precision by moving the sample using a piezo translation stage (Physik Instrumente, P-527) and was optimized to obtain maximum signal intensity at the wire end. In simulations, a post-processing of near-field data according to the experimental configuration is required [as detailed in Sec. 4.4.2] to yield images equivalent to the experimental images recorded by the microscope.

7.3 Analytical model

The principle of the experiment and all light propagation channels are sketched in Fig. 7.3a, showing the time evolution of the optical near-fields upon nanowire excitation as obtained from numerical simulations. The geometry was chosen to match high resolution SEM and AFM images and includes, for example, the soft edges [Fig. 7.1e,f]. Optical properties of the gold are modeled according to Sec. 3.1, while the refractive index of the glass was set to $n = 1.46$.

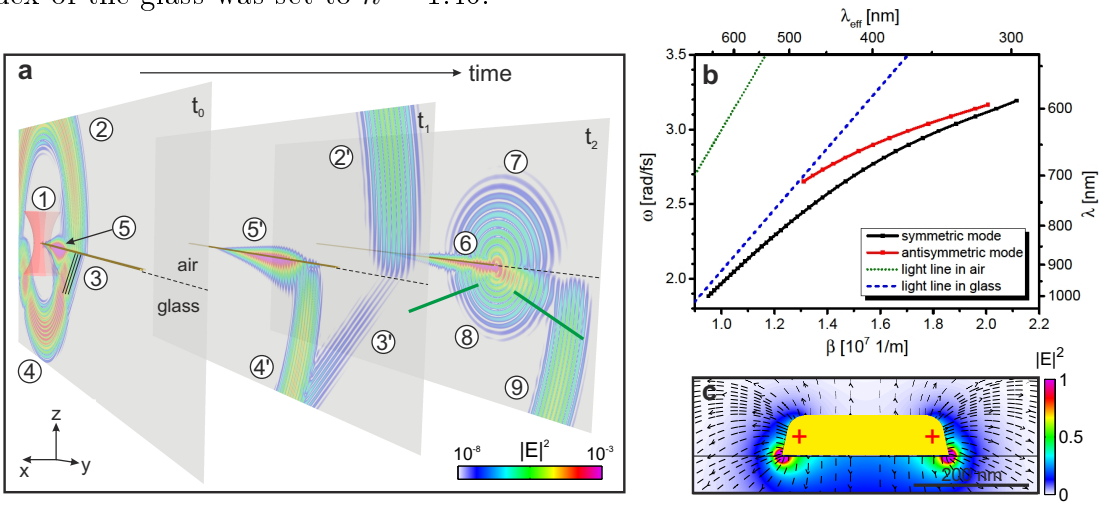

Figure 7.3: (a) Sketch of free-space and guided fields involved in the excitation of gold nanowires by a focused laser pulse as obtained from FDTD simulations. Progress in time is illustrated by field intensity distributions (logarithmic scale) in a plane through the nanowire long axis perpendicular to the substrate at time steps t_0, t_1, and t_2. In contrast to the actual experiment a longer wire of 20 μm length with a shorter pulse of only 5 fs duration is used in the simulation to improve the discrimination of the different contributions. (1) Focused Gaussian source illumination from the glass half-space; (2) scattered and transmitted light above the glass surface leading to (3) refracted waves at the air–glass interface; (4) scattered and reflected light below the air–glass interface; (5) launched plasmon pulse at time t_0; (2')-(5') as (2)-(5) but at later time t_1. (6) plasmon pulse at time t_2; light emission from the wire end (7) above and (8) below the air–glass interface; (9) scattered and reflected light below the air–glass interface at time t_2 leading to additional scattered fields at the wire end. The (green) lines below the glass surface symbolize the limited accepting angle of the objective with NA = 1.3. (b) Dispersion relation obtained from FDFD simulations using the experimentally realized nanowire dimensions for the symmetric (black) and antisymmetric (red) plasmonic mode as well as the light lines in glass (blue, dashed) and air (green, dotted). (c) Transverse profile of the nanowire's symmetric mode at vacuum wavelength $\lambda = 800$ nm. Electric field lines are indicated by the thin black lines.

The tightly focused laser at the incoupling end of the nanowire [Fig. 7.3a(1)] launches a plasmon with about 30% efficiency [Fig. 7.3a(5)] that propagates toward the distal end [Fig. 7.3a(6)], where it is partly radiated into the surrounding media [Fig. 7.3a(7) and (8)], while about 40% of the plasmon field is reflected and propagates back along

the wire, leading to Fabry-Pérot-type standing waves [191, 192]. Additional propagating fields - in the following referred to as air-wave and glass-wave [Fig. 7.3a(2) and (4)] - are launched by the partial scattering of the excitation source at the incoupling end. While about 30% of the laser energy is coupled into the nanowire, about 50% of the energy is scattered into the glass half-space, leading to a spherical wave originating from the incoupling end of the wire. The remaining 20% are transmitted into the air half-space, where they also evolve as spherical waves.

Another contribution to propagating waves in the glass half-space arises from light refracted at the air–glass interface [Fig. 7.3a(3)], which propagates into the glass as a plane wave under an angle of about 43° (critical angle for total internal reflection) and thus within the acceptance angle of the objective. This wave leads to a distinct pattern in the wire far-field images that vanishes for low-NA imaging. The air-wave and the glass-wave originating from the excitation position are not directly detected by the camera for different reasons. While the air-wave propagates away from the collecting objective lens above the interface, the glass-wave is strongly suppressed by the beam block at the intermediate image plane. However, as we detail below, the interaction of these propagating waves of different effective wavelengths with the distal wire end leads to interference and beating effects in the light intensity emitted by the wire ends which is detected by the camera.

From the simulated dispersion relation [Fig. 7.3b], as obtained by the eigenmode solver [Sec. 4.3], two guided plasmonic modes of symmetric and antisymmetric nature can be identified for the considered nanowire dimensions. However, at the chosen vacuum wavelength ($\lambda = 800\,\mathrm{nm}$) the propagation along the nanowire is single-mode, since only the dispersion relation of the symmetric mode [see Fig. 7.3c for the associated transverse mode profile] remains below both air and glass light line. This also confirms that the corresponding plasmon wave couples to the far field only at the wire terminations.

Based on Fabry-Pérot theory, the field amplitude ψ_T that is transmitted by a waveguide of length L via one single eigenmode and emitted into the detection path can be expressed as [192]

$$\psi_\mathrm{T} = \frac{\psi_0\ \eta\ t\ e^{-(\alpha+i\beta)L}}{1-\left(\Gamma e^{-(\alpha+i\beta)L}\right)^2}. \tag{7.1}$$

Here, ψ_0 is the amplitude of the Gaussian excitation beam, η is a (complex valued) efficiency factor comprising the combined effects of incoupling into the waveguide and detecting the emitted signal, and $\Gamma = |\Gamma|e^{i\theta_\Gamma}$ and t are the complex plasmon reflection and transmission coefficients, respectively. These coefficients are assumed to be identical for both wire terminations. Furthermore, the mode's attenuation constant α and its wave vector β are related to the mode's intensity decay length l_decay and its effective wavelength λ_eff via Eqs. (3.8) and (3.9), respectively. Both air-wave and glass-wave can be approximated by propagating spherical waves. The respective amplitudes scattered from the wire far end at a distance L away from the incoupling end toward

the detector can be expressed as

$$\psi_{\text{medium}} = \psi_0 \eta_{\text{medium}} \frac{e^{-i\beta_{\text{medium}} L}}{L}, \tag{7.2}$$

where $\beta_{\text{medium}} = 2\pi/\lambda_{\text{medium}}$ is the wave vector and λ_{medium} is the wavelength of light in the respective medium, i.e., air and glass. The complex quantity η_{medium} denotes a combined efficiency factor accounting for the efficiency of scattering of the excitation field ψ_0 at the incoupling wire end, thus generating the spherical wave in the respective medium, as well as for the efficiency for scattering of this wave at the wire's far end into the detection path. All fields originating from the waveguide end interfere at the detector according to

$$I_{\text{total}} = |\psi_{\text{T}} + \psi_{\text{air}} + \psi_{\text{glass}}|^2. \tag{7.3}$$

7.4 Simulation and experiment

Simulated and experimentally obtained far-field images for a wire of 8 μm length are displayed in Figs. 7.4a and b, respectively. The effect of the beam block used for spatially blocking the high-intensity reflection spot resulting from the focused laser excitation of the nanowire input terminal is visible by the nearly circular areas of reduced intensity around the excitation spot. Apart from a somewhat increased scattering in the experiment, simulated and experimental images agree exceptionally well.

For a detailed analysis of plasmon transmission through the nanowires we extract for each nanowire the simulated far-field intensity as well as experimental CCD image counts by integrating $1\times1\,\mu\text{m}^2$ regions centered at the wire end [red and blue squares in Fig. 7.4]. The resulting simulated wire transmission values are plotted as a function of the wire length [Fig. 7.5a, blue "+"]. The data are normalized such that the resulting decay curve (interleaved dark green line) passes an intensity value of 1/e at a wire length matching l_{decay}. The detected intensity as a function of the wire length exhibits an exponential decay modulated by an oscillatory behavior. A short-wavelength and a superimposed longer-wavelength oscillation are distinguishable. First, the simulation data is compared to the proposed model by fitting Eq. (7.3) to the data.

In order to reduce the number of free parameters, the mode's propagation properties ($\lambda_{\text{eff}} = 505\,\text{nm}$, $l_{\text{decay}} = 4960\,\text{nm}$) and its reflection coefficient at the wire termination ($|\Gamma| = 0.42$, $\theta_\Gamma = 1.39$ – see Sec. 4.4.4) are obtained from FDFD and FDTD simulations, respectively. The initial phase offsets of both air-wave and glass-wave with respect to the propagating plasmon are set to a fixed value of π. With these constraints the amplitudes of the launched wire plasmon, the air-wave, and the glass-wave at the incoupling position remain the only free parameters of the model. The resulting fit to the simulation data [red line in Fig. 7.5a] shows perfect agreement.

The corresponding plot resulting from experimentally determined far-field images is shown in Fig. 7.5b. From all 306 measured nanowires, only about 1% showed unexpected signals that we attribute to structural defects and therefore we excluded

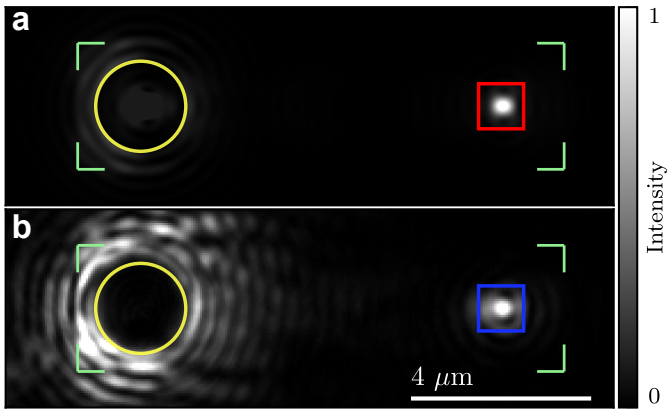

Figure 7.4: (a) Simulated far-field intensity of an 8 μm long nanowire obtained via the post-processing method illustrated in Sec. 4.4.2. (b) Corresponding experimental CCD image. The yellow circle visualizes the position of the beam block, and the green corners mark the borders between gold platelet on glass and bare glass [see Fig. 7.2]. The red (blue) square marks the area that was integrated to obtain the intensity in simulation (experiment). Experimental data is scaled to match the simulated peak intensity within the integration area. Figure taken from [179]. © 2017 American Chemical Society.

them from further analysis. The amplitude ratio of the three contributions is adopted from the fit to the simulation data, so that the final fit to the experimental data has only one remaining amplitude parameter. A fabrication-induced length offset of 85 nm has to be introduced, which accounts for a systematic difference between the nominal and the actual wire length. Its value is precisely determined by fitting the position of the Fabry-Pérot oscillations. While high-resolution SEM measurements support this effect, contrast and charging-induced uncertainties in the measured length are larger than the uncertainty in the fitted length-offset.

The Fourier transformations of the length-dependent data [insets of Fig. 7.5] show two distinct peaks. The highest frequency component corresponds to a periodicity of 252 nm and therefore matches $\lambda_{\text{eff}}/2$ as anticipated by the Fabry-Pérot model. The slower oscillation (wavelength of about 1300 nm) agrees with the calculated beating wavelength of the excitation's vacuum wavelength and the Fabry-Pérot modulated plasmon emission at $\lambda_{\text{beating}}^{\text{air–fpt}} = 1372\,\text{nm}$ and is thus attributed to the interference of the spherical air-wave scattered at the wire end and the emitted plasmons.

This origin is further supported by numerical simulations using a tailored mode source to directly excite the plasmons without launching spherical waves. Since the modal profile of the electromagnetic source (positioned at a cut plane 100 nm after the wire start) and propagating medium (the wire) are perfectly matched all energy is coupled into the wire mode. This way, the excitation of free-space waves is strongly suppressed. The result is a smooth length dependent decay modulated by Fabry-Pérot oscillations only [Fig. 7.6a]. In contrast to the results for Gaussian beam excitation, almost no beating is visible in the Fourier transformation [Fig. 7.6b]. The very weak residual beating is most likely caused by small scattering artifacts of the source and

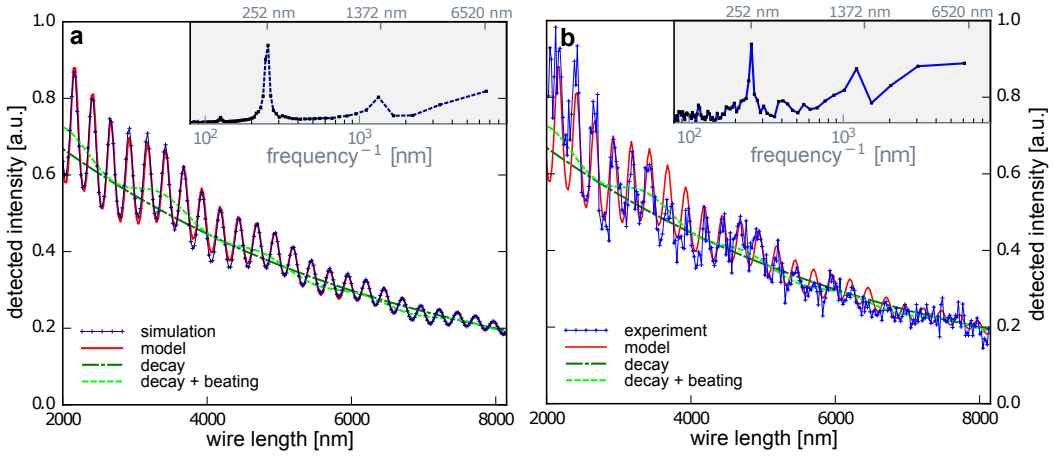

Figure 7.5: (a) Simulated and (b) experimentally detected signal (blue "+", thin blue line to guide the eye) within the integration box at the wire end. Superimposed is the fitted model (solid red line) together with the intensity decay curve (interleaved dark green line) and a curve of the model with Fabry-Pérot reflectivity $|\Gamma| = 0$ visualizing the oscillations from the beating between the Fabry-Pérot model and the scattered free-space waves in air and glass at the wire end (dashed light green line); (insets) Fourier-transformed (a) simulated and (b) experimental data. The expected peak positions from the Fabry-Pérot oscillation (252 nm), the beating between the transmitted light and the air-wave (1372 nm), and the beating between the transmitted light and the glass-wave (6520 nm) are indicated. Figure adapted from [179]. © 2017 American Chemical Society.

the scattering at the emission end.

In addition, the model predicts a beating between the plasmon emission and the glass-wave showing a periodicity of about $\lambda_{\text{beating}}^{\text{glass-fpt}} = 6520\,\text{nm}$. This beating wavelength is about the same as the length difference between longest and shortest measured wire ($\Delta L_{\text{max}} = 6100\,\text{nm}$) and close to the length scale of the plasmonic intensity decay ($l_{\text{decay}} = 4960\,\text{nm}$). While it is not clearly resolved in the Fourier transformation data, it is important to note that, within the observation window, it will appear as an additional slope of the exponential decay curve. Neglecting this additional component will, depending on its relative phase, lead to either an under- or overestimation of the decay length. In our case a fit to the experimental data without taking the glass-wave into account leads to a 20% underestimation of the decay length as compared to the simulated plasmon decay. This deviation can also be inferred from Fig. 7.5a by observing that the light green curve oscillates (visible beating $\lambda_{\text{beating}}^{\text{air–fpt}} = 1372\,\text{nm}$) above the dark green decay curve due to the additional intensity caused by the beating between the spherical wave in glass and the Fabry-Pérot modulated plasmon emission.

To observe and distinguish these different contributions in the experiment, the requirements on the sample's geometrical precision are demanding. By validating our experimental data against a model that includes artificial errors, i.e., by comparing the residuals, we determine the upper limits for the uncertainties (standard deviation) of our structures' geometrical parameters and experimental conditions, i.e., wire length,

width, and random intensity fluctuations, to be 32 nm, 8 nm, and 7%, respectively. For the wire length this corresponds to a relative error of less than 0.4%, which is, taking into account the nonconductive substrate, smaller than the experimentally accessible resolution limit of current state-of-the-art SEM techniques.

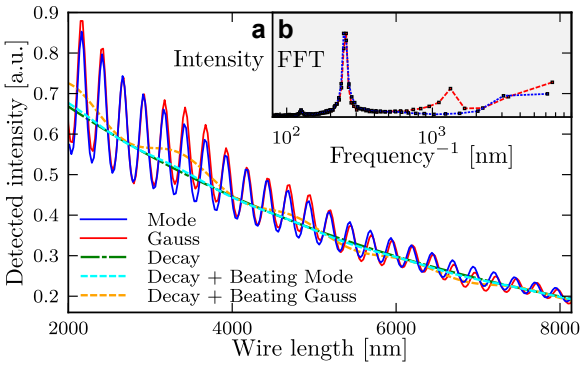

Figure 7.6: (a) Simulated far-field intensity for Gaussian beam (red line) and mode source (blue line) excitation, a corresponding intensity decay curve (interleaved dark green line), and curves of the model with Fabry-Pérot reflectivity $|\Gamma| = 0$ visualizing the oscillations from the beating between the Fabry-Pérot model and the scattered free-space waves in air and glass at the wire end (orange: mode source; light green: Gaussian source). (b) Fourier transformation of the wire length dependent intensity data for Gaussian (red line) and mode source (blue line). Figure adapted from [179]. © 2017 American Chemical Society.

7.5 Conclusion

We conclude that the high-precision and reproducibility of the fabricated nanowires allowed us to reveal the nonnegligible influence of air and substrate waves on their apparent length-dependent transmission. Our experiments also show that by inclusion of these additional waves simulated and experimental data agree quantitatively within the remaining small experimental uncertainties. The effect of the air wave reveals itself as a beating superimposed to the Fabry-Pérot standing wave pattern. The role of the substrate wave is less obvious. The very long beating wavelength of the substrate wave with the wire plasmon causes unavoidable uncertainty for the fitting of the decay length because the corresponding oscillatory behavior cannot be captured experimentally even for the longest wires, since the overall damping of the plasmon becomes too strong. The resulting uncertainty regarding the starting phase of the substrate wave is likely responsible for measurements of decay lengths that reported too long or too short decay lengths [181, 183]. The presence of additional waves due to the different group velocities could influence the temporal structure of plasmon pulses transmitted through plasmonic nanowires [158, 180]. The interference effect inherent to plasmon propagation in a single wire could also lead to ultracompact realizations of interferometric sensing schemes, which may exploit changes of the launching phases of the involved excitations.

Chapter 8

Multimode plasmon excitation and *in situ* analysis

The quantitative agreement between simulation and experiment, even including eigenmode properties, as confirmed in Chap. 7, allows us in the following to confidently apply numerical simulations for the deliberate design and analysis of functional plasmonic devices beyond the previously studied simple single-mode linear nanowires. Still, experimental verification of fabricated devices, that were predetermined by simulations, is given, which was carried out by other members of the work group, mainly Peter Geisler and Enno Krauss.

In this chapter, we increase device complexity by using multimode TWTLs as a basis. The proposed device allows the synthesis and *in situ* analysis of multimode plasmonic excitations. The guidance and processing of such deterministic eigenmode superpositions at subwavelength scales in highly integrated optical nanocircuits may become important in future information processing technology including quantum communication. The results of this chapter have been published in [193]. Most parts of text and graphics are taken one-to-one from this publication.

8.1 Motivation

While single-mode operation is a design goal for dielectric waveguides, in plasmonic nanocircuits multimode interference leads to enhanced functionality based on the control of near-field intensity patterns [77–79]. Previous work toward the realization of optical nanocircuits relied on chemically grown single-wire waveguides pioneered by Ditlbacher *et al.* [147], that were introduced in Sec. 5.1. In such systems the plasmon excitation and emission efficiencies depend on the wire diameter, which at the same time also determines the spectrum of modes and their respective dispersion relations. By combining careful selection and micromanipulation of chemically grown nanowires, indeed prototypes of optical nanocircuitry have been demonstrated in which multimode interference is exploited [56, 69].

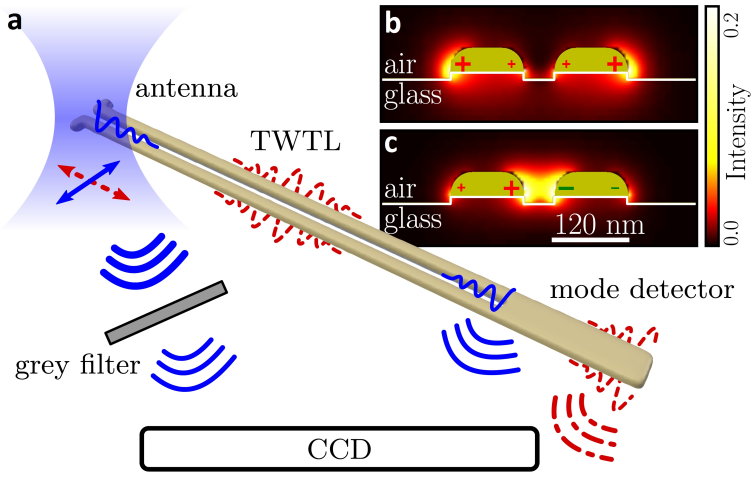

Figure 8.1: Principle of the nanocircuit. (a) Cartoon: launching, propagation and re-emission of TWTL modes. (b,c) Simulated transverse modal profiles in an infinitely long TWTL on glass for the symmetric (b) and antisymmetric eigenmode (c). Instantaneous charge distributions are symbolized by "+" and "-". Eigenmode properties (free-space wavelength 830 nm) take values of $\lambda_{\mathrm{eff}} = 480\,\mathrm{nm}$, $l_{\mathrm{decay}} = 2628\,\mathrm{nm}$, and $v_{\mathrm{g}} = 1.26 \cdot 10^8 m/s$ for the symmetric and $\lambda_{\mathrm{eff}} = 434\,\mathrm{nm}$, $l_{\mathrm{decay}} = 1892\,\mathrm{nm}$, and $v_{\mathrm{g}} = 1.16 \cdot 10^8 m/s$ for the antisymmetric eigenmode, respectively. Figure taken from [193]. © 2013 American Physical Society.

Despite these achievements, it is a necessary next step toward advanced plasmonic nanodevices to obtain independent control over light coupling and propagation in optical nanocircuits by a deterministic synthesis of multimodal excitations. The existence of a transverse and a longitudinal mode in chains of closely spaced plasmonic nanoparticles [26, 29] led to a proposal of deterministic coherent control of a routing functionality in a branched particle-chain waveguide circuit [79]. Later on, easier to fabricate MIM-type waveguides, such as grooves and channels [32] were applied e.g., to implement logic operations, albeit via single-mode interference [55].

To obtain more flexibility and control in terms of excitation schemes and available modes, TWTLs are eligible candidates since they offer a symmetric and an antisymmetric mode [194], as introduced in Sec. 5.2.2. However, experiments so far have only considered the antisymmetric mode [67, 68, 195]. Importantly, TWTLs can be combined with linear dipole antennas to tailor the in- and outcoupling of light [64, 67, 68, 196].

Deterministic synthesis and *in situ* analysis of multimode plasmonic excitations is an indispensable requirement for exploiting the full power of TWTLs as building blocks of functional plasmonic nanocircuits. To this end, we design nanocircuits, as sketched in Fig. 8.1a, consisting of an optimized incoupling antenna (generator), a TWTL with a mode-dependent characteristic impedance, and a mode detector (load). While the general properties of guided TWTL modes have already been addressed in Chap. 5, the efficiency of their excitation by a diffraction-limited excitation spot is subject of Sec. 8.2 elucidating the role of the incoupling antenna's dimensions on amplitude and

phase of the excited modes. Subsequent modal analysis is performed by a single-shot *in situ* far-field readout of two mode-specific spatially separated emission spots of the mode detector termination, as investigated both numerically and experimentally in Sec. 8.3. We further show that by a combined polarization and position control [Sec. 8.4] of the diffraction-limited excitation spot with respect to the incoupling antenna any superposition of TWTL modes can be launched. To illustrate the power of the approach we selectively determine the group velocities and time delays of pure-mode contributions of a multimode ultrafast plasmon pulse [Sec. 8.5]. This part of the study was carried out in the work group of Tobias Brixner[1].

8.2 Synthesis of multimode plasmonic excitations

The basic device functionality is not determined by the exact dimensions of e.g. the TWTL, so that without loss of generality the experimentally realized device dimensions[2] are adopted in all simulations of this chapter. For the chosen dimensions only two TWTL eigenmodes with considerable propagation length ($>1\,\mu$m) exist, a symmetric (quasi-TM) and an antisymmetric (quasi-TE) one as illustrated in Figs. 8.1b,c. The corresponding eigenmode properties are summarized in the caption of Fig. 8.1. The longer propagation length, larger effective wavelength, as well as higher group velocity observed for the symmetric mode are consistent with its lower field confinement, confirming the previous results of Chap. 5. The transverse modal profile of any multimodal excitation propagating along the TWTL at a fixed position therefore is a superposition of these two eigenmodes after transients have expired [64].

The excitation efficiency of both TWTL modes can be engineered by utilizing an incoupling structure that links the field profile of the excitation beam to the modal profiles of the TWTL. Here we use a simple dipole antenna [12] where the length and width of the antenna arms influence the antenna impedance and therefore the transfer of power to the respective waveguide mode [64]. We first consider an isolated dipole antenna, i.e. two head-to-head aligned nanorods separated by a small gap. Figure 8.2a shows the intensity enhancement in the center of a 50 nm gap as a function of the overall antenna length at a fixed wavelength of $\lambda = 830$ nm. Antenna widths have been chosen to be 60 nm, 80 nm, and 100 nm.

For excitation along the antenna axis (bluish curves) a fundamental resonance builds up for overall antenna lengths around 370 nm. Additionally, for narrow antennas a characteristic shift toward shorter resonant lengths accompanied by a more pronounced resonance feature is visible. This harmonic oscillator-like antenna behavior is also manifest in its phase response, as illustrated in Fig. 8.2b. It reveals a characteristic transition from an approximately 0 to π phase shift of the local plasmon field in the

[1] Institut für Physikalische und Theoretische Chemie, Universität Würzburg, Am Hubland, 97074 Würzburg, Germany

[2] Nanocircuits were fabricated from a large monocrystalline gold platelet (38 nm thickness) deposited on a cover glass. FIB milling results in gold wires with rounded upper corners on glass elevations.

antenna gap with respect to the driving field as the antenna length is increased from below to above its resonance length. The trends for the perpendicular polarization (reddish curves) are less pronounced, showing neither a resonance feature nor a phase transition but a rather constant phase.

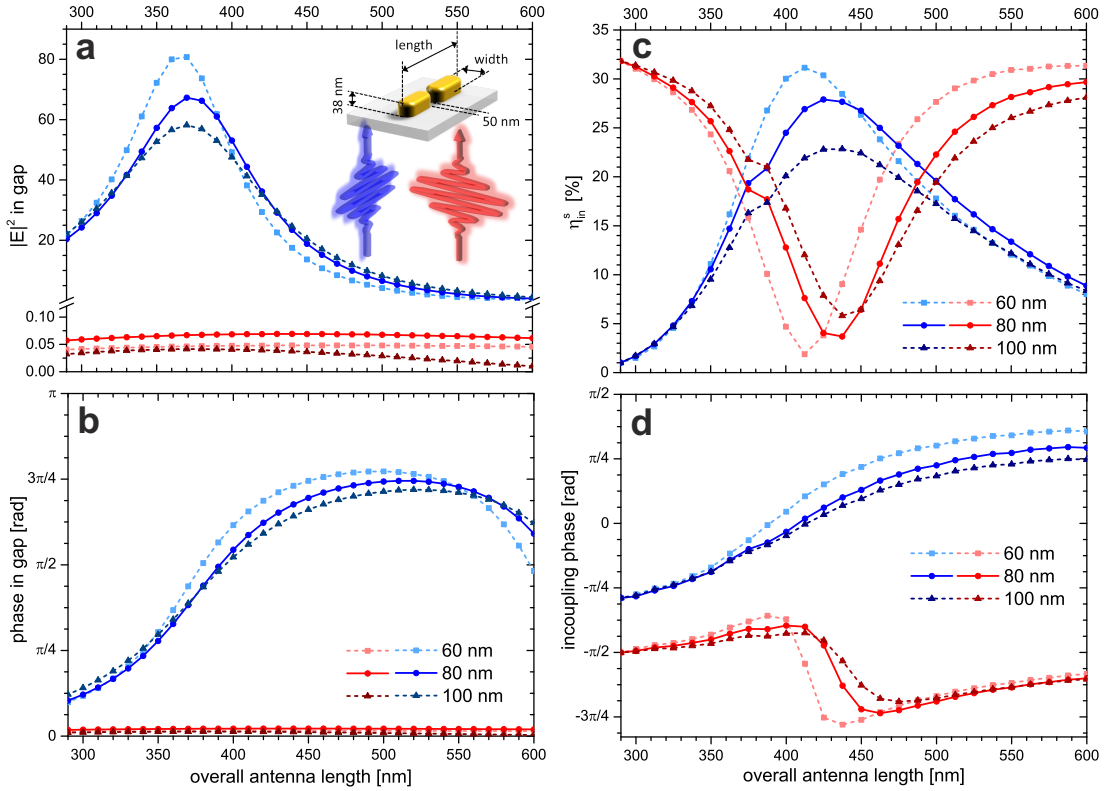

Figure 8.2: Linear dipole antenna coupled to TWTL. (a) Simulated near-field intensity enhancement in the gap center of isolated dipole antennas vs. overall antenna length and various widths as indicated. The excitation polarization is along the antenna axis (bluish curves) and perpendicular to it (reddish curves), respectively. (inset) Sketch of the antenna geometry. Arrows indicate the polarization of the excitation field. (b) Phase response of isolated dipole antennas. In (a,b) intensity and phase without antenna are used as reference. (c) Simulated incoupling efficiency vs. overall antenna length for same set of antenna widths. Illumination parallel (perpendicular) to the TWTL excites the symmetric (antisymmetric) mode, as shown by the reddish (bluish) curves. (d) Corresponding initial phases of both TWTL modes at the position of the incoupling antenna.

In the following, we consider a TWTL-connected dipole antenna acting as a receiving antenna. In Fig. 8.2c the simulated incoupling efficiencies η^s_{in} into either TWTL mode are shown, obtained as detailed in Sec. 4.4.3, as a function of the overall antenna length (the 290 nm simulation corresponds to the "no-antenna" – "wire-only" case) for a fixed antenna width (80 nm, solid lines). For polarization parallel to the TWTL (red solid line) the incoupling efficiency of the symmetric mode decreases from a large value of >30% in the case without antenna to a narrow minimum of <5% at around

425 nm overall antenna length and then largely recovers for a further increase of the antenna length. Excitation of the antisymmetric mode is symmetry forbidden for this polarization unless the focus is displaced [see Sec. 8.4]. For a polarization perpendicular to the TWTL (blue solid line) the behavior is quite the opposite. Without antenna the antisymmetric mode can hardly be excited ($\eta_{in}^{s}<2\%$). By increasing the antenna length to about 425 nm the incoupling efficiency reaches a maximum of almost 30% and then decreases toward another minimum for even longer antennas in accordance with classical antenna theory. Notably, affected by the attached TWTL the optimum antenna length differs from the resonance length of an isolated dipole antenna of same width [Fig. 8.2a]. For this polarization, in turn, coupling to the symmetric mode is symmetry forbidden.

Considering different incoupling antenna widths [see dashed lines in Fig. 8.2c] it is found that the optimal overall antenna length qualitatively shifts similarly to the resonance length for isolated dipole antennas [Fig. 8.2a]. Moreover, there is a clear trend of increasing incoupling efficiency for thinner antennas, in practice however limited due to fabrication constrains. Similarly, the minimum in excitation efficiency for parallel polarization is more pronounced for thinner antennas, while its position does not depend strongly on the antenna width. Other parameters, such as TWTL width and gap, additionally influence the incoupling efficiency. A decreased gap width, e.g., results in an increased incoupling efficiency for the antisymmetric mode due to a stronger antenna resonance, albeit at the cost of significantly increased TWTL propagation losses. Additionally, in view of the results of Chap. 6 passive elements such as stubs may also be employed to increase the coupling efficiency from far-field power into guided TWTL modes [176].

Moreover, not only the incoupling efficiency but also the respective mode's initial phase can be tuned considerably by the antenna geometry [Fig. 8.2d], revealing an altered phase transition compared to the isolated dipole antenna case [Fig. 8.2b]. For multimode device operation, as exploited in Chap. 9, this provides an option to adjust the relative phase between pure-mode contributions and thus a positional shift of the resulting beating pattern.

8.3 Analysis of multimode plasmonic excitations

The mode detector attached to the far end of the TWTL can be read out via a diffraction-limited far-field measurement and therefore provides direct *in situ* feedback on the actual modal composition. Its operation principle relies on the different interaction of symmetric and antisymmetric modes with different types of TWTL discontinuities. Due to an intensity node in the gap the symmetric eigenmode is not affected by a termination of the gap while it is strongly reflected and radiated at a complete termination of the circuit. The antisymmetric eigenmode exhibits an intensity maximum in the gap and is thus strongly reflected and radiated as soon as the gap is terminated. A sequence of a gap shortcut followed by a complete termination

of the TWTL therefore acts as a mode detector by spatially separating the respective emission spots.

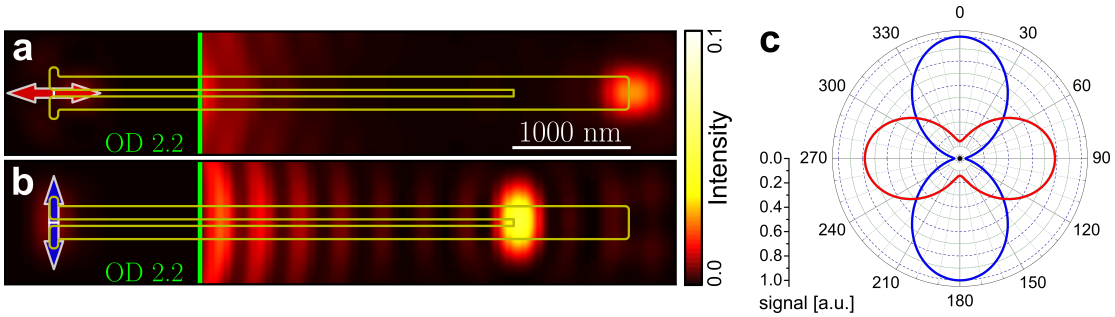

Figure 8.3: (a,b) Simulated far-field images [see Sec. 4.4.2] for a pure symmetric (a) and antisymmetric mode (b) arriving at the mode detector. Pure modes are excited by illuminating the incoupling antenna (overall length 450 nm) with a focused beam polarized parallel (a) and perpendicular (b) to the TWTL. The intensity scale is normalized to the reflected intensity at the glass/air interface. To match the experiments the antenna reflections have been attenuated numerically using an optical density OD 2.2 (left of the vertical green line). The arrows indicate the excitation polarization. The nanocircuit outline is superimposed as a guide to the eye. (c) Emission signal vs. polarization analyzer angle for a pure symmetric (red) and antisymmetric mode (blue) arriving at the mode detector. Panels a,b adapted from [193]. © 2013 American Physical Society.

Figures 8.3a,b show far-field FDTD simulations of the mode detector interacting with either of the two eigenmodes. The 1 μm spacing between the discontinuities results in two clearly separated emission spots whose intensities are proportional to the amplitudes of the respective eigenmode contributions. The emission is mostly polarized parallel to the TWTL axis for the symmetric and perpendicular for the antisymmetric mode emission spot [Fig. 8.3c], with an analyzer in cross polarization extincting about 80% and 95% of the total emission signal, respectively.

For a quantitative determination of the power in each mode the respective radiation efficiencies of the two emission points have to be taken into account. As a figure of merit (FOM) for the ability of the mode detector to separate modal contributions we define for an incoming pure symmetric (antisymmetric) mode plasmon $\mathrm{FOM_i} = I_\mathrm{i} / \sum_\mathrm{i} I_\mathrm{i}$, $\mathrm{i} = \{\mathrm{sym.}, \mathrm{antisym.}\}$, where I_i is the emission intensity at the symmetric (antisymmetric) emission spot. Perfect mode selectivity corresponds to $\mathrm{FOM_i} = 1$. Due to the small amount of scattered light at the position of the mode detector we achieve typical figure of merits of 0.98 in simulations (and experiment).

SEM images of a fabricated plasmonic nanocircuit are shown in Figs. 8.4a,b visualizing the rounded shape of the TWTL wires caused by secondary sputtering processes during FIB milling. In order to experimentally characterize the launching and emission of plasmon excitations, the cover glass supporting the nanocircuit is mounted onto the same home-built inverted microscope setup including the small beam block (OD 2.2) as introduced in Chap. 7. Unlike there, the laser wavelength has been tuned to

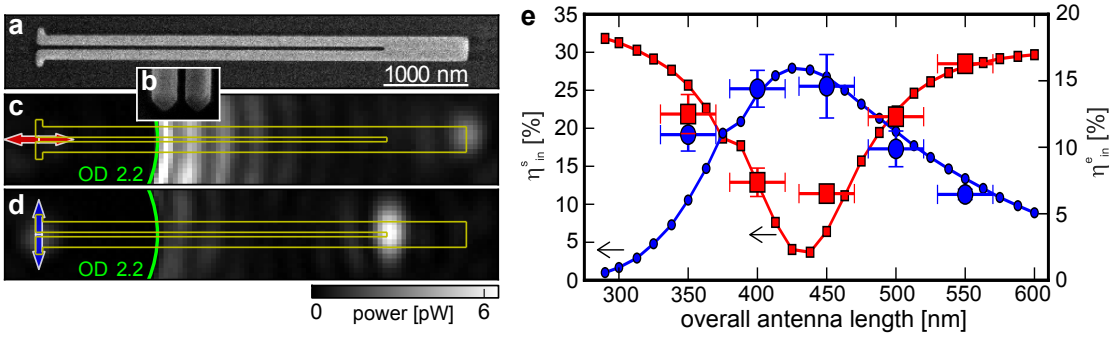

Figure 8.4: Experimental verification. (a) SEM image of the plasmonic nanocircuit. (b) SEM image of the TWTL cross section (52° observation angle). (c,d) CCD images (detected power per pixel) showing the attenuated (OD 2.2, indicated by the green circle-segment) reflected spot at the incoupling antenna position and the mode detector emission spots (100 nW excitation power). The arrows indicate the polarization. The nanocircuit outline is superimposed as a guide to the eye. All images show background "fringes" from direct laser scattering which have no influence on the transmission and thus the outcome of the experiment. (e) Simulated (lines, small symbols, η^s_{in}) and experimentally obtained incoupling efficiency (large symbols with error bars, η^e_{in}) vs. total antenna length. Symmetric mode: Illumination parallel to the TWTL (red). Antisymmetric mode: Illumination perpendicular to the TWTL (blue). Figure adapted from [193]. © 2013 American Physical Society.

$\lambda = 830\,\mathrm{nm}$ and delivers 100 nW average power measured in front of the objectives back aperture. Once the diffraction-limited excitation spot is overlapped with the incoupling antenna of the structure, plasmons are excited and subsequently re-emitted at its far end, as schematically sketched in Fig. 8.1a. Figures 8.4c,d show experimental far-field images of the structure being excited at the antenna and re-emitting light at the mode detector structure for excitation polarizations parallel [Fig. 8.4c] and perpendicular [Fig. 8.4d] to the TWTL. To launch the antisymmetric mode the polarization was rotated by 90° while the excitation spot was kept fixed. This demonstrates the possibility to excite a well-defined superposition of both modes simply by adjusting the laser polarization. It is interesting to observe that not only the positions of the far-field emission spots match very well the simulations in Figs. 8.3a,b but also the respective spot shapes.

To experimentally verify the predictions for the simulated antenna incoupling efficiency [Fig. 8.2c], two nominally identical arrays consisting of 5 nanocircuits with varying antenna lengths have been fabricated. By taking into account the damping of the modes along the TWTL and the radiation efficiencies of the mode detector emission spots, the power in each mode at the antenna position can be extrapolated. We plot the experimental incoupling efficiency η^e_{in} [Fig. 8.4e, large symbols], defined in the style of Eq. (4.19) as

$$\eta^e_{\mathrm{in}} = \frac{p_{\mathrm{out}}}{p_0} \times \left[\eta_{\mathrm{out}} \times e^{-L/l_{\mathrm{decay}}}\right]^{-1} , \tag{8.1}$$

where p_{out} is the integrated emitted power at an emission spot, p_0 the excitation power measured in front of the objective, η_{out} the radiation efficiency of either emission spot corrected by the collection solid angle of the objective lens (about 25% for both modes), L the length of the TWTL, and l_{decay} the simulated decay length. While the experimental data very well reproduce the general trend the absolute experimental values for the incoupling efficiency are smaller by about a factor of 2. Such a deviation can be caused by experimental decay lengths that are about 25% shorter than predicted by simulations. The reason for such deviations is unclear but effects like surface scattering of electrons likely contribute.

8.4 Polarization and position dependent excitation efficiency

So far we have assumed an excitation focal spot perfectly centered on the incoupling antenna (neglecting small displacements along the TWTL) leading to the excitation of pure modes for the two fundamental polarizations. We test the stability of such a configuration by recording the excitation efficiencies into both modes for parallel and perpendicular polarization as a function of beam displacements. Breaking the symmetry, such displacements lead to a significant increase in the excitation efficiency of the respective symmetry forbidden modes [154].

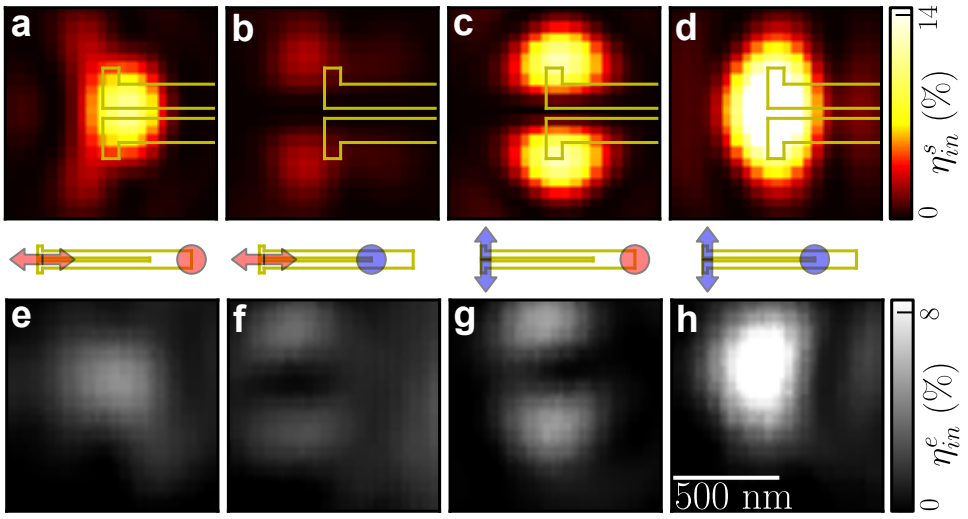

Figure 8.5: Focal spot position dependent modal excitation efficiency maps (450 nm overall antenna length): (a-d) simulations, (e-h) experiment. Middle panel: pictograms indicating excitation polarization and emission position. When centered on the antenna the antisymmetric mode (d,h) is more efficiently excited than the symmetric mode (a,e) consistent with Fig. 8.4e. Figure adapted from [193]. © 2013 American Physical Society.

Figures 8.5a-d show simulated excitation efficiency maps for both fundamental polarizations obtained by recording the integrated emission intensity at the respective positions of the mode detector as a function of excitation spot position over a range of 1×1 μm. For parallel (perpendicular) polarization the maps feature a single connected region roughly centered on the incoupling antenna if the emission is recorded at the corresponding emission position of the symmetric (antisymmetric) mode. If the "wrong" mode detector port emission is recorded, then, despite the seemingly wrong polarization, the corresponding modes can still be detected if the beam is displaced perpendicular to the TWTL axis. This results in two disconnected areas in the excitation efficiency maps which are reproduced in experiments [Figs. 8.5e-h]. We conclude that excitation of pure modes requires both control of the polarization and nanometer-scale precision for the positioning of the excitation spot. We further conclude that both degrees of freedom, polarization and focal spot position, can be used to synthesize linear combinations of pure modes.

8.5 Group velocity of pure-mode contributions

As an application we demonstrate the selective determination of the group velocities of symmetric and antisymmetric contributions of a multimode ultrafast plasmon pulse. We create such a plasmon pulse using a well-positioned excitation spot polarized at 45° with respect to the TWTL [Fig. 8.6a]. The experiment is performed using ultrashort pulses (800 nm central wavelength, 53 nm FWHM, 80 MHz repetition rate, 2 nW average excitation power) on a dedicated setup [145, 146] using one of the TWTL arrays of Fig. 8.4e. A time-averaging detector imaging the mode detector records about equal intensities for both ports. However, since both modes travel at different group velocities, the symmetric and the antisymmetric pulse contributions actually arrive at their ports at slightly different instants after correcting for the total propagation distance. Such minute time delays as well as absolute propagation times can be measured using spectral-interference microscopy [145]. Its principle is outlined in Fig. 8.6b. From the determined propagation times we calculate the respective modal group velocities. The results are displayed in Fig. 8.6c and compared to simulated values. Within the error margins quantitative agreement between experiment and theory is found and the small differences in the modal group velocities can be clearly resolved. As expected, the less-confined symmetric mode is closer to the free-space propagation speed (about 10% faster than the antisymmetric mode). No systematic influence of the antenna length on the pulse propagation time is observed.

8.6 Conclusion

In summary, plasmon excitations in top-down fabricated monocrystalline gold TWTL nanocircuits can be prepared in deterministic eigenmode superpositions by positioning

a tightly focused laser beam with respect to the incoupling antenna attached to the TWTL and by adjusting its polarization. This enables the controlled superposition and interference of multiple eigenmodes allowing, e.g., for spatio-temporal control of nano-optical fields. This yields the possibility to tap new degrees of freedom in creating advanced circuit functionality beyond single-mode interference. In linear nanocircuits such new functionality will include coherent control of the optical path taken by an excitation in the circuit. This is subject of the next chapter. Such control of confined fields can also be used for the implementation of nonlinear optical switching effects and the controlled interaction of guided modes with single quantum emitters [60, 197].

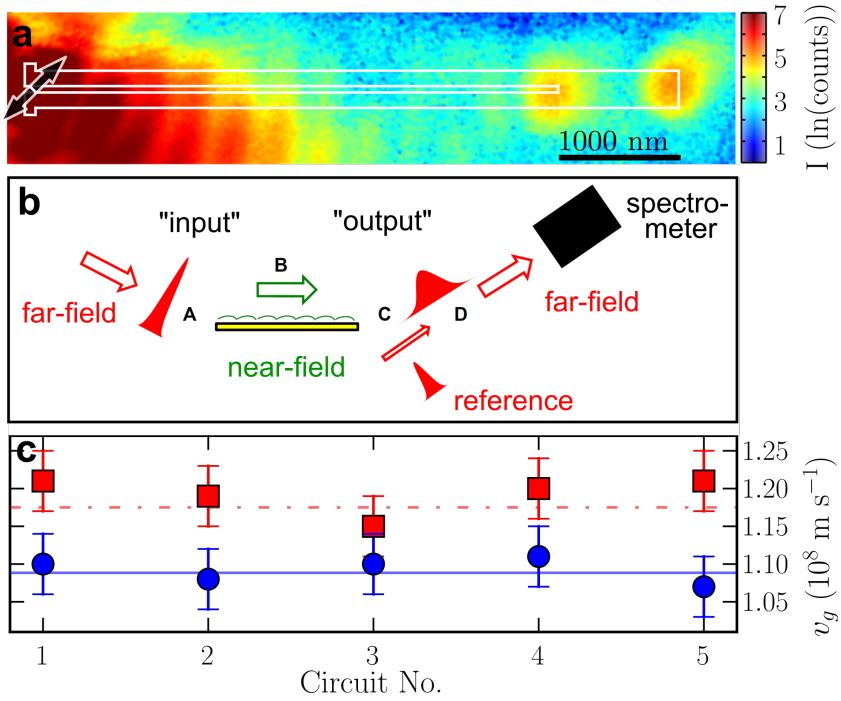

Figure 8.6: (a) Emitted intensity scan (log-scale, no attenuation of direct scattering) of the circuit using 45° polarized illumination ($\lambda = 800\,\mathrm{nm}$) [145, 146]. (b) Scenario of response function characterization using spectral interferometry. A pulsed far-field light source excites propagating plasmons (A) that are processed by the plasmonic device (B). After propagation the pulses are converted back into far-field detectable signals (C) and full characterization (amplitude and phase) is facilitated via spectral interferometry [144] using a reference pulse (D). (c) Group velocities of symmetric (red squares, dashed line) and antisymmetric mode contributions (blue circles, solid line) of ultrafast plasmon pulses determined for one of the arrays used in Fig. 8.4e. Quantitative agreement between experimental data (symbols with error bars) and simulation results (horizontal lines) is obtained. Panels a and c adapted from [193]. Panel b taken from [145].

Chapter 9

Coherent control of plasmon propagation in a nanocircuit

With identification of the finite spectrum of eigenmodes present in TWTLs [Chap. 5] and their deterministic synthesis [Chap. 8] we now have the indispensable tools at hand to design and optimize essential elements of functional plasmonic nanocircuits. In this chapter, we introduce a nanoscale directional coupler, i.e., a nanocircuit with a single input port and two output ports, which exploits a controlled near-field interference mechanism. Due to the intuitive and optimized design varying the linear input polarization is enough to switch between both output ports.

The results of this chapter have been published in [158] and [198]. Parts of text and graphics are taken one-to-one from these publications. All presented experiments have been performed in a close collaboration within the work group of Tobias Brixner[1].

9.1 Motivation

The miniaturization of optical devices is a prerequisite for broadband data processing technology to compete with cutting-edge nanoelectronic circuits. For these future nano-optical circuits, controlling the spatial and temporal evolution of surface plasmons is a key feature. So far, the strong subwavelength electromagnetic energy confinement [11, 35, 48] of propagating plasmonic modes supported by noble-metal nanowires led to the realization of nanometer-scale proof-of-concept circuits with well-defined built-in (passive) functionality [58, 75, 76] such as splitting or filtering [33]. Moreover, (active) coherent control of femtosecond optical energy localization in nanoscale random structures and V-shapes [77] as well as coherent control of plasmon routing has been proposed [78, 79]. Coherent control of nonpropagating near-fields was achieved experimentally using closed-loop learning algorithms [199, 200] and open-loop control schemes [201]. In all these schemes, a far-field laser pulse - determined by its spectral amplitude, phase, and polarization - excites a particular superposition of near-field modes, which then evolve into a desired state, e.g., a local field enhanced by orders

[1]Institut für Physikalische und Theoretische Chemie, Universität Würzburg, Am Hubland, 97074 Würzburg, Germany

of magnitude [77]. It is customary in the literature [77–79] to call such a scheme "coherent control". Thus we will also use the term here even when there is no clear separation between an external "source" for a propagating signal and another field acting as "control" on that signal. The "control" can rather also be part of the "source".

First experiments to manipulate propagating plasmons have been performed using networks of chemically grown silver nanowires [56, 69–73] or slot-less gold nanostructures [74]. However, only recent advances in the understanding and fabrication of plasmonic nanocircuits based on optical antennas [12, 64–66] and TWTLs [67, 68] have enabled the quantitative selective excitation of multiple eigenmodes [193], as presented in Chap. 8. Our findings there prepare the ground for an experimental demonstration of coherent control of plasmon propagation based on linear interference of multiple well-defined plasmonic modes, similar to concepts used in dielectric waveguides [202].

In this chapter, we report on plasmon routing by open-loop coherent control in a plasmonic nanoscale directional coupler. By careful design of the device [Sec. 9.2] it is possible to achieve efficient coherent control of highly confined propagating near-fields using the simplest possible control field, i.e., linearly polarized light, thereby avoiding the use of closed-loop learning algorithms. In contrast to classical electronic circuits, where a symmetric bifurcation inevitably causes an equal splitting of any input current pulse towards the two output ports, we induce a fundamentally different behavior in the plasmonic nanoscale directional coupler by exploiting the existence of multiple eigenmodes and coherence - both not accessible in classical electronics. We therefore demonstrate the potential and importance of optical coherent control in the design and operation of plasmonic nanocircuitry. In Sec. 9.3 we experimentally demonstrate open-loop ultrafast spatial and spatiotemporal coherent control of plasmon propagation by manipulating the input polarization of ultrashort pulses and pulse pairs and by characterizing the light emitted from both output ports. Our experiments represent a very intuitive classical analogue to quantum control in molecules.

However, true conditional switching action as occurring in electric transistors requires the utilization of nonlinear effects. One way to realize nonlinearities in plasmonic nanocircuitry consists in the combination of plasmonic materials with dielectrics having large higher-order susceptibilities. For example, the use of chalcogenide glasses has been proposed [177, 203]. However, the high precision required to embed such materials into plasmonic nanostructures constitutes a major obstacle for their realization. An alternative approach consists in directly using the nonlinear Kerr-type response of the electron plasma in metals [204] which has been demonstrated for example by four-wave mixing at gold surfaces supporting surface plasmons [205, 206] and in experiments showing third-harmonic generation in single plasmonic nanoparticles [207] and optical nanoantennas [208, 209]. The latter type of experiments make use of the fact that the inherent optical nonlinearity of plasmonic materials can be enhanced in well-designed, high-quality nanostructures in which considerable near-field intensity enhancement can be achieved.

The design of plasmonic circuitry, in which effects of the third-order nonlinearity of gold can be observed, suffers from the lack of reliable knowledge of the nonlinear optical

constants in the relevant spectral range. Uncertainties are related to the dependence of the nonlinear response on the crystalline structure, as data obtained so far was recorded for multi-crystalline thin films [210–214] and data for monocrystalline gold films does not exist. Furthermore, the effect of the nonlinear refractive index on propagation phenomena in plasmonic circuits is rather unclear. In this overall context, our proposed nanoscale directional coupler can also be seen as a phase-sensitive nanointerferometer to investigate effects of a third-order nonlinearity in plasmonic nanocircuitry. This allows us to retrieve upper bounds for nonlinear effects in plasmon propagation and the formation of mode superpositions, as is detailed in Sec. 9.3.3. These results offer some insight into the feasibility of nonlinear all-plasmonic switching based on gold.

9.2 Directional coupler design and simulation

Commonly, the polarization state of monochromatic light beams and their transformation is displayed via a spherical representation of the normalized Stokes parameters S_1, S_2, and S_3, the so-called Poincaré sphere [Fig. 9.1a]. In this representation, linear polarization states are situated on the equator, with orthogonal polarizations being opposing points, while the spin eigenstates – left- and right-handed circular polarization – are localized at the poles.

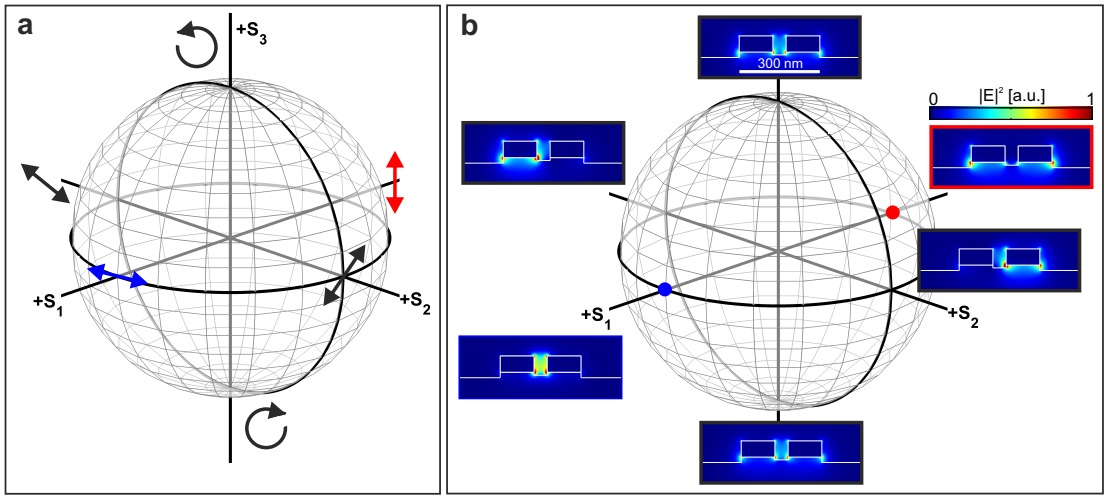

Figure 9.1: Poincaré spheres. (a) Classical Poincaré sphere for light beams and (b) equivalent Poincaré sphere for TWTL modes. Fundamental polarization states and modes are indicated, respectively.

Our nanoscale directional coupler is based on a TWTL situated on a glass-air interface that supports the familiar symmetric and antisymmetric eigenmodes, just as our mode detector device in Chap. 8. As shown there, the two orthogonal linear excitation polarizations of a well-positioned laser spot can directly be mapped onto the two TWTL eigenmodes and thus any other polarization state of the TWTL can be

expressed as a superposition of both eigenmodes. Therefore, taking the orthogonal modes of the TWTL as a basis we can now represent the polarization state in our plasmonic device via an equivalent Poincaré sphere [Fig. 9.1b].

The differing effective wavelengths ($\lambda_{\mathrm{eff}}^{\mathrm{sym}} = 517\,\mathrm{nm}$ and $\lambda_{\mathrm{eff}}^{\mathrm{antisym}} = 471\,\mathrm{nm}$ for 800 nm vacuum wavelength) and propagation lengths ($l_{\mathrm{decay}}^{\mathrm{sym}} = 4.83\,\mu\mathrm{m}$ and $l_{\mathrm{decay}}^{\mathrm{antisym}} = 2.53\,\mu\mathrm{m}$) of the two TWTL eigenmodes directly influence the behavior of the device under multimode excitation. The former is the characteristic of a birefringent medium, where a differential phase delay between both modes accumulates with unchanged amplitude ratio. The latter is the characteristic of a dichroic medium, where one polarization state is preferentially attenuated. The birefringent character is well visible in the TWTL's near-field by the formation of a beating pattern along the propagation direction whose phase, and thereby the position of field maxima and minima, can be controlled by the polarization of the incoming light. Figures 9.2a,b show the simulated S-like near-field intensity and instantaneous charge distributions obtained for a +45° linear excitation polarization, respectively. To mimic the experimental conditions, the device illumination was modeled from the substrate side using a tightly focused Gaussian beam ($\lambda = 800\,\mathrm{nm}$ in vacuum, NA = 1.4) centered on the incoupling antenna gap. We note that alternatively the beating pattern can be obtained by considering the TWTL as two (strongly) coupled single-wire waveguides supporting identical modes [215, 216].

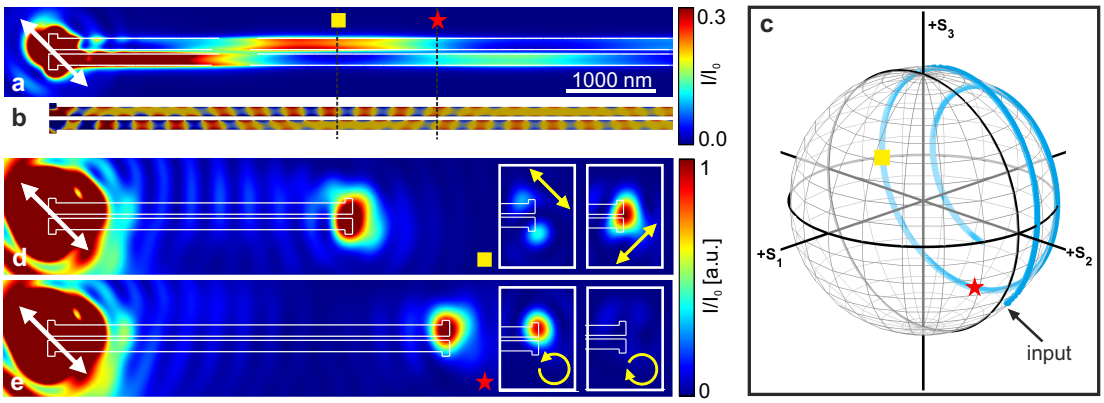

Figure 9.2: Multimode excitation of a TWTL. (a) Simulated steady-state near-field beating pattern and (b) corresponding instantaneous surface charge distribution produced by a near equal-amplitude superposition of symmetric and antisymmetric mode. The white arrow indicates the incoupling polarization. All near-field intensity distributions of this chapter are recorded in a plane 10 nm below the glass–air interface and are normalized to the input intensity I_0. (c) Evolution of the polarization state along the TWTL represented on the Poincaré sphere. (d,e) Simulated far-field images for a (d) 3.4 μm and (e) 4.5 μm long TWTL with antenna terminations on both sides. (insets) Emission spots for various polarization analyzers (indicated in yellow). Panel a adapted from [158].

In terms of the Poincaré sphere representation, birefringence manifests itself in a circling of the polarization state [Fig. 9.2c], i.e. evolving from a linear to a circular,

back to a linear polarization state and so on ad nauseam. Dichroism, in turn, leads to a spiral on the Poincaré sphere due to the drift of the polarization state onto that side of the sphere belonging to the mode with less damping, here the symmetric mode. As a direct consequence, it is impossible to reach the initial polarization state by a simple ongoing propagation. It is noted that the deviation of the initial polarization state from the corresponding +45° of the excitation light is a direct consequence of the different incoupling phases of both modes, as displayed in Fig. 8.2d.

The different polarization states can be coupled to the far field by a second antenna terminating the TWTL, with the exact TWTL length adjusting the relative phase of the emitted field components. Thus and counter-intuitively, a linear dipole antenna can be driven to emit any arbitrary far-field polarization state – in contrast to classical antennas, that only emit with polarization along the antenna axis. For instance, a 3.4 μm long TWTL operates as a half-wave plate with most of the antenna emission still being linearly polarized but rotated by 90° with respect to the input polarization [Fig. 9.2d], while a 4.5 μm long TWTL operates as a quarter-wave plate by emitting circularly polarized light [Fig. 9.2e].

In order to realize a branching region for the TWTL and achieve phase-sensitive directional coupling, two additional wires are added on both sides of the TWTL. These four wires then split up adiabatically into a set of two uncoupled parallel TWTLs supporting the same eigenmodes as the input line. Figure 9.3a illustrates the principle of directional coherent control in this coupler. We follow the evolution of the beating pattern into the four-wire region, which supports the four eigenmodes displayed in Figs. 9.3b-e. For +45° input polarization an intensity maximum appears at the lowest wire after about 2300 nm propagation. We exploit this observation and split the four wires at this point via a sine-curved S-bend so that the +45° polarization results in propagation of light in one branch only. The resulting simulated near-field intensity distribution for the optimized device is displayed in Fig. 9.4a. Indeed, in the far-field the intensity is successfully routed to the right branch and emitted from output port A as shown in Fig. 9.4b.

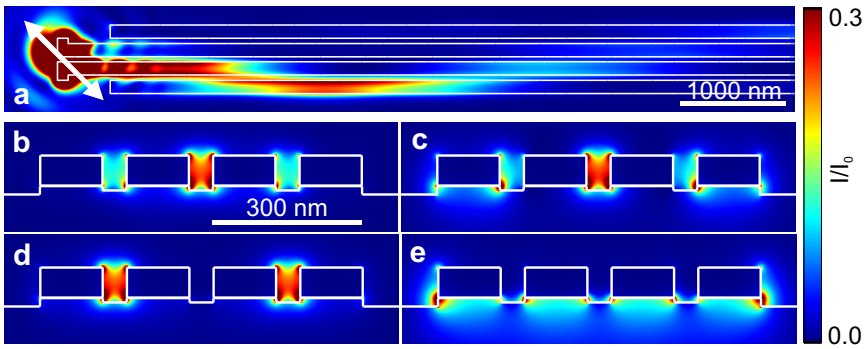

Figure 9.3: Four-wire transmission line. (a) Beating pattern extending over all wires of a four-wire transmission line supporting two antisymmetric (b,c) and two symmetric (d,e) eigenmodes. Panel a adapted from [158].

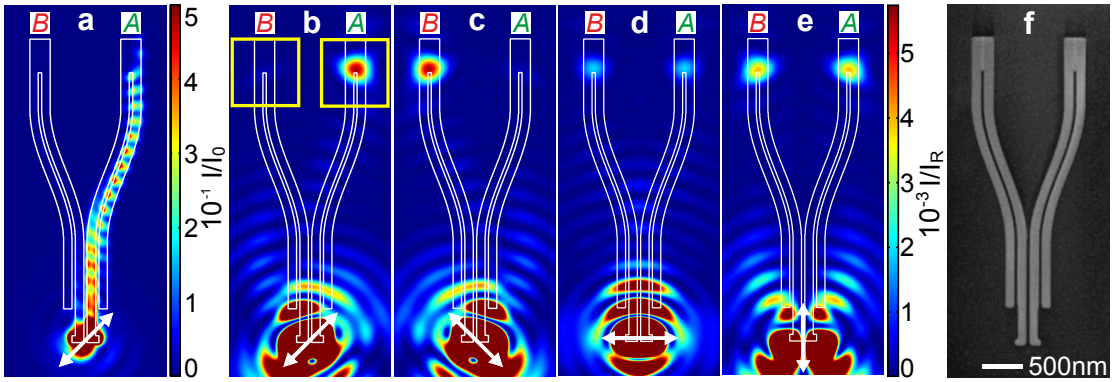

Figure 9.4: Nanoscale directional coupler. (a) Simulated steady-state near-field intensity distribution for excitation with +45° input polarization (white arrow) demonstrating routing to the right branch (output port A). The standing wave pattern is due to reflection at the termination. (b) Corresponding far-field projection. (c-e) Far-field projection for (c) −45°, (d) 0°, and (e) 90° input polarization. Far-field projections consider the properties of the imaging system, as described in Sec. 4.4.2, and additionally include an analyzer oriented perpendicular to the nanostructure's symmetry axis, thus only the dominating antisymmetric mode emission from the output ports is recorded. The intensity is normalized to an unstructured gold surface reflection I_R. (f) SEM image of the fabricated coupler. Figure adapted from [158].

To quantify the control performance of our device we define the spatial contrast sc as

$$\mathrm{sc} = \frac{E(A) - E(B)}{E(A) + E(B)}, \tag{9.1}$$

where the emitted energy E in each output port is determined by the background-corrected integral in $1 \times 1\,\mu\mathrm{m}^2$ regions indicated by the yellow squares in Fig. 9.4b. This quantity combined with an overall high throughput of the device served as the figure of merit in numerical structure optimization. To this end, several parameters were tuned, among others cross-sectional TWTL geometry, four-wire transmission line starting position, branching position and bending angle. Furthermore, the antenna geometry (overall length 400 nm, width 100 nm) was chosen so that it provides similar excitation efficiencies for both eigenmodes, which is important for maximum near-field interference. The four-wire starting position was optimized to minimize reflections due to impedance mismatch. The distance between the start of the four-wire transmission line and the branching position has to be sufficiently large to allow most of the fields to locate at an outermost wire of the nanostructure, while the branching position was optimized such that the spatial contrast is maximal for ±45° linear excitation. Furthermore, a high signal throughput was achieved by keeping the radii of curvature in the bending region as large as possible (thus reducing propagation losses) while still being able to clearly spatially separate the two output ports by far-field optical microscopy. The best directional coupler, which was found within this optimization and is shown in this chapter, yields in simulations a spatial contrast sc = 0.90 for the design wavelength of 800 nm.

Due to symmetry, output port B lights up for an input polarization of $-45°$ [Fig. 9.4c]. For $0°$ or $90°$ excitation, the plasmon splits up equally into both branches [Figs. 9.4d,e], equivalent to a spatial contrast $\mathrm{sc} = 0$. Beyond the branching region, the modal composition of the propagating optical near field is dominated by the antisymmetric mode that is localized in the gap and, therefore, radiates to the far field at the point where the gap is short cut [193]. The choice of the branching position as well as the design of the antenna lead to simple rather than complex [199, 217] optical control fields.

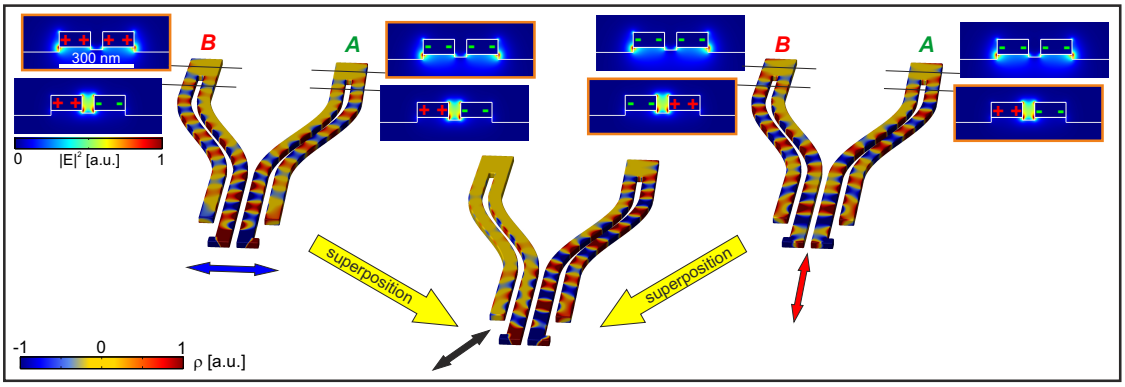

Figure 9.5: Origin of plasmon routing. Instantaneous charge distributions for excitation with $0°$ (left), $90°$ (right), and $+45°$ (center) input polarization. The orange boxes indicate modes that experience a phase shift of π between output ports A and B.

The charge distributions upon pure eigenmode excitation, as shown in Fig. 9.5, allow further insight into the origin of plasmon routing. Although in both cases pure modes are excited in the first place, after the bend a mixture of both eigenmodes is present. Symmetry considerations suggest different phases of the respective converted eigenmode (i.e. the initially not excited eigenmode) between output ports A and B. Consequently, for appropriate structure dimensions a linear superposition of both cases (resembling an excitation with $+45°$ polarization) leads to a cancellation (addition) of the charges on output port B (A) and thus to a dark (bright) far-field emission spot of output port B (A). The degree of cancellation depends on how similar one can get the mode powers for the two orthogonal excitation polarizations. To this end, deliberate mode conversion proves to be indispensable. This can be achieved, at least to some extent, by plasmonic elements such as a simple TWTL curve or the S-like bend in our directional coupler, acting similarly to the structures described in [194, 218]. In the latter case [Fig. 9.6a], the exact geometry of the S-shaped bending region determines the conversion efficiencies, which are calculated as the fraction of the power in the respective mode right after the bend to the input mode power right before the bend and thus include the regular mode decay along the bend segment. Conversion to the initially not excited mode is favorable for bends with larger extension in y-direction, as displayed in Fig. 9.6b. Alternatively, single TWTL bends are even more promising candidates for mode conversion, as the S-shaped bend partially reverses the mode conversion of a single bend. Therefore, an almost perfect conversion of one into

the other mode is feasible with the correct curve radius [Fig. 9.6c]. The conversion capabilities as a function of the bend radius are summarized in Fig. 9.6d. Chapter 11 provides an outlook on our spin-optical nano-device implementing this type of mode converter.

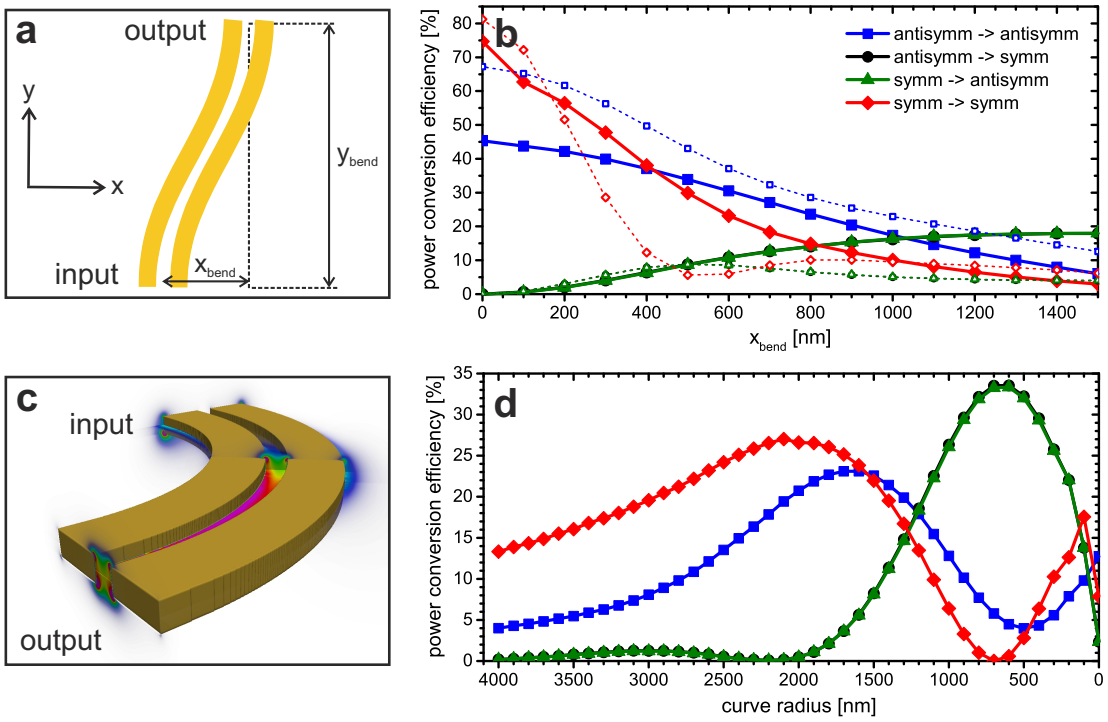

Figure 9.6: Plasmonic mode converting elements. (a) Geometry of TWTL S-like bend and (b) mode conversion efficiency for $y_{\mathrm{bend}} = 2\,\mu\mathrm{m}$ (solid lines) and $y_{\mathrm{bend}} = 1\,\mu\mathrm{m}$ (dashed lines). (c) TWTL curve (radius = 700 nm) converting from symmetric input to antisymmetric output mode. (d) Mode conversion efficiency for varying curve radii.

Regarding the spectral behavior of the spatial contrast [Eq. (9.1)], simulations show that, even though the beating wavelength and thus the beating pattern varies across the spectrum, the functionality of the nanoscale directional coupler is robust in a sufficiently broad wavelength region around the design wavelength of 800 nm. The spatial contrast is $\mathrm{sc}_{\mathrm{sim}} = \pm 0.63$ for 750 nm and $\mathrm{sc}_{\mathrm{sim}} = \pm 0.89$ for 850 nm.

We have, therefore, successfully implemented coherent control over plasmon propagation for a system in which the light-matter interaction responsible for the control is spatially separated from the decisive branching region, as first proposed by Sukharev and Seideman [78]. In coherent (nanooptical) control schemes, the local electric field in the frequency domain $\vec{E}_{\mathrm{local}}(\vec{r},\omega) = \mathbf{A}(\vec{r},\omega)\vec{E}_{\mathrm{ext}}(\omega)$ depends on both the tensorial linear response function of the (nano-)system $\mathbf{A}(\vec{r},\omega)$ and the external field $\vec{E}_{\mathrm{ext}}(\omega)$ [79]. Usually the response function is fixed and coherent control is exerted by manipulating the properties of the excitation light, i.e., amplitude, phase, and polarization. E.g., in the prototype quantum control problem for chemical reactions [217], a complex elec-

tric field $\vec{E}_{\mathrm{ext}}(t)$ is required that excites a particular wavepacket, which preferentially evolves from the initial state into a selected final state. In our case an appropriate coherent control field leads to surface plasmon polariton propagation to a selected output port. Therefore, our experiment represents a very intuitive classical analogue to quantum control. However, as opposed to the conventional coherent control problem, here we do not seek the optimal $\vec{E}_{\mathrm{ext}}(t)$ for a given system but rather design the system response $\mathbf{A}(\vec{r},\omega)$ so that a given simple control field (varying linear polarization) leads to the desired result. Thus, the simple pulse shape that leads to control is not a sign of an incoherent control scheme but it is rather a desired feature.

We further note that although the behavior appears to be similar to that of a polarizing beam splitter, the physics of plasmon routing is different. The polarizer-like behavior only occurs due to the specific design of the incoupling antenna as well as the length of the four-wire coupling region. For example, by an appropriate choice of the four-wire coupling region length, routing with right versus left circularly polarized light could be easily obtained. By additionally detuning the antenna and thereby the weight of both eigenmodes corresponding elliptical polarization states would be required as input fields.

In addition, the mode interference in the proposed device can be utilized to detect changes of the spectral phase difference between the modes. If one considers the propagation phase of a near-field mode that is subject to small changes when excited at different intensities, such changes can be monitored by sophisticated near-field probe methods (e.g., NSOM [219] and PEEM [220]) or spectral interferometry [144–146]. The latter reconstructs the complete plasmon propagation phase, but the extraction of small excitation-intensity-induced changes remains challenging. We therefore propose the use of our nanocircuit as a phase-sensitive plasmonic nanointerferometer that intrinsically translates differences of the propagation phase into a far-field intensity variation, which can directly be measured by conventional optical imaging techniques. Again, a $+45°$ linearly polarized Gaussian excitation leads to a predominant routing of the intensity to the right branch and emission from output port A [Fig. 9.7a].

A nonlinear refractive index leads to a phase variation of the propagating plasmons. We expect the process to occur in the antenna region where the local field is largest. If the nonlinear effect varies in magnitude between the two superimposed plasmon modes, e.g., because of different field localization and enhancement, a relative phase change is introduced. Due to the decaying intensities of the propagating modes, phase changes upon propagation caused by nonlinear effects likely only play a minor role. The potential benefit of this kind of structure for studies of nonlinear effects lies in the phase sensitivity of the spatial contrast sc, as can be seen in the reduced spatial contrast in Fig. 9.7b obtained for a relative phase change of $-\pi/10\,\mathrm{rad}$. There the effect of a nonlinearity has been approximated by introducing a phase difference between horizontally and vertically aligned excitation components, corresponding to an effectively elliptical excitation. In the case considered here of a relative phase change of $-\pi/10\,\mathrm{rad}$, the spatial contrast decreases from 0.75 to 0.53 for the structure featuring an overall antenna length of 425 nm.

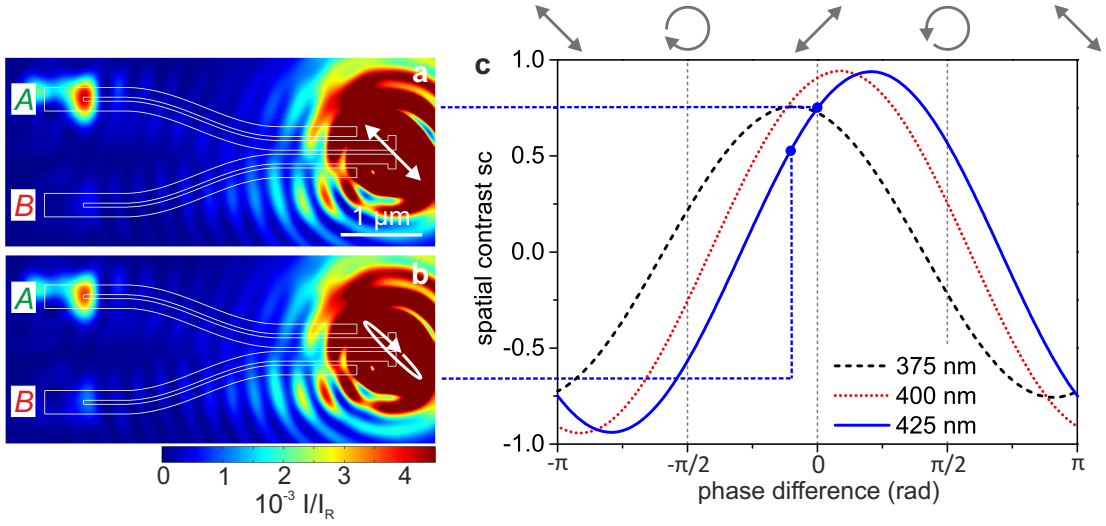

Figure 9.7: Principle functionality of the device as phase-sensitive plasmonic nanointerferometer. (a) Simulated far-field image of the device excited at the input antenna (overall length 425 nm) with a focused Gaussian beam polarized at +45° with respect to the antenna axis, as indicated by the white arrow. (b) Simulated far-field image of the identical structure assuming a change by $-\pi/10$ rad in phase difference between the two eigenmodes, i.e., increasing the ellipticity of the excitation polarization. The intensity scale is normalized to an unstructured gold surface reflection I_R. (c) Spatial contrast as a function of the introduced change in phase difference between the two eigenmodes for input antenna lengths of 375 nm (black dashed line), 400 nm (red dotted line), and 425 nm (blue solid line). The corresponding effective excitation polarization is depicted above. Figure modified from [198]. © 2016 Springer-Verlag Berlin Heidelberg.

To investigate this further, we consider structures that are nominally identical except for the input antenna length, that influences the amplitude of each excited mode [193]. Consequently, in simulations the structures show varying spatial contrasts for the same +45° linearly polarized excitation. The respective results for input antenna lengths of 375 nm, 400 nm, and 425 nm are presented in Fig. 9.7c. A closer look at the spatial contrast as a function of the introduced relative phase change between the two eigenmodes reveals that the structure with overall antenna length of 400 nm shows the highest spatial contrast for +45° polarized excitation, whereas the other structures have slightly detuned antenna lengths leading to a reduced spatial contrast. On the contrary, the spatial contrast of the interferometer with 425 nm antenna length is expected to have the highest sensitivity for relative phase changes since its spatial contrast graph shows the steepest slope. The behavior of these structures under varying excitation intensity is investigated experimentally in Sec. 9.3.3.

9.3 Experiments

The nanoscale directional coupler – again fabricated by FIB milling from a monocrystalline gold platelet grown in solution and deposited on a cover glass – is shown in Fig. 9.4f. Femtosecond laser pulses with a peak wavelength of $\lambda_0 = 800\,\mathrm{nm}$ and a spectral full width at half maximum (FWHM) of 48 nm are coupled into a (home-built) confocal microscope that has the ability of selectively detecting particular emission spots independent of the excitation position using a piezo tip-tilt mirror in combination with a Keplerian telescope and a pinhole. Furthermore, heterodyne spectral detection is realized with a reference pulse [145]. The setup records light emitted in the sample plane with diffraction-limited resolution and further detects the temporal position of emission signals with respect to the reference pulse with femtosecond resolution. This allows, e.g., to measure the group velocity of propagating plasmons [146], as demonstrated in Sec. 8.5. In addition to the piezo tip-tilt option for spectral interferometry measurements, we can image a large sample area onto a charge-coupled device (CCD) camera. When using this visualization option, the piezo tip-tilt mirror is bypassed and the image is relayed via a different Keplerian telescope. This telescope adjusts the image size on the two-dimensional CCD chip and allows to insert a circular beam attenuator (OD 2) in the focal plane [as familiar from Chapters 7 and 8] that suppresses most of the strong reflection and scattering of the excitation spot at the input end of the nanostructure. In all experiments an analyzer with its transmission axis oriented perpendicular to the symmetry axis of the nanostructure is used. Thus, only the dominating emission of the antisymmetric mode at the output ports is detected.

Since control in the designed nanoscale directional coupler relies on active polarization and phase manipulation, a Mach–Zehnder delay line is used to produce two collinearly propagating pulses. The polarization in one arm of the delay line is rotated by 90° using a half-wave plate in combination with a polarizer. We carefully checked that both pulses have the same focal size, focal position, and excitation power in the sample plane. Hence, we are able to produce two orthogonally polarized excitation pulses, termed x-polarized and y-polarized, with an arbitrary temporal separation. This includes the possibility of temporal overlap, yielding more complex temporal polarization patterns. In the temporal overlap region the polarization state depends on the relative phase $\Delta\Phi$ between the two pulses. If the relative phase is, e.g., scanned from $\Delta\Phi = 0$ to $\pi/2$, the resulting polarization state changes from linear (at 45°) over elliptical, to circular. Using the delay line we are able to control the separation of the two pulses with 0.1 fs accuracy (experimentally determined via spectral-interference measurements). This corresponds to a relative path-length difference of 30 nm, or a relative phase of $\Delta\Phi = 0.075\pi$ at 800 nm wavelength. Therefore, we are able to precisely manipulate the relative phase of both pulses, i.e., the polarization state of the excitation field. Compared to polarization pulse shaping based on a zero-dispersion compressor and spatial light modulator [221], the Mach–Zehnder setup avoids complications originating from space–time coupling [222–224] that become especially relevant

with high-NA focusing and excitation position sensitivity. The observed control effects are therefore indeed due to spectral phase properties only and not due to spatially modified excitation.

9.3.1 Single-pulse routing and coherent spatiotemporal control

To experimentally demonstrate single-pulse routing the nanostructure was mounted so that the symmetry axis coincided with the diagonal of the coordinate system spanned by the two orthogonal polarizations. In this configuration an $x(y)$-polarized pulse is expected to excite the superposition of eigenmodes that leads to far-field emission only at output port $A(B)$ [Figs. 9.8a,b].

Figures 9.8c,d show experimental time-integrated intensity maps recorded at the output port region of the nanoscale directional coupler. As predicted, only output port $A(B)$ emits light for the $x(y)$-polarized excitation. The high spatial contrast (sc $= 0.79$ and sc $= -0.88$ for x- and y-polarized excitation pulses, respectively) confirms the spectrally broadband operation of the device required by ultrashort laser pulses.

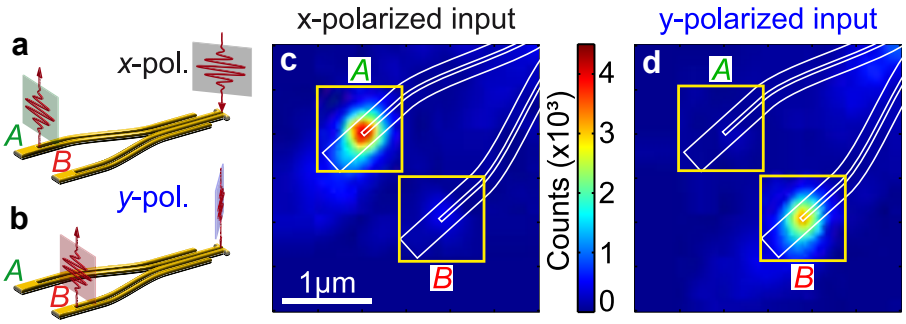

Figure 9.8: Single-pulse routing. (a,b) Sketch: Routing of plasmon pulses for x-polarized (a) and y-polarized (b) excitation pulses. (c,d) Spatial maps show the measured time-integrated sample emission upon excitation with the x-polarized (c) and y-polarized (d) pulse. Due to the orientation of the directional coupler (white outline), the $x(y)$-polarized pulse corresponds to $+(-)45°$ polarization and causes routing to output port $A(B)$. Figure taken from [158].

In the measurements described so far, the nanostructure was excited either by a single x- or y-polarized pulse. If pulses of both polarizations are incident with a fixed time delay, both output ports emit light successively [Fig. 9.9a]. Indeed, in the time-integrated spatial map of the emission region shown in Fig. 9.9b both output ports of the nanostructure light up. To resolve the temporal separation between the two emitted pulses we use spectral-interference microscopy [145]. Figure 9.9c shows the reconstructed temporal envelopes of the signals from both output ports. The temporal signature corresponds to the scheme in Fig. 9.9a and confirms that the light at the two output ports is emitted successively as expected. Here, the y-polarized pulse arrives later than the x-polarized pulse. This can be inferred from the temporal envelopes

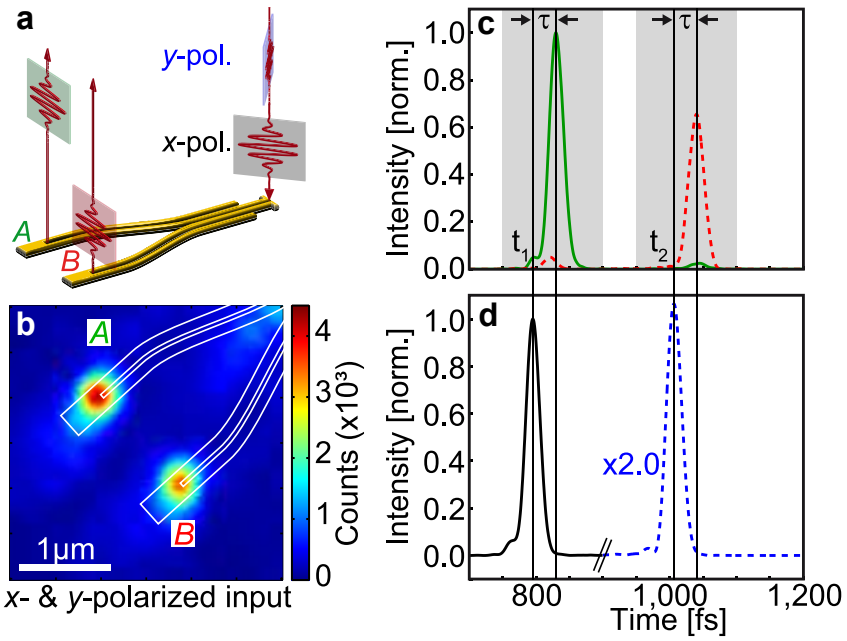

Figure 9.9: Coherent spatiotemporal control. (a) Two orthogonally polarized excitation pulses are incident on the nanostructure with a temporal delay leading to the emission of separate pulses at each output port at different times. (b) Time-integrated sample emission map showing light emission from both output ports. (c) Reconstructed temporal envelopes of emission in output port A (green solid) and B (red dashed). (d) Reconstructed temporal envelope of the input field showing two peaks. The time trace below 900 fs (black solid) represents the x-polarized pulse, whereas the part above 900 fs (blue dashed) is attributed to the y-polarized pulse. The contribution above 900 fs was multiplied by a factor of 2.0 to account for the polarization-dependent transfer function from the sample plane to the detectors (i.e., the ratio of separately measured integrated spectra). The x-polarized pulse was delayed by 800 fs with respect to the reference pulse. Figure taken from [158].

of the x- and the y-polarized input pulses in Fig. 9.9d. Because the envelopes were measured using the reflections from an unstructured gold platelet, the temporal separation of their maxima (210 fs) indicates the starting time difference of the plasmons launched by the respective pulses [145, 146]. Since the plasmons propagate with a certain group velocity [146], the output signals in Fig. 9.9c both peak at a time $\tau = 34$ fs after the maxima of the respective input pulses in Fig. 9.9d. Due to the symmetry of the nanoscale directional coupler the value of τ is the same for both output ports and is, within its error and considering the fabrication uncertainties, in good agreement with the simulated value of $\tau_{\mathrm{sim}} = 30$ fs.

To quantify the control performance, we define the temporal contrast for a given output port as

$$\mathrm{tc} = \frac{\hat{E}(t_1) - \hat{E}(t_2)}{\hat{E}(t_1) + \hat{E}(t_2)}, \tag{9.2}$$

where the energy $\hat{E}(t_\mathrm{i})$ is the integral under the chosen temporal envelope curve in the respective shaded areas in Fig. 9.9c. We obtain tc = 0.94 for output port A and tc = −0.86 for output port B. These values confirm the successful implementation of spatiotemporal coherent control. We note that the temporal separation of the excitation pulses can be adjusted at will so that almost arbitrary temporal sequential routing of plasmon pulses is possible with femtosecond resolution.

9.3.2 Coherent switching

We now change the reference frame by reorienting the structure so that the x polarization is parallel to its symmetry axis. In this case each far-field polarization separately excites the corresponding pure eigenmode (symmetric for the x polarization and antisymmetric for the y polarization). As a result, each polarization causes simultaneous emission at both output ports with equal intensity. Thus, if the excitation pulses are well separated in time, both output ports emit a corresponding pair of pulses as sketched in Fig. 9.10a. In the time-integrated map for a pulse separation of $\Delta t = -107.8\,\mathrm{fs}$ shown in Fig. 9.10b this cannot be distinguished from the case in Fig. 9.9(b), where each output port emits a single pulse but at a different time. The emitted intensity is approximately the same in both output ports as confirmed by the spatial contrast curve in Fig. 9.10e, which has a value close to zero (sc = −0.06) at this separation of the pulses. Again, the energy E emitted at each output port was determined by the background corrected integral in $1 \times 1\,\mu\mathrm{m}^2$ regions as indicated with the yellow squares in Figs. 9.10b-d. If, on the other hand, both pulses are superimposed in time, the instantaneous polarization of the excitation field varies as a function of the time delay. By using such polarization-shaped laser pulses [221–224], it is possible to control and visualize a coherent process of alternating routing by scanning the temporal overlap stepwise and recording the spatial map of time-integrated sample emission for each step. As seen in Fig. 9.10e, the spatial contrast remains constant with decreasing temporal separation of the excitation pulses as long as both pulses are not superimposed in time. However, as soon as temporal overlap occurs the light emission alternates between both output ports with increasing spatial contrast. Near the perfect temporal overlap [Fig. 9.10f] changing the time delay by $\Delta t = 1.3\,\mathrm{fs}$, corresponding to a half of the optical field oscillation cycle, is enough to invert the spatial contrast from sc ≈ +1 to sc ≈ −1, i.e., to switch the routed signal between both output ports. This switching is illustrated in Fig. 9.10c (emission from A at $\Delta t = 0.0\,\mathrm{fs}$) and Fig. 9.10d (emission from B at $\Delta t = 1.3\,\mathrm{fs}$).

To illustrate further potential of polarization-shaped pulses, we now consider time delays comparable to the bandwidth-limited pulse length. A quasi-3D representation of the excitation pulse for the delay of $\Delta t = 22.7\,\mathrm{fs}$ is shown in Fig. 9.10g. The pulse was simulated using measured spectra and zero spectral phase for the x-polarized pulse as well as 22.7 fs linear spectral phase for the y-polarized pulse and is approximately linearly polarized with orientation evolving from x to −45° and finally to y polarization. Feeding this pulse into the nanoscale directional coupler results in output pulses as

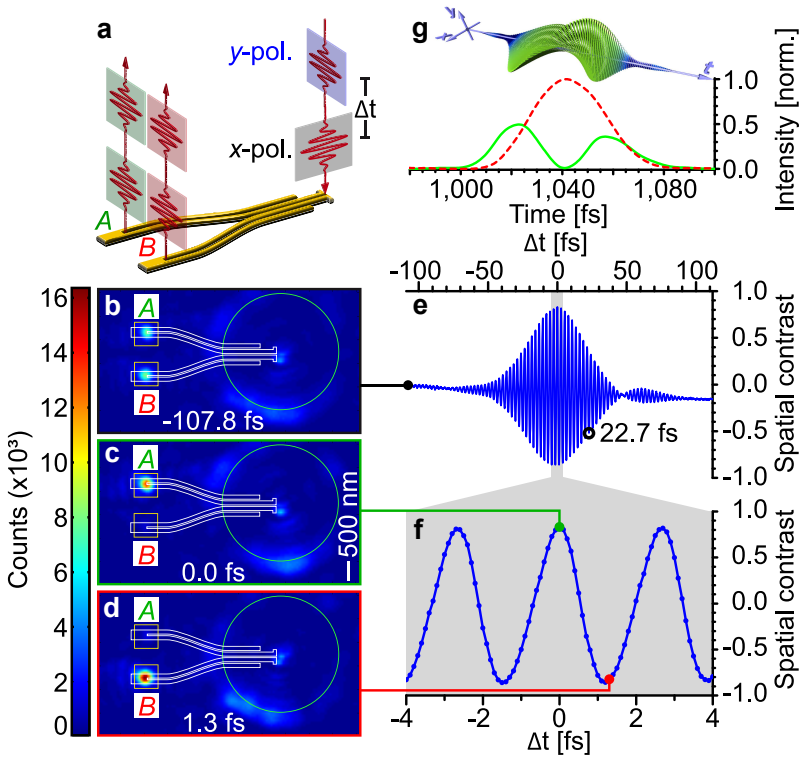

Figure 9.10: Alternating routing. (a) Reference frame sketch: x-polarized pulse is parallel to the symmetry axis of the directional coupler. (b,c,d) Spatial maps of the measured time-integrated sample emission are shown for the two excitation pulses well separated in time ($\Delta t = -107.8\,\mathrm{fs}$) and overlapping with $\Delta t = 0.0\,\mathrm{fs}$ and $\Delta t = 1.3\,\mathrm{fs}$. Outlines of the nanostructure (white) and of a circular beam attenuator (green) that suppresses most of the excitation spot reflection and scattering are shown. (e) Spatial contrast curve as a function of the time delay and (f) a zoom into the temporal overlap region. (g) Reconstructed temporal envelopes (bottom) from measurements at output port A (green solid) and B (red dashed) are shown for a pulse separation of $\Delta t = 22.7\,\mathrm{fs}$ [black open circle in (e)] together with a quasi-3D representation of the input field (top). Figure taken from [158].

shown in the lower panel in Fig. 9.10g: The temporal evolution of the emission in output port B follows the projection of the polarization onto the $-45°$ axis, whereas in output port A it follows the projection onto the $+45°$ axis. Consequently, output port A emits a closely spaced double pulse.

9.3.3 Nonlinear relative phase change

This study was performed with a modified experimental setup using a Ti:Sapphire oscillator with subsequent LCD-based pulse shaper and high-NA microscope [145, 225]. The oscillator emits laser pulses with a spectrum from 650 nm to 950 nm (foot width) [225] at a repetition rate of 80 MHz. In combination with a pair of chirped mirrors,

the dispersion from transmissive optics is pre-compensated in the pulse shaper. By using the phase-resolved interferometric spectral modulation (PRISM) algorithm [226], a pulse length of below 10 fs is reached at the sample position, measured by second-order autocorrelation. The beam waist of the immersion-oil objective (NA = 1.4) has been characterized [225] to be about 260 nm (beam waist for $I = I_{max}/e^2$).

For power-dependent scans, we use a broadband half-wave plate in combination with a linear polarizer. The angle of the wave plate and thereby the power transmitted through the subsequent polarizer is varied in a precise and reproducible way by a motorized rotation stage. The excitation position of the sample is selected by mounting it on a piezo scanner. The emission position is set independently using a piezo tip-tilt mirror in combination with confocal detection. Spatial maps are scanned and detected in reflection through the same objective by avalanche photodiodes. Instead of confocal detection, a two-dimensional image of the sample plane can be mapped onto a two-dimensional CCD chip (Princeton Instruments, Acton Pixis2kB) [145].

For the experiments the linear excitation polarization is kept fixed at +45°, resulting in an emission mainly from output A [see Fig. 9.7a]. As described in Sec. 9.2, the spatial contrast is modulated if the relative phase between the two excited near-field modes varies. Such a variation would be expected to result from a nonuniform nonlinear refractive index. We test for such a phase change to occur by varying the power of light incident on two identical series of nanointerferometers, S_1 and S_2. Within each series, the overall input antenna length is increased from structure to structure, resulting in slightly different relative amplitudes of the excited near-field modes. Apart from that, the geometry of the structures is identical.

We selected four of these nanostructures, three of them from series S_1, one from series S_2. The former are shown in the SEM picture in Fig. 9.11a. The antenna lengths for these structures are 375 nm for structure S_1 s (small), 400 nm for structure S_1 m (medium), and 425 nm for the identical structures S_1 l and S_2 l (large). Figures 9.11c-e show the spatial contrast between the output ports in power-dependent experiments for structures with different antenna lengths (425 nm in Fig. 9.11c, 400 nm in Fig. 9.11d, and 375 nm in Fig. 9.11e). Subsequent series of measurements M_i on the same structure are labeled by the index i in chronological order. The error bars show the standard deviation of all measurements taken at the same power in a single series of measurements. Within each series of measurements, multiple up and down scans of the excitation power (called loops from now on) were performed. The intensity scan in a single loop is sketched in the inset of Fig. 9.11e. Each loop consists of a scan with increasing intensity (labeled U) followed by a scan with decreasing intensity (labeled D). A series of measurements was stopped when the average spatial contrast within U differed by more than 10% from the average spatial contrast within D in a single loop. Those irregularities can be an indicator for sample drift, because the spatial contrast is dependent on the exact incoupling position (cf. Chap. 8). Since the contrast changes occurred mainly after a few loops close to the antenna damage threshold, we attribute it to sample degradation after an initial antenna deformation at the highest power within a loop.

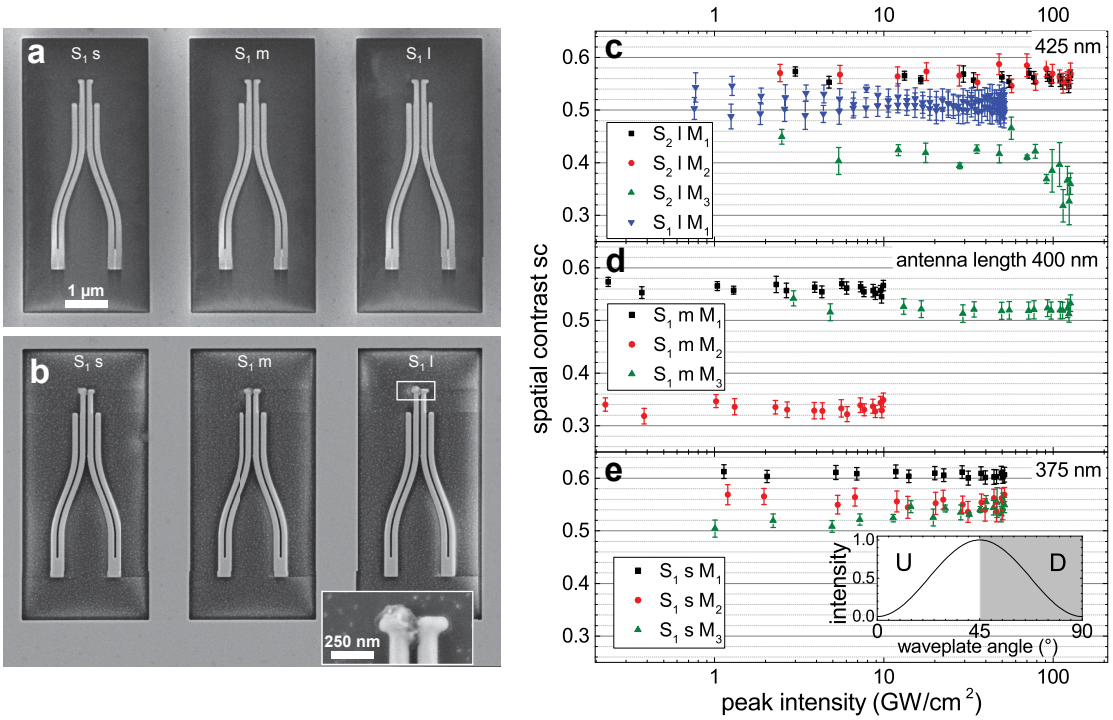

Figure 9.11: SEM pictures of the three used structures of series S_1 (a) right after fabrication and (b) after power-dependent excitation scans. All three antennas with lengths 375 nm, 400 nm, and 425 nm (left to right) have clearly taken damage. The inset in (b) shows the partly melted 425 nm antenna of structure S_1 l. (c-e) Power-dependent scans of the spatial contrast in nanointerferometers. Each color shows a power-dependent series of measurements M_i on nanointerferometers with overall antenna lengths of (c) 425 nm, (d) 400 nm, and (e) 375 nm. Each series M_i consists of multiple up-and-down scans (loops) in excitation power. A single loop is depicted in the inset in (e). Figure taken from [198]. © 2016 Springer-Verlag Berlin Heidelberg.

SEM pictures of the three structures of series S_1 taken right after the intensity-dependent scans are shown in Fig. 9.11b. The antennas have suffered visible damage and are deformed, which can be seen more clearly in the inset showing the 425 nm antenna of structure S_1 l. All three antennas were damaged at some point during the measurements, regardless if the highest used peak intensity was 52 GW/cm^2 or 127 GW/cm^2. Therefore, we determine the damage threshold of the investigated phase-sensitive plasmonic nanointerferometers to an upper bound of 52 GW/cm^2, corresponding to a threshold intensity a factor of 0.23 relative to the threshold for homogenous gold layers determined from z-scan measurements (for details see [198]). In terms of pulse energy per area, damage occurs at 0.48 J/cm^2.

The fact that the spatial contrast remained constant during a series of measurements until a rapid change at a certain point gives a hint that, until then, the nanointerferometers also withstood the incident laser pulses without taking damage. When a series

of measurements was repeated afterwards on the same wire, the spatial contrast again was constant for multiple loops. Nevertheless, the tendency that the absolute value of the spatial contrast gets smaller for repeated series of measurements on the same structure can be seen for all three antenna lengths. This tendency was also observed in simulations, where parts of one antenna arm were removed to mimic the damage. Within one series of measurements, the power-dependent deviation of the spatial contrast is in the range of the error bars, i.e., no nonlinear effect is observable. Typical errors are on the order of 5% of the spatial contrast value. To achieve experimentally detectable spatial contrast variations exceeding the measurement uncertainties using our most sensitive structures (S_1 l and S_2 l with an overall antenna length of 425 nm), according to the simulation model [Fig. 9.7c] a phase difference between the two eigenmodes of 0.07 rad or more would be required. Thus, we conclude that the experimentally achieved nonlinear relative phase change between the symmetric and the antisymmetric plasmonic eigenmode is below 0.07 rad.

9.4 Conclusion

In conclusion, we successfully demonstrated ultrafast spatial and spatiotemporal coherent control of plasmon propagation in a nanoscale directional coupler by exploiting the interference of well-characterized multiple eigenmodes, thus realizing light guidance [78] and femtosecond energy localization at the nanoscale [77] without the use of learning algorithms. Our results show the potential and importance of coherent control in the design and operation of plasmonic nanocircuitry. Furthermore, our findings open an interesting route to femtosecond pump–probe experiments on the nanoscale [227]. The demonstrated coherent control of spatial–temporal emission characteristics can be further improved using a polarization pulse shaper [221] providing access to arbitrary output pulse patterns limited only by the excitation pulse bandwidth. By changing the branching position of the nanoscale directional coupler its function can be adapted, e.g., to achieve switching using circularly polarized light [see Chap. 11]. Reciprocity implies that a carefully selected superposition of near-field modes, excited at the two output ports, can drive the linear input antenna to radiate any far-field polarization state. Moreover, extension of the nanoscale directional coupler to a nanointerferometer, which might enable probing, e.g., quantum optical properties of single plasmons [197] or phase differences in plasmonic systems induced by optical nonlinearities [228, 229], was studied. The interferometers showed damage thresholds below the onset of noticeable nonlinear effects. Their sensitivity can potentially be further enhanced by the use of shorter laser pulses and by fine-tuning the design of the plasmonic nanointerferometers.

Chapter 10

Normal-incidence PEEM imaging of propagating plasmon modes

In the previous chapter, we designed a high-end plasmonic nanocircuit, i.e. a nanoscale directional coupler, and demonstrated by far-field optical characterization deterministic coherent control of plasmon propagation and routing based on multimode SPP interference. In view of the ever increasing device complexity with simultaneously decreasing tolerance toward fabrication uncertainties, quantitative nanoimaging tools for accessing near-field distributions of optical nanocircuits are urgently needed.

In this chapter, normal-incidence two-photon photoemission electron microscopy (PEEM) is applied to image the propagation, interference, and routing of multiple guided modes using our directional coupler as a showcase nanocircuit. We find that the recorded photoemission yield can be heuristically modeled with high precision by considering the 4^{th} power of the numerically simulated electric near-field around the nanocircuit, paving the road for a future widespread application of normal-incidence PEEM. The presented PEEM experiments have been performed in the work group of Martin Aeschlimann[1]. Most of this chapter has been published nearly identically in [80].

10.1 Motivation

Complex devices for future ultrafast integrated nano-optical circuitry require accurate fabrication techniques with minimal uncertainties such as substrate inhomogeneities or small structural defects, e.g. a conductive bridge forming a short circuit. Therefore, dedicated nanoimaging tools are needed that provide detailed information about the propagation of plasmonic modes in order to verify functionality. In this framework, multiphoton PEEM [220] has been established as a powerful tool to image and characterize propagating SPPs along planar metal films [230–234], chemically-grown [235] and microfabricated [236] noble-metal nanowires, organic nanofibers [237], and photonic waveguides [238–240]. However, the observation of the propagation and

[1]Department of Physics and Research Center OPTIMAS, University of Kaiserslautern, Erwin-Schrödinger-Str. 46, 67663 Kaiserslautern, Germany

interference of a finite spectrum of eigenmodes on a complex, functional plasmonic waveguide device relevant for future nano-optical circuits has never been attempted.

Conventional PEEM setups have successfully exploited grazing-incidence illumination in many studies, e.g., coherent superposition of multiple localized surface plasmon (LSP) modes in small rice-shaped silver nanoparticle structures using few cycle laser pulses [241] and polarization of the LSP resonances in metallic flat nanoprisms [242]. However, when investigating more complicated structures, due to phase retardation effects such asymmetric illumination leads to complex photoemission patterns thereby obstructing the direct visualization of optical near-fields. Only recently normal-incidence illumination PEEM was introduced [243] removing these difficulties. Normal-incidence illumination PEEM will have a major impact as it is expected to allow direct imaging of SPPs near-field intensity distributions with, e.g., the observed fringe spacing in a standing wave directly resembling the effective wavelengths of the involved plasmons. So far, just proof of principle measurements of plasmon polaritons have been published using this technique [243].

In the following, for the first time we use normal-incidence PEEM to visualize the propagation of distinct superpositions of multiple plasmonic modes responsible for the operation of our nanoscale directional coupler. The photoemission process induced by plasmons propagating a 1D transmission line is expected to differ markedly from that of surface plasmon propagation on a 2D metal film. Indeed, it is unknown which field components at which position of the sample contribute most to the emission of photoelectrons. It is therefore beneficial if plasmon modes and their superpositions have been characterized before by independent methods, as is done in Chap. 9 employing diffraction-limited far-field optical characterization. In that study, only emission from the structure's terminations was observed, since propagating modes don't result in any far-field radiation. Of course, in the presented PEEM study the imaged near-field distribution differs from the one present in Chap. 9 due to the different excitation scheme. Here, the widefield plane wave illumination of the whole structure is responsible for a simultaneous launching of plasmon modes at all the device's input/output ports. In addition, for certain polarization, the plane wave illumination directly excites an off-resonant near-field intensity in the TWTL gap that coherently superimposes to the guided mode field. In Sec. 10.2 we reveal excellent agreement between PEEM images and simulation data by using the 4^{th} power of the mostly transverse field components propagating in the transmission line gaps as a measure for the photoemission yield. We further show that PEEM signals of different pure plasmonic modes vary strongly in amplitude depending on the mode. In Sec. 10.3 we demonstrate that interference of plasmonic mode fields forming standing waves within the device with the illumination field has to be taken into account to correctly explain the obtained patterns in PEEM. The observation of a distinct switching behavior with PEEM can be obscured by the above mentioned launching of plasmon modes at all device's input/output ports, as detailed in Sec. 10.4.

10.2 Numerical modelling of PEEM yield

Figure 10.1 shows a sketch of the experiment. The directional coupler is illuminated with a mode-locked Ti:Sa laser of 25 fs pulse duration and an 80 MHz repetition rate at a center wavelength of $\lambda = 795$ nm. The laser beam comes in at normal incidence from the air half-space and is focused to a roughly 100 μm diameter spot on the sample resulting in an evenly illuminated structure. The studied photoemission process is a two-photon photoemission process (2PPE), i.e. two photons must be absorbed in order to free one electron. The spatial distribution of photo-emitted electrons is imaged using a photoemission electron microscope (Focus IS PEEM) with a spatial resolution of < 40 nm [243]. The inset of Fig. 10.1 shows an SEM image of the investigated directional coupler fabricated from a monocrystalline gold platelet (60 nm thickness). To avoid charging in SEM and PEEM, the sample was covered with an additional 2 nm thin gold layer before the FIB process.

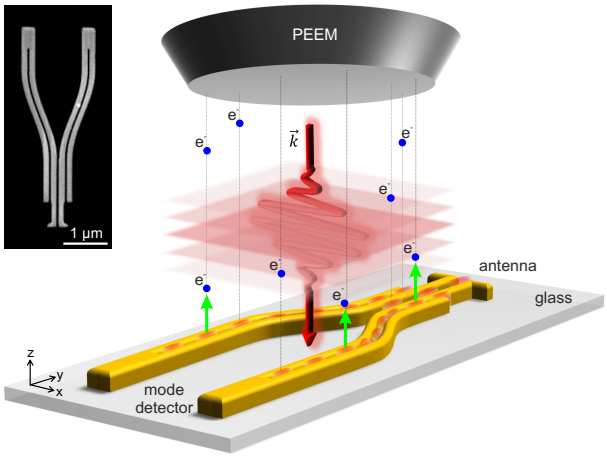

Figure 10.1: Principle of the experiment. The entire directional coupler is illuminated by a short plane wave laser pulse at normal incidence resulting in the excitation of counter-propagating plasmon modes forming a standing wave pattern. The spatially varying photoemission of electrons (sketched as blue dots) is imaged by PEEM. Inset: SEM image of investigated structure. Figure taken from [80]. © 2016 American Chemical Society.

We model the expected distribution of the PEEM signal using the FDTD method [Sec. 4.1] to simulate the near-fields in the structure's vicinity. To mimic the experiment [Fig. 10.1], the entire nanostructure is homogeneously illuminated by a plane wave source of 800 nm wavelength under normal incidence from the air half-space. To account for the two-photon nature of the photoemission process and the electron extraction toward the air half-space, in simulations we calculate $|E|^4$ in a cross section at midheight through the structure and use this as a measure for the simulated PEEM intensity. Note that this choice results in much better agreement to experimental PEEM data compared to a plane closely above the structure in the air half-space due to an increased weight of electron emission originating from the gap. Although the local fields in this case are totally parallel to the substrate and perpendicular to the direction of the electron detector, a nice correspondence of PEEM data and simulated $|E|^4$-maps is obtained, as given below.

In this way, we obtain simulated PEEM intensity maps for an excitation with linearly polarized light in x-direction [Fig. 10.2a] and y-direction [Fig. 10.2b], respectively. For x-polarized excitation (parallel to the antenna axis) the simulated PEEM intensity shown in Fig. 10.2a is confined in the gap between the two wires indicating the excitation of the antisymmetric near-field mode [cf. Fig. 9.2b]. Indeed, a detailed analysis of the terminations' emission patterns using the reciprocity theorem [85] shows that the antisymmetric mode is excited at both types of terminations with nearly equal efficiency. This is obvious by inspection of the numerically calculated far-field emission patterns [for details see Sec. 4.4.1] in Fig. 10.2c at a mode detector end (left) and the antenna (right) obtained by driving the respective terminations with the antisymmetric mode, both showing similar intensities for an emission angle of 0° (corresponding to normal-incidence excitation). The interference of the resulting counter-propagating antisymmetric plasmon modes causes the intensity modulations (standing wave pattern) observed in the gap regions in Fig. 10.2a.

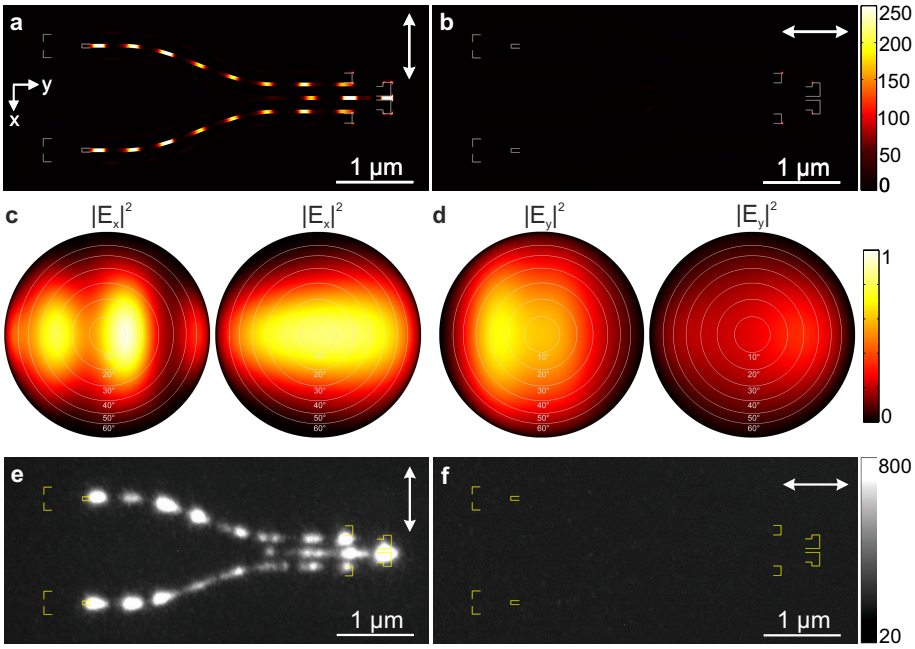

Figure 10.2: (a,b) Simulated PEEM intensity maps, i.e. near-field distribution $|E|^4$ in the x-y plane at midheight through the structure. The plane wave laser light ($\lambda = 800\,\mathrm{nm}$) hits the sample at normal incidence with (a) x- and (b) y-polarization. (c,d) Projected far-field emission patterns for the (c) antisymmetric and (d) symmetric TWTL mode at a mode detector end (left) and the antenna (right). All emission patterns have the same scaling and have been projected to a hemisphere above the structure. The circular rings mark the angle of emission in steps of 10°. (e,f) Experimental PEEM images of the directional coupler at normal incidence illumination by a laser of wavelength $\lambda = 795\,\mathrm{nm}$ with (e) x- and (f) y-polarization. In (f) hardly any photoelectrons can be detected. Figure adapted from [80].

For the in-plane orthogonal y-polarized excitation the simulated PEEM intensity shown in Fig. 10.2b is much weaker despite identical excitation power. For this excitation polarization the symmetric near-field mode [cf. Fig. 9.2a] is also excited at both types of terminations. While for this mode the excitation efficiency at the mode detector end is approximately twice as large as at the antenna, they both are comparable to that of the antisymmetric mode for x-polarized excitation [see Fig. 10.2d]. Therefore, as for the x-polarized excitation, counter-propagating symmetric plasmon modes are excited, which, however, do not lead to any detectable photoelectron emission due to the very weak overall near-field intensity close to the structure.

For PEEM experiments, we first used off-resonant imaging to reveal the exact position and orientation of the nanostructure. Experimental PEEM images for resonant excitation at a laser wavelength of $\lambda = 795\,\mathrm{nm}$ with x-polarization (y-polarization) leading to the excitation of pure modes are shown in Fig. 10.2e (Fig. 10.2f). The comparison of simulated [Fig. 10.2a,b] and experimental [Fig. 10.2e,f] photoemission patterns reveals good agreement, confirming the reasonable assumptions underlying the simple photoemission model used to obtain the simulated PEEM intensity maps. The nice match includes the number and positions of the emission spots for x-polarized excitation [Fig. 10.2a,e] as well as correctly predicting the observation of negligible photoemission for y-polarized light excitation [Fig. 10.2b,f]. The latter can be explained by the fact that the near-field intensity of the symmetric mode is mostly guided at the interface between glass and gold [see Fig. 9.2a]. Considering that the electron escape length is only $1 - 2\,\mathrm{nm}$, this mode is likely not detectable with PEEM since the excited electrons cannot be efficiently released from the solid. Additionally, for the same mode power, the antisymmetric mode exhibits higher surface fields (and also more fields in the gold), which is another possible explanation why only photoemission from the antisymmetric mode can be detected in PEEM. As opposed to this, there are situations where PEEM can reveal otherwise optically dark modes, as shown e.g. for nanoparticles placed at subnanometer distance to a metal film [244].

Notably, toward both left and right structure ends the spots get brighter, evident in both simulation [Fig. 10.2a] and experiment [Fig. 10.2e]. This is due to the mode intensity being highest at the terminals and decaying away from them. Some intensity variations (e.g., an asymmetry between both arms) are, however, not reproduced by the FDTD simulations. We explain these differences with changes in the work function across the surface caused by inevitable formation of contaminant monolayers at ambient experimental conditions, while small fabrication induced structural imperfections are expected to have only a minor contribution.

10.3 PEEM pattern periodicity

In normal-incidence PEEM one may expect that the observed periodicity of a standing wave pattern matches one half of the effective wavelength λ_{eff} of the corresponding propagating plasmon mode. However, as shown by Kahl et al. for SPPs on epitaxial

silver islands [243], the interference with the excitation field increases the observed fringe spacing to λ_{eff}. To verify this behavior for the present structure, the simulated PEEM intensity map for x-polarized illumination is again shown in Fig. 10.3b. For comparison we also plot the corresponding near-field intensity distribution for the identical nanostructure illuminated as in Chap. 9, i.e. with a *localized* Gaussian source focused to the position of the incoupling antenna [on the right-hand side in Fig. 10.3d]. The different excitation geometries are illustrated in Figs. 10.3a and 10.3c, respectively. In both cases standing wave patterns are observed. Since only the antisymmetric mode is visible in PEEM images, the resulting intensity patterns are caused by the antisymmetric mode ($\lambda_{\text{eff}} = 456\,\text{nm}$). The blue lines in Fig. 10.3 exhibit a spacing of $\lambda_{\text{eff}}/2$ and serve as a guide for the eye. Indeed, for local excitation [Fig. 10.3d] the expected periodicity of $\lambda_{\text{eff}}/2$ resulting from the back reflection of the antisymmetric mode at the gap termination of the two mode detectors is observed. However, in the simulated PEEM intensity map [Fig. 10.3b] every second intensity maximum is missing which leads to an apparent doubling of the periodicity.

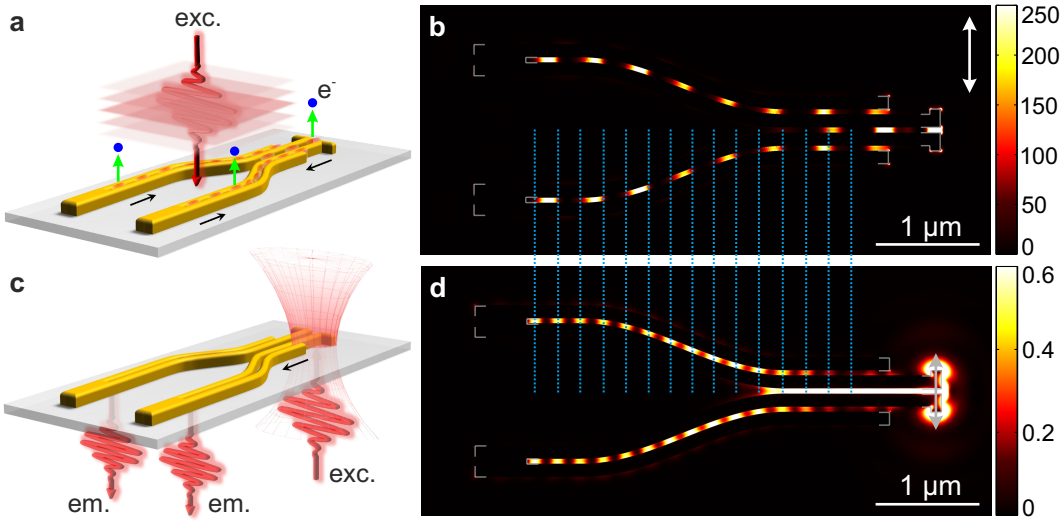

Figure 10.3: Periodicity of near-field intensity distributions. (a) Normal-incidence PEEM excitation geometry with x-polarized laser light illumination. (b) Corresponding simulated PEEM intensity map. (c) Excitation geometry used for optical propagation measurements. The identical nanostructure is illuminated with an x-polarized tightly focused Gaussian beam (NA = 1.3) from the substrate side centered on the antenna gap. The incoupled intensity is equally emitted at both mode detector terminations, preferentially to the substrate side. (d) Corresponding simulated near-field intensity distribution $|E|^2$ for focused excitation. The structure's corners are superimposed in gray as a guide to the eye. The vertical blue lines have a spacing of $\lambda_{\text{eff}}/2$ of the antisymmetric mode. Figure taken from [80]. © 2016 American Chemical Society.

We conclude that even for normal-incidence laser illumination, PEEM images do not just show the standing wave pattern resulting from counter-propagating plasmons that get simultaneously excited at all three terminals of the structure due to the large illumination area. Instead, the near-field distribution mapped in PEEM is due to the additional interference of the mode's standing wave pattern with the polarization dependent non-resonantly enhanced excitation field along the whole structure. Its impact is obvious from the simulated PEEM images for an infinitely long TWTL excited by x- and y-polarized plane waves impinging under normal incidence in Figs. 10.4a,b and 10.4c,d, respectively. Only in the case of x-polarized plane wave excitation [Fig. 10.4a], the excitation field can efficiently penetrate into the gap region of the TWTL [Fig. 10.4b] where it superimposes to the TWTL mode field. This interference process, in combination with the two-photon nonlinearity of PEEM, causes the change in the observed oscillation period [see Fig. 10.4e-j]. Therefore, normal-incidence PEEM truly images the total near-field intensity present at the sample surface.

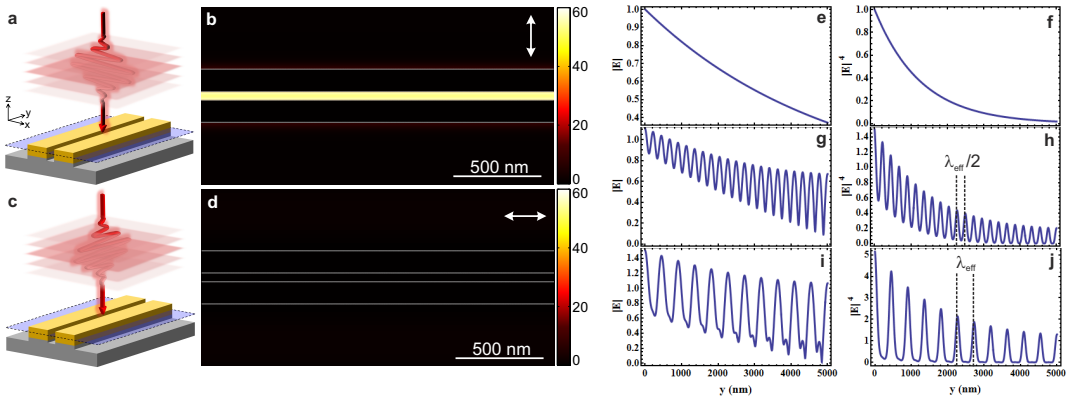

Figure 10.4: Simulated near-field intensity distribution $|E|^4$ along an infinitely long TWTL for x-polarized (a,b) and y-polarized (c,d) plane wave excitation ($\lambda = 800\,\mathrm{nm}$) impinging under normal incidence. The intensity maps are recorded in a cut at midheight through the structure, as indicated by the blue planes in (a),(c). The structure's outline is superimposed in gray as a guide to the eye. Position dependent near-field amplitude $|E|$ (e) and intensity $|E|^4$ (f) of the antisymmetric mode propagating along an infinitely long TWTL in positive y-direction. The initial mode's amplitude is set to 1 without loss of generality. Position dependent near-field amplitude $|E|$ (g) and intensity $|E|^4$ (h) of the antisymmetric mode including the back reflection at a termination ($y = 5000\,\mathrm{nm}$). The mode's reflection amplitude and phase at the termination have arbitrarily been set to 0.8 and 0, respectively. The exact values only influence the modulation depth and the absolute position of the maxima, but not the oscillation wavelength. Position dependent near-field amplitude $|E|$ (i) and intensity $|E|^4$ (j) of the superposition of the standing wave pattern in (g,h) with a constant complex offset (offset amplitude = 0.4, offset phase = 0) along the whole length describing the non-resonantly enhanced excitation field. A different value for the offset phase again just leads to a shift of the pattern without changing the periodicity. Figure adapted from [80]. © 2016 American Chemical Society.

For completeness the superior interpretation capabilities enabled by using normal-incidence PEEM are shown in Fig. 10.5 exhibiting a comparison of FDTD simulated beat patterns for the directional coupler illuminated with light under normal-incidence [Fig. 10.5a-c] and grazing-incidence [Fig. 10.5d-f], respectively. For the latter one, the laser pulse is incident from the antenna side and its propagation direction and the surface normal comprise an angle of 65°, as illustrated in Fig. 10.5d. The simulated PEEM intensity maps for s- and p-polarized excitation are shown in Figs. 10.5e,f, respectively.

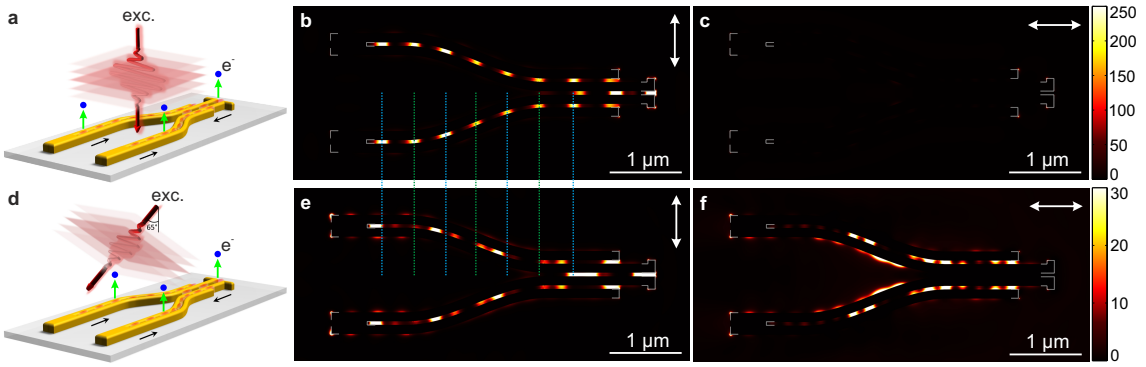

Figure 10.5: Comparison of normal-incidence vs. grazing-incidence illumination. (a) Normal-incidence PEEM excitation geometry with x-polarized laser light illumination. (b) Corresponding simulated PEEM intensity map. (c) Simulated PEEM intensity map with y-polarized laser light illumination at normal-incidence. (d) Grazing-incidence PEEM excitation geometry with s-polarized laser light illumination. (e) Corresponding simulated PEEM intensity map. (f) Simulated PEEM intensity map with p-polarized laser light illumination at grazing-incidence. The structure's corners are superimposed in gray as a guide to the eye. The vertical lines have a spacing of λ_{eff} of the antisymmetric mode. Figure taken from [80].

Obviously, the PEEM patterns for grazing-incidence illumination show more complex features. Thus, the normal-incidence PEEM technique is clearly favorable to get physical insight into our nanostructures. Particularly, in contrast to illumination under normal-incidence for p-polarization at grazing-incidence there is also photoemission signal to be expected due to the existence of an additional out-of-plane component of the electric field which can contribute dominantly to the PEEM signal. Furthermore, at grazing-incidence we additionally have phase retardation effects, that affect the interference along the structure and result in a changed beating periodicity, as already previously observed [230, 243]. For s-polarization under grazing-incidence illumination [Fig. 10.5e], the observed fringe spacing in the transmission line is roughly $2{\cdot}\lambda_{\mathrm{eff}}$ (considering only the high intensity spots), in contrast to the λ_{eff}-spacing observed at normal-incidence [Fig. 10.5b]. This fits with the fringe spacing obtained by the Moiré condition for the employed excitation geometry [243].

10.4 Spatial switching in optical and PEEM measurements

Using a localized excitation source focused to the position of the incoupling antenna to the right at +45° polarization [Fig. 10.6a] causes a distinct superposition of modes to be launched. As a result, routing of intensity can be observed in far-field propagation measurements. In experiments, light emission is observed at the upper mode detector terminal as shown in Fig. 10.6b [158]. The appearance of two separate emission spots at the mode detector reveals the fact that both the symmetric and the antisymmetric mode are propagating in the TWTL [193]. The image is obtained with the same home-built inverted microscope setup introduced in Sec. 7.2. Near-field simulation results considering the corresponding illumination with a tightly focused Gaussian beam centered on the antenna gap are shown in Fig. 10.6c. As this illumination geometry is the one used for design and optimization of the structure in Chap. 9, it is confirmed that the equal-amplitude superposition of both TWTL modes excited at the antenna is selectively directed into the upper arm of the device. Routing to the lower arm is achieved using -45° polarization.

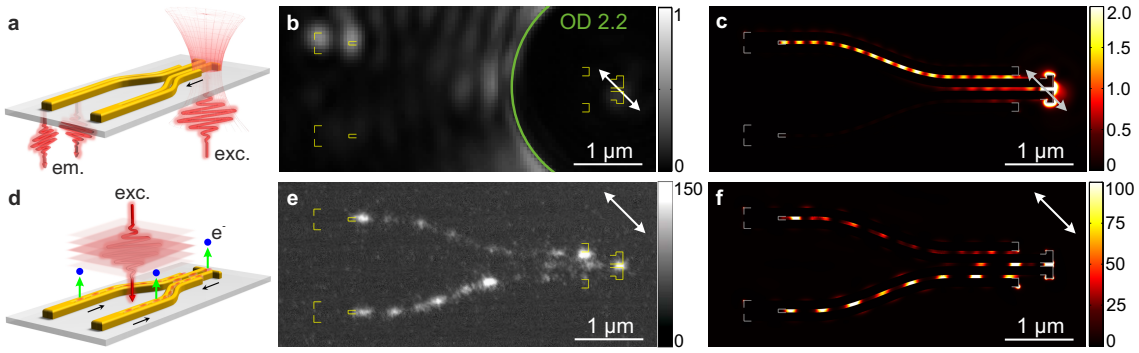

Figure 10.6: (a) Sketch of the excitation geometry used for optical propagation measurements of the directional coupler excited by a localized source at +45° linearly polarized light. (b) Corresponding experimental optical propagation measurement result. To avoid saturation of the CCD, the strong reflection of the excitation spot at the incoupling antenna position is suppressed by a small beam block in an intermediate image plane (indicated by the green circle segment). The structure's outline is superimposed as a guide to the eye. (c) Simulated near-field intensity distribution $|E|^2$ in a cross section at midheight through the structure for focused Gaussian excitation. (d) Normal-incidence PEEM excitation geometry with linearly polarized laser light illumination at +45°. (e) Experimental PEEM image of the directional coupler. (f) Corresponding simulated PEEM intensity map. Figure taken from [80].

Such a distinct switching behavior as a function of the polarization is not expected to be directly reproduced in our PEEM measurements of the same device. All three terminals of the structure are fed simultaneously due to the large illumination area, which results in a more complex near-field distribution that is mapped with PEEM. The experimental PEEM intensity map for +45° polarization [as sketched in Fig. 10.6d] shown in Fig. 10.6e gives rise to an asymmetric PEEM signal with the lower arm of the structure being brighter than the upper arm, again in good agreement with the simulated PEEM intensity map shown in Fig. 10.6f. Corresponding experimental and simulated PEEM signals for -45° excitation polarization show the upper arm brighter. The brightness difference in both arms is clear proof that the symmetric mode, although not directly observable in PEEM, is nevertheless excited and affects the measured PEEM signal by interference with the antisymmetric mode. However, those brightness differences between the two arms cannot be directly related to the directional propagation observed for local illumination in Figs. 10.6b,c. We note that the occurring near-field interference effects strongly depend on the relative phases of the plasmon waves in the structure. For slight differences in the geometry (e.g. changing the TWTL length by less than $\lambda_{\text{eff}}/2$), the behavior of upper and lower arm can be exchanged.

10.5 Conclusion

In conclusion, we have used normal incidence PEEM to study the imaging of propagating plasmons in a showcase plasmonic nanocircuit - our directional coupler introduced in Chap. 9. Despite the rather complex mechanisms involved in photoelectron generation, here the photemission yield is assumed to be proportional to the 4^{th} power of the electric field distribution in a plane midheight through the structure. Using this assumption we are able to compare simulated PEEM images to experiments which we find to be in excellent agreement. While both modes can be efficiently excited, only the antisymmetric mode is directly detectable with PEEM. For standing wave patterns resulting from pure modes we observe a doubling of the expected periodicity. This can be attributed to the interference of the guided localized plasmon with the broad plane wave excitation, which - for the correct polarization - penetrates into the TWTL gap. Finally, we study directional coupling of a plasmon mode superposition in the device. When considering the incoupling of light at all terminals of the structure and subsequent interference effects PEEM can offer unique and quantitative insights into the functionality of optical nanocircuitry opening the field for a widespread application of PEEM to integrated functional nano-optical structures.

Chapter 11

Prospects of plasmonic nanocircuitry

The recent advances in the field of plasmonic nanocircuitry, among others the results of the preceding chapters, pave the way for a future widespread application of plasmonic nanocircuitry. This chapter sheds light onto two of its most promising branches, i.e. spin-optical [Sec. 11.1] and quantum plasmonic nanocircuitry [Sec. 11.2]. The results of Sec. 11.2 have been published in [245].

11.1 Spin-optical nanocircuitry

The spin-orbit coupling, i.e. the interaction of a particle's intrinsic spin state with its motion state, is well known from quantum physics. A prominent manifestation of this phenomenon is the splitting of atomic energy levels due to the interaction between the spin of electrons and the magnetic field accompanying their orbiting around the nucleus. In semiconductors spin-dependent electron transport can be realized, establishing the field of spintronics with novel device technology [246–248]. There and in contrast to classical electronics the spin of electrons provides an additional degree of freedom as efficient storage and carrier of information besides the traditionally exploited electron charge.

However, the same limitations concerning bandwidth as for traditional electronics [see Chap. 1] also apply for spintronics. A transfer of its conceptual idea to photonics enables the processing of quantum information with bandwidths increased by orders of magnitude. Here, the spin angular momentum of light associated with the wave's circular polarization state takes the place of the electron's spin state. The emergence of a geometric phase, commonly termed Berry phase [249–251], acquired over the course of a cyclic path in the parameter space is closely related to spin-orbit interaction. It was demonstrated for closed loops in the polarization space [252] and in wound single mode optical fibers [253].

A broad range of novel effects and applications arises from exploiting the strongly enhanced and localized optical fields in plasmonics [254]. Chirality-dependent scattering and directed excitation of plasmons due to coupling between the helicity state of photons and their orbital angular momentum (e.g. the beam trajectory) can be

observed [255]. Spin-orbit phenomena at interfaces of the far-field and waveguides can be used for the sorting of photons with different helicity by the directed excitation of photonic [256, 257] or plasmonic [258–260] waveguide modes. The latter are subwavelength in size and intrinsically couple well with single emitters potentially allowing for quantum computing [260].

Polarization dependent photon fluxes were already reported in Chap. 9, however without exploiting circularly polarized photons. In the following, the full potential of spin-orbit interaction for plasmonic nanocircuitry is briefly demonstrated. Therefore, we design and optimize a plasmonic nano-device capable of sorting photons by their natural base, their chirality, and restoring the photons' initial polarization state after spatial sorting by means of numerical simulations. The device's operation relies on the two well-defined eigenmodes of a TWTL [as detailed in Sec. 5.2.2], which enable the complete characterization of the polarization state during the whole propagation. The representation of the plasmon polarization state in the device can be done via mapping of the photon polarization state onto plasmonic mode states as described via the equivalent Poincaré sphere [see Sec. 9.2].

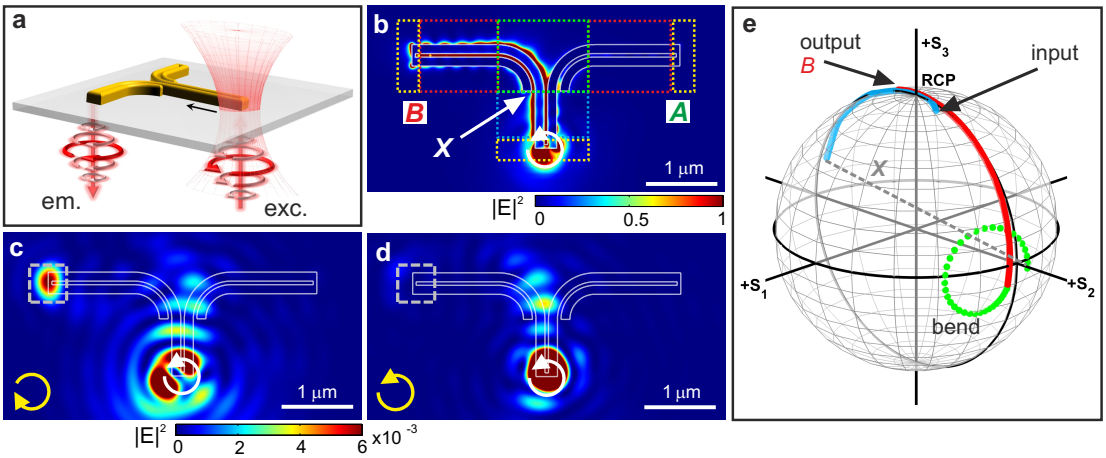

Figure 11.1: Nanoscale spin sorter. (a) Sketch of the investigated device. (b) Simulated steady-state near-field intensity distribution for excitation with right circular input polarization (white arrow) demonstrating routing to the left branch (output port B). (c,d) Corresponding far-field images with analyzer in detection path to filter (c) right and (d) left circularly polarized light emission (marked by yellow arrows). Excitation and emission detection are performed via an objective of NA = 1.4 at a wavelength $\lambda = 800\,\mathrm{nm}$. The gray squares ($500 \times 500\,\mathrm{nm}^2$ regions) indicate the integration areas for the emission intensities used to calculate the polarization contrast. (e) Polarization state along the device in the Poincaré sphere representation.

The proposed nanocircuit is sketched in Fig. 11.1a. Essentially, it can be divided into four types of elements [as marked in Fig. 11.1b]: interfacing elements between far-field photons and plasmonic modes (yellow), the propagation on linear TWTL segments (blue and red), the abrupt waveguide splitting (position X), and the TWTL

bending (green). It is noted that a short mode detector element (i.e. a 50 nm long bridge at the TWTL terminations short-circuiting the wires) forms the interfacing element due to the previously observed high in-/outcoupling efficiency of around 30% and its facilitated fabrication compared to the dipole antennas used in Chaps. 8 - 10. Upon excitation of the device by right circularly polarized light (as defined from the point of view of the source) the near-field intensity [Fig. 11.1b] is guided toward the left output port and is subsequently re-emitted into the far-field. The emission polarization is again circularly polarized, as evident from the simulated far-field images in Figs. 11.1c,d [for method see Sec. 4.4.2] taking an analyzer for circular polarization within the detection beam path into account. The circular excitation polarization state prepares an initial mode superposition, which in terms of the Poincaré sphere representation is situated close to one of its poles [Fig. 11.1e]. The further evolution of the polarization state along the linear TWTL segment is based on the birefringent and dichroic character of the mode propagation in TWTLs [as already addressed for the directional coupler in Chap. 9]. After acquiring a certain propagation phase, at the splitting position X the near-field mode superposition is overall asymmetrically shifted to the left (depending on the initial chirality state). At this position the polarization state discontinuously jumps to almost the opposite side of the Poincaré sphere. The subsequent bending of the TWTL converts the eigenmodes [as illustrated in Fig. 9.6] and manifests itself in a closed loop on the Poincaré sphere. Such closed loops are typically associated with a Berry phase, which might enable further applications for the presented device, e.g. in interferometric circuitry. Right after the bend the polarization state is shifted toward the antisymmetric mode's hemisphere. By a further birefringent and dichroic propagation along a TWTL segment of appropriate length the initial circular polarization state is recovered.

As a figure of merit for the switching capability of the device the spatial contrast sc, as introduced in Eq. (9.1), can be employed. The optimized device yields sc = -0.95, confirming an almost perfect spatial helicity sorting. Moreover, the preservation of the photons' helicity state is characterized by a second figure of merit defined in the style of the spatial contrast, namely the polarization contrast pc. It is obtained for the primary emission port by relating the energy E detected through an analyzer of same chirality to the total emitted energy of this port. In case of right circularly polarized excitation the polarization contrast of output port B is defined via

$$\mathrm{pc}(B) = \frac{E_{\circlearrowright}(B) - E_{\circlearrowleft}(B)}{E_{\circlearrowright}(B) + E_{\circlearrowleft}(B)}, \tag{11.1}$$

and takes a value of $\mathrm{pc}(B) = 0.87$. The emitted photons regain an exceptionally high degree of circular polarization and thus conserve their initial quantum information. Similarly, when exciting the structure with linear polarization along or perpendicular to the structure's symmetry axis (data not shown), both output ports emit circularly polarized light with identical intensity (i.e. $\mathrm{sc} = 0$) but opposing helicity. All simulation results have been reproduced in experiments with high precision (data not shown) yielding similar values for both spatial and polarization contrast.

11.2 Quantum plasmonic nanocircuity

Future technologies such as secure communication, quantum computation, quantum simulation, and quantum metrology are boosted by progress in quantum photonics. There, the pivotal challenge is the miniaturization of integrated circuit designs that combine single photon sources, linear optical components, and detectors on a single chip. Plasmonic nanocircuits are ideally suited for quantum photonics applications [261]. In this context, single photons can be emitted by colloidal nanocrystals and nitrogen vacancy centers in diamond nanocrystals [262, 263], or originate from nonlinear optical processes [63, 264]. However, the reported approaches suffer from different disadvantages and are hardly suited for scalable on-chip devices. The former suffer from bleaching, blinking, poor control of the orientation of the transition dipole moment, and often broadband emission, that is not easily excited electrically. The latter only yield low photon rates by requiring bulky crystals.

Self-assembled semiconductor quantum dots instead are stable and nonblinking single photon sources that are electrically drivable and have well-defined orientations of the transition dipole moments [265–267]. Integrating such emitters into dielectric on-chip devices by structuring the semiconductor material has been achieved [268, 269]. However, the coupling with surface plasmons is hampered by the high refractive index of the semiconductor host material, as the conventional way of bringing emitters in the vicinity of plasmonic structures [262, 263, 270–272] does not work. The solution for the integration of self-assembled semiconductor quantum dots as single-photon sources in plasmonic nanocircuits presented in the following employs releasing of the emitters from the bulk crystal and exploiting an indirect-coupling approach.

An SEM image of the proposed nanocircuit is given in Fig. 11.2a. The device is centered around a bar of AlGaAs heterostructure containing a GaAs quantum dot. This is placed on a SiO_2 substrate and gold wires are fabricated on both sides of the bar constituting an in-plane version of a hybrid waveguide [274]. Transformation of the hybrid into a plasmonic waveguide is achieved by tapering the semiconductor bar such that the gold wires finally form a TWTL. GaAs quantum dot emission is first efficiently coupled into the hybrid waveguide and afterwards again coupled with high throughput into surface plasmons propagating along the TWTL toward an optical antenna with high emission efficiency.

In raster-scanned confocal microscopy images upon excitation of the quantum dot in the AlGaAs bar with a stationary focus of a continuous-wave laser (532 nm wavelength) bright and stable emission at the position of both the quantum dot and the antenna on the right is observed [Fig. 11.2b]. This experimental result agrees with the simulated far-field image of Fig. 11.2c. Photoluminescence spectra taken from both emission spots exhibit exactly the same features in terms of the spectral position and width of the sharp lines and their relative intensities [Fig. 11.2d]. As these features are a fingerprint for each quantum dot, this spectral correlation confirms the quantum dot as the source of the antenna emission. The neutral exciton peaks (X) of both spectra have the same FWHM of 116 μeV, which is only slightly broadened compared to an

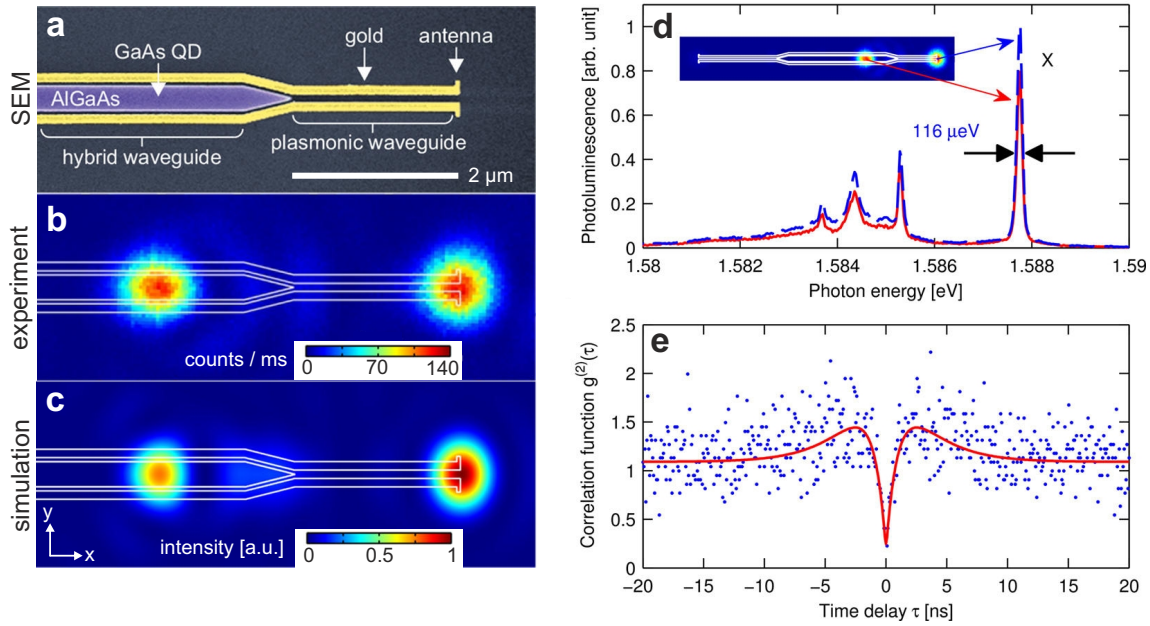

Figure 11.2: Single-plasmon nanocircuit driven by a self-assembled quantum dot. (a) SEM image of the fabricated structure (right part only). (b) Photoluminescence micrograph of the structure ($T = 10\,\mathrm{K}$). The quantum dot is excited by a stationary laser focus and the y-polarized emission is collected by raster-scanning a confocal detection focus. (c) Numerically simulated far-field image following the experimental structure and conditions closely. The excitation source is a pair of incoherent x- and y-polarized dipoles at the quantum dot position of panel (b), and only $|E_y|^2$ in the image plane is plotted. (d) Spectra collected at the position of the quantum dot (red solid line) and antenna at the right end of the structure (blue dashed line). (e) Measured second-order cross-correlation function $g^{(2)}(\tau)$ between the antenna and quantum dot (blue dots). The red line is a fit to model [273], taking the off-resonant excitation conditions into account. Figure modified from [245]. © 2017 American Chemical Society.

unprocessed quantum dot ($60\,\mu\mathrm{eV}$) due to the sample fabrication. Furthermore, the quantum statistics of the quantum dot emission is preserved by the device and truly single plasmons are launched, as obvious from the antibunching dip at time delay $\tau = 0$ in the measured second-order cross-correlation function $g^{(2)}(\tau)$ between the emission in the exciton line collected at the antenna and the quantum dot [Fig. 11.2e]. For additional in depth information the reader is referred to the full publication of this work [245].

In conclusion, these spectral and statistical properties make the introduced single-plasmon source suitable for quantum optical experiments. More complex plasmonic as well as photonic circuits can be developed on the basis of this approach, e.g. coupling of multiple quantum dots via plasmonic circuits to achieve photonic transistors [53]. Transitions of the quantum dot may be tuned into resonance electrically by applying voltages on the conducting gold wires. Moreover, electrical excitation of the

quantum dot [275, 276] and electrical detection of single plasmons [277, 278] can be implemented to make all-on-chip circuits. The present work shows that by making use of self-assembled quantum dots, quantum plasmonic circuits can also be built on semiconductor platforms, and it thus opens the way to integrate electronic, photonic, and plasmonic devices on one semiconductor chip for applications of quantum technologies.

Chapter 12

Summary & outlook

Modern information society possesses an insatiable hunger for an increasing amount of processed information per unit of time, i.e. higher and higher bit rates. The chase after ever smaller, faster, and more efficient electronic integrated circuits has enabled truly nanoelectronic circuits with feature sizes approaching 10 nm, but at the same time uncovered fundamental limitations in the achievable bit rates when processing data with electrons. In contrast, processing data with photons is incredibly fast and thus the method of choice in photonic circuits for digital communication. However, there the same miniaturization as in state-of-the-art nanoelectronic circuits is hampered by the fundamental law of diffraction. In quest of new chip-scale device technologies that can bridge the gap between nanoscale electronics and microscale photonics, plasmonics has evolved as a promising candidate, owing the intriguing properties of noble metals when interacting with visible light.

At the beginning of this thesis, the field of plasmonic nanocircuitry was still in its infancy. From a theoretical perspective, the power of electronic circuit design is based on the fact that complex circuitry can be created by arranging simple circuit elements into networks. In particular, the circuit properties can then be calculated using Kirchhoff's laws. However, due to the short wavelengths involved in plasmonic nanocircuitry the applicability of these laws cannot be taken for granted any more. In fact, their validity in plasmonic nanocircuitry was not yet answered satisfactorily, even though they would serve as valuable guidelines for the design of complex nanophotonic circuitry based on simple building blocks. This thesis tackles this issue by studying a junction of plasmonic TWTLs, which represents a fundamental building block of nanophotonic circuitry. A new phenomenological parameter relating the junction's geometrical parameters to the plasmon wavelength is identified, which allows to judge the degree of validity of Kirchhoff's laws. To illustrate the power of this approach a system composed of a TWTL and a nanoantenna as a load is investigated. By addition of a parallel stub designed according to Kirchhoff's laws maximum signal transfer to the nanoantenna is achieved.

From an experimental perspective and stimulated by potential applications for on-chip integrated optical signal guidance and processing, a variety of plasmon waveguide designs have already been prototyped. Experimental studies so far concentrated on single-mode operation in selected waveguide geometries and simple device functionality

almost exclusively in networks of chemically grown nanowires. The simultaneous use of multiple eigenmodes in specifically designed top-down fabricated nanocircuits has not yet been attempted. The scope of the present work is to bridge this gap by using numerical simulations for the design of functional plasmonic nanocircuits, which allow fundamental control of photon flow at the nanometer scale.

At first, the prejudice of plasmonics always being an inaccurate science is dispelled. Indeed, even the simple problem of plasmon transmission through a nanowire, which is of key importance for any functional device in the field of plasmonic nanocircuitry, has caused discussion in the literature. The reason for this lies mainly in the limited reproducibility of fabricated nanostructures. This thesis presents a systematic numerical study of monochromatic light transmission through gold nanowires of equal cross section but variable length. Propagation channels that were until now unnoticed but noticeably modulate the wire transmission signals are revealed. Quantitatively, this modulation can analytically be described by incorporating these additional channels into the usual Fabry-Pérot resonator model. Optical measurements of high quality structures produced from monocrystalline gold platelets by focused-ion beam milling show unprecedented agreement with only small remaining sources of uncertainty.

Thus, the use of numerical simulations for the deliberate design and analysis of functional plasmonic nanocircuits can safely be extended beyond the simple single-mode linear nanowires. As the logical next step, an increase in device complexity is obtained by engineering a nanodevice on the basis of TWTLs, which support two orthogonal eigenmodes. The proposed device allows the synthesis and in situ analysis of multimode plasmonic excitations. Preparation of deterministic eigenmode superpositions is simply achieved by proper positioning of a tightly focused laser beam with respect to the incoupling antenna attached to the TWTL and by adjusting its polarization. This controlled superposition and interference of multiple eigenmodes yields the possibility to tap new degrees of freedom to create advanced circuit functionality beyond single-mode interference, e.g. coherent control of the optical path taken by an excitation in the circuit. This is subsequently studied in a dedicated nanoscale directional coupler device.

In contrast to classical electronic circuits, where a symmetric bifurcation inevitably causes an equal splitting of any input current pulse toward the two output ports, a fundamentally different behavior can be induced in plasmonic circuitry by exploiting the existence of multiple eigenmodes and coherence - both not accessible in classical electronics. An intuitive and optimized design enables a switching between both output ports by simply varying the linear input polarization. By manipulating the input polarization of ultrashort pulses and pulse pairs open-loop ultrafast spatial and spatiotemporal coherent control of plasmon propagation is experimentally demonstrated representing a very intuitive classical analogue to quantum control in molecules.

In view of the ever increasing device complexity with simultaneously decreasing tolerance toward fabrication uncertainties, quantitative nano-imaging tools for accessing near-field distributions of optical nanocircuits are urgently needed. The capabilities of normal-incidence two-photon PEEM for this purpose are examined. Therefore, the pre-

viously introduced directional coupler is used as a showcase nanocircuit enabling the successful imaging of propagation, interference, and routing of multiple guided modes. Heuristically, the recorded photoemission yield can be modeled with high precision by considering the 4^{th} power of the numerically simulated electric near-field around the nanocircuit, paving the road for a future widespread application of normal-incidence PEEM.

The advances made in this work directly allow for a plethora of new and interesting devices, such as spin-optical nano devices and single-plasmon nanocircuits. The former uses the spin of photons as a carrier of information and might enable a variety of novel devices, just as spintronics did in electronics by using the intrinsic spin of electrons. The latter uses a self-assembled quantum dot that efficiently excites narrow-band single plasmons and demonstrates the feasibility of fully on-chip plasmonic nanocircuits for quantum optical applications. Therefore, the concept of plasmonic nanocircuitry has a bright future.

Zusammenfassung & Ausblick

Unsere moderne Informationsgesellschaft besitzt einen unersättlichen Hunger nach zunehmenden Bitraten, d.h. einer ständig größer werdenden Menge an zu verarbeitenden Informationen pro Zeiteinheit. Diese Jagd nach immer kleineren, schnelleren und effizienteren integrierten elektronischen Schaltkreisen hat zu wirklich nanoelektronischen Schaltungen mit Strukturgrößen um 10 Nanometer geführt. Gleichzeitig sind grundlegende Einschränkungen in den erreichbaren Bitraten bei der Datenverarbeitung mit Elektronen aufgedeckt worden. Im Gegensatz dazu erfolgt die Datenverarbeitung mit Photonen unglaublich schnell und ist somit die Methode der Wahl in photonischen Schaltkreisen zur digitalen Kommunikation. Allerdings verhindert das Beugungslimit der Photonik die gleiche Miniaturisierung wie bei modernsten nanoelektronischen Schaltkreisen. Auf der Suche nach neuen Technologien, die mit der Mikrochipherstellung kompatibel sind und die Lücke zwischen nanoskaliger Elektronik und mikroskaliger Photonik schließen können, hat sich die Plasmonik als vielversprechender Kandidat entwickelt. Dies ist den faszinierenden Eigenschaften von Edelmetallen bei der Wechselwirkung mit sichtbarem Licht zu verdanken.

Zu Beginn dieser Arbeit befand sich das Fachgebiet der plasmonischen Nanoschaltkreistechnik noch in den Kinderschuhen. Die Leistungsfähigkeit des Schaltungsentwurfs in der Elektronik basiert aus theoretischer Sicht darauf, dass komplexe Schaltkreise durch das Anordnen einfacher Schaltungselemente in Netzwerken erzeugt werden können. Insbesondere können deren Eigenschaften dann nach den Kirchhoffschen Regeln berechnet werden. Aufgrund der kurzen Plasmonenwellenlängen kann deren Anwendbarkeit in Nanoschaltkreisen jedoch nicht mehr als selbstverständlich angesehen werden und tatsächlich wurde ihre Gültigkeit auch noch nicht zufriedenstellend beantwortet, obwohl dies wertvolle Richtlinien für die Gestaltung komplexer nanophotonischer Schaltkreise aus einfachen Bausteinen liefern würde. Diese Arbeit untersucht eine Verzweigung plasmonischer Zweidrahtwellenleiter - einen grundlegenden Baustein vieler nanophotonischer Schaltungen. Hierbei lässt sich ein neuer phänomenologischer Parameter identifizieren, der die Geometrie der Verzweigung mit der Plasmonenwellenlänge in Beziehung setzt und es erlaubt, den Gültigkeitsgrad der Kirchhoffschen Regeln zu beurteilen. Zur Veranschaulichung der Stärke dieses Ansatzes wird daraufhin ein System bestehend aus einem Zweidrahtwellenleiter und einer Nanoantenne als Verbraucher untersucht. Durch die gezielte Parallelschaltung einer nach den Kirchhoffschen Regeln entworfenen Stichleitung kann die Signalübertragung an die Nanoantenne maximiert werden.

Motiviert durch mögliche Anwendungen zur integrierten optischen Signalführung und -verarbeitung auf Mikrochips wurden in Experimenten bereits vielfältige Prototypen von Plasmonenwellenleitern hergestellt. Bisher konzentrieren sich experimentelle Studien auf den Einmodenbetrieb in ausgewählten Wellenleitergeometrien und einfache Funktionalitäten fast ausschließlich in Netzwerken von chemisch gewachsenen Nanodrähten. Die gleichzeitige Verwendung mehrerer Eigenmoden in gezielt entworfenen und mittels Abwärtsstrukturierung gefertigten Nanoschaltkreisen wurde bisher noch nicht versucht. Das Ziel der vorliegenden Arbeit besteht darin, diese Lücke durch Einsatz numerischer Simulationen zu schließen und funktionelle plasmonische Nanoschaltkreise zu entwerfen, die eine Steuerung des Photonenflusses im Nanometerbereich ermöglichen.

Zuerst wird mit dem Vorurteil Plasmonik sei eine ungenaue Wissenschaft aufgeräumt. In der Tat löste sogar das einfache Problem der Plasmonenübertragung durch einen Nanodraht, was für jede Funktionseinheit auf dem Gebiet der plasmonischen Nanoschaltungen von zentraler Bedeutung ist, Diskussionen in der Literatur aus. Der Grund hierfür liegt insbesondere in der begrenzten Reproduzierbarkeit von gefertigten Nanostrukturen. Diese Arbeit stellt eine systematische numerische Studie der monochromatischen Lichttransmission durch Golddrähte mit gleichem Querschnitt aber variabler Länge dar. Bis jetzt unbemerkte Ausbreitungskanäle, die das Übertragungssignal aber spürbar modulieren, werden aufgedeckt. Analytisch und quantitativ korrekt kann diese Modulation durch den Einbau dieser zusätzlichen Kanäle in das übliche Fabry-Pérot-Resonatormodell beschrieben werden. Optische Messungen an hochwertigen Strukturen, die durch das Fräsen aus monokristallinen Goldplättchen mittels fokussierten Ionenstrahlen hergestellt werden, zeigen eine noch nie dagewesene Übereinstimmung mit nur geringen noch verbleibenden Unsicherheitsquellen.

Die Verwendung numerischer Simulationen für die gezielte Gestaltung und Analyse funktioneller plasmonischer Nanoschaltkreise kann somit auf sichere Weise über den einfachen Einmodenbetrieb linearer Drähte hinaus erweitert werden. Im logisch nächsten Schritt wird die Komplexität durch Konstruktion eines Nanoschaltkreises auf der Basis von Zweidrahtwellenleitern, die zwei orthogonale Eigenmoden unterstützen, erhöht. Die vorgeschlagene Vorrichtung ermöglicht die Synthese und In-situ-Analyse von plasmonischen Multimodenanregungen. Die Präparation deterministischer Überlagerungen dieser Eigenmoden wird in einfacher Weise mittels korrekter Positionierung eines fokussierten Laserstrahls und durch Einstellung von dessen Polarisation in Bezug auf die am Zweidrahtwellenleiterende angebrachte Einkopplungsantenne erreicht. Die mittels der gezielten Interferenz dieser Eigenmoden erschlossenen zusätzlichen Freiheitsgrade ermöglichen erweiterte Schaltungsfunktionalitäten jenseits von Einmodeninterferenz, z.B. die kohärente Steuerung des optischen Weges einer Anregung im Schaltkreis. Dies wird anschließend in einer dedizierten nanoskaligen Richtkopplerschaltung untersucht.

Im Gegensatz zu klassischen elektronischen Schaltkreisen, bei denen eine symmetrische Bifurkation zwangsläufig eine gleichmäßige Aufteilung eines Eingangsstromimpulses auf beide Ausgangsanschlüsse bewirkt, kann ein grundsätzlich unterschied-

liches Verhalten in plasmonischen Schaltkreisen induziert werden, indem die Existenz von mehreren Eigenmoden und Kohärenz ausgenutzt wird - beide nicht zugänglich in der klassischen Elektronik. Ein intuitives und optimiertes Design ermöglicht ein Umschalten zwischen beiden Ausgängen durch einfaches Variieren der linearen Eingangspolarisation. Durch Manipulation der Eingangspolarisation ultrakurzer Pulse und Pulspaare wird ultraschnelle räumliche und räumlich-zeitliche kohärente Steuerung der Plasmonenausbreitung experimentell demonstriert, was ein sehr intuitives klassisches Analogon zur Quantenkontrolle in Molekülen darstellt.

Angesichts der ständig wachsenden Komplexität plasmonischer Bauelemente bei gleichzeitig abnehmender Toleranz gegenüber Fertigungsungenauigkeiten werden dringend quantitative Verfahren zur Visualisierung der Nahfeldverteilungen von optischen Nanoschaltkreisen benötigt. Die Eignung von Zwei-Photonen Photoemissionselektronenmikroskopie unter senkrechtem Lichteinfall wird zu diesem Zweck untersucht. Hierzu wird der zuvor eingeführte Richtkoppler als Beispielstruktur verwendet, der die erfolgreiche Abbildung von Ausbreitung, Interferenz und Lenkung mehrerer geführter Eigenmoden ermöglicht. Heuristisch kann man die registrierte Photoemissionsausbeute mit hoher Präzision modellieren, indem man die vierte Potenz der simulierten elektrischen Nahfeldstärke um den Nanoschaltkreis betrachtet. Dies ebnet den Weg für eine zukünftig weit verbreitete Anwendung von Photoemissionselektronenmikroskopie unter senkrechtem Lichteinfall.

Der mit dieser Arbeit erzielte Fortschritt erlaubt direkt eine Fülle neuer und interessanter Anwendungen von spinoptischen bis quantenphotonischen Nanoschaltkreisen. Erstere nutzen den Spin von Photonen als Informationsträger und können eine Vielzahl neuartiger Funktionalitäten ermöglichen, genauso wie die Spintronik neue Anwendungsmöglichkeiten in der Elektronik durch die Verwendung des intrinsischen Elektronenspins schaffte. Letztere verwenden selbstorganisierte Quantenpunkte zur effizienten, schmalbandigen Anregung einzelner Plasmonen und demonstrieren die Machbarkeit von plasmonischen Nanoschaltkreisen auf einem Mikrochip für quantenoptische Anwendungen. Das Konzept der plasmonischen Nanoschaltkreise wird daher auch eine goldene Zukunft haben.

Appendix A

Analytical model for eigenmodes of cylindrical nanowires

Here, the analytical model for the eigenmode determination of chemically grown plasmonic nanowires with cylindrical cross section, as sketched in Fig. 5.1a, is reproduced [35, 48]. Their cylindrical shape directly evolves from rolling up a single metal-dielectric interface. The metal and dielectric domains are characterized by dielectric functions $\varepsilon_1(\omega)$ and ε_2, respectively.

Plasmonic modes of this cylindrical nanowire are obtained by solving the full vector wave equations (2.17) and (2.18) in cylindrical coordinates (r,φ,z), which is well documented in the literature [87, 136]. By expressing the fields $\mathbf{F}$ (both $\mathbf{E}$ and $\mathbf{H}$), that propagate along the nanowire, in separable form

$$\mathbf{F}(r,\varphi,z) = \hat{\mathbf{F}}(r,\varphi)\, e^{i(k_{\mathrm{SPP}} z - \omega t)}, \tag{A.1}$$

the wave equation reduces to Bessel's second order differential equation with solutions $\hat{\mathbf{F}}_{nm}$ for mode (n,m) of the form

$$\hat{\mathbf{F}}_{n,m}(r,\varphi) \propto e^{im\varphi} \begin{cases} J_n(\kappa_1 r) & \text{for} \quad 0 \le r < R \\ H_n^{(1)}(\kappa_2 r) & \text{for} \quad r > R. \end{cases} \tag{A.2}$$

Here, J_n and $H_n^{(1)}$ are cylindrical Bessel and Hankel functions of the first kind of order n that describe the radial dependence within and outside of the metal cylinder, respectively. These solutions ensure both a finite field value at the nanowire center as well as the proper behavior at infinity. The azimuthal dependence of the fields in each domain is described by a harmonic dependence of order m. The transverse wave vector κ_i in medium (domain) $i \in \{1,2\}$ is denoted by

$$\kappa_i = \sqrt{k_0^2 \varepsilon_i - \gamma^2}, \tag{A.3}$$

with the vacuum wave vector $k_0 = 2\pi/\lambda$.[1]

[1] It is important to note, that the square root with positive imaginary part must always be taken for κ_2 to satisfy the radiation condition at infinity [48].

The continuity of the tangential components of the E- and H-fields [cf. Sec. 2.4] at the domain boundary $r = R$ dictates a system of four homogeneous equations. Specifically, in case of the fundamental TM_0 mode, a single transcendental equation [135]

$$\frac{\varepsilon_1(\lambda)}{\kappa_1 R}\frac{J_1(\kappa_1 R)}{J_0(\kappa_1 R)} - \frac{\varepsilon_2(\lambda)}{\kappa_2 R}\frac{H_1^{(1)}(\kappa_2 R)}{H_0^{(1)}(\kappa_2 R)} = 0 \tag{A.4}$$

remains for the complex propagation constant k_{SPP}, from which λ_{eff} and l_{decay} can be deduced.

Appendix B

Analytical model of systems involving stubs and load antennas

B.1 Parallel connection of stub and infinite TWTL

In the following, we adopt well-known formulas from the RF regime, as can be found in standard textbooks [176], in order to describe plasmonic systems and validate Kirchhoff's analysis at optical frequencies. Let Z_{open} be the impedance of the open-circuit 'load'. A stub with length L can be seen as an open-circuit load attached to a segment of TWTL with length L, therefore its impedance Z_{stub} can be described via

$$Z_{stub} = Z_0 \frac{Z_{open} + Z_0 \tanh(kd)}{Z_0 + Z_{open} \tanh(kd)}. \tag{B.1}$$

If this stub is parallel-connected to an infinite TWTL, the total input impedance Z_{tot} measured at the stub connection position is the parallel of Z_{stub} and Z_0, i.e.

$$\frac{1}{Z_{tot}} = \frac{1}{Z_{stub}} + \frac{1}{Z_0}. \tag{B.2}$$

Therefore, the reflection coefficient Γ_{tot} at this reference plane can be evaluated as

$$\Gamma_{tot} = \frac{Z_{tot} - Z_0}{Z_{tot} + Z_0} \tag{B.3}$$

and is plotted as the blue solid lines in Fig. 6.4c.

B.2 Reflection coefficient of load antenna

If a TWTL with characteristic impedance Z_0 is loaded by an antenna with impedance Z_L attached to the TWTL termination [as shown in Fig. B.1a], the reflection coefficient Γ measured at the load position can be written as

$$\Gamma = \frac{Z_L - Z_0}{Z_L + Z_0}. \tag{B.4}$$

Numerically simulated values of Γ obtained by fitting the total intensity I_{total} of the standing wave patterns building up along the input TWTL [Fig. B.1b] with the analytical model described by Eq. (4.20) are displayed in Fig. B.1c for varying antenna length l_{ant}. The reflection amplitude can be strongly controlled by choosing a certain antenna length.

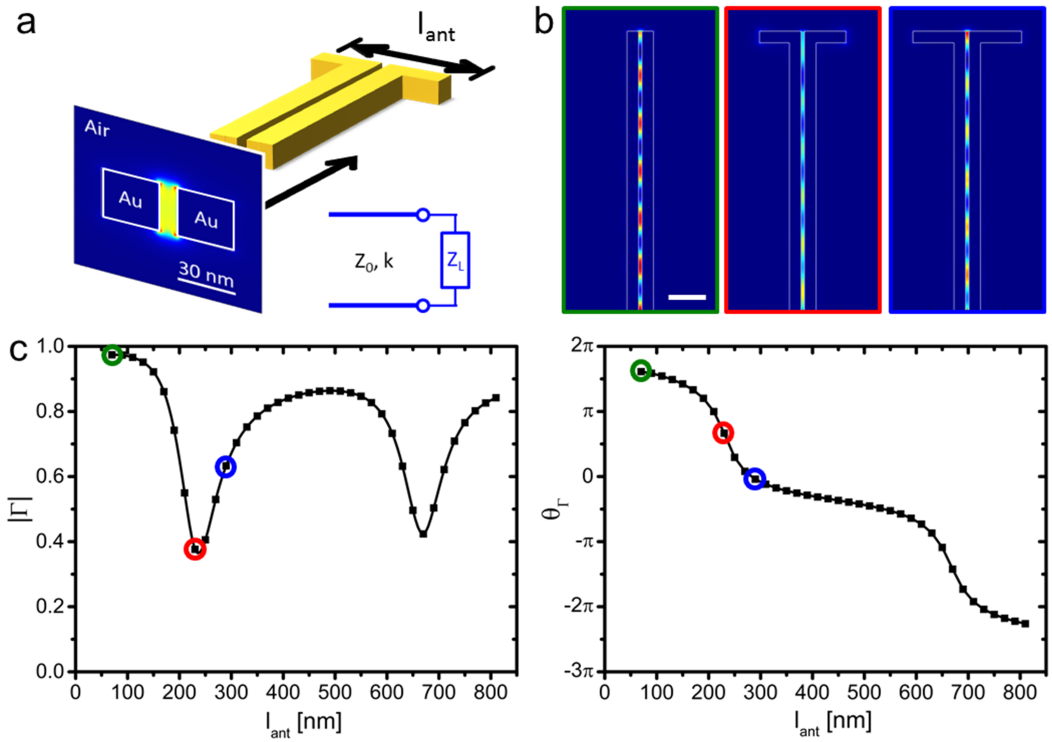

Figure B.1: Tuning the reflectivity by a load antenna's total length. (a) Sketch of the investigated system of a TWTL terminated by an optical antenna of length l_{ant}. The displayed antisymmetric mode is directly launched from the left and propagates along the nano-sized TWTL. Inset: Equivalent circuit representation of the system. (b) Simulated mode's standing wave pattern along a cut at midheight through the TWTL for an open end termination (left), antenna with $l_{\text{ant}} = 230\,\text{nm}$ (center), and antenna with $l_{\text{ant}} = 290\,\text{nm}$ (right). The scale bar in panel b is 100 nm. (c) Reflection amplitude (left) and phase (right) for varying antenna length. Figure taken from [157].

B.3 Parallel connection of stub and load antenna terminated finite TWTL

With the knowledge of the antenna impedance Z_L, it is further necessary to derive the input impedance Z_{in} of a system composed of an additional TWTL segment of length d terminated by such an antenna. In analogy to Eq. B.1, Z_{in} can be calculated as

$$Z_{in} = Z_0 \frac{Z_L + Z_0 \tanh(kd)}{Z_0 + Z_L \tanh(kd)}. \tag{B.5}$$

The parallel connection of Z_{in} and Z_{stub} gives the total input impedance Z'_{tot} of the system shown in Fig. 6.5a, which reads

$$\frac{1}{Z'_{tot}} = \frac{1}{Z_{stub}} + \frac{1}{Z_{in}}. \tag{B.6}$$

Again, the reflection coefficient Γ'_{tot} measured at the stub connection position can be evaluated as

$$\Gamma'_{tot} = \frac{Z'_{tot} - Z_0}{Z'_{tot} + Z_0}, \tag{B.7}$$

and is plotted for certain combinations of antenna length l_{ant}, stub distance d, and stub length L as the blue solid lines in Figs. 6.5b-c, B.2, B.3, and B.4.

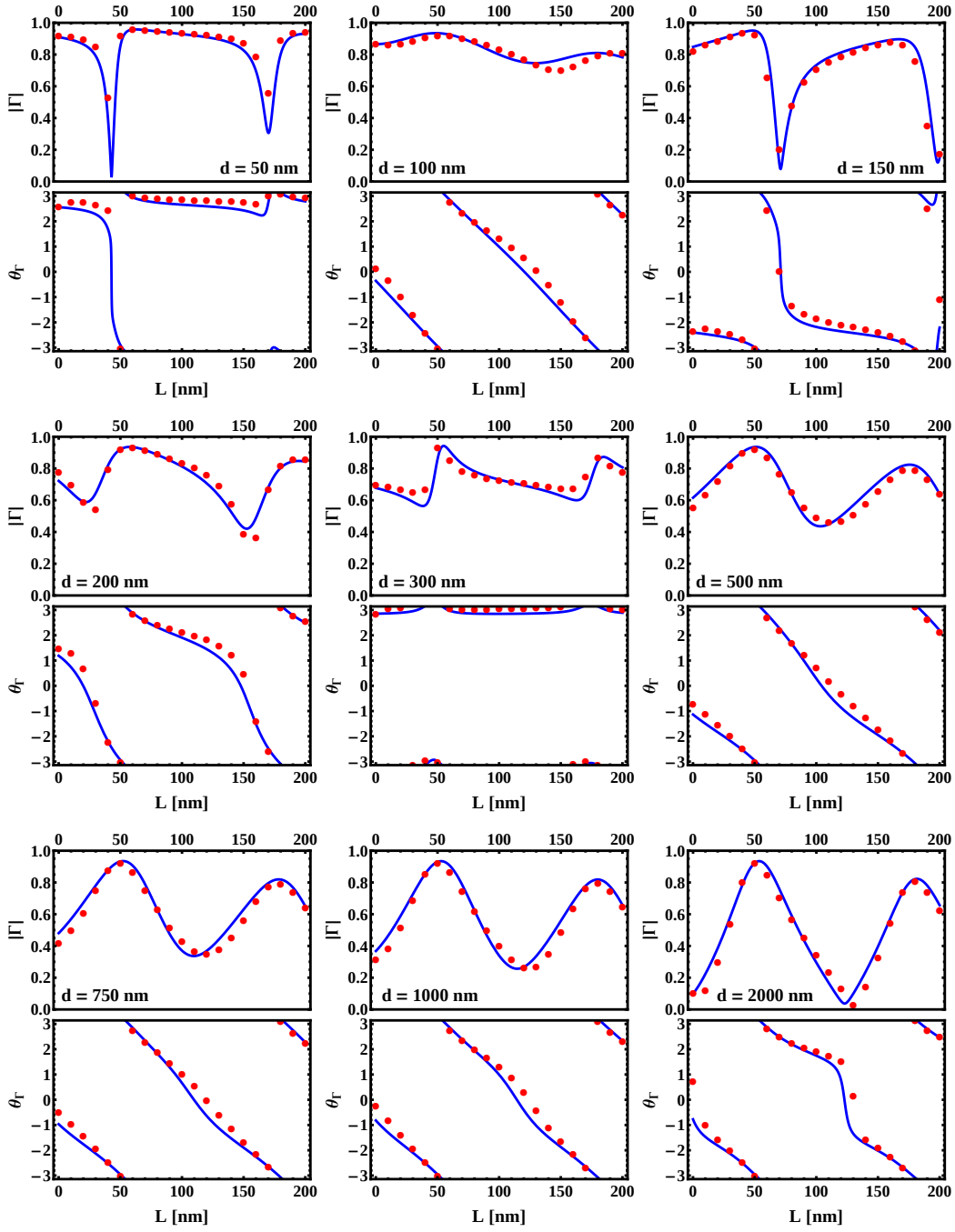

Figure B.2: Reflection amplitude and phase of a system composed of a finite stub of varying length L connected in parallel with an open end terminated TWTL of length $d = 50\,\text{nm}$, $100\,\text{nm}$, $150\,\text{nm}$, $200\,\text{nm}$, $300\,\text{nm}$, $500\,\text{nm}$, $750\,\text{nm}$, $1000\,\text{nm}$, and $2000\,\text{nm}$ (from top left to bottom right). The red dots are obtained by fitting of FDTD simulation data, while the blue solid lines are obtained by the analytical model.

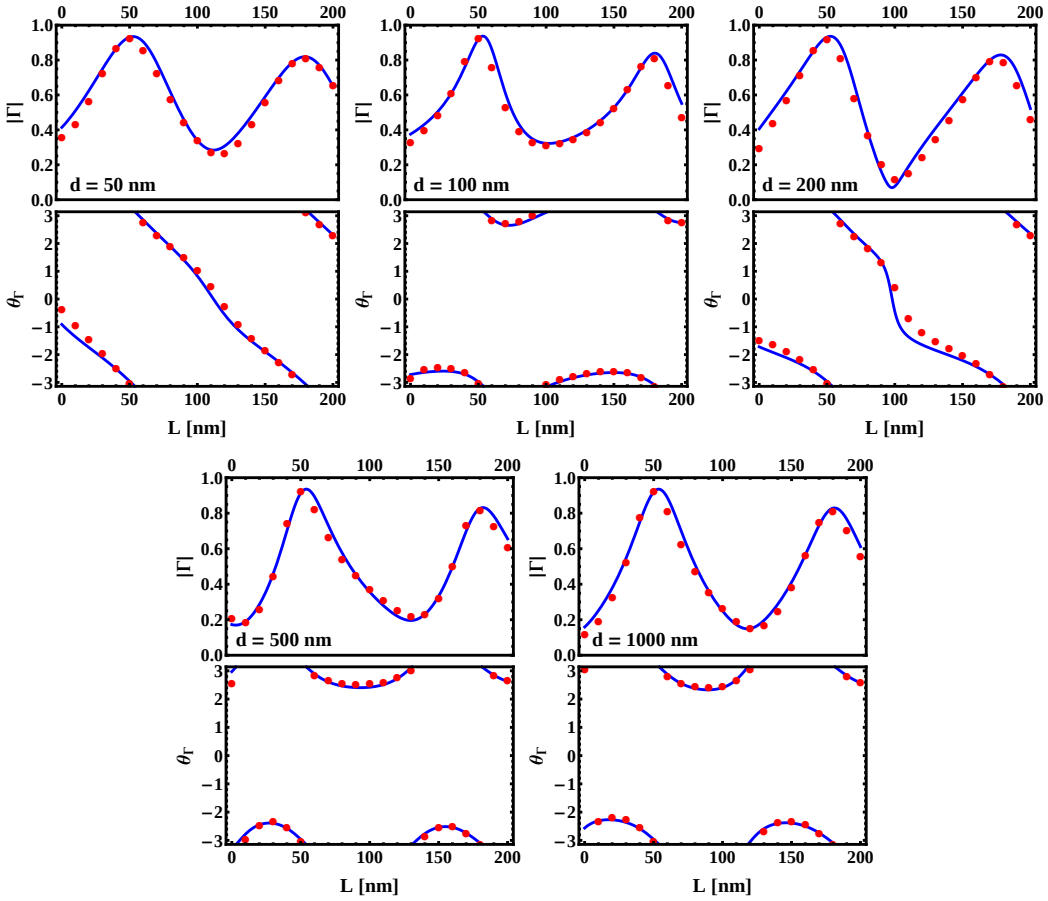

Figure B.3: Reflection amplitude and phase of a system composed of a finite stub of varying length L connected in parallel with a TWTL of length $d = 50\,\text{nm}$, $100\,\text{nm}$, $200\,\text{nm}$, $500\,\text{nm}$, and $1000\,\text{nm}$ (from top left to bottom right) terminated by a resonant antenna of length $l_{\text{ant}} = 230\,\text{nm}$. The red dots are obtained by fitting of FDTD simulation data, while the blue solid lines are obtained by the analytical model. Figure taken from [157].

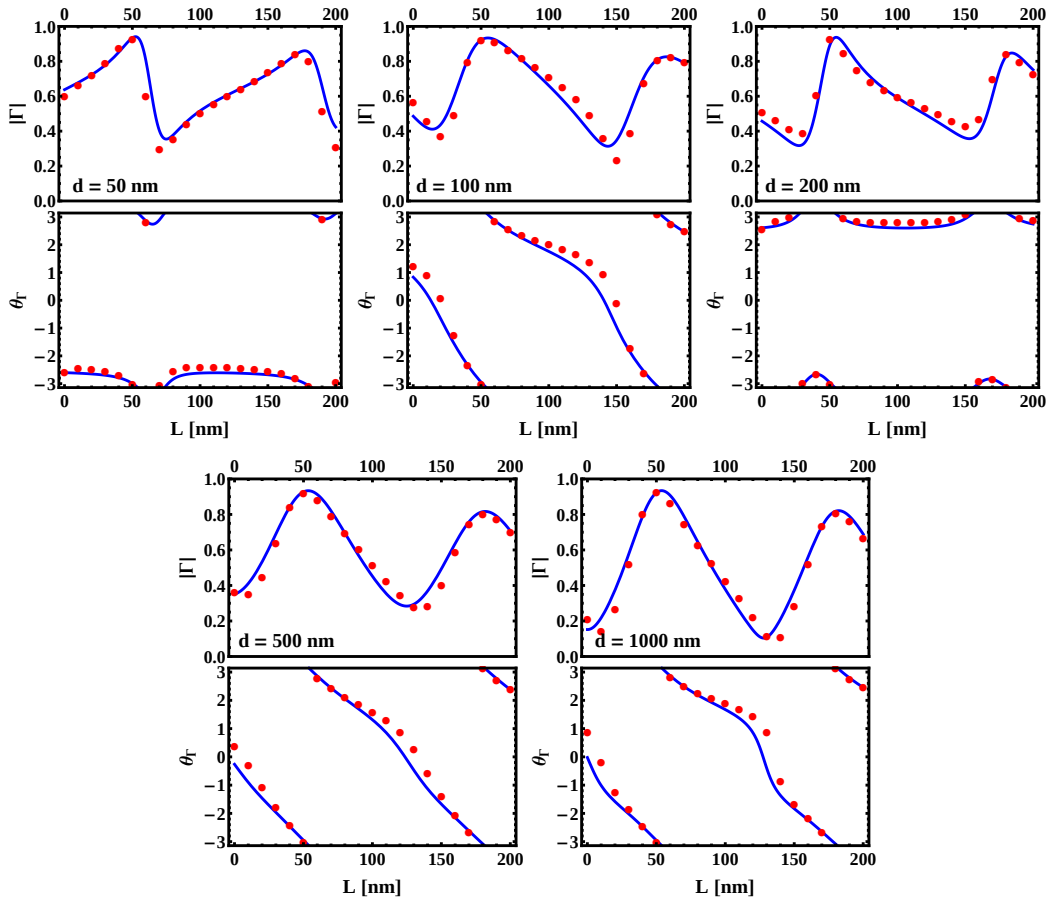

Figure B.4: Reflection amplitude and phase of a system composed of a finite stub of varying length L connected in parallel with a TWTL of length $d = 50\,\text{nm}$, $100\,\text{nm}$, $200\,\text{nm}$, $500\,\text{nm}$, and $1000\,\text{nm}$ (from top left to bottom right) terminated by a resonant antenna of length $l_{\text{ant}} = 290\,\text{nm}$. The red dots are obtained by fitting of FDTD simulation data, while the blue solid lines are obtained by the analytical model. Figure taken from [157].

Bibliography

[1] G. E. Moore. *Cramming More Components Onto Integrated Circuits.* Electronics **38** (8), pp. 114–117 (1965).

[2] G. E. Moore. *Progress in digital integrated electronics.* IEEE International Electron Devices Meeting, Tech. Digest pp. 11–13 (1975).

[3] R. Zia, J. A. Schuller, A. Chandran, and M. L. Brongersma. *Plasmonics: the next chip-scale technology.* Mater. Today **9** (7), pp. 20–27 (2006).

[4] K. Banerjee, A. Mehrotra, A. Sangiovanni-Vincentelli, and C. Hu. *On thermal effects in deep sub-micron VLSI interconnects.* In *Proceedings of the 36th annual ACM/IEEE Design Automation Conference*, pp. 885–891 (1999).

[5] T.-Y. Chiang, B. Shieh, and K. C. Saraswat. *Impact of Joule Heating on Deep Sub-Micron Cu/low-k Interconnects.* IEEE Symp. VLSI Circuits, Dig. Tech. Papers pp. 38–39 (2002).

[6] D. A. B. Miller. *Rationale and challenges for optical interconnects to electronic chips.* Proc. IEEE **88** (6), pp. 728–749 (2000).

[7] D. A. B. Miller and H. M. Ozaktas. *Limit to the bit-rate capacity of electrical interconnects from the aspect ratio of the system architecture.* J. Parallel Distrib. Comput. **41** (1), pp. 42–52 (1997).

[8] J. W. Goodman, F. J. Leonberger, S.-Y. Kung, and R. A. Athale. *Optical interconnections for VLSI systems.* Proc. IEEE **72** (7), pp. 850–866 (1984).

[9] D. A. B. Miller. *Physical Reasons for Optical Interconnection.* Int. J. Optoelectronics **11** (3), pp. 155–168 (1997).

[10] D. A. B. Miller. *Optical interconnects to silicon.* IEEE J. Sel. Top. Quantum Electron. **6** (6), pp. 1312–1317 (2000).

[11] W. L. Barnes, A. Dereux, and T. W. Ebbesen. *Surface plasmon subwavelength optics.* Nature **424** (6950), pp. 824–830 (2003).

[12] P. Mühlschlegel, H.-J. Eisler, O. J. F. Martin, B. Hecht, and D. W. Pohl. *Resonant optical antennas.* Science **308** (5728), pp. 1607–1609 (2005).

[13] J. A. Schuller, E. S. Barnard, W. Cai, Y. C. Jun, J. S. White, and M. L. Brongersma. *Plasmonics for extreme light concentration and manipulation.* Nat. Mater. **9** (3), pp. 193–204 (2010).

[14] S. Lal, S. Link, and N. J. Halas. *Nano-optics from sensing to waveguiding.* Nat. Photonics **1** (11), pp. 641–648 (2007).

[15] J. N. Anker, W. P. Hall, O. Lyandres, N. C. Shah, J. Zhao, and R. P. Van Duyne. *Biosensing with plasmonic nanosensors.* Nat. Mater. **7** (6), pp. 442–453 (2008).

[16] N. Liu, M. Mesch, T. Weiss, M. Hentschel, and H. Giessen. *Infrared Perfect Absorber and Its Application As Plasmonic Sensor.* Nano Lett. **10** (7), pp. 2342–2348 (2010).

[17] M. Mesch, B. Metzger, M. Hentschel, and H. Giessen. *Nonlinear Plasmonic Sensing.* Nano Lett. **16** (5), pp. 3155–3159 (2016).

[18] A. Kinkhabwala, Z. Yu, S. Fan, Y. Avlasevich, K. Müllen, and W. E. Moerner. *Large single-molecule fluorescence enhancements produced by a bowtie nanoantenna.* Nat. Photonics **3** (11), pp. 654–657 (2009).

[19] R. Zhang, Y. Zhang, Z. C. Dong, S. Jiang, C. Zhang, L. G. Chen, L. Zhang, Y. Liao, J. Aizpurua, Y. Luo, J. L. Yang, and J. G. Hou. *Chemical mapping of a single molecule by plasmon-enhanced Raman scattering.* Nature **498** (7452), pp. 82–86 (2013).

[20] A. B. Taylor and P. Zijlstra. *Single-Molecule Plasmon Sensing: Current Status and Future Prospects.* ACS Sensors **2** (8), pp. 1103–1122 (2017).

[21] M. A. Noginov, G. Zhu, A. M. Belgrave, R. Bakker, V. M. Shalaev, E. E. Narimanov, S. Stout, E. Herz, T. Suteewong, and U. Wiesner. *Demonstration of a spaser-based nanolaser.* Nature **460** (7259), pp. 1110–1112 (2009).

[22] R. F. Oulton, V. J. Sorger, T. Zentgraf, R.-M. Ma, C. Gladden, L. Dai, G. Bartal, and X. Zhang. *Plasmon lasers at deep subwavelength scale.* Nature **461** (7264), pp. 629–632 (2009).

[23] M. Sivis, M. Duwe, B. Abel, and C. Ropers. *Extreme-ultraviolet light generation in plasmonic nanostructures.* Nat. Phys. **9** (5), pp. 304–309 (2013).

[24] H. A. Atwater and A. Polman. *Plasmonics for improved photovoltaic devices.* Nat. Mater. **9** (3), pp. 205–213 (2010).

[25] S. Linic, P. Christopher, and D. B. Ingram. *Plasmonic-metal nanostructures for efficient conversion of solar to chemical energy.* Nat. Mater. **10** (12), pp. 911–921 (2011).

[26] M. Quinten, A. Leitner, J. R. Krenn, and F. R. Aussenegg. *Electromagnetic energy transport via linear chains of silver nanoparticles.* Opt. Lett. **23** (17), pp. 1331–1333 (1998).

[27] J. R. Krenn, A. Dereux, J. C. Weeber, E. Bourillot, Y. Lacroute, J. P. Goudonnet, G. Schider, W. Gotschy, A. Leitner, F. R. Aussenegg, and others. *Squeezing the optical near-field zone by plasmon coupling of metallic nanoparticles.* Phys. Rev. Lett. **82** (12), pp. 2590–2593 (1999).

[28] M. L. Brongersma, J. W. Hartman, and H. A. Atwater. *Electromagnetic energy transfer and switching in nanoparticle chain arrays below the diffraction limit.* Phys. Rev. B **62** (24), pp. R16356–R16359 (2000).

[29] S. A. Maier, P. G. Kik, H. A. Atwater, S. Meltzer, E. Harel, B. E. Koel, and A. A. Requicha. *Local detection of electromagnetic energy transport below the diffraction limit in metal nanoparticle plasmon waveguides.* Nat. Mater. **2** (4), pp. 229–232 (2003).

[30] S. I. Bozhevolnyi, J. Erland, K. Leosson, P. M. W. Skovgaard, and J. M. Hvam. *Waveguiding in Surface Plasmon Polariton Band Gap Structures.* Phys. Rev. Lett. **86** (14), pp. 3008–3011 (2001).

[31] I. V. Novikov and A. A. Maradudin. *Channel polaritons.* Phys. Rev. B **66** (3), p. 035403 (2002).

[32] S. I. Bozhevolnyi, V. S. Volkov, E. Devaux, and T. W. Ebbesen. *Channel Plasmon-Polariton Guiding by Subwavelength Metal Grooves.* Phys. Rev. Lett. **95** (4), p. 046802 (2005).

[33] S. I. Bozhevolnyi, V. S. Volkov, E. Devaux, J.-Y. Laluet, and T. W. Ebbesen. *Channel plasmon subwavelength waveguide components including interferometers and ring resonators.* Nature **440** (7083), pp. 508–511 (2006).

[34] E. Moreno, S. G. Rodrigo, S. I. Bozhevolnyi, L. Martín-Moreno, and F. J. García-Vidal. *Guiding and Focusing of Electromagnetic Fields with Wedge Plasmon Polaritons.* Phys. Rev. Lett. **100** (2), p. 023901 (2008).

[35] J. Takahara, S. Yamagishi, H. Taki, A. Morimoto, and T. Kobayashi. *Guiding of a one-dimensional optical beam with nanometer diameter.* Opt. Lett. **22** (7), pp. 475–477 (1997).

[36] J.-C. Weeber, A. Dereux, C. Girard, J. R. Krenn, and J.-P. Goudonnet. *Plasmon polaritons of metallic nanowires for controlling submicron propagation of light.* Phys. Rev. B **60** (12), pp. 9061–9068 (1999).

[37] P. Berini. *Plasmon-polariton waves guided by thin lossy metal films of finite width: Bound modes of symmetric structures.* Phys. Rev. B **61** (15), pp. 10484–10503 (2000).

[38] P. Berini. *Plasmon-polariton waves guided by thin lossy metal films of finite width: Bound modes of asymmetric structures.* Phys. Rev. B **63** (12), p. 125417 (2001).

[39] J. R. Krenn, B. Lamprecht, H. Ditlbacher, G. Schider, M. Salerno, A. Leitner, and F. R. Aussenegg. *Non–diffraction-limited light transport by gold nanowires.* Europhys. Lett. **60** (5), p. 663 (2002).

[40] K. Tanaka and M. Tanaka. *Simulations of nanometric optical circuits based on surface plasmon polariton gap waveguide.* Appl. Phys. Lett. **82** (8), pp. 1158–1160 (2003).

[41] F. Kusunoki, T. Yotsuya, J. Takahara, and T. Kobayashi. *Propagation properties of guided waves in index-guided two-dimensional optical waveguides.* Appl. Phys. Lett. **86** (21), p. 211101 (2005).

[42] G. Veronis and S. Fan. *Guided subwavelength plasmonic mode supported by a slot in a thin metal film.* Opt. Lett. **30** (24), pp. 3359–3361 (2005).

[43] L. Liu, Z. Han, and S. He. *Novel surface plasmon waveguide for high integration.* Opt. Express **13** (17), pp. 6645–6650 (2005).

[44] D. F. P. Pile, T. Ogawa, D. K. Gramotnev, Y. Matsuzaki, K. C. Vernon, K. Yamaguchi, T. Okamoto, M. Haraguchi, and M. Fukui. *Two-dimensionally localized modes of a nanoscale gap plasmon waveguide.* Appl. Phys. Lett. **87** (26), p. 261114 (2005).

[45] J. A. Dionne, H. J. Lezec, and H. A. Atwater. *Highly Confined Photon Transport in Subwavelength Metallic Slot Waveguides.* Nano Lett. **6** (9), pp. 1928–1932 (2006).

[46] L. Chen, J. Shakya, and M. Lipson. *Subwavelength confinement in an integrated metal slot waveguide on silicon.* Opt. Lett. **31** (14), pp. 2133–2135 (2006).

[47] A. Manjavacas and F. J. García de Abajo. *Robust Plasmon Waveguides in Strongly Interacting Nanowire Arrays.* Nano Lett. **9** (4), pp. 1285–1289 (2009).

[48] L. Novotny and C. Hafner. *Light propagation in a cylindrical waveguide with a complex, metallic, dielectric function.* Phys. Rev. E **50** (5), pp. 4094–4106 (1994).

[49] R. M. Dickson and L. A. Lyon. *Unidirectional Plasmon Propagation in Metallic Nanowires.* J. Phys. Chem. B **104** (26), pp. 6095–6098 (2000).

[50] A. W. Sanders, D. A. Routenberg, B. J. Wiley, Y. Xia, E. R. Dufresne, and M. A. Reed. *Observation of Plasmon Propagation, Redirection, and Fan-Out in Silver Nanowires.* Nano Lett. **6** (8), pp. 1822–1826 (2006).

[51] Y. Huang, Y. Fang, Z. Zhang, L. Zhu, and M. Sun. *Nanowire-supported plasmonic waveguide for remote excitation of surface-enhanced Raman scattering.* Light Sci. Appl. **3** (8), p. e199 (2014).

[52] J. A. Hutchison, S. P. Centeno, H. Odaka, H. Fukumura, J. Hofkens, and H. Uji-i. *Subdiffraction Limited, Remote Excitation of Surface Enhanced Raman Scattering.* Nano Lett. **9** (3), pp. 995–1001 (2009).

[53] D. E. Chang, A. S. Sørensen, E. A. Demler, and M. D. Lukin. *A single-photon transistor using nanoscale surface plasmons.* Nat. Phys. **3** (11), pp. 807–812 (2007).

[54] M. W. Knight, N. K. Grady, R. Bardhan, F. Hao, P. Nordlander, and N. J. Halas. *Nanoparticle-Mediated Coupling of Light into a Nanowire.* Nano Lett. **7** (8), pp. 2346–2350 (2007).

[55] Y. Fu, X. Hu, C. Lu, S. Yue, H. Yang, and Q. Gong. *All-Optical Logic Gates Based on Nanoscale Plasmonic Slot Waveguides.* Nano Lett. **12** (11), pp. 5784–5790 (2012).

[56] H. Wei, Z. Wang, X. Tian, M. Käll, and H. Xu. *Cascaded logic gates in nanophotonic plasmon networks.* Nat. Commun. **2**, p. 387 (2011).

[57] S. Raza, M. Esfandyarpour, A. L. Koh, N. A. Mortensen, M. L. Brongersma, and S. I. Bozhevolnyi. *Electron energy-loss spectroscopy of branched gap plasmon resonators.* Nat. Commun. **7**, p. 13790 (2016).

[58] Y. Fang and M. Sun. *Nanoplasmonic waveguides: towards applications in integrated nanophotonic circuits.* Light Sci. Appl. **4** (6), p. e294 (2015).

[59] D. E. Chang, A. S. Sørensen, P. R. Hemmer, and M. D. Lukin. *Quantum Optics with Surface Plasmons.* Phys. Rev. Lett. **97** (5), p. 053002 (2006).

[60] A. V. Akimov, A. Mukherjee, C. L. Yu, D. E. Chang, A. S. Zibrov, P. R. Hemmer, H. Park, and M. D. Lukin. *Generation of single optical plasmons in metallic nanowires coupled to quantum dots.* Nature **450** (7168), pp. 402–406 (2007).

[61] E. Bermúdez-Ureña, C. Gonzalez-Ballestero, M. Geiselmann, R. Marty, I. P. Radko, T. Holmgaard, Y. Alaverdyan, E. Moreno, F. J. García-Vidal, S. I. Bozhevolnyi, and R. Quidant. *Coupling of individual quantum emitters to channel plasmons.* Nat. Commun. **6**, p. 7883 (2015).

[62] D. Martín-Cano, L. Martín-Moreno, F. J. García-Vidal, and E. Moreno. *Resonance Energy Transfer and Superradiance Mediated by Plasmonic Nanowaveguides.* Nano Lett. **10** (8), pp. 3129–3134 (2010).

[63] R. W. Heeres, L. P. Kouwenhoven, and V. Zwiller. *Quantum interference in plasmonic circuits.* Nat. Nanotechnol. **8** (10), pp. 719–722 (2013).

[64] J.-S. Huang, T. Feichtner, P. Biagioni, and B. Hecht. *Impedance Matching and Emission Properties of Nanoantennas in an Optical Nanocircuit.* Nano Lett. **9** (5), pp. 1897–1902 (2009).

[65] L. Novotny and N. van Hulst. *Antennas for light.* Nat. Photonics **5** (2), pp. 83–90 (2011).

[66] P. Biagioni, J.-S. Huang, and B. Hecht. *Nanoantennas for visible and infrared radiation.* Rep. Prog. Phys. **75** (2), p. 024402 (2012).

[67] P. M. Krenz, R. L. Olmon, B. A. Lail, M. B. Raschke, and G. D. Boreman. *Near-field measurement of infrared coplanar strip transmission line attenuation and propagation constants.* Opt. Express **18** (21), pp. 21678–21686 (2010).

[68] M. Schnell, P. Alonso-González, L. Arzubiaga, F. Casanova, L. E. Hueso, A. Chuvilin, and R. Hillenbrand. *Nanofocusing of mid-infrared energy with tapered transmission lines.* Nat. Photonics **5** (5), pp. 283–287 (2011).

[69] Y. Fang, Z. Li, Y. Huang, S. Zhang, P. Nordlander, N. J. Halas, and H. Xu. *Branched Silver Nanowires as Controllable Plasmon Routers.* Nano Lett. **10** (5), pp. 1950–1954 (2010).

[70] Z. Li, S. Zhang, N. J. Halas, P. Nordlander, and H. Xu. *Coherent Modulation of Propagating Plasmons in Silver-Nanowire-Based Structures.* Small **7** (5), pp. 593–596 (2011).

[71] H. Wei, Z. Li, X. Tian, Z. Wang, F. Cong, N. Liu, S. Zhang, P. Nordlander, N. J. Halas, and H. Xu. *Quantum Dot-Based Local Field Imaging Reveals Plasmon-Based Interferometric Logic in Silver Nanowire Networks.* Nano Lett. **11** (2), pp. 471–475 (2011).

[72] D. Singh, M. Raghuwanshi, and G. V. P. Kumar. *Propagation of light in serially coupled plasmonic nanowire dimer: Geometry dependence and polarization control.* Appl. Phys. Lett. **101** (11), p. 111111 (2012).

[73] H. Wei and H. Xu. *Controlling surface plasmon interference in branched silver nanowire structures.* Nanoscale **4** (22), pp. 7149–7154 (2012).

[74] R. Könenkamp, R. C. Word, J. P. S. Fitzgerald, A. Nadarajah, and S. D. Saliba. *Controlled spatial switching and routing of surface plasmons in designed single-crystalline gold nanostructures.* Appl. Phys. Lett. **101** (14), p. 141114 (2012).

[75] E. Ozbay. *Plasmonics: Merging Photonics and Electronics at Nanoscale Dimensions.* Science **311** (5758), pp. 189–193 (2006).

[76] D. K. Gramotnev and S. I. Bozhevolnyi. *Plasmonics beyond the diffraction limit.* Nat. Photonics **4** (2), pp. 83–91 (2010).

[77] M. I. Stockman, S. V. Faleev, and D. J. Bergman. *Coherent Control of Femtosecond Energy Localization in Nanosystems.* Phys. Rev. Lett. **88** (6), p. 067402 (2002).

[78] M. Sukharev and T. Seideman. *Phase and Polarization Control as a Route to Plasmonic Nanodevices.* Nano Lett. **6** (4), pp. 715–719 (2006).

[79] P. Tuchscherer, C. Rewitz, D. V. Voronine, F. J. García de Abajo, W. Pfeiffer, and T. Brixner. *Analytic coherent control of plasmon propagation in nanostructures.* Opt. Express **17** (16), pp. 14235–14259 (2009).

[80] G. Razinskas, D. Kilbane, P. Melchior, P. Geisler, E. Krauss, S. Mathias, B. Hecht, and M. Aeschlimann. *Normal-Incidence PEEM Imaging of Propagating Modes in a Plasmonic Nanocircuit.* Nano Lett. **16** (11), pp. 6832–6837 (2016).

[81] A. Einstein. *Maxwell's influence on the development of the conception of physical reality.* In *James Clerk Maxwell: A Commemoration Volume.* Cambridge University Press (1931).

[82] M. Planck. *Über irreversible Strahlungsvorgänge.* Ann. Phys. **306** (1), pp. 69–122 (1900).

[83] A. Einstein. *Zur Elektrodynamik bewegter Körper.* Ann. Phys. **322** (10), pp. 891–921 (1905).

[84] J. D. Jackson. *Classical Electrodynamics.* John Wiley & Sons, New York, 3rd edition (1998).

[85] L. Novotny and B. Hecht. *Principles of Nano-Optics.* Cambridge University Press, Cambridge, 2nd edition (2012).

[86] J. C. Maxwell. *A Dynamical Theory of the Electromagnetic Field.* Phil. Trans. R. Soc. Lond. **155**, pp. 459–512 (1865).

[87] J. A. Stratton. *Electromagnetic Theory.* McGraw-Hill, New York (1941).

[88] J.-S. Huang, V. Callegari, P. Geisler, C. Brüning, J. Kern, J. C. Prangsma, X. Wu, T. Feichtner, J. Ziegler, P. Weinmann, M. Kamp, A. Forchel, P. Biagioni, U. Sennhauser, and B. Hecht. *Atomically flat single-crystalline gold nanostructures for plasmonic nanocircuitry.* Nat. Commun. **1**, p. 150 (2010).

[89] X. Wu, R. Kullock, E. Krauss, and B. Hecht. *Single-crystalline gold microplates grown on substrates by solution-phase synthesis.* Cryst. Res. Technol. **50** (8), pp. 595–602 (2015).

[90] R. Esteban, A. G. Borisov, P. Nordlander, and J. Aizpurua. *Bridging quantum and classical plasmonics with a quantum-corrected model.* Nat. Commun. **3**, p. 825 (2012).

[91] M. S. Tame, K. R. McEnery, Ş. K. Özdemir, J. Lee, S. A. Maier, and M. S. Kim. *Quantum plasmonics.* Nat. Phys. **9** (6), pp. 329–340 (2013).

[92] J. A. Scholl, A. L. Koh, and J. A. Dionne. *Quantum plasmon resonances of individual metallic nanoparticles.* Nature **483** (7390), pp. 421–427 (2012).

[93] J. Zuloaga, E. Prodan, and P. Nordlander. *Quantum Description of the Plasmon Resonances of a Nanoparticle Dimer.* Nano Lett. **9** (2), pp. 887–891 (2009).

[94] H. Duan, A. I. Fernández-Domínguez, M. Bosman, S. A. Maier, and J. K. W. Yang. *Nanoplasmonics: Classical down to the Nanometer Scale.* Nano Lett. **12** (3), pp. 1683–1689 (2012).

[95] K. J. Savage, M. M. Hawkeye, R. Esteban, A. G. Borisov, J. Aizpurua, and J. J. Baumberg. *Revealing the quantum regime in tunnelling plasmonics.* Nature **491** (7425), pp. 574–577 (2012).

[96] P. B. Johnson and R. W. Christy. *Optical Constants of the Noble Metals.* Phys. Rev. B **6** (12), pp. 4370–4379 (1972).

[97] P. G. Etchegoin, E. C. Le Ru, and M. Meyer. *An analytic model for the optical properties of gold.* J. Chem. Phys. **125** (16), p. 164705 (2006).

[98] A. Vial, A.-S. Grimault, D. Macías, D. Barchiesi, and M. L. de la Chapelle. *Improved analytical fit of gold dispersion: Application to the modeling of extinction spectra with a finite-difference time-domain method.* Phys. Rev. B **71** (8), p. 085416 (2005).

[99] P. G. Etchegoin, E. C. Le Ru, and M. Meyer. *Erratum: "An analytic model for the optical properties of gold".* J. Chem. Phys. **127** (18), p. 189901 (2007).

[100] H. Raether. *Surface Plasmons on Smooth and Rough Surfaces and on Gratings.* Springer, Berlin (1988).

[101] A. Otto. *Excitation of nonradiative surface plasma waves in silver by the method of frustrated total reflection.* Z. Phys. **216** (4), pp. 398–410 (1968).

[102] E. Kretschmann. *Die Bestimmung optischer Konstanten von Metallen durch Anregung von Oberflächenplasmaschwingungen.* Z. Phys. A **241** (4), pp. 313–324 (1971).

[103] A. Bouhelier and G. P. Wiederrecht. *Excitation of broadband surface plasmon polaritons: Plasmonic continuum spectroscopy.* Phys. Rev. B **71** (19), p. 195406 (2005).

[104] E. Hecht. *Optics.* Addison-Wesley, San Francisco, 4th edition (2002).

[105] R. Zia, M. D. Selker, P. B. Catrysse, and M. L. Brongersma. *Geometries and materials for subwavelength surface plasmon modes.* J. Opt. Soc. Am. A **21** (12), pp. 2442–2446 (2004).

[106] E. N. Economou. *Surface Plasmons in Thin Films.* Phys. Rev. **182** (2), pp. 539–554 (1969).

[107] J. J. Burke, G. I. Stegeman, and T. Tamir. *Surface-polariton-like waves guided by thin, lossy metal films.* Phys. Rev. B **33** (8), pp. 5186–5201 (1986).

[108] I. Avrutsky, I. Salakhutdinov, J. Elser, and V. Podolskiy. *Highly confined optical modes in nanoscale metal-dielectric multilayers.* Phys. Rev. B **75** (24), p. 241402 (2007).

[109] B. Prade, J. Y. Vinet, and A. Mysyrowicz. *Guided optical waves in planar heterostructures with negative dielectric constant.* Phys. Rev. B **44** (24), pp. 13556–13572 (1991).

[110] S. A. Maier. *Plasmonics: Fundamentals and Applications.* Springer, Berlin (2007).

[111] Z. Han and S. I. Bozhevolnyi. *Radiation guiding with surface plasmon polaritons.* Rep. Prog. Phys. **76** (1), p. 016402 (2013).

[112] J. A. Dionne, L. A. Sweatlock, H. A. Atwater, and A. Polman. *Plasmon slot waveguides: Towards chip-scale propagation with subwavelength-scale localization.* Phys. Rev. B **73** (3), p. 035407 (2006).

[113] S. I. Bozhevolnyi. *Effective-index modeling of channel plasmon polaritons.* Opt. Express **14** (20), pp. 9467–9476 (2006).

[114] S. I. Bozhevolnyi, V. S. Volkov, E. Devaux, J.-Y. Laluet, and T. W. Ebbesen. *Channelling surface plasmons.* Appl. Phys. A **89** (2), pp. 225–231 (2007).

[115] D. J. Bergman and M. I. Stockman. *Surface Plasmon Amplification by Stimulated Emission of Radiation: Quantum Generation of Coherent Surface Plasmons in Nanosystems.* Phys. Rev. Lett. **90** (2), p. 027402 (2003).

[116] S. A. Maier. *Gain-assisted propagation of electromagnetic energy in subwavelength surface plasmon polariton gap waveguides.* Opt. Commun. **258** (2), pp. 295–299 (2006).

[117] M. A. Noginov, G. Zhu, M. Mayy, B. A. Ritzo, N. Noginova, and V. A. Podolskiy. *Stimulated Emission of Surface Plasmon Polaritons.* Phys. Rev. Lett. **101** (22), p. 226806 (2008).

[118] I. De Leon and P. Berini. *Amplification of long-range surface plasmons by a dipolar gain medium.* Nat. Photonics **4** (6), pp. 382–387 (2010).

[119] J. A. Dionne, L. A. Sweatlock, H. A. Atwater, and A. Polman. *Planar metal plasmon waveguides: frequency-dependent dispersion, propagation, localization, and loss beyond the free electron model.* Phys. Rev. B **72** (7), p. 075405 (2005).

[120] D. Sarid. *Long-Range Surface-Plasma Waves on Very Thin Metal Films.* Phys. Rev. Lett. **47** (26), pp. 1927–1930 (1981).

[121] A. Boltasseva, T. Nikolajsen, K. Leosson, K. Kjaer, M. Larsen, and S. Bozhevolnyi. *Integrated optical components utilizing long-range surface plasmon polaritons.* J. Lightwave Technol. **23** (1), pp. 413–422 (2005).

[122] G. Mie. *Beiträge zur Optik trüber Medien, speziell kolloidaler Metallösungen.* Ann. Phys. **330** (3), pp. 377–445 (1908).

[123] C. F. Bohren and D. R. Huffman. *Absorption and Scattering of Light by Small Particles.* John Wiley & Sons, New York (1983).

[124] D. B. Davidson. *Computational Electromagnetics for RF and Microwave Engineering.* Cambridge University Press (2005).

[125] A. Taflove and S. C. Hagness. *Computational Electrodynamics: The Finite-Difference Time-Domain Method.* Artech House, Boston, 3rd edition (2005).

[126] {Lumerical Solutions Inc.}. *Lumerical Knowledge Base.* URL: https://kb.lumerical.com/en/index.html (2017).

[127] K. Yee. *Numerical solution of initial boundary value problems involving maxwell's equations in isotropic media.* IEEE Trans. Antennas Propag. **14** (3), pp. 302–307 (1966).

[128] U. S. Inan and R. A. Marshall. *Numerical Electromagnetics: The FDTD Method.* Cambridge University Press, Cambridge; New York (2011).

[129] J.-P. Berenger. *A perfectly matched layer for the absorption of electromagnetic waves.* J. Comput. Phys. **114** (2), pp. 185–200 (1994).

[130] D. S. Katz, E. T. Thiele, and A. Taflove. *Validation and extension to three dimensions of the Berenger PML absorbing boundary condition for FD-TD meshes.* IEEE Microw. Guided Wave Lett. **4** (8), pp. 268–270 (1994).

[131] R. L. Olmon, B. Slovick, T. W. Johnson, D. Shelton, S.-H. Oh, G. D. Boreman, and M. B. Raschke. *Optical dielectric function of gold.* Phys. Rev. B **86** (23), p. 235147 (2012).

[132] K. S. Chiang. *Review of numerical and approximate methods for the modal analysis of general optical dielectric waveguides.* Optical and Quantum Electronics **26** (3), pp. S113–S134 (1994).

[133] R. Scarmozzino, A. Gopinath, R. Pregla, and S. Helfert. *Numerical techniques for modeling guided-wave photonic devices.* IEEE J. Sel. Top. Quantum Electron. **6** (1), pp. 150–162 (2000).

[134] Z. Zhu and T. Brown. *Full-vectorial finite-difference analysis of microstructured optical fibers.* Opt. Express **10** (17), pp. 853–864 (2002).

[135] L. Novotny. *Effective Wavelength Scaling for Optical Antennas.* Phys. Rev. Lett. **98** (26), p. 266802 (2007).

[136] A. W. Snyder and J. Love. *Optical Waveguide Theory.* Chapman and Hall, London; New York (1983).

[137] A. Yariv and P. Yeh. *Photonics : Optical Electronics in Modern Communications.* Oxford University Press, New York, 6th edition (2007).

[138] J. A. Dionne, K. Diest, L. A. Sweatlock, and H. A. Atwater. *PlasMOStor: A Metal-Oxide-Si Field Effect Plasmonic Modulator.* Nano Lett. **9** (2), pp. 897–902 (2009).

[139] W. Cai, J. S. White, and M. L. Brongersma. *Compact, High-Speed and Power-Efficient Electrooptic Plasmonic Modulators.* Nano Lett. **9** (12), pp. 4403–4411 (2009).

[140] J. Wen, P. Banzer, A. Kriesch, D. Ploss, B. Schmauss, and U. Peschel. *Experimental cross-polarization detection of coupling far-field light to highly confined plasmonic gap modes via nanoantennas.* Appl. Phys. Lett. **98** (10), p. 101109 (2011).

[141] C. Ni, P. A. Hassan, and E. W. Kaler. *Structural Characteristics and Growth of Pentagonal Silver Nanorods Prepared by a Surfactant Method.* Langmuir **21** (8), pp. 3334–3337 (2005).

[142] M. I. Stockman. *Nanofocusing of Optical Energy in Tapered Plasmonic Waveguides.* Phys. Rev. Lett. **93** (13), p. 137404 (2004).

[143] D. K. Gramotnev. *Adiabatic nanofocusing of plasmons by sharp metallic grooves: Geometrical optics approach.* J. Appl. Phys. **98** (10), p. 104302 (2005).

[144] L. Lepetit, G. Cheriaux, and M. Joffre. *Linear techniques of phase measurement by femtosecond spectral interferometry for applications in spectroscopy.* J. Opt. Soc. Am. B **12** (12), pp. 2467–2474 (1995).

[145] C. Rewitz, T. Keitzl, P. Tuchscherer, S. Goetz, P. Geisler, G. Razinskas, B. Hecht, and T. Brixner. *Spectral-interference microscopy for characterization of functional plasmonic elements.* Opt. Express **20** (13), pp. 14632–14647 (2012).

[146] C. Rewitz, T. Keitzl, P. Tuchscherer, J.-S. Huang, P. Geisler, G. Razinskas, B. Hecht, and T. Brixner. *Ultrafast Plasmon Propagation in Nanowires Characterized by Far-Field Spectral Interferometry.* Nano Lett. **12** (1), pp. 45–49 (2012).

[147] H. Ditlbacher, A. Hohenau, D. Wagner, U. Kreibig, M. Rogers, F. Hofer, F. R. Aussenegg, and J. R. Krenn. *Silver Nanowires as Surface Plasmon Resonators.* Phys. Rev. Lett. **95** (25), p. 257403 (2005).

[148] Z. Li, K. Bao, Y. Fang, Y. Huang, P. Nordlander, and H. Xu. *Correlation between Incident and Emission Polarization in Nanowire Surface Plasmon Waveguides.* Nano Lett. **10** (5), pp. 1831–1835 (2010).

[149] T. Shegai, V. D. Miljković, K. Bao, H. Xu, P. Nordlander, P. Johansson, and M. Käll. *Unidirectional Broadband Light Emission from Supported Plasmonic Nanowires.* Nano Lett. **11** (2), pp. 706–711 (2011).

[150] M. Song, A. Bouhelier, P. Bramant, J. Sharma, E. Dujardin, D. Zhang, and G. Colas-des Francs. *Imaging Symmetry-Selected Corner Plasmon Modes in Penta-Twinned Crystalline Ag Nanowires.* ACS Nano **5** (7), pp. 5874–5880 (2011).

[151] J. Dorfmüller, R. Vogelgesang, W. Khunsin, C. Rockstuhl, C. Etrich, and K. Kern. *Plasmonic Nanowire Antennas: Experiment, Simulation, and Theory.* Nano Lett. **10** (9), pp. 3596–3603 (2010).

[152] E. Prodan, C. Radloff, N. J. Halas, and P. Nordlander. *A Hybridization Model for the Plasmon Response of Complex Nanostructures.* Science **302** (5644), pp. 419–422 (2003).

[153] P. Nordlander, C. Oubre, E. Prodan, K. Li, and M. I. Stockman. *Plasmon Hybridization in Nanoparticle Dimers.* Nano Lett. **4** (5), pp. 899–903 (2004).

[154] J.-S. Huang, J. Kern, P. Geisler, P. Weinmann, M. Kamp, A. Forchel, P. Biagioni, and B. Hecht. *Mode Imaging and Selection in Strongly Coupled Nanoantennas.* Nano Lett. **10** (6), pp. 2105–2110 (2010).

[155] P. J. Schuck, D. P. Fromm, A. Sundaramurthy, G. S. Kino, and W. E. Moerner. *Improving the Mismatch between Light and Nanoscale Objects with Gold Bowtie Nanoantennas.* Phys. Rev. Lett. **94** (1), p. 017402 (2005).

[156] S. Berweger, J. M. Atkin, R. L. Olmon, and M. B. Raschke. *Light on the Tip of a Needle: Plasmonic Nanofocusing for Spectroscopy on the Nanoscale.* J. Phys. Chem. Lett. **3** (7), pp. 945–952 (2012).

[157] G. Razinskas, P. Biagioni, and B. Hecht. *Limits of Kirchhoff's Laws in Plasmonics.* Sci. Rep. **8** (1921), pp. 1–9 (2018).

[158] C. Rewitz, G. Razinskas, P. Geisler, E. Krauss, S. Goetz, M. Pawłowska, B. Hecht, and T. Brixner. *Coherent Control of Plasmon Propagation in a Nanocircuit.* Phys. Rev. Applied **1** (1), p. 014007 (2014).

[159] N. Engheta, A. Salandrino, and A. Alù. *Circuit Elements at Optical Frequencies: Nanoinductors, Nanocapacitors, and Nanoresistors.* Phys. Rev. Lett. **95** (9), p. 095504 (2005).

[160] A. Alù and N. Engheta. *Tuning the scattering response of optical nanoantennas with nanocircuit loads.* Nat. Photonics **2** (5), pp. 307–310 (2008).

[161] J. Berthelot, A. Bouhelier, C. Huang, J. Margueritat, G. Colas-des Francs, E. Finot, J.-C. Weeber, A. Dereux, S. Kostcheev, H. I. E. Ahrach, A.-L. Baudrion, J. Plain, R. Bachelot, P. Royer, and G. P. Wiederrecht. *Tuning of an Optical Dimer Nanoantenna by Electrically Controlling Its Load Impedance.* Nano Lett. **9** (11), pp. 3914–3921 (2009).

[162] J.-J. Greffet, M. Laroche, and F. Marquier. *Impedance of a Nanoantenna and a Single Quantum Emitter.* Phys. Rev. Lett. **105** (11), p. 117701 (2010).

[163] A. Alù and N. Engheta. *Wireless at the Nanoscale: Optical Interconnects using Matched Nanoantennas.* Phys. Rev. Lett. **104** (21), p. 213902 (2010).

[164] N. Liu, F. Wen, Y. Zhao, Y. Wang, P. Nordlander, N. J. Halas, and A. Alù. *Individual Nanoantennas Loaded with Three-Dimensional Optical Nanocircuits.* Nano Lett. **13** (1), pp. 142–147 (2013).

[165] R. L. Olmon and M. B. Raschke. *Antenna–load interactions at optical frequencies: impedance matching to quantum systems.* Nanotechnology **23** (44), p. 444001 (2012).

[166] B. Abasahl, C. Santschi, and O. J. F. Martin. *Quantitative Extraction of Equivalent Lumped Circuit Elements for Complex Plasmonic Nanostructures.* ACS Photonics **1** (5), pp. 403–407 (2014).

[167] D. Li and E.-P. Li. *Impedance calculation and equivalent circuits for metal–insulator–metal plasmonic waveguide geometries.* Opt. Lett. **38** (17), p. 3384 (2013).

[168] A. Alù and N. Engheta. *Input Impedance, Nanocircuit Loading, and Radiation Tuning of Optical Nanoantennas.* Phys. Rev. Lett. **101** (4), p. 043901 (2008).

[169] T. Kaiser, S. B. Hasan, T. Paul, T. Pertsch, and C. Rockstuhl. *Impedance generalization for plasmonic waveguides beyond the lumped circuit model.* Phys. Rev. B **88** (3), p. 035117 (2013).

[170] Y. Xu, E. Tucker, G. Boreman, M. B. Raschke, and B. A. Lail. *Optical Nanoantenna Input Impedance.* ACS Photonics **3** (5), pp. 881–885 (2016).

[171] P. Ginzburg and M. Orenstein. *Plasmonic transmission lines: from micro to nano scale with λ/4 impedance matching.* Opt. Express **15** (11), pp. 6762–6767 (2007).

[172] S. E. Kocabas, G. Veronis, D. A. B. Miller, and S. Fan. *Transmission Line and Equivalent Circuit Models for Plasmonic Waveguide Components.* IEEE J. Sel. Top. Quantum Electron. **14** (6), pp. 1462–1472 (2008).

[173] G. Veronis, Ş. E. Kocabaş, D. A. B. Miller, and S. Fan. *Modeling of Plasmonic Waveguide Components and Networks.* J. Comput. Theor. Nanosci. **6** (8), pp. 1808–1826 (2009).

[174] A. Pannipitiya, I. D. Rukhlenko, M. Premaratne, H. T. Hattori, and G. P. Agrawal. *Improved transmission model for metal-dielectric-metal plasmonic waveguides with stub structure.* Opt. Express **18** (6), pp. 6191–6204 (2010).

[175] T. H. Taminiau, F. D. Stefani, and N. F. van Hulst. *Optical Nanorod Antennas Modeled as Cavities for Dipolar Emitters: Evolution of Sub- and Super-Radiant Modes.* Nano Lett. **11** (3), pp. 1020–1024 (2011).

[176] D. K. Cheng. *Field and wave electromagnetics.* Addison-Wesley Publishing Company, 2nd edition (1989).

[177] A. Reiserer, J.-S. Huang, B. Hecht, and T. Brixner. *Subwavelength broadband splitters and switches for femtosecond plasmonic signals.* Opt. Express **18** (11), pp. 11810–11820 (2010).

[178] K. Kurokawa. *Power Waves and the Scattering Matrix.* IEEE Trans. Microw. Theory Tech. **13** (2), pp. 194–202 (1965).

[179] P. Geisler, E. Krauss, G. Razinskas, and B. Hecht. *Transmission of Plasmons through a Nanowire.* ACS Photonics **4** (7), pp. 1615–1620 (2017).

[180] Y. Gorodetski, T. Chervy, S. Wang, J. A. Hutchison, A. Drezet, C. Genet, and T. W. Ebbesen. *Tracking surface plasmon pulses using ultrafast leakage imaging.* Optica **3** (1), pp. 48–53 (2016).

[181] B. Wild, L. Cao, Y. Sun, B. P. Khanal, E. R. Zubarev, S. K. Gray, N. F. Scherer, and M. Pelton. *Propagation Lengths and Group Velocities of Plasmons in Chemically Synthesized Gold and Silver Nanowires.* ACS Nano **6** (1), pp. 472–482 (2012).

[182] A. Andryieuski, R. Malureanu, G. Biagi, T. Holmgaard, and A. Lavrinenko. *Compact dipole nanoantenna coupler to plasmonic slot waveguide.* Opt. Lett. **37** (6), pp. 1124–1126 (2012).

[183] P. Kusar, C. Gruber, A. Hohenau, and J. Krenn. *Measurement and reduction of damping in plasmonic nanowires.* Nano Lett. **12** (2), pp. 661–665 (2012).

[184] B. J. Wiley, D. J. Lipomi, J. Bao, F. Capasso, and G. M. Whitesides. *Fabrication of Surface Plasmon Resonators by Nanoskiving Single-Crystalline Gold Microplates.* Nano Lett. **8** (9), pp. 3023–3028 (2008).

[185] B. Radha, D. Jayaraj, G. U. Kulkarni, S. Heun, D. Ercolani, and L. Sorba. *Large-Area Ohmic Top Contact to Vertically Grown Nanowires Using a Free-Standing Au Microplate Electrode.* ACS Appl. Mater. Interfaces **4** (4), pp. 1860–1864 (2012).

[186] F. Pashaee, R. Hou, P. Gobbo, M. S. Workentin, and F. Lagugné-Labarthet. *Tip-Enhanced Raman Spectroscopy of Self-Assembled Thiolated Monolayers on Flat Gold Nanoplates Using Gaussian-Transverse and Radially Polarized Excitations.* J. Phys. Chem. C **117** (30), pp. 15639–15646 (2013).

[187] X. Xia, M. Rycenga, D. Qin, and Y. Xia. *A silver nanocube on a gold microplate as a well-defined and highly active substrate for SERS detection.* J. Mater. Chem. C **1** (38), pp. 6145–6150 (2013).

[188] Z. Yan, Y. Bao, U. Manna, R. A. Shah, and N. F. Scherer. *Enhancing Nanoparticle Electrodynamics with Gold Nanoplate Mirrors.* Nano Lett. **14** (5), pp. 2436–2442 (2014).

[189] M. Song, B. Wu, G. Chen, Y. Liu, X. Ci, E. Wu, and H. Zeng. *Photoluminescence Plasmonic Enhancement of Single Quantum Dots Coupled to Gold Microplates.* J. Phys. Chem. C **118** (16), pp. 8514–8520 (2014).

[190] X. Wu, P. Geisler, E. Krauss, R. Kullock, and B. Hecht. *Silica–gold bilayer-based transfer of focused ion beam-fabricated nanostructures.* Nanoscale **7** (39), pp. 16427–16433 (2015).

[191] C. Fabry and A. Pérot. *Théorie et applications d'une nouvelle méthode de spectroscopie interférentielle.* Ann. Chim. Phys. **16** (7), pp. 115–144 (1899).

[192] D. Hofstetter and R. L. Thornton. *Theory of loss measurements of Fabry Perot resonators by Fourier analysis of the transmission spectra.* Opt. Lett. **22** (24), pp. 1831–1833 (1997).

[193] P. Geisler, G. Razinskas, E. Krauss, X.-F. Wu, C. Rewitz, P. Tuchscherer, S. Goetz, C.-B. Huang, T. Brixner, and B. Hecht. *Multimode Plasmon Excitation and In Situ Analysis in Top-Down Fabricated Nanocircuits.* Phys. Rev. Lett. **111** (18), p. 183901 (2013).

[194] Y.-T. Hung, C.-B. Huang, and J.-S. Huang. *Plasmonic mode converter for controlling optical impedance and nanoscale light-matter interaction.* Opt. Express **20** (18), pp. 20342–20355 (2012).

[195] D.-S. Ly-Gagnon, K. C. Balram, J. S. White, P. Wahl, M. L. Brongersma, and D. A. Miller. *Routing and photodetection in subwavelength plasmonic slot waveguides.* Nanophotonics **1** (1), pp. 9–16 (2012).

[196] J. Wen, S. Romanov, and U. Peschel. *Excitation of plasmonic gap waveguides by nanoantennas.* Opt. Express **17** (8), pp. 5925–5932 (2009).

[197] R. Kolesov, B. Grotz, G. Balasubramanian, R. J. Stöhr, A. A. L. Nicolet, P. R. Hemmer, F. Jelezko, and J. Wrachtrup. *Wave–particle duality of single surface plasmon polaritons.* Nat. Phys. **5** (7), pp. 470–474 (2009).

[198] S. Goetz, G. Razinskas, E. Krauss, C. Dreher, M. Wurdack, P. Geisler, M. Pawłowska, B. Hecht, and T. Brixner. *Investigation of the nonlinear refractive index of single-crystalline thin gold films and plasmonic nanostructures.* Appl. Phys. B **122** (4), p. 94 (2016).

[199] M. Aeschlimann, M. Bauer, D. Bayer, T. Brixner, F. J. García de Abajo, W. Pfeiffer, M. Rohmer, C. Spindler, and F. Steeb. *Adaptive subwavelength control of nano-optical fields.* Nature **446** (7133), pp. 301–304 (2007).

[200] M. Aeschlimann, M. Bauer, D. Bayer, T. Brixner, S. Cunovic, F. Dimler, A. Fischer, W. Pfeiffer, M. Rohmer, C. Schneider, F. Steeb, C. Strüber, and D. V. Voronine. *Spatiotemporal control of nanooptical excitations.* Proc. Natl. Acad. Sci. U.S.A. **107** (12), pp. 5329–5333 (2010).

[201] P. Melchior, D. Bayer, C. Schneider, A. Fischer, M. Rohmer, W. Pfeiffer, and M. Aeschlimann. *Optical near-field interference in the excitation of a bowtie nanoantenna.* Phys. Rev. B **83** (23), p. 235407 (2011).

[202] J.-m. Liu. *Photonic Devices.* Cambridge University Press, Cambridge, England (2005).

[203] G. Lenz, J. Zimmermann, T. Katsufuji, M. E. Lines, H. Y. Hwang, S. Spälter, R. E. Slusher, S.-W. Cheong, J. S. Sanghera, and I. D. Aggarwal. *Large Kerr effect in bulk Se-based chalcogenide glasses.* Opt. Lett. **25** (4), pp. 254–256 (2000).

[204] P. Ginzburg, A. Hayat, N. Berkovitch, and M. Orenstein. *Nonlocal ponderomotive nonlinearity in plasmonics.* Opt. Lett. **35** (10), pp. 1551–1553 (2010).

[205] S. Palomba and L. Novotny. *Nonlinear Excitation of Surface Plasmon Polaritons by Four-Wave Mixing.* Phys. Rev. Lett. **101** (5), p. 056802 (2008).

[206] J. Renger, R. Quidant, N. van Hulst, and L. Novotny. *Surface-Enhanced Nonlinear Four-Wave Mixing.* Phys. Rev. Lett. **104** (4), p. 046803 (2010).

[207] M. Lippitz, M. A. van Dijk, and M. Orrit. *Third-Harmonic Generation from Single Gold Nanoparticles.* Nano Lett. **5** (4), pp. 799–802 (2005).

[208] T. Hanke, G. Krauss, D. Träutlein, B. Wild, R. Bratschitsch, and A. Leitenstorfer. *Efficient Nonlinear Light Emission of Single Gold Optical Antennas Driven by Few-Cycle Near-Infrared Pulses.* Phys. Rev. Lett. **103** (25), p. 257404 (2009).

[209] M. Hentschel, T. Utikal, H. Giessen, and M. Lippitz. *Quantitative Modeling of the Third Harmonic Emission Spectrum of Plasmonic Nanoantennas.* Nano Lett. **12** (7), pp. 3778–3782 (2012).

[210] R. W. Boyd, Z. Shi, and I. De Leon. *The third-order nonlinear optical susceptibility of gold.* Opt. Commun. **326**, pp. 74–79 (2014).

[211] D. D. Smith, Y. Yoon, R. W. Boyd, J. K. Campbell, L. A. Baker, R. M. Crooks, and M. George. *Z-scan measurement of the nonlinear absorption of a thin gold film.* J. Appl. Phys. **86** (11), p. 6200 (1999).

[212] P. Wang, Y. Lu, L. Tang, J. Zhang, H. Ming, J. Xie, F.-H. Ho, H.-H. Chang, H.-Y. Lin, and D.-P. Tsai. *Surface-enhanced optical nonlinearity of a gold film.* Opt. Commun. **229**, pp. 425–429 (2004).

[213] N. Rotenberg, A. D. Bristow, M. Pfeiffer, M. Betz, and H. M. van Driel. *Nonlinear absorption in Au films: Role of thermal effects.* Phys. Rev. B **75** (15), p. 155426 (2007).

[214] E. Xenogiannopoulou, P. Aloukos, S. Couris, E. Kaminska, A. Piotrowska, and E. Dynowska. *Third-order nonlinear optical properties of thin sputtered gold films.* Opt. Commun. **275** (1), pp. 217–222 (2007).

[215] D. K. Gramotnev, K. C. Vernon, and D. F. P. Pile. *Directional coupler using gap plasmon waveguides.* Appl. Phys. B **93** (1), pp. 99–106 (2008).

[216] A. Kriesch, S. P. Burgos, D. Ploss, H. Pfeifer, H. A. Atwater, and U. Peschel. *Functional Plasmonic Nanocircuits with Low Insertion and Propagation Losses.* Nano Lett. **13** (9), pp. 4539–4545 (2013).

[217] A. Assion, T. Baumert, M. Bergt, T. Brixner, B. Kiefer, V. Seyfried, M. Strehle, and G. Gerber. *Control of Chemical Reactions by Feedback-Optimized Phase-Shaped Femtosecond Laser Pulses.* Science **282** (5390), pp. 919–922 (1998).

[218] W.-H. Dai, F.-C. Lin, C.-B. Huang, and J.-S. Huang. *Mode Conversion in High-Definition Plasmonic Optical Nanocircuits.* Nano Lett. **14** (7), pp. 3881–3886 (2014).

[219] E. Verhagen, M. Spasenović, A. Polman, and L. K. Kuipers. *Nanowire Plasmon Excitation by Adiabatic Mode Transformation.* Phys. Rev. Lett. **102** (20), p. 203904 (2009).

[220] M. Cinchetti, A. Gloskovskii, S. A. Nepjiko, G. Schönhense, H. Rochholz, and M. Kreiter. *Photoemission Electron Microscopy as a Tool for the Investigation of Optical Near Fields.* Phys. Rev. Lett. **95** (4), p. 047601 (2005).

[221] T. Brixner and G. Gerber. *Femtosecond polarization pulse shaping.* Opt. Lett. **26** (8), pp. 557–559 (2001).

[222] M. M. Wefers and K. A. Nelson. *Space-time profiles of shaped ultrafast optical waveforms.* IEEE J. Quant. Electron. **32** (1), pp. 161–172 (1996).

[223] F. Frei, A. Galler, and T. Feurer. *Space-time coupling in femtosecond pulse shaping and its effects on coherent control.* J. Chem. Phys. **130**, p. 034302 (2009).

[224] D. Brinks, R. Hildner, F. D. Stefani, and N. F. v. Hulst. *Beating spatio-temporal coupling: implications for pulse shaping and coherent control experiments.* Opt. Express **19** (27), pp. 26486–26499 (2011).

[225] M. Pawłowska, S. Goetz, C. Dreher, M. Wurdack, E. Krauss, G. Razinskas, P. Geisler, B. Hecht, and T. Brixner. *Shaping and spatiotemporal characterization of sub-10-fs pulses focused by a high-NA objective.* Opt. Express **22** (25), pp. 31496–31510 (2014).

[226] T. Wu, J. Tang, B. Hajj, and M. Cui. *Phase resolved interferometric spectral modulation (PRISM) for ultrafast pulse measurement and compression.* Opt. Express **19** (14), pp. 12961–12968 (2011).

[227] T. Brixner, F. J. García de Abajo, J. Schneider, and W. Pfeiffer. *Nanoscopic Ultrafast Space-Time-Resolved Spectroscopy.* Phys. Rev. Lett. **95** (9), p. 093901 (2005).

[228] A. R. Davoyan, I. V. Shadrivov, A. A. Zharov, D. K. Gramotnev, and Y. S. Kivshar. *Nonlinear Nanofocusing in Tapered Plasmonic Waveguides.* Phys. Rev. Lett. **105** (11), p. 116804 (2010).

[229] S. H. Crutcher, A. Osei, and A. Biswas. *Nonlinear evolution equations for surface plasmons for nano-focusing at a Kerr/metallic interface and tapered waveguide.* Opt. Laser Technol. **44** (4), pp. 1156–1162 (2012).

[230] A. Kubo, N. Pontius, and H. Petek. *Femtosecond Microscopy of Surface Plasmon Polariton Wave Packet Evolution at the Silver/Vacuum Interface.* Nano Lett. **7** (2), pp. 470–475 (2007).

[231] L. Zhang, A. Kubo, L. Wang, H. Petek, and T. Seideman. *Imaging of surface plasmon polariton fields excited at a nanometer-scale slit.* Phys. Rev. B **84** (24), p. 245442 (2011).

[232] C. Lemke, T. Leißner, S. Jauernik, A. Klick, J. Fiutowski, J. Kjelstrup-Hansen, H.-G. Rubahn, and M. Bauer. *Mapping surface plasmon polariton propagation via counter-propagating light pulses.* Opt. Express **20** (12), pp. 12877–12884 (2012).

[233] C. Lemke, C. Schneider, T. Leißner, D. Bayer, J. W. Radke, A. Fischer, P. Melchior, A. B. Evlyukhin, B. N. Chichkov, C. Reinhardt, M. Bauer, and M. Aeschlimann. *Spatiotemporal Characterization of SPP Pulse Propagation in Two-Dimensional Plasmonic Focusing Devices.* Nano Lett. **13** (3), pp. 1053–1058 (2013).

[234] N. Buckanie, P. Kirschbaum, S. Sindermann, and F.-J. Meyer zu Heringdorf. *Interaction of light and surface plasmon polaritons in Ag Islands studied by nonlinear photoemission microscopy.* Ultramicroscopy **130**, pp. 49–53 (2013).

[235] L. I. Chelaru and F.-J. Meyer zu Heringdorf. *In situ monitoring of surface plasmons in single-crystalline Ag-nanowires.* Surf. Sci. **601** (18), pp. 4541–4545 (2007).

[236] L. Douillard, F. Charra, Z. Korczak, R. Bachelot, S. Kostcheev, G. Lerondel, P.-M. Adam, and P. Royer. *Short Range Plasmon Resonators Probed by Photoemission Electron Microscopy.* Nano Lett. **8** (3), pp. 935–940 (2008).

[237] T. Leißner, C. Lemke, S. Jauernik, M. Müller, J. Fiutowski, L. Tavares, K. Thilsing-Hansen, J. Kjelstrup-Hansen, O. Magnussen, H.-G. Rubahn, and M. Bauer. *Surface plasmon polariton propagation in organic nanofiber based plasmonic waveguides.* Opt. Express **21** (7), pp. 8251–8260 (2013).

[238] J. P. S. Fitzgerald, R. C. Word, S. D. Saliba, and R. Könenkamp. *Photonic near-field imaging in multiphoton photoemission electron microscopy.* Phys. Rev. B **87** (20), p. 205419 (2013).

[239] R. C. Word, J. P. S. Fitzgerald, and R. Könenkamp. *Direct coupling of photonic modes and surface plasmon polaritons observed in 2-photon PEEM.* Opt. Express **21** (25), pp. 30507–30520 (2013).

[240] J. P. S. Fitzgerald, R. C. Word, and R. Könenkamp. *Subwavelength visualization of light in thin film waveguides with photoelectrons.* Phys. Rev. B **89** (19), p. 195129 (2014).

[241] E. Mårsell, A. Losquin, R. Svärd, M. Miranda, C. Guo, A. Harth, E. Lorek, J. Mauritsson, C. L. Arnold, H. Xu, A. L'Huillier, and A. Mikkelsen. *Nanoscale Imaging of Local Few-Femtosecond Near-Field Dynamics within a Single Plasmonic Nanoantenna.* Nano Lett. **15** (10), pp. 6601–6608 (2015).

[242] C. Awada, T. Popescu, L. Douillard, F. Charra, A. Perron, H. Yockell-Lelièvre, A.-L. Baudrion, P.-M. Adam, and R. Bachelot. *Selective Excitation of Plasmon Resonances of Single Au Triangles by Polarization-Dependent Light Excitation.* J. Phys. Chem. C **116** (27), pp. 14591–14598 (2012).

[243] P. Kahl, S. Wall, C. Witt, C. Schneider, D. Bayer, A. Fischer, P. Melchior, M. Horn-von Hoegen, M. Aeschlimann, and F.-J. Mayer zu Heringdorf. *Normal-Incidence Photoemission Electron Microscopy (NI-PEEM) for Imaging Surface Plasmon Polaritons.* Plasmonics **9** (6), pp. 1401–1407 (2014).

[244] F. Schertz, M. Schmelzeisen, R. Mohammadi, M. Kreiter, H.-J. Elmers, and G. Schönhense. *Near Field of Strongly Coupled Plasmons: Uncovering Dark Modes.* Nano Lett. **12** (4), pp. 1885–1890 (2012).

[245] X. Wu, P. Jiang, G. Razinskas, Y. Huo, H. Zhang, M. Kamp, A. Rastelli, O. G. Schmidt, B. Hecht, K. Lindfors, and M. Lippitz. *On-Chip Single-Plasmon Nanocircuit Driven by a Self-Assembled Quantum Dot.* Nano Lett. **17** (7), pp. 4291–4296 (2017).

[246] S. A. Wolf, D. D. Awschalom, R. A. Buhrman, J. M. Daughton, S. Von Molnar, M. L. Roukes, A. Y. Chtchelkanova, and D. M. Treger. *Spintronics: a spin-based electronics vision for the future.* Science **294** (5546), pp. 1488–1495 (2001).

[247] I. Žutić, J. Fabian, and S. D. Sarma. *Spintronics: Fundamentals and applications.* Rev. Mod. Phys. **76** (2), pp. 323–410 (2004).

[248] T. Jungwirth, J. Wunderlich, and K. Olejník. *Spin Hall effect devices.* Nat. Mater. **11** (5), pp. 382–390 (2012).

[249] R. Y. Chiao and Y.-S. Wu. *Manifestations of Berry's Topological Phase for the Photon.* Phys. Rev. Lett. **57** (8), pp. 933–936 (1986).

[250] M. Berry. *The Adiabatic Phase and Pancharatnam's Phase for Polarized Light.* J. Mod. Opt. **34** (11), pp. 1401–1407 (1987).

[251] K. Y. Bliokh, A. Niv, V. Kleiner, and E. Hasman. *Geometrodynamics of spinning light.* Nat. Photonics **2** (12), pp. 748–753 (2008).

[252] T. H. Chyba, R. Simon, L. J. Wang, and L. Mandel. *Measurement of the Pancharatnam phase for a light beam.* Opt. Lett. **13** (7), pp. 562–564 (1988).

[253] D. L. P. Vitullo, C. C. Leary, P. Gregg, R. A. Smith, D. V. Reddy, S. Ramachandran, and M. G. Raymer. *Observation of Interaction of Spin and Intrinsic Orbital Angular Momentum of Light.* Phys. Rev. Lett. **118** (8), p. 083601 (2017).

[254] K. Y. Bliokh, F. J. Rodríguez-Fortuño, F. Nori, and A. V. Zayats. *Spin-orbit interactions of light.* Nat. Photonics **9** (12), pp. 796–808 (2015).

[255] F. J. Rodríguez-Fortuño, G. Marino, P. Ginzburg, D. O'Connor, A. Martínez, G. A. Wurtz, and A. V. Zayats. *Near-Field Interference for the Unidirectional Excitation of Electromagnetic Guided Modes.* Science **340** (6130), pp. 328–330 (2013).

[256] J. Petersen, J. Volz, and A. Rauschenbeutel. *Chiral nanophotonic waveguide interface based on spin-orbit interaction of light.* Science **346** (6205), pp. 67–71 (2014).

[257] P. Lodahl, S. Mahmoodian, S. Stobbe, A. Rauschenbeutel, P. Schneeweiss, J. Volz, H. Pichler, and P. Zoller. *Chiral quantum optics.* Nature **541** (7638), pp. 473–480 (2017).

[258] Y. Lefier and T. Grosjean. *Unidirectional sub-diffraction waveguiding based on optical spin–orbit coupling in subwavelength plasmonic waveguides.* Opt. Lett. **40** (12), pp. 2890–2893 (2015).

[259] D. Pan, H. Wei, L. Gao, and H. Xu. *Strong Spin-Orbit Interaction of Light in Plasmonic Nanostructures and Nanocircuits.* Phys. Rev. Lett. **117** (16), p. 166803 (2016).

[260] S. Mahmoodian, P. Lodahl, and A. S. Sørensen. *Quantum Networks with Chiral-Light-Matter Interaction in Waveguides.* Phys. Rev. Lett. **117** (24), p. 240501 (2016).

[261] J. L. O'Brien, A. Furusawa, and J. Vučković. *Photonic quantum technologies.* Nat. Photonics **3** (12), pp. 687–695 (2009).

[262] N. P. d. Leon, M. D. Lukin, and H. Park. *Quantum Plasmonic Circuits.* IEEE J. Sel. Top. Quantum Electron. **18** (6), pp. 1781–1791 (2012).

[263] A. Huck and U. L. Andersen. *Coupling single emitters to quantum plasmonic circuits.* Nanophotonics **5** (3), pp. 483–495 (2016).

[264] J. S. Fakonas, H. Lee, Y. A. Kelaita, and H. A. Atwater. *Two-plasmon quantum interference.* Nat. Photonics **8** (4), pp. 317–320 (2014).

[265] A. J. Shields. *Semiconductor quantum light sources.* Nat. Photonics **1** (4), pp. 215–223 (2007).

[266] O. Gazzano, M. P. Almeida, A. K. Nowak, S. L. Portalupi, A. Lemaître, I. Sagnes, A. G. White, and P. Senellart. *Entangling Quantum-Logic Gate Operated with an Ultrabright Semiconductor Single-Photon Source.* Phys. Rev. Lett. **110** (25), p. 250501 (2013).

[267] M. Müller, S. Bounouar, K. D. Jöns, M. Glässl, and P. Michler. *On-demand generation of indistinguishable polarization-entangled photon pairs.* Nat. Photonics **8** (3), pp. 224–228 (2014).

[268] P. Lodahl, S. Mahmoodian, and S. Stobbe. *Interfacing single photons and single quantum dots with photonic nanostructures.* Rev. Mod. Phys. **87** (2), pp. 347–400 (2015).

[269] C. P. Dietrich, A. Fiore, M. G. Thompson, M. Kamp, and S. Höfling. *GaAs integrated quantum photonics: Towards compact and multi-functional quantum photonic integrated circuits.* Laser Photon. Rev. **10** (6), pp. 870–894 (2016).

[270] H. S. Lee, M. S. Kim, Y. Jin, G. H. Han, Y. H. Lee, and J. Kim. *Efficient Exciton–Plasmon Conversion in Ag Nanowire/Monolayer MoS2 Hybrids: Direct Imaging and Quantitative Estimation of Plasmon Coupling and Propagation.* Adv. Opt. Mater. **3** (7), pp. 943–947 (2015).

[271] J. de Torres, P. Ferrand, G. Colas des Francs, and J. Wenger. *Coupling Emitters and Silver Nanowires to Achieve Long-Range Plasmon-Mediated Fluorescence Energy Transfer.* ACS Nano **10** (4), pp. 3968–3976 (2016).

[272] J.-C. Weeber, K. Hammani, G. Colas-des Francs, A. Bouhelier, J. Arocas, A. Kumar, F. Eloi, S. Buil, X. Quélin, J.-P. Hermier, M. Nasilowski, and B. Dubertret. *Colloidal Quantum Dot Integrated Light Sources for Plasmon Mediated Photonic Waveguide Excitation.* ACS Photonics **3** (5), pp. 844–852 (2016).

[273] D. V. Regelman, U. Mizrahi, D. Gershoni, E. Ehrenfreund, W. V. Schoenfeld, and P. M. Petroff. *Semiconductor Quantum Dot: A Quantum Light Source of Multicolor Photons with Tunable Statistics.* Phys. Rev. Lett. **87** (25), p. 257401 (2001).

[274] R. F. Oulton, V. J. Sorger, D. A. Genov, D. F. P. Pile, and X. Zhang. *A hybrid plasmonic waveguide for subwavelength confinement and long-range propagation.* Nat. Photonics **2** (8), pp. 496–500 (2008).

[275] Z. Yuan, B. E. Kardynal, R. M. Stevenson, A. J. Shields, C. J. Lobo, K. Cooper, N. S. Beattie, D. A. Ritchie, and M. Pepper. *Electrically Driven Single-Photon Source.* Science **295** (5552), pp. 102–105 (2002).

[276] A. J. Bennett, D. C. Unitt, P. See, A. J. Shields, P. Atkinson, K. Cooper, and D. A. Ritchie. *Microcavity single-photon-emitting diode.* Appl. Phys. Lett. **86** (18), p. 181102 (2005).

[277] A. L. Falk, F. H. L. Koppens, C. L. Yu, K. Kang, N. de Leon Snapp, A. V. Akimov, M.-H. Jo, M. D. Lukin, and H. Park. *Near-field electrical detection of optical plasmons and single-plasmon sources.* Nat. Phys. **5** (7), pp. 475–479 (2009).

[278] R. W. Heeres, S. N. Dorenbos, B. Koene, G. S. Solomon, L. P. Kouwenhoven, and V. Zwiller. *On-Chip Single Plasmon Detection.* Nano Lett. **10** (2), pp. 661–664 (2010).

Acknowledgements

While my name may be alone on the front cover of this thesis, it goes without saying that the achievements reported here are rather a result of an outstanding working atmosphere, excellent teamwork, and fruitful scientific collaborations. Hence, I would like to acknowledge some people explicitly in the following.

Foremost, I would like to express my sincere gratitude to Prof. Dr. Bert Hecht for giving me the opportunity to work in this exciting research field. I have learned a lot and have benefited greatly from his continuous support, his enthusiasm and ideas, and his steady and valuable feedback in countless stimulating discussions.

I would also like to thank Prof. Dr. Tobias Brixner for his important contributions and joint innovative efforts within the DFG priority program "Ultrafast Nanooptics" (SPP 1391). His expertise and the regular meetings helped me to develop a broader perspective to my thesis.

I am also very thankful to Prof. Dr. Martin Aeschlimann, Dr. Deirdre Kilbane, and Dr. Pascal Melchior for providing a pleasant level of cooperation in the PEEM study of our plasmonic nanocircuits.

This work would have been impossible without the prosperous teamwork with my colleagues Peter Geisler, Enno Krauss, Dr. Christian Rewitz, Dr. Monika Pawłowska, and Sebastian Götz, which greatly promoted our joint research on plasmonic nanocircuitry. They have never been afraid of devoting their time to experimentally realizing ideas grown in the computer and continuously delivered great experimental results that needed a solid backing from simulations.

I further want to give thanks to Dr. Jer-Shing Huang, Dr. Paolo Biagioni, and Dr. Xiaofei Wu for various scientific discussions, which gave many valuable insights.

A big thanks goes to all former and current members of the Lehrstuhl für Experimentelle Physik V for the enjoyable and cooperative atmosphere. Especially, I appreciate the feedback from all members of the Hecht group at our weekly group meetings.

Words cannot express how thankful I am to all members of my family and family in-law for their continuous support and all the sacrifices you've made on my behalf. The love and guidance of my parents are with me in whatever I pursue. Dad was often in my thoughts on this journey - you are missed.

Finally, and most importantly, I wish to thank my beloved wife Stefanie and our wonderful children Lisa and David. Your incredible support, encouragement, patience, and unlimited love provide endless inspiration and the most incredible moments in my life. You always remind me of what is really important.